Computational Investigations of Heavy Element Complexes

Emma Margaret O'Grady

University College London

This thesis is submitted for the degree of PhD in Chemistry

ProQuest LLC
789 East Eisenhower Parkway
P.O. Box 1346
Ann Arbor, MI 48106-1346

Abstract

This thesis reports the computational studies of the ground state electronic properties of $[AnOX_5]^{n-}$ (An=Pa, n=2; U, n=1; Np, n=0; X=F, Cl, Br), of $[ClM(PH_3)]_2$ (M=Cu, Ag, Au, [111]) and of MX_3 (M=La-Lu, Ac-Lr; X=H, F, Cl, Br, I) using Density Functional Theory (DFT) and ab initio methods. Before presenting the results from these studies, the first chapter introduces computational studies of heavy element compounds through a discussion of selected studies taken from the literature. The second chapter introduces the electronic structure methods that were used during the course of this research. The results of this research are presented in chapters 3 to 5.

Chapter 3 discusses DFT studies of the inverse *trans* influence (ITI) of $[AnOX_5]^{n-}$ (An=Pa, n=2; U, n=1; Np, n=0; X=F, Cl, Br). These studies show that the ITI is due mainly to electronic factors; at the equilibrium geometry, the $9a_1$ molecular orbital of $[AnOX_5]^{n-}$, which is π^* along the An-X_{cis} bond, plays a key role in elongating the *cis* bond.

In chapter 4, the metallophilic interactions of the 6d transactinide coinage metal, [111], are presented. Comparison of the interaction energies of $[ClM(PH_3)]_2$ (M=Cu, Ag, Au, [111]), shows that with the exception of MP2, the post-HF (QCISD, CCSD and CCSD(T)) methods calculate that the interaction energies for the four complexes are approximately constant.

The final results chapter (chapter 5) examines the influence of the 4f orbitals in determining the extent of pyramidality of LnX_3 (Ln=La-Lu; X=H, F-I) using the B3PW91 method. This study reports that the 4f orbitals reduce the extent of pyramidality via a reduction in the 5d orbital-based second-order Jahn-Teller distortion. A comparison between LnX_3 and AnX_3 (An=Ac-Lr; X=H, F-I) is also made. The final chapter summarises the research.

Acknowledgements

First, I would like to thank Nik for his supervision and help throughout my PhD. I greatly appreciate the opportunities and support that he has given me during my four years at UCL.

I would also like to thank everyone with whom I have had the pleasure of sharing an office (formerly G25 and more recently G19). Of those, I would like to extend a special thank you to Giusy and Natalie. In addition, I would like to thank Linnea, who has been a great colleague and a great friend - I appreciate her support, and the many helpful comments that she gave me during the writing of this thesis.

Many thanks also to my family, and especially to my parents, for their never failing support throughout my life.

Last, and by no means least, I thank Damien, whose constant encouragement cannot be overemphasised; thank you for always being there.

Contents

List of Figures

List of Tables

Chapter 1

Overview of Chemistry of Heavy Elements

In the context of this thesis, in which the computational studies of heavy elements are reported, the aim of this chapter is to give a brief summary of some previous computational studies that have been carried out on lanthanide, actinide and transactinide compounds. I do not intend to provide an exhaustive review of all of the studies that have been published, but instead I would like to focus on studies that highlight some of the main characteristics of 4f, 5f and 6d elements. This summary is intended to provide a general introduction, since more specific introductions to the case studies of this work are given at the beginning of each of the individual chapters.

The first section is a very brief introduction to relativistic effects in heavy elements since a more detailed discussion of relativity in the context of computational approaches is given in section 2.5. In the second section, a general overview of the lanthanides and actinides are discussed. The aim of the initial part of this section is to highlight how the lanthanides and actinides differ in their electronic structures. This subject is then developed by considering specific examples of computational studies of the lanthanide and actinide compounds that highlight these differences. In this part, the role of the cyclooctatetraenyl, arene and cyclopentadienyl ligands in organolanthanide and organoactinide chemistry are first discussed. Subsequently the actinyl ion and actinide halides are described, which demonstrate the high oxidation states of the early actinides that are not present

for the lanthanides.

The third section briefly considers the results from studies that have been carried out on the 6d transactinides. The aim of this section is to consider the effect of relativity on these elements. This section is followed by a summary of the chapter.

1.1 Relativistic Effects on Heavy Elements

Comprehensive reviews of relativistic effects in chemistry can be found in the literature (e.g. references 1 and 2), which discuss the importance of relativity in studies of the lanthanides, actinides and transactinides. As the atomic number increases, relativity becomes more important, and for the cases of the transactinides, it is necessary to include relativity to produce even qualitatively correct data.[3]

When relativity is taken into account, the valence s and p orbitals experience a direct relativistic orbital contraction, and because this leads to increased nuclear shielding, the d and f orbitals experience an indirect relativistic orbital expansion. Given the increase in the number of electrons and of the interactions between electrons, the effects of correlation and spin-orbit coupling must often be taken into consideration too. A rule of thumb suggested by Dolg and Stoll[4] states that configurations with higher d and f occupations are stabilised by electron correlation but destabilised by relativity, and conversely, configurations with higher s and p occupations are stabilised by relativity. For the case of a lanthanide atom, this means that the $4f^n5d^16s^2$ configuration is stabilised by relativity but $4f^{n+1}6s^2$ is stabilised by electron correlation.

The fact that the reader will encounter references to relativity throughout this chapter highlights its importance when considering elements that are members of the lower part of the periodic table.

1.2 The f Elements

Although the lanthanides (Ce $\rightarrow$ Lu) are often referred to as 'rare-earth' metals, this is a misleading phrase since, apart from promethium, for which there are no stable isotopes, all of the lanthanides are found in greater abundance than iodine. The principal mineral source of the lanthanides is monazite, which is a mixed lanthanide phosphate. From this mineral, lanthanides can be obtained and separated.[5]

In contrast to the lanthanides, only thorium, protactinium and uranium of the actinide elements (Th $\rightarrow$ Lr) are naturally occurring. In fact, uranium is the heaviest naturally occurring element. Thorium can be obtained from monazite, and uranium is found in many oxide minerals, whereas protactinium is found in only trace amounts in uranium ores. The other actinides, the transuranium elements, are produced in nuclear reactors or via nuclear explosions.[5]

In this section, I present a brief description of the electronic structures of the chemically uniform lanthanides. This is followed by a description of the electronic structures of the actinides, which consists of the more chemically diverse early actinide series and the more chemically uniform later actinide elements.

1.2.1 Electronic Structures of the Lanthanides

In the lanthanide series, the valence orbitals are the 4f, 5d and 6s orbitals. The effect of relativity on the orbital energies and on the expectation values of the orbital radii for the lanthanide series is shown in figure 1.1 (figure 1.1(a) and 1.1(b) respectively).[4] This figure illustrates how the 6s orbital is relativistically stabilised and contracted. Also evident is that both the 5d and 4f orbitals are relativistically destabilised and expanded. This figure also illustrates the effect of spin-orbit splitting on the valence 5d (d+ and d-) and 4f (f+ and f-) orbitals, which increases quite noticeably for the 4f orbitals as the lanthanides are traversed.

Although the 4f orbitals of the lanthanides are comparable in energy with the other valence 5d and 6s orbitals, the 4f shell is spatially much more contracted. These contracted and radially nodeless 4f orbitals experience a high effective nuclear charge. Given an atomic ground state electronic configuration of f^n6s^2, in a molecule the lanthanide can generally give up its two 6s electrons and one of its 4f electrons to give a ground state electronic configuration of $f^{n-1}6s^0$. The remaining f electrons experience an even higher effective nuclear charge than in the atom, which contracts them and makes them extremely difficult to remove.[6] Hence, the members of the lanthanide series generally exhibit a common oxidation state of +3 and are consequently chemical uniform, as was mentioned earlier. The only exceptions to this occur in cerium (Ce), europium (Eu) and ytterbium (Yb) for which the tendency to have an empty, a half-full and a full 4f shell stabilises the Ce(IV), Eu(II) and Yb(II) oxidation states respectively.

The core-like 4f orbitals and the high effective nuclear charge of the lanthanides influences their bonding behaviour to be predominantly ionic.[6] The extent to which ionic interactions dictate lanthanide chemistry is illustrated in a study of

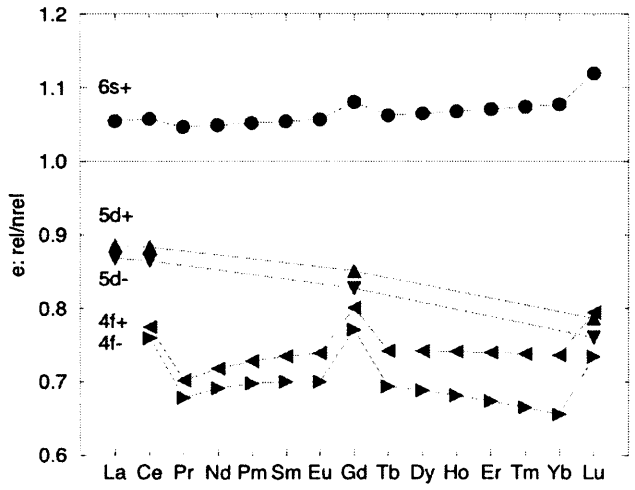

(a) Orbital energies

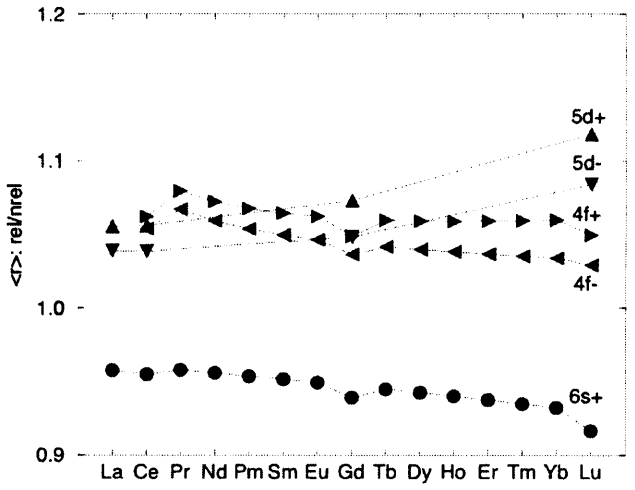

(b) Orbital radii

Figure 1.1: Ratio of relativistic and nonrelativistic orbital energies and expectation values of orbital radii for the valence orbitals of the lanthanide atoms in their ground state configuration. Reproduced from reference 4.

the lanthanide alkoxide [$LnCp_2OPh$] (Ln=La, Lu; Cp=η^5-C_5H_5; Ph=C_6H_5).[7] The linearity of the Ln-O-C(Ph) fragment was found to result from the electrostatic

repulsion between the α-C of the phenyl and the lanthanide centre, rather than due to π interactions. In fact, the authors find that the Ln-O π orbitals are non-bonding and reside on the oxygen, indicating a lack of covalent bonding.

The ionicity of the lanthanides and the additional fact that the lanthanides have a relatively large coordination sphere, rationalises why cyclopentadienyl ligands are particularly well suited to forming bonds with lanthanide centres; they are monoanionic ligands that occupy three coordination sites, so they are ideal providers of electrostatic and steric stabilisation in lanthanide chemistry.[8] This aspect is further discussed in section 1.3.3, in which selected computational studies of cyclopentadienyl lanthanide chemistry are discussed.

As the lanthanide series is traversed, the number of electrons, and hence the effective nuclear charge increases. This contributes to a contraction of the bond between the lanthanide centre and a particular ligand across the lanthanide series, which is known as the 'lanthanide contraction'. This contraction is generally defined as the difference between the metal-ligand bond for lanthanum and lutetium (i.e. $\Delta(r(\text{La-X})\text{-}r(\text{Lu-X}))$). Although there is some dependence on the contraction on the ligand in question (see chapter 5), it has been shown that the lanthanide contraction is mainly due to the ineffective screening of the nucleus by the 4f orbitals with a small contribution from relativity (10-30%).[2,9] Further, for the heavier 5f series, it has been found that the corresponding actinide contraction is more pronounced due to increased relativistic effects (40-50%).[9–11]

One final point to note before discussing the actinides is the role of computational methods in lanthanide chemistry. Although lanthanide compounds have partially filled f shells and hence are very often open shell systems, since the 4f electrons are considered to be core-like, it is often considered unnecessary to ac-

count for all possible states arising from the different ways that a given number of electrons can occupy the f orbitals. In fact, in many cases, the ground state properties of the molecules, such as the vibrational frequencies and bond lengths, have been shown to be unaffected by the specific electronic state. In this case, it is appropriate and convenient to describe all electronic states of the same f configuration by one superconfiguration. This so-called 'superconfiguration model' has been shown to be adequate (e.g. CeO discussed in reference 12) provided the 4f orbitals do not lose their core-like character in bonding.

1.2.2 Electronic Structures of the Actinides

The actinides, like the lanthanides, have partially filled f orbitals, but in contrast to the 4f orbitals of the lanthanides, the 5f orbitals of the actinides have a radial node. This is particularly significant for the early actinides, for which the 5f orbitals are more diffuse than the analogous lanthanide 4f orbitals, and can participate more in bonding. This gives the early actinides a chemical diversity that is not seen for the lanthanides since in addition to the 6d and 7s orbitals, the 5f orbitals are also available for chemical interaction. (Note that the 6p orbitals have also been shown to be involved in bonding, which is discussed in more detail below). For the later actinides, however, the effective nuclear charge increases, which causes the 5f orbitals to contract and become more core-like. Thus, the transamericium elements are generally considered to be more chemically similar to the lanthanides than to the earlier members of the actinides.

Similar to the lanthanides, the actinide s and p orbitals undergo a direct relativistic contraction, and the d and f orbitals undergo an indirect relativistic expansion. A comparison of the nonrelativistic and relativistic orbital energies for

uranium and neodymium is given in figure 1.2. At the nonrelativistic level (left side of figure 1.2), both neodymium and uranium exhibit orbital energies with $(n-2)\mathrm{f} \ll (n-1)\mathrm{d} < n\mathrm{s}$, although even without relativity, the 4f shell is more contracted than the 5f shell. This is a consequence of the greater influence of the nuclear charge in the 4f orbitals because the radial node in the 5f orbitals is absent in the 4f orbitals.

When relativity is included, both sets of orbitals show an expansion of the f and d orbitals and a contraction of the s orbitals. However, this effect is much more pronounced for uranium, the effect of which even shows a reversal of the ordering of the 6d and 7s orbitals (i.e. 5f < 7s < 6d). Uranium also exhibits more obvious spin-orbit splitting of the d and f orbitals. Thus figure 1.2 shows that the effect of relativity is more pronounced in the actinides than in the lanthanides.

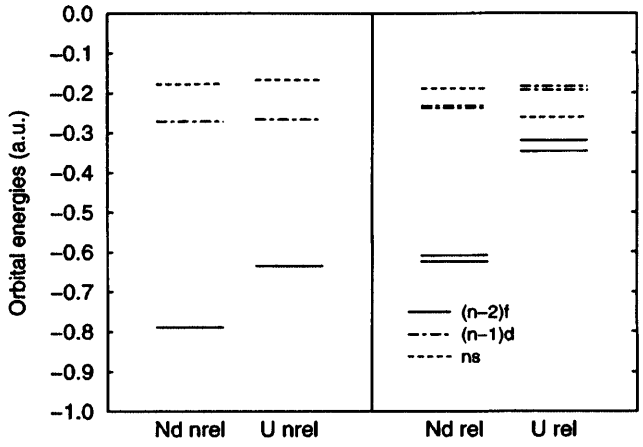

Figure 1.2: Nonrelativistic and relativistic orbital energies of neodymium and uranium (via Hartree Fock and Dirac Hartree Fock calculations) for $4f^3 5d^1 6s^2$ and $5f^3 6d^1 7s^2$ configurations respectively. Reproduced from reference 13.

One final aspect of the early actinides that I would like to point out is the role of the 6p orbitals. Although they lie lower in energy than the valence 5f, 6d and

7s orbitals, they have a similar radial extension, and so they are often referred to as 'semi-core'. This is illustrated for uranium in figure 1.3, from which it can clearly be seen that the maximum of the 6p orbital occurs between those of the 5f and 6d orbitals. One consequence of the 6p orbitals is the 'pushing from below' mechanism in the bonding of the uranyl ion, which is discussed in section 1.4.1.

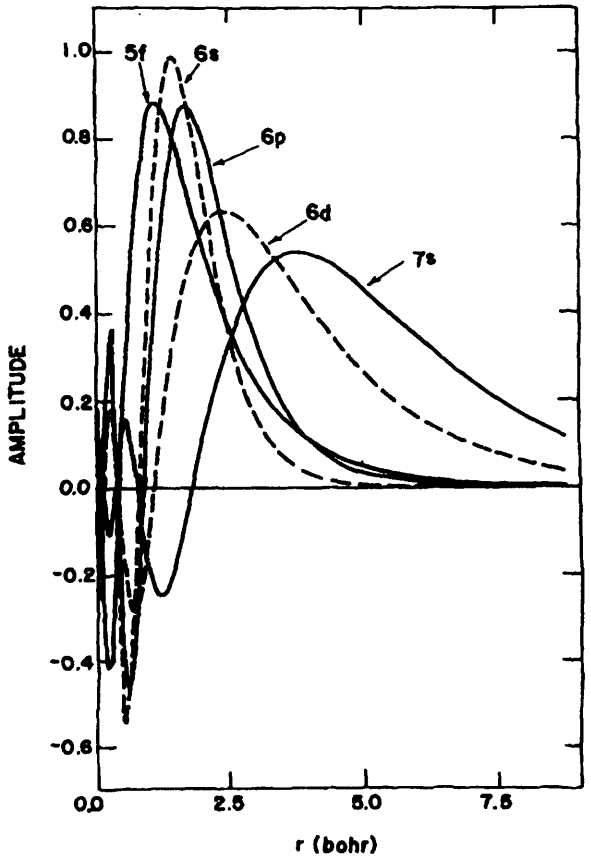

Figure 1.3: Amplitudes of the valence orbitals of the uranium atom from ab initio relativistic effective core potential calculations. Reproduced from reference 14.

1.3 Organometallics of the f-Block

I have already mentioned that the early actinides exhibit a chemical diversity that is not evident for the lanthanides. In this section, I will present selected results from previous computational studies of organolanthanide and organoactinide compounds, with the specific aim of highlighting some of the differences between the 4f and 5f block. Section 1.3.1 briefly discusses some examples of bis(cyclooctatetraenyl) complexes ($M(\eta^8\text{-}C_8H_8)_2$) of both the lanthanides and actinides. This discussion focuses on the contrasting $Ce(COT)_2$ and $Th(COT)_2$ ($COT=\eta^8\text{-}C_8H_8$), a situation that clearly shows differences between the lanthanides and actinides. This is followed by a description of MBz_2 ($Bz=\eta^6\text{-}C_6H_6$) for the lanthanides and actinides, which provides a second example of contrasting behaviour between lanthanide and actinide organometallic complexes. Subsequently the role of the cyclopentadienyl ligand ($\eta^5\text{-}C_5H_5$) in lanthanide and actinide chemistry is discussed.

1.3.1 Cyclooctatetraenyl Chemistry of the f-Block ($M(\eta^8\text{-}C_8H_8)_2$)

Since the prediction in 1963[15] and subsequent synthesis in 1968[16] of uranocene ($U(COT)_2$ ($COT=\eta^8\text{-}C_8H_8$)), many theoretical studies have been carried out on the 5f actinocenes. In the related lanthanide-containing complexes, a key factor was the synthesis in 1976 of $Ce(COT)_2$,[17] a molecule that has been the subject of relatively recent computational studies.

In this section, I will first give a brief description of the ground state electronic structure of D_{8h} $An(COT)_2$ (see figure 1.4). Here I focus mainly on the results

from two key contributions reported by Boerrigter, Baerends and Snijders[18] and by Chang and Pitzer,[19] and the more recent relativistic Density Functional calculations of f^1 $Pa(COT)_2$.[20,21] Further information about key computational studies of $An(COT)_2$ that have "played a key role in understanding their chemistry" is given in Pepper and Bursten's 1991 review of the electronic structure of actinides.[22]

Secondly, I will discuss $Ce(COT)_2$ as an example of a lanthanocene complex, and mention selected computational studies that have led to the conclusion that cerium is in an oxidation state of +3, rather than the value of +4 that is present in the actinide complex, $Th(COT)_2$. In addition, I will consider computational investigations of $Ln(COT)_2^-$ and the more elusive $Ln(COT)_2$, which have been carried out by Dolg, Fulde and co-workers, and I will mention the comparisons with the actinide complexes that have been made throughout.

Before I consider the bonding in $M(COT)_2$, I present first a conceptual view of the molecular orbitals in COT_2^{4-} in D_{8h} symmetry. In this case the two COT^{2-} rings are in an eclipsed conformation (as in figure 1.4 with the metal centre removed). The ordering of the energy levels in COT^{2-} and COT_2^{4-} and the COT molecular orbitals (MOs) that arise from the out-of-phase p orbitals of each carbon of the ring (the 'π' MOs; i.e. there is a node in the plane of the ring) are shown in figure 1.5. Note that these π MOs are occupied by 10 electrons (a_{2u}+e_{1g}+e_{2u}), which is consistent with Hückel's ($4N$+2) rule for aromaticity (that is, an aromatic system should have ($4N$+2) π electrons, where N is an integer). Also note that as the number of nodes (perpendicular to the ring) of a given MO increases, so too does the MO energy. This is also consistent with the ordering of the energy levels of other aromatic rings (e.g. benzene). Finally, the right-hand side of

figure 1.5 shows the splitting of the COT MOs when both rings are considered, which is due to the in-phase and out-of-phase interligand interactions of the two rings.

When this conceptually simple MO picture is extended to include an actinide at the centre of the two rings, the e_{2g} and e_{2u} MOs of COT_2^{4-} play key roles in the An-COT bonding. These two ligand MOs can interact with the metal MO of δ symmetry. The former e_{2g} MO can overlap with the $6d_\delta$ MO of the metal, and the latter e_{2u} MO can overlap with its $5f_\delta$ MO, both metal MOs lying higher in energy than the ligand orbitals. The fact that these interactions do occur shows covalency in the complex, and for $U(COT)_2$ and the other early actinocenes, this has been found to be significant in both cases. Other covalent interactions also arise from e_{1g}-$6d_\pi$ interactions and e_{3u}-$5f_\phi$ interactions.

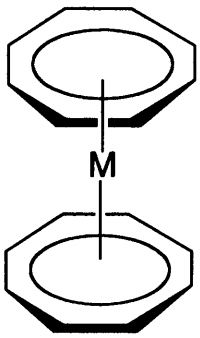

Figure 1.4: Schematic representation of $M(COT)_2$ with D_{8h} symmetry. The COT rings are orientated above and below the metal centre, and the centroid(COT)-M-centroid(COT) are collinear. The COT rings are eclipsed and parallel with each other and perpendicular to the centroid(COT)-M-centroid(COT) plane.

Boerrigter et al.'s Hartree Fock Slater (HFS) study of $An(COT)_2$ (An=Th, Pa,

U, Np, Pu) looked at both the effect of relativity (including spin-orbit coupling) and the effect of the actinide metal on the bonding in the actinocenes.[18] From this study, they found that in both the nonrelativistic and relativistic calculations the actinide 5f and 6d orbitals were involved in bonding. When relativity is included in the bonding description there is an increase in the $6d_\delta$ interactions and a decrease in the $5f_\delta$ interactions with the ligands. The authors attribute this to the balance between the relativistic upward shift of the energy levels versus the radial expansion of the orbitals; in the 6d orbitals, the latter is more important, so the $6d_\delta$ metal orbitals extend further and the e_{2u}-$6d_\delta$ interactions are relativistically enhanced. In contrast, the upward shift of energy levels dominate the relativistic effects in the e_{2g}-$5f_\delta$ interactions, so the poorer energy matching lowers the extent of these interactions. This also accounts for the increase in the $5f_\phi$ interactions with the higher-lying unoccupied e_{3u} ligand MO when relativity is included. The differential effect of relativity on the 5f and 6d orbitals is also reflected in the change of the orbital ordering on $Th(COT)_2$, in which the 6d orbitals lie lower in energy than the 5f orbitals.

However, despite the relativistically reduced 5f interactions, the spread of the f-orbital manifold indicates substantial involvement of the f_δ in bonding at both the nonrelativistic and relativistic levels of theory. Moreover, as the actinides are traversed (Th $\rightarrow$ Pu), the 5f interactions become more important, and there is greater spin-orbit splitting in the 5f manifold in the relativistic calculations.

The ordering of e_{2u} and e_{2g} is $e_{2u} < e_{2g}$, indicating that the 6d interactions with the ligand are more substantial than the 5f interactions, resulting in greater stabilisation of the e_{2u} orbital. This is consistent with a subsequent study by Chang and Pitzer in $U(COT)_2$ using relativistic effective core potentials and spin-

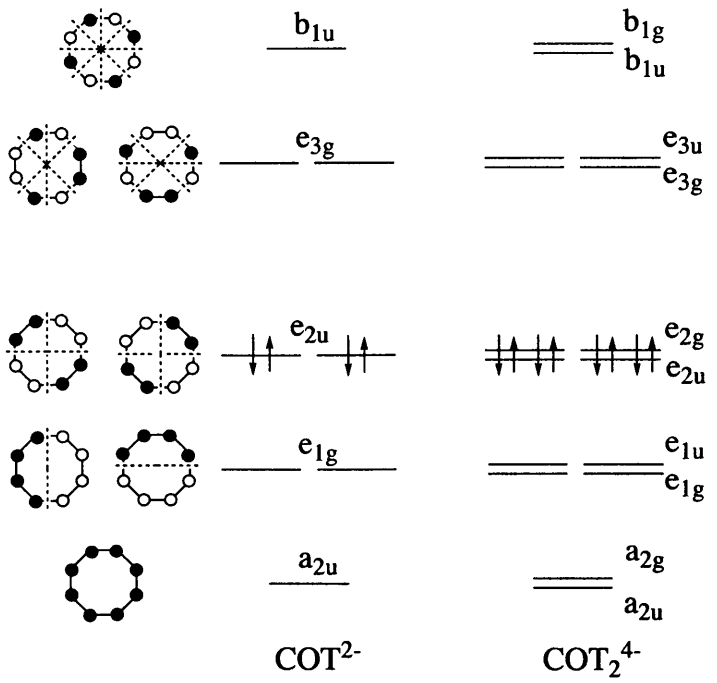

Figure 1.5: Qualitative molecular orbital (MO) diagram of COT^{2-} and COT_2^{4-} in D_{8h} symmetry. The COT π MOs are illustrated, showing contributions from the out-of plane p AO components of each carbon viewed down the C_8 axis of rotation. Nodal planes that occur perpendicular to the ring are also indicated via dashed lines.

orbit configuration interaction method, in which they found that the 6d orbitals of uranium play the more important role in covalent bonding with the ligands, and the role of the 5f orbitals is secondary, although it is the ordering of the occupation of the 5f orbitals that determines the ground state.[19]

One other aspect found at both the nonrelativistic and the relativistic levels is that the occupied 6p orbitals participate in bonding with occupied low-lying ligand-based MOs (although relativity does reduce the participation), supporting the 6p 'semi-core' role in bonding in actinide-containing molecules.[18]

More recent discrete-variational Xα calculations in $Pa(COT)_2$ have focused on the optical transitions, although its ground state electronic structure has also been discussed.[20] The study agrees with previous calculations that relativity reduces the 5f participation in the e_{2u} metal-ligand bonding orbital, found quantitatively in this study to reduce from 32% to 16-18%. The contribution from the semi-core 6p orbital is also reduced by relativity. Subsequent calculations using quasi-relativistic gradient-corrected functional methods on $Pa(COT)_2$ found that the energy difference between eclipsed D_{8h} and staggered D_{8d} structure less than 1kcal/mol, suggesting that the rings can freely rotate.[21] In addition, the geometry optimisation showed a tilt inwards of the H atoms of the COT ring towards the Pa central atom, rather than the assumed planarity of previous calculations.

The oxidation state of the actinide in $An(COT)_2$ has been consistently found to be An(IV) (i.e. COT_2^{4-}). In contrast, the lanthanocenes are generally found as anionic $Ln(COT)_2^-$,[23] and only $Ce(COT)_2$ has been synthesised as a neutral complex.[17] It is the latter that allows direct comparison with the actinides. In 1989, Neumann and Fulde reported semi-empirical calculations on $Ce(COT)_2$ that suggested that the cerium exists in the complex as Ce(III) rather than as the Ce(IV) that might be expected based on the actinocenes.[24] Later, relativistic effective core potential multiconfiguration calculations were reported, which supported the notion of Ce having one f electron and hence existing as Ce(III).[25] Experiments by Edelstein et al. were subsequently reported, which provide support for these calculations.[26]

A comparison of $Th(COT)_2$ and $Ce(COT)_2$ using relativistic effective core potentials with the multi-reference configuration interaction method has shown that whereas $Th(COT)_2$ was found to be adequately described using only one

configuration ($5f^0e^4_{2u}$), the cerium complex is best described as 80% $4f^1e^3_{2u}$ with a 20% contribution from the closed shell $4f^0e^4_{2u}$.[27] Thus, it is more appropriate to describe the bonding in cerocene as Ce^{3+} and $2(COT^{1.5-})$. Further, the thorium complex shows covalent interactions, mainly due to the 6d orbitals of the metal, which is consistent with the earlier study of Boerrigter et al.[18]

Dolg et al.'s multireference studies have been extended to include $Ln(COT)_2$ (Ln=Nd, Tb, Yb), which have not yet been successfully synthesised.[13] This study shows that, similar to their cerium study, $4f^ne^3_{2u}$ is the most suitable description of the lanthanocenes considered, in contrast to the $4f^3e^4_{2u}$ configuration of one of the actinocenes, $U(COT)_2$. In addition, the admixture of $4f^{n-1}e^4_{2u}$ that was found to contribute to 20% of the cerocene, was found to be significantly reduced for the heavier lanthanocenes, with the $4f^ne^3_{2u}$ state contributing to 97%, 89% and 100% of the ground state configuration for Nd, Tb and Yb respectively. In this paper, the authors also hypothesise that the heavier actinocenes might also be best described as An(III) rather than An(IV). Finally multireference calculations on $M(COT)_2^-$ (M=Ce, Nd, Tb, Yb) show that the extra electron of the anion compared with the neutral lanthanocene is situated on the ligands (i.e. $f^ne^4_{2u}$).[28]

1.3.2 Arene Chemistry of the f-Block ($M(\eta^6\text{-}C_6H_6)_2$)

In contrast to the cyclooctatetrane ligand that was considered in the previous section, benzene is aromatic without any formal transfer of electrons from a metal centre. As such, the metal-ligand interactions in MBz_2 (Bz=η^6-C_6H_6) are weaker than in the corresponding biscyclooctatetraenyl complexes, which is reflected in longer M-centroid(Bz) bond lengths.[29] Despite this, bisarene lanthanide complexes have been successfully synthesised,[30,31] and their bonding has been studied

computationally.[29,32,33]

Ab initio (HF, MP2, CCSD(T), MRCI) calculations on D_{6h} MBz_2 (M=Ce, Nd, Gd, Tb, Lu, Th, U) showed that at the HF level, there was no significant binding between the metal and the two arene rings, and that binding was predicted only when correlated methods were implemented.[29] These calculations show that the ground state configuration of the $LnBz_2$ complexes was found to be best described by $4f^n e_{2g}^3$. Conversely, the ground state of $ThBz_2$ and UBz_2 complexes, were found to be best described using multireference methods, with the major contribution to the ground states coming from the e_{2g}^4 and $5f^2e_{2g}^4$ configurations respectively. A comparison of the Mulliken population analyses for $NdBz_2$ and UBz_2 indicate that whereas the actinide complex shows evidence of 5f backbonding, i.e. U(5f)=1.95, the lanthanide complex does not i.e. Nd(4f)=2.99. This is attributed to the relativistic 5f orbital expansion, which enhances the 5f-ligand interactions. It also provides an explanation for the stronger M-Bz bonding in the actinides compared with the lanthanides.

Subsequent quasi-relativistic DFT calculations on $AnBz_2$ (An=Th→Am), however, showed that the previous authors' assumption of D_{6h} symmetry (that is, centroid(Bz)-An-centroid(Bz)=180°) is not the most stable geometry for the actinide complexes[32] and that the experimental linear geometry of $GdTBB_2$ (TBB=η^6-1,3,5-$C_6H_3^tBu$),[30] on which this assumption was based, is the most stable geometry for the analogous actinide complexes only when sterically bulky substituents are placed on the benzene rings. Moreover, the most stable geometry occurs with centroid(Bz)-An-centroid(Bz)=135-142°, occurring lower in energy than the linear geometries by 0.3-10 kcal/mol. This preference for a bent geometry was attributed to an increased Bz→An(6d) and Bz→An(5f) donation that is enhanced by

the lower bond angle. A further study by the authors of the original D_{6h} study subsequently confirmed that the bent $AnBz_2$ geometry is more stable (by about 5 kcal/mol).[33] However, they also found that for the only lanthanide complex that they considered, $LuBz_2$, a linear geometry is preferred. Thus, consistent with computational studies of the biscyclooctatetraenyl f element complexes, the bis-arene complexes of the early actinides compared with the lanthanides have shown stronger 5f interactions than the core-like 4f orbitals in the bisarene complexes.

1.3.3 Cyclopentadienyl Chemistry of the f-Block ($M(\eta^5\text{-}C_5H_5)_3$)

Many computational studies of cyclopentadienyl-containing (cyclopentadienyl ≡ Cp=C_5H_5) actinide complexes have been carried out. Bursten and co-workers, in particular, carried out a series of studies at the end of the 1980s[34–37] and this body of work, in addition to work by others, is summarised in a detailed review by Bursten and Strittmatter.[38] In this section, however, I would like to focus on the contrasting behaviour of the lanthanides and actinides. First I will give a brief introduction to the bonding in Cp_3An, which is one of the most common cyclopentadienyl actinide moieties, and which is known to exist for An=Th → Cf. As an extension, I will compare the actinides with the lanthanide analogues. Although there are also examples of studies of cyclopentadienyl An(IV) complexes (e.g. Cp_4An [39] and Cp_3An^+ [40]), I will confine this discussion to An(III), since the actinide in this oxidation state lends itself to more direct comparison with the lanthanide analogues. In addition, since the electronic structures of MCp_3 and MCl_3 are similar, with both having one σ and two π filled orbitals on each ligand, which can contribute to bonding with the metal centre, this section provides a

general introduction to chapter 5 for $LnCl_3$ and $AnCl_3$.

The cyclopentadienyl ($Cp=C_5H_5$) ligand has a formal charge of -1, and can exist as an η^5 bonding ligand, which formally occupies 3 coordination sites. It is often referred to as a spectator ligand in f-element chemistry,[5] since it stabilises the complex but tends not to participate in reaction chemistry. Therefore, the focus of computational studies of f element cyclopentadienyl chemistry has often been on the extent of d vs f participation in the ground state electronic structure.

Similar to the manner in which $An(COT)_2$ can be thought of as An(IV) in the centre of D_{8h} COT_2^{4-}, Cp_3M can be viewed by first considering C_{3v} Cp_3^{3-} ligand field (the centroids of each Cp ring corresponding to the vertex of a trigonal planar - pseudo-D_{3h} - or of the slightly less symmetric trigonal pyramidal structure) as shown in figure 1.6. In this case, the π_2 MOs of the three Cp rings are bases for the a_1+2e+a_2 representations in C_{3v} symmetry, the latter of which is highest in energy due to the interligand antibonding interactions. When this Cp_3^{3-} fragment bonds with an f element, the d and f orbitals can interact with any of the a_1 and e ligand orbitals using symmetry arguments, but only the f_ϕ orbital can interact with the a_2 MO of the Cp_3^{3-}. This has been proposed as the reason for the large number of triscyclopentadienyl f element complexes compared with the scarcity of transition metal analogues.[36]

Quasi-relativistic Xα calculations on base-free Cp_3An (An=Th $\rightarrow$ Pu) have shown that for the earlier actinides (Th $\rightarrow$ Pa) the $6d_{z^2}$ orbital lies lower in energy than the 5f orbitals and is orientated along the C_3 axis of rotation, towards a vacant coordination site.[35] In contrast, the transuranium base-free complexes show a $5f^n6d^0$ ground state. For all of the actinides, the 6d orbitals are more important in ligand bonding than the 5f orbitals due to the radially contracted

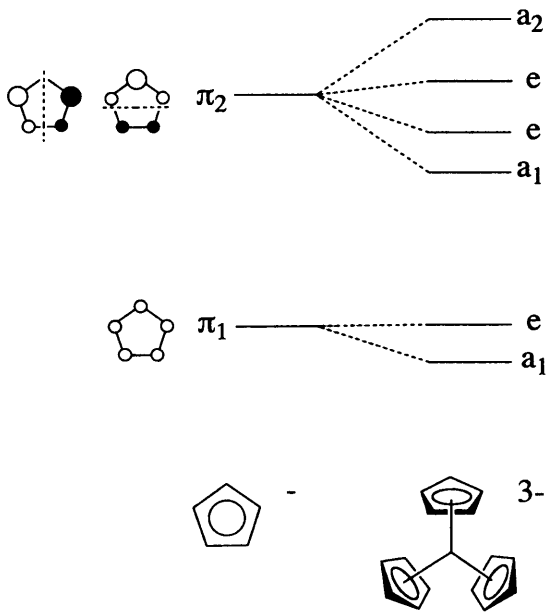

Figure 1.6: Qualitative molecular orbital (MO) diagram of Cp^- and Cp_3^{3-} in C_{3v} symmetry. The Cp MOs are illustrated, showing contributions from the out-of plane p AO components of each carbon from above the ring viewed down the C_5 axis of rotation of a single Cp ring. Nodal planes that occur perpendicular to the ring are also indicated via dashed lines.

nature of the latter, especially as the actinides are traversed. (This is known as the feudal concept - **f**s essentially **u**naltered, **d**s **a**ccommodate ligands).

An extension of this study includes a comparison of the Cp_3An (An=U $\rightarrow$ Cf) complexes with the lanthanide analogues (Cp_3Ln; Ln=Ce $\rightarrow$ Dy).[37] In this case, it was found that the relative orbital energies of the valence f and d orbitals for the early lanthanides resemble those of the mid-actinides, and that the f and d orbital energies for the later actinides and lanthanides are comparable. A comparison of the bonding in the triscyclopentadienyl complexes shows that whereas there is

some involvement of the 7s orbitals in bonding of the actinides, the 6s orbitals of the lanthanides do not participate in bonding with the ligands. There are also greater antibonding interactions due to the 5p orbitals of the lanthanides than in the case of the 6p orbitals of the lanthanides. The main difference between the early actinide complexes compared with the later actinide complexes and the lanthanide complexes, however, is the greater covalency in the early actinide complexes. Covalency in the uranium complex is further seen in a computational study of [Cp_3UCO], in which the U-CO σ bond arises primarily via the U(6d) orbitals, and there is also evidence of U(5f)-CO(π^*) backbonding.[34]

A more recent comparison of Cp_3Th with Cp_3Ce has shown that the aforementioned $6d^1$ ground state of the thorium complex is due to relativity, since at the nonrelativistic level of theory, its ground state is $5f^1$.[20] This is consistent with the ordering of the energy levels in $Th(COT)_2$ that was mentioned in the previous section. In contrast to Cp_3Th, the authors found that the ground state of Cp_3Ce was $4f^1$ at both the nonrelativistic and relativistic levels of theory.

Thus, by comparing the biscyclooctatetraenyl, bisarene and triscyclopentadienyl complexes of the lanthanides and early actinides, it is clear that the 5f orbitals of the latter are more available to bond with ligands and that the actinides exhibit greater covalency. Conversely, for the lanthanide analogues the bonding is predominantly ionic, and, even for $Ce(COT)_2$ there is a preference for a +3 oxidation state. The next section considers specific cases in which the early actinides exist with higher oxidation states than have thus far been considered. In these cases, no lanthanide analogues have been considered.

1.4 Specific Examples of Early Actinide Molecules

In this section, some computational studies of the early actinides, particularly uranium, are described. The two specific examples that will be considered are the actinyl ions, and in particular the uranyl ion that features prominently in uranium chemistry, and the actinide halides, most computational studies of which have been concerned with uranium hexahalide. Uranium in both the uranyl and uranium hexahalide complexes exhibit a formal oxidation state of +6, similar to the oxidation state of uranium in $UOCl_5^-$, which is discussed in chapter 3.

1.4.1 Actinyl Ions

The uranyl ion (UO_2^{2+}) has been studied extensively using computational methods. It is an extremely stable unit with a U-O triple bond, and provides an interesting example of covalent bonding in the early actinides. The focus of the computational studies on the uranyl ion has dealt with three key issues; the ordering of the highest occupied MOs in UO_2^{2+}, the linear geometry (i.e. α(OUO)$\approx$180°) of the uranyl moiety in its complexes (e.g. $[UO_2Cl_4]^{2-}$), which contrasts to the bent structures of MoO_2^{2+}, CeO_2 and ThO_2, and the stability of isoelectronic and other related triatomic units.

The near degeneracy of the valence MOs in UO_2^{2+} has led to much debate over their ordering. Much attention has been given to finding a conclusive answer to this problem, including a comprehensive survey of optical measurements, photoelectron spectroscopy and molecular orbital calculations that was published by Denning in 1992.[41] He suggested that the ordering of the highest occupied MOs is $\pi_g \approx \pi_u < \sigma_g \ll \sigma_u$. Although, some more recent electronic structure calculations have shown varying levels of agreement,[42–45] recent quasi-relativistic

density functional calculations have confirmed Denning's proposal, showing that $\pi_g < \pi_u < \sigma_g \ll \sigma_u$.[46]

The unusually high energy of the HOMO (σ_u) can be explained using the 'pushing from below' mechanism that was initially put forward by Jørgensen and Reisfeld to explain the MO ordering.[47] This mechanism arises because the semi-core 6p orbitals are spatially similar to the valence 5f, 6d and 7s orbitals (see figure 1.3 on page 9). The filled σ_u MO interacts with the filled uranium 6p orbital, destabilising the former. This was confirmed by a study carried out by Kaltsoyannis, in which the energy levels of UO_2^{2+} when the 6p orbitals were allowed to participate in bonding were compared with the situation of having the 6p orbitals frozen.[46] In the latter, the HOMO - HOMO-1 (σ_u - σ_g) energy gap was found to be appreciably smaller than the former case, in which the HOMO was significantly less stable.

It has also been proposed that the 'pushing from below' mechanism is responsible for the linearity of UO_2^{2+} compared with the non-linear moieties such as MoO_2 and ThO_2.[48] The destabilisation of the HOMO in UO_2^{2+} allows stronger O(2p)-U(5f) interactions, which are favoured by a linear geometry. However, the case is not straight forward, and others have claimed that the role of the 6p orbitals does not affect the bond angle significantly.[49] Pyykkö et al. compare relativistic extended Huckel calculation results of linear UO_2^{2+} with those of bent ThO_2, and attribute the bond angle differences to three factors.[50] Firstly, the uranium-oxygen bond is short (approximately 170 pm depending on the equatorial ligands), enhancing 6p interactions with the oxygen-based π_u occupied MO, which are favoured by a linear geometry. Secondly, the 6d orbitals in the uranyl ion are relatively high in energy, so although greater overlap with the 6d orbitals

is attained by a bent geometry, this is negligible in UO_2^{2+}. Finally, UO_2^{2+} has low-lying 5f orbitals, allowing O(σ)-U($5f_\sigma$) interactions. These are favoured in a linear geometry. In contrast, ThO_2 has longer thorium-oxygen bonds, low-lying 6d orbitals, and relatively high 5f orbitals, all contributing to a more stable bent geometry.

More recently, Dyall suggested that the O(2p)-An(6d) π_g and σ_g interactions are consistent for all of ThO_2, PaO_2^+ and UO_2^{2+}, and that the bond angle depends on the extent of 6d-5f hybridisation.[43] Greater 6d contributions to the hybrid, as in ThO_2 tend to result in bent geometries, whereas greater 5f contributions, as in UO_2^{2+} increases the tendency to linear geometries. He also acknowledges that there is a probable influence of the actinide 6p 'hole'.

The energy differences between linear UO_2^{2+} ('trans' uranyl) and bent UO_2^{2+} ('cis' uranyl) has been discussed by Schreckenbach, Hay and Martin for $[UO_2X_4]^{2-}$ (X=F, Cl, OH)[51,52]). Using DFT methods with relativistic effective core potentials they calculated an energy difference of only 10-30 kcal/mol between *cis* ($113° < \alpha(OUO) < 132°$) and *trans* uranyl conformations. From these data, they propose that multidentate and/or bulky ligands might help to achieve a *cis* arrangement of the uranyl ion.

One final area that has received attention in recent years is the existence of species that are isoelectronic with UO_2^{2+}. Pyykkö found that all of XUY^n (XY^n=CN^-, CO, NN, NO^+) were stable with respect to the XY^n fragments using quasi-relativistic HF.[53] Of these, NUN and CUO had already been observed,[54–56] and NUO^+ has since been synthesised.[57] More recently, CUO has received some attention because of its different ground state properties in an argon matrix compared with a neon matrix.[58–60] It has been shown recently using gradient-corrected

quasi-relativistic methods that when CUO is coordinated to a neon atom, it exhibits a singlet ground state, which changes to a triplet ground state when coordinated by heavier noble gas atoms (argon, krypton and xenon).[60] This is accompanied by an elongation of the U-C bond length and shorter U-Ng (Ng=Ar, Kr, Xe) bond lengths.

UN_2 has been shown to have a similar electronic structure to UO_2^{2+} with the same ordering of the frontier MOs ($\pi_g < \pi_u < \sigma_g \ll \sigma_u$), and U-N exhibiting greater covalency than U-O.[46] A comparison of UON^+ with UO_2^{2+} and UN_2 shows that the U-O bonding MOs lie lower in energy than those of U-N, but that the ordering of π below σ stays the same. For the more complicated $UO(NPH_3)^{3+}$ and $U(NPH_3)_2^{4+}$, U-N σ levels lie lower in energy than the π levels, due to significant N-P σ contributions. In addition, the tendency towards linearity in the latter cases is attributed to steric rather than electronic effects.

Calculations carried out by Hay et al. on other AnO_2^{2+} (An=Np, Pu) have shown that there is an actinyl bond length contraction from U to Pu, but a reduction in the vibrational frequency values, which they attribute to a decrease in the overlap between the ligand and 5f overlap, a consequence of 5f orbital contraction as the actinides are traversed.[61]

1.4.2 Actinide Halides

Most calculations that have been carried out on the actinide halides have focused on UF_6, and particularly to test the suitability of computational methods and basis sets in describing actinide complexes. Although many of these benchmark calculations have been concerned with reproducing the optical spectrum of UF_6, here I will summarise the studies of the ground state properties of UF_6.

It has been shown in a comparison of UF_6 results from relativistic discrete-variational (DV)-Dirac-Slater and nonrelativistic DV-Hartree-Fock-Slater calculations that relativity must be included to describe the bonding in UF_6.[62–64] The relativistic 6s stabilisation reduces the antibonding interactions between the uranium and fluorine ligands. The relativistic expansion of the f and d orbitals was also found to be important, since this results in greater bonding interactions. The increased bonding interactions and decreased antibonding interactions cause a small bond length contraction, and increase the dissociation energy of UF_6 by 70% above the nonrelativistic value.[65]

More recent calculations have used UF_6 as a test molecule to show that Density Functional Theory (DFT) methods with relativistic effective core potentials (RECPs) show good agreement with experimental bond lengths and vibrational frequencies.[52,66–68] The best agreement is found using hybrid-DFT and a 60 electron RECP rather than a 78 electron RECP, especially for the bond dissociation of the uranium fluorine bond.[68] Computational investigations of AnF_6 (An=Pa, U, Np) have shown that the decrease in r(An-F) from Pa to Np is reproduced well using DFT and RECP descriptions, and especially using a 60 electron RECP with the hybrid-DFT method, B3PW91.[68]

The computational study of f^1 PaX_6^{2-} (X=F, Cl, Br, I), UX_6^- (X=F, Cl, Br) and NpF_6 using relativistic DV-Xα method shows significant metal-ligand covalent bonding via the 6d and 5f metal orbitals.[64] The f character was found to increase from Pa to Np, consistent with the stabilisation of the 5f orbitals as the actinides are traversed, and there is an increase in 6d contribution from UF_6^- to UBr_6^-. The latter is also seen for the protactinium compounds but to a lesser extent. The one unpaired electron is almost entirely localised on the actinide centre.

The few computational studies of UF_5 agree that there is a small energy difference between the trigonal bipyramidal (D_{3h}) and square pyramidal (C_{4v}) structures, which is of the order of only a few kcal/mol.[68–70] Without spin-orbit coupling, the C_{4v} structure was found to be more stable by just 1 kcal/mol, which is reversed to a more stable D_{3h} structure by 1 kcal/mol when spin-orbit coupling is included.[69] From these data, the authors predict a fluxional UF_5 structure via a C_{2v} pathway. The similar energy C_{4v} and D_{3h} structures were subsequently confirmed using DV-DS and DV-HFS, and DFT-RECP methods[68,70] The former also suggest that the difference between the bonding in these structures is small. They also find that, similar to UF_6, relativity increases the U-F overlap, in this case by a factor of two.

1.5 Summary of the f Elements

In the previous sections, a brief overview of the f elements was given. Initially a description was given of the differences between the lanthanide and actinide atoms, which are due to relativity and to the more diffuse 5f orbitals of the actinides compared with the contracted nodeless 4f orbitals of the lanthanides. This leads to the lanthanides being dominated by the +3 oxidation state, in contrast to a more diverse chemistry for the early actinides. These differences were then considered in the chemistry of the f elements, by initially contrasting the behaviour of the trivalent lanthanides in the lanthanocenes ($Ce(COT)_2$, in particular) and the tetravalent actinides in the actinocenes. A second example of the organometallic complexes that was considered was the bisarene complexes, which also exhibit contrasting behaviour between the lanthanides and the actinides. Thirdly, the set

of triscyclopentadienyl complexes were discussed, from which it can be seen that there is greater covalency in the actinide complexes compared with the lanthanide complexes. The final examples that were discussed were the actinyl ions and actinide halides, since they provide good examples of the higher oxidation states that are common in actinide chemistry but not in lanthanide chemistry.

1.6 Transactinide Compounds

The known transactinide elements are those from Z=104, rutherfordium, to element 112 (and there are current attempts to synthesise elements 114 and 116). These elements are also called superheavy elements (SHEs) because they exist only due to nuclear shell structure effects[1]; since the transactinides have half-lives of greater than 10^{-14} s, they are considered to be valid elements, and since this is a direct result of the nuclear shell structure effects, they satisfy the conditions for a SHE.[71]

Due to the short half-lives of the transactinides and their low production rates, transactinide chemistry is carried out on an 'atom-at-a-time' scale. Of the reported transactinides, gas phase chemistry has been carried out only on elements 104-108 (rutherfordium, dubnium, seaborgium, bohrium and hassium), with further aqueous chemistry only on the first three of these elements.[71] Thus, computational studies can potentially provide information that would be much more difficult, if not impossible, to obtain experimentally.

This section gives a brief summary of some computational studies that have been carried out on the transactinide elements and their compounds. Further

[1]Note that in a similar manner to electronic structure effects, particles of the nuclei arrange themselves in a shell-like manner resulting in nuclear shell structure effects, which affect the stability of the nuclei.

information can be found in a Pershina's 1996 review,[72] and a more specific introduction to element 111 is given in chapter 4.

1.6.1 Relativistic Effects on the Transactinides

The aforementioned direct relativistic s and p orbital contraction and indirect relativistic d and f expansion has led to some debate over the ground state electronic structure of rutherfordium (Z=104), the first member of the transactinides. Relativistic multiconfiguration calculations proposed that its ground state was 80% $6d^17s^27p^1$ rather than the $(n-1)d^2ns^2$ configuration of the earlier members of group 4.[73] This was subsequently disputed by Eliav et al., who showed using CCSD that the ground state was actually $6d^27s^2$, which indicates that it should behave like the other d elements in group 4.[74] Eliav et al. attributed this discrepancy between the CCSD and the multiconfiguration results to the fact that the CCSD calculations include dynamical correlation.

Multireference calculations on dubnium (Z=105) and seaborgium (Z=106) predict $6d^37s^2$ and $6d^47s^2$ ground state configurations, placing them in groups 5 and 6 of the periodic table respectively.[72] As the transactinides are traversed, the relativistic contraction of the s orbitals becomes apparent, and for the case of element 111, instead of the ground state of $d^{10}s^1$ that is present in gold, it has a d^9s^2 atomic ground state.[75] This aspect of element 111 is discussed further in section 4.1.3 in chapter 4 (beginning page 114).

There are two ways that the effect of relativity can be seen on the bond lengths of 6d transactinide-containing bonds. Firstly, a direct comparison between non-relativistic and relativistic geometry optimisations is possible, and secondly, the bond lengths of the 6d elements can be compared with those of the lighter 5d ele-

ments. A comparison of nonrelativistic and relativistic all electron SCF geometry optimisations by Malli and co-workers on $RfCl_4$,[76] $SgBr_6$[77] and HsO_4[78] have shown bond length contractions of 6-7 pm. Other calculations by Schwerdtfeger et al. using ECPs on compounds of the later transactinides [111]H,[3] $[112]H^+$, $[112]F_2$ and $[112]F_4$[79] predict somewhat larger relativistic bond length contractions of 42, 37, 9 and 16 pm for the heavier transactinides.

Alternatively, table 1.1 compares the calculated bond lengths of the 6d transactinides with their lighter 5d congeners from a series of computational studies that have been carried out. These data are included here to show that most of these calculations predict that the 6d-containing bonds are only slightly longer than the 5d analogues. A comparison of element 111 data with the corresponding gold data shows that the [111] bond lengths are actually shorter than the analogous gold bond lengths in selected cases. The data from reference 3, which indicate that r([111]-H) is 5 pm shorter than r(Au-H), led the authors to hypothesise that element 111 might be smaller than gold, which they attributed to the 'gold maximum' of relativistic effects. A similar trend is seen for element 112 compared with mercury in CCSD(T) calculations by the same author.[79] However, other data[80] raise the question of whether this is actually the case since, as table 1.1 shows, this is not necessarily true for all compounds.

Apart from the bond lengths, relativity also affects the molecular bonding in transactinide molecules. For the molecules in which electronegative ligands are involved, e.g. $RfCl_4$, $SgBr_6$, BhO_3Cl, HsO_4, the character of the relativistic occupied valence molecular orbitals does not seem to differ significantly from the non-relativistic occupied valence molecular orbitals, since both sets are dominated by contributions from the ligands rather than from the transactinides. The trans-

Table 1.1: Comparison of optimised bond lengths (in pm) of molecules of selected compounds of the 5d and 6d elements from the literature.

	Method	Bond	5d	6d	Δ(6d-5d)	Ref.
^{105}Dubnium (5d element: Tantalum)						
MCl_5	MP2/RECP	r(M-Cl_{ax})	232.3	238.0	5.7	81
(D_{3h})		r(M-Cl_{eq})	227.6	234.4	6.8	
MBr_5	MP2/RECP	r(M-Br_{ax})	248.1	253.6	5.5	81
(D_{3h})		r(M-Br_{eq})	243.5	249.9	6.4	
^{106}Seaborgium (5d element: Tungsten)						
MO_2Cl_2	CCSD(T)/RECP	r(M=O)	170.8	175.6	4.8	
		r(M-Cl)	228.1	233.9	5.8	81
$M(CO)_6$	CCD RECP	r(M-C)	206.5	211.2	4.7	82
MO_4^{2-}	Rel. DFT	r(M=O)	178	183	5	83
^{108}Bohrium (5d element: Rhenium)						
MO_3Cl	Rel. DFT	r(M=O)	171	177	6	84
(C_{3v})		r(M-Cl)	228	237	9	
^{109}Hassium (5d element: Osmium)						
MO_4	Rel. DFT	r(M=O)	175.6	182.0	6.4	85
	All electron DF		166	173	7	78
Element 111 (5d element: Gold)						
MH	HF/RECP	r(M-H)	157.8	150.6	-7.2	3
	DKS/FC		153.7	154.6	0.9	80
MF_2^-	MP2/RECP	r(M-F)	195.9	196.7	0.8	86
MCl	DKS/KS	r(M-Cl)	222.8	225.2	2.4	80
MBr		r(M-Br)	235.1	239.1	4.0	80
MO		r(M-O)	183.1	180.8	-2.3	80
Element 112 (5d element: Mercury)						
MH^+	CCSD(T)/SORECP	r(M-H)	159	152	-7	79
MF_2	QCISD(T)/RECP	r(M-F)	192.4			79
	MP2/RECP	r(M-F)		192.9	0.5	
MF_4	QCISD(T)/RECP	r(M-F)	188.4			79
	MP2/RECP	r(M-F)		193.7	5.3	

actinide complexes, however, do show an increase in covalency relative to their 5d congeners.[76–78,84,85]

A study of $M(CO)_6$ (M=W, Sg) shows that the relativistic destabilisation of the 6d orbitals results in greater Sg(6d) $\rightarrow$ CO backbonding, which is reflected in a longer r(C-O) and in lower vibrational frequencies of the C-O bond in $Sg(CO)_6$ compared with $W(CO)_6$.[82] Studies of MO_4 (M=Os, Hs) showed that the tetrahedral hassium complex is more stable with respect to dissociation than the equivalent osmium complex.[78] This was attributed to the relativistic destabilisation of the 6d orbitals and also, the relativistic stabilisation of the 7s orbitals, the result of which gives a smaller s-d energy gap in Hs than in Os. This leads to a greater tendency for sd^3 hybridisation in Hs, and hence greater stability of the tetrahedral complex.

Thus, from the limited computational studies that have been carried out on the 6d transactinides, the relativistic stabilisation of the 7s orbitals and the relativistic destabilisation of the 6d orbitals have been shown to influence both the bond lengths and the bonding character in their molecules.

1.7 Summary

The aim of this chapter was to give a brief introduction to computational studies of heavy element chemistry. Initially the f elements were discussed. In this discussion, the different roles of the contracted 4f orbitals in lanthanide chemistry and the more diffuse 5f orbitals in actinide chemistry were considered. These differences were highlighted in the organometallic complexes, $M(COT)_2$, MBz_2 and MCp_3. This discussion introduces concepts that are relevant to the study

of MX_3 (M=La-Lu; Ac-Lr; X=H, F, Cl, Br, I) that is reported in chapter 5. In particular, the electronic structures of the metal trichlorides can be related to that of the metal triscyclopentadienyl complexes, since both the chloride and the cyclopentadienyl ligands possess $\sigma+2\pi$ filled orbitals that can interact with the metal centre. In chapter 5, the role of the 4f and 5f orbitals in determining the extent of pyramidalisation in MX_3 is discussed.

A discussion of the actinyl ions and the actinide hexahalides was provided in section 1.4 to highlight the ability for the early actinides to exhibit high oxidation states. This is relevant to the $[AnOX_5]^{n-}$ (An=Pa (n=2), U (n=1), Np (n=0); X=F, Cl, Br) series of complexes that are discussed in chapter 3 in the context of the inverse *trans* influence (i.e. the shorter *trans* bond relative to the *cis* bonds). In this study, the source of the inverse *trans* influence of $[AnOX_5]^{n-}$ is considered and compared with the *trans* influence (i.e. the longer *trans* bond relative to the *cis* bonds) of the transition metal complex, $[OsNCl_5]^{2-}$.

Finally, the 6d transactinides were considered in section 1.6. In this section, the role of relativity was the focus, and examples of how relativity affects both the bond lengths and the bonding in the 6d transactinide compounds compared with analogous 5d compounds was discussed. This final topic relates to the 6d transactinide, element 111. Element 111 is compared with copper, silver and gold in chapter 4 in the context of their metallophilicity in $[ClM(PH_3)]_2$ (M=Cu, Ag, Au, [111]). Initially, the role of relativity in determining the bond lengths of the metal-chlorine and metal-phosphorus bonds in the monomer, $[ClM(PH_3)]$ is discussed, and thereafter, the metallophilicity of each metal in the dimer is explicitly considered.

Chapter 2

Electronic Structure Theory

The aim of this chapter is to provide a brief introduction to the theoretical models, on which the computational methodology for subsequent chapters is based. The chapter is broadly divided into four sections. The first section describes Hartree-Fock and post-Hartree-Fock methods, which are introduced through the electronic Schrödinger equation. This also provides the starting point for Density Functional Theory, which is described in the second section. The focus changes slightly in the third section to the specific question of suitable mathematical descriptions of atoms and molecules (basis sets), and to how these mathematical functions can be related to the more commonly encountered principles of chemistry e.g. atomic and molecular orbitals, and chemical bonding. In this part, one of the problems of using basis sets, i.e. basis set superposition error, is considered and the merits of population analysis schemes are discussed. Next, the specific difficulties of considering relativity, a necessity in heavy element systems, are considered. The Zeroth Order Regular Approximation (ZORA) and relativistic Effective Core Potential (ECP) approaches are discussed in this section. Finally, the chapter ends with a brief summary.

2.1 The Schrödinger Equation

Given a wave function Ψ containing all of the information about a quantum system, and the Hamiltonian operator $\hat{H}$ representing the total energy, it is possible to evaluate the energy E of the system using the Schrödinger Equation (SE). The

non-relativistic, time-independent SE is given (in atomic units) by:

$$\hat{H}\Psi = E\Psi \tag{2.1}$$

$$\hat{H} = \hat{T} + \hat{V} \tag{2.2}$$

$$\hat{T} = \hat{T}_{\mathrm{n}} + \hat{T}_{\mathrm{e}} \tag{2.3}$$

$$= -\frac{1}{2}\sum_{A=1}^{M}\frac{1}{M_A}\nabla_A^2 - \frac{1}{2}\sum_{i=1}^{N}\nabla_i^2$$

$$\text{(where } \nabla^2 = \frac{\partial^2}{\partial x^2} + \frac{\partial^2}{\partial y^2} + \frac{\partial^2}{\partial z^2}\text{)}$$

$$\hat{V} = \hat{V}_{\mathrm{nn}} + \hat{V}_{\mathrm{ee}} + \hat{V}_{\mathrm{ne}} \tag{2.4}$$

$$= -\sum_{A=1}^{M}\sum_{B>A}^{M}\frac{Z_A Z_B}{R_{AB}} + \sum_{i=1}^{N}\sum_{j>i}^{N}\frac{1}{r_{ij}} + \sum_{i=1}^{N}\sum_{A=1}^{M}\frac{Z_A}{r_{iA}}$$

The Hamiltonian is made up of the sum of the kinetic energy operator $\hat{T}$ and the potential energy operator $\hat{V}$. The kinetic energy component (equation 2.3) can be divided into the kinetic energy contributions from the nuclei (denoted by $\hat{T}_{\mathrm{n}}$) and from the electrons (denoted by $\hat{T}_{\mathrm{e}}$). Similarly, the potential energy component (equation 2.4) is given by the potential energy due to the repulsive interactions between pairs of nuclei ($\hat{V}_{\mathrm{nn}}$), between pairs of electrons ($\hat{V}_{\mathrm{ee}}$), and attractive interactions between the electrons and the nuclei ($\hat{V}_{\mathrm{ne}}$).

As a first step towards solving the SE, the Born-Oppenheimer (BO) approximation provides a simplification, which is based on the observation that given the large mass of the nuclei compared with the mass of the electrons, the electrons move much more quickly than the nuclei. Hence, it is sufficient to assume that the nuclei do not move ($\hat{T}_{\mathrm{n}} = 0$) and it is then possible to consider the electronic solutions to the Hamiltonian for a set of fixed nuclear positions. In this situation,

the potential energy contribution from interacting nuclei ($\hat{V}_{\mathrm{nn}}$) becomes constant (v_{nn}). Mathematically, this can be summarised in equations 2.5-2.8.

$$\Psi = \Psi_{\mathrm{e}}(\mathbf{r};\mathbf{R})\Psi_{\mathrm{n}}(\mathbf{R}) \tag{2.5}$$

$$\hat{H}_{\mathrm{e}} = \hat{T}_{\mathrm{e}} + \hat{V}_{\mathrm{ee}} + \hat{V}_{\mathrm{ne}} + \hat{V}_{\mathrm{nn}} \tag{2.6}$$

$$= \hat{T}_{\mathrm{e}} + \hat{V}_{\mathrm{ee}} + \hat{V}_{\mathrm{ne}} + v_{\mathrm{nn}} \tag{2.7}$$

$$\hat{H}_{\mathrm{e}}\Psi_{\mathrm{e}}(\mathbf{r};\mathbf{R}) = E(\mathbf{R})\Psi_{\mathrm{e}}(\mathbf{r};\mathbf{R}) \tag{2.8}$$

Effectively this means that for a given set of fixed positions of the nuclei, $\{\mathbf{R}\}$, solutions to the electronic SE can be obtained that depend only parametrically on $\mathbf{R}$, and this results in a potential energy surface given by a set of values of E($\mathbf{R}$) on which the nuclei move. If the wave function is normalised (i.e. $\int_0^\infty \Psi^*\Psi d\tau = 1$), the solution to the SE can be written as:

$$E = \langle\Psi|\hat{H}|\Psi\rangle \quad \left(= \int_0^\infty \Psi^*\hat{H}\Psi d\tau\right) \tag{2.9}$$

i.e. the energy is the expectation value of Ψ over the operator $\hat{H}$. Hereafter, only the electronic SE is discussed (so the subscript e and the notation of parametric dependence of the electronic SE on the nuclear positions ($\mathbf{R}$) are dropped).

Having elucidated a suitable expression for the electronic Hamiltonian, the next step is to consider the electronic wave function, Ψ. From a chemical viewpoint, it makes sense to think of the total wave function as having contributions from atomic/molecular orbitals. More specifically, the concept of a set of orthonormal one-electron spin orbitals is introduced. A spin orbital is a function that describes the position and spin of individual electrons, denoted $\psi(\mathbf{r}_i,\omega)$, where $\mathbf{r}_i$ is the position of the electron and ω is its spin, which can be either spin-up (α)

or spin-down (β).

The Slater determinant, Ψ_{SD} (equation 2.10), consisting of contributions from spin orbitals, provides an approximate representation of the total wave function. The rows of the Slater determinant correspond to the electrons ($\mathbf{x}_i$) of a wave function and the columns correspond to the constituent spin orbitals (ψ_i). This determinant changes sign if either two rows or two columns are interchanged so the wave function is antisymmetric for the simultaneous interchange of the space and spin coordinates of any two electrons. This ensures that the Pauli exclusion principle is obeyed. Also, if two rows or columns are equal, then Ψ_{SD}=0, which means that two electrons cannot occupy the same orbital and have the same spin.

$$\Psi_{\mathrm{SD}} = \frac{1}{\sqrt{N!}} \begin{vmatrix} \psi_1(\mathbf{x}_1) & \psi_2(\mathbf{x}_1) & \cdots & \psi_N(\mathbf{x}_1) \\ \psi_1(\mathbf{x}_2) & \psi_2(\mathbf{x}_2) & \cdots & \psi_N(\mathbf{x}_2) \\ \vdots & \vdots & & \vdots \\ \psi_1(\mathbf{x}_N) & \psi_2(\mathbf{x}_N) & \cdots & \psi_N(\mathbf{x}_N) \end{vmatrix} \tag{2.10}$$

Even beginning with Ψ_{SD} as a trial wave function, searching for the true wave function is a non-trivial problem. One tool that aids this search is the Variation Principle. It states that the best description of a wave function in a finite set, is the one that corresponds to the minimum energy. For the specific case of Ψ_{SD}, this means that the most appropriate spin orbitals should be chosen to give the lowest energy. Although the Slater determinant is not a complete representation of the true wave function, it does provide a starting point for solving the SE, and this approach is now discussed in terms of Hartree-Fock theory.

2.1.1 Hartree-Fock Theory

The basic principle behind Hartree-Fock (HF) theory is that the many-electron SE equation is replaced by a series of one-electron equations, in which each electron experiences the effects of the other electrons in an average way. Beginning with the electronic SE (equation 2.9), there are three main assumptions to the HF approach:

1. Ψ_{SD} is a good description of the true wave function, and the best choice of Ψ_{SD} is one that yields the lowest energy (i.e. energy is variational).

2. The spin orbitals are orthonormal, and must remain orthonormal throughout any calculation.

3. Using Ψ_{SD} leads to the assumption that it is sufficient to consider that each electron is affected by the other electrons in an average way (see below).

Using Ψ_{SD} as the wave function (assumption (1)), the expression for the HF energy can be written in terms of the constant value of v_{nn} from the nucleus-nucleus attraction (or from any other constant external potential), and in terms of the expectation values due to the one-electron operator $\hat{h}$ and due to the two-electron operators $\hat{J}$ and $\hat{K}$.

$$\begin{aligned} E_{\mathrm{HF}} &= \langle \Psi_{\mathrm{SD}} | \hat{H} | \Psi_{\mathrm{SD}} \rangle \\ &= v_{\mathrm{nn}} + \sum_{i=1}^{N} \langle \psi_i(\mathbf{x}_1) | \hat{h}_i | \psi_i(\mathbf{x}_1) \rangle + \\ &\quad \frac{1}{2} \sum_{i,j=1}^{N} \left(\langle \psi_i(\mathbf{x}_1) | \hat{J}_j(\mathbf{x}_2) | \psi_i(\mathbf{x}_1) \rangle - \langle \psi_i(\mathbf{x}_1) | \hat{K}_j(\mathbf{x}_2) | \psi_i(\mathbf{x}_1) \rangle \right) \end{aligned} \tag{2.11}$$

$$\hat{h}_i = -\frac{1}{2}\nabla^2 - \sum_{A=1}^{M} \frac{Z_A}{r_{iA}} \tag{2.12}$$

$$\hat{J}_j(\mathbf{x}_2)|\psi_i(\mathbf{x}_1)\rangle = \langle\psi_j(\mathbf{x}_2)|\frac{1}{r_{12}}|\psi_j(\mathbf{x}_2)\rangle|\psi_i(\mathbf{x}_1)\rangle \quad (2.13)$$

$$\hat{K}_j(\mathbf{x}_2)|\psi_i(\mathbf{x}_1)\rangle = \langle\psi_j(\mathbf{x}_2)|\frac{1}{r_{12}}|\psi_j(\mathbf{x}_1)\rangle|\psi_i(\mathbf{x}_2)\rangle \quad (2.14)$$

The one-electron operator, $\hat{h}$ is due to the contributions to the energy from the electron kinetic energy and the interaction energy of the electrons with the nuclei, both of which are independent of the other electrons (i.e. the term depends only on the i^{th} electron and the fixed positions of the nuclei). The two-electron operators are the Coulomb operator, $\hat{J}$ and the Exchange operator, $\hat{K}$, and are less convenient than $\hat{h}$ because they do depend on the other electrons (j dependence), as can clearly be seen in equations 2.13 and 2.14. The Coulomb term represents the potential that electron i experiences due to the charge distribution of electron j, and resembles the classical notion of Coulomb repulsion between electrons. The Exchange term involves the exchange of electrons 1 and 2 between ψ_i and ψ_j and has no classical analogue. One aspect of both of these terms is that they collectively summarise the effect that each electron experiences from the interactions with all of the other electrons as an effective one-electron potential. This means that each electron sees the effect of the other electrons as a distribution, rather than an instantaneous interaction, resulting in assumption (3) above.

Having found an expression for E_{HF}, assumptions (1) and (2) above can be applied to find the best spin orbitals within the HF approximation that give the lowest energy and that are orthonormal. Details of this process are given elsewhere[87] but for the purposes here, it is sufficient to look at the significance of the final result, which is a series of N one-electron HF integro-differential equations:

$$\hat{f}_i\psi_i = \varepsilon_i\psi_i \qquad i = 1, 2, \ldots, N \quad (2.15)$$

$$\hat{f}_i = \hat{h}_i + \sum_{j=1}^{N} \left(\hat{J}_j + \hat{K}_j \right) \tag{2.16}$$

In this case, ε_i is the energy of the i^{th} spin orbital, and the operators $\hat{h}_i$, $\hat{J}_j$ and $\hat{K}_j$ are the same as those in equations 2.12, 2.13 and 2.14. (Note however that the total energy of the system is not simply the sum of the orbital energies, since this would result in accounting for the electron-electron repulsion of each pair of electrons twice.) So, although solving the SE for one many-electron wave function has been reduced to solving a set of one-electron equations, each equation still depends on the other $N - 1$ spin orbitals. Therefore, solving the i^{th} HF equation requires knowing the expressions for the other $N - 1$ spin orbitals before its evaluation. This leads to the Self-Consistent Field (SCF) method, in which the energy is evaluated for a set of trial spin orbitals, which are systematically varied until the minimum energy is found.

Now solving the HF equations has become a question of finding the most suitable set of spin orbitals $\{\psi_i(\mathbf{x})\}$. From the chemists' view of orbitals, it is sensible to consider a spatial, spin-restricted molecular orbital (MO) $\psi(\mathbf{r})$ instead of a spin orbital, and to define the MO as a linear combination of atomic orbitals (LCAO), defined as:

$$\psi_i(\mathbf{r}) = \sum_{a=1}^{P} c_{ia} \phi_a(\mathbf{r}) \tag{2.17}$$

In this case a series of P basis functions $\phi_a(\mathbf{r})$ are linearly combined using a set of variable coefficients c_{ia}. For an infinite set of basis functions ($P \rightarrow \infty$), the MO description would be exact within the HF formalism, but clearly this is not computationally possible, so a finite set is considered. The mathematical form of

$\phi_a(\mathbf{r})$ is discussed in section 2.4, but for now the consideration is the coefficients, c_{ia}. They determine the extent to which each $\phi_a(\mathbf{r})$ contributes to each molecular orbital ψ_i, so they are the quantities that are varied to find the best solutions to the HF equations.

Replacing ψ_i in equation 2.15 with the expression from equation 2.17 (and accounting for the use of spatial MOs instead of spin orbitals) gives:

$$\hat{f}_i \sum_{a=1}^{P} c_{ia}\phi_a = \varepsilon_i \sum_{a=1}^{P} c_{ia}\phi_a \tag{2.18}$$

$$\hat{f}_i = \hat{h}_i + \sum_j \left(2\hat{J}_j - \hat{K}_j\right)^1 \tag{2.19}$$

Manipulation of this equation (see references 87 and 88), gives equation 2.20, and when all of the MOs are considered, this becomes the Roothaan equation (equation 2.21), which summarises the set of HF equations in the particular set of basis functions. In this case, **F** is the Fock matrix, **C** is the coefficient matrix, **S** is the overlap matrix, and ε is the MO energy matrix.

$$\sum_b c_{ib}\langle\phi_a^*|\hat{f}_i|\phi_b\rangle = \varepsilon_i \sum_b c_{ib}\langle\phi_a^*|\phi_b\rangle \tag{2.20}$$

$$\mathbf{FC} = \mathbf{SC}\varepsilon \tag{2.21}$$

The Fock matrix elements consist of one-electron integral terms, coming from $\hat{h}$ in equation 2.16, of two-electron integral terms, coming from $\hat{J}$ and $\hat{K}$, and of a density matrix, **P**. The density matrix results from factorising the coefficients from the one- and two-electron integrals, such that the density matrix elements P_{ab}, are the only terms of the Fock matrix elements that depend on the coefficients

[1] In this equation, the factor of 2 preceding $\hat{J}$ but not $\hat{K}$, is because the former considers the interactions of both α and β electrons but the latter considers only the exchange of parallel-spinned electrons. A step-by-step description of this process is given in reference 87.

$\{c_{ia}\}$.

$$P_{ab} = 2\sum_{u} c_{au}^{*} c_{ub} \tag{2.22}$$

The HF SCF convergence process is now an issue of finding the density matrix for a set of $\{\phi_a\}$ that satisfies the Roothaan equation, which once again is an iterative process.

2.1.2 Electron Correlation

It has already been noted that HF theory accounts for interactions between electrons only in an average way. This limitation of the theory means that it cannot account for the instantaneous interactions between electrons (known as electron correlation), so HF is referred to as an uncorrelated method. Although electron correlation typically only contributes to about 1% of the total energy,[88] when looking at changes in energy, e.g. bond breaking and forming, this percentage can be extremely important.

Because HF is an uncorrelated method, it overestimates the time that electrons spend close to each other. This leads to an overestimation of the electrostatic repulsion energy, and hence the HF energy is higher than the true energy. This difference between the true energy, E_0, and the HF energy is defined as the correlation energy.

$$E_{\text{CORR}} = E_{\text{HF}} - E_0$$

If, however, instead of just one determinant, the total wave function is made up of a linear combination of determinants of coefficients $\{a_i\}$, as in equation 2.23,

it is possible to recover the electron correlation. In this way, the Configuration Interaction (CI) wave function is constructed, which is discussed in more detail in the next section. For now it is noteworthy that the determinants are generated from the HF orbitals by considering the ground state (Ψ_{HF}) and the excitation of one or more electrons to give singly, doubly, triply, ..., excited determinants (denoted Ψ_S, Ψ_D, Ψ_T, ..., etc.).

$$\Psi_{CI} = a_0\Psi_{HF} + \sum_l a_{S,l}\Psi_S + \sum_m a_{D,m}\Psi_D + \sum_n a_{T,n}\Psi_T + \cdots \quad (2.23)$$

For a given set of basis functions, this retrieves all of the electron correlation energy, which can now be defined as the difference in energy between the HF energy and the configuration interaction energy.

$$E_{corr} = E_{HF} - E_{CI} \quad (2.24)$$

Although the correlation energy is a mathematical concept, it can broadly be divided into two separate effects, dynamical and non-dynamical correlation. If the coefficient a_0 in equation 2.23 is unity, and all other coefficients are zero, then the HF energy is returned and the correlation energy is zero. If a_0 is slightly less than unity, then the HF determinant is still the main contributor to the energy, with small contributions from other effects. In this case, E_{corr} can broadly be attributed to dynamical correlation, associated with the correlation of the motion of electrons in their orbitals. This is considered to be a short-range effect. On the other hand, if a_0 is significantly smaller than unity, this means that the true wave function now has significant contributions from more than one determinant and E_{corr} can be considered as mainly a result of non-dynamical correlation (to

distinguish it from dynamical correlation).

First, non-dynamical correlation is briefly considered. Non-dynamical correlation results from the poor representation of the ground state by a single electronic configuration. This is often the case when bonds are stretched (e.g. dissociation of a molecule into its fragments) and so, is referred to as a long-range effect. In this case, it is possible that HF does not even give the correct qualitative view of the system. One approach to correcting this problem is multiconfiguration self-consistent field (MCSCF) theory, in which the virtual orbitals as well as the occupied orbitals are optimised, so that a combination of configurations can be considered. This specific problem is not dealt with in this research, so it is not discussed further. Details of non-dynamical correlation and multireference methods can be found in references 87–89.

The focus of the remaining part of this section is on the dynamical correlation, which as has been mentioned, is a short-range effect, due to the motion of electrons in their orbitals. Attempts to incorporate this are now considered in two different ways. The first approach considers the wave function as a combination of different Slater determinants in a linear manner, as in equation 2.23, via Configuration Interaction (CI) methods, or alternatively using an exponential operator to generate the determinants via Coupled Cluster (CC) methods. Second, the effect of correlation is considered as a perturbation to the HF wave function via Møller Plesset (MP) methods. Having considered all three methods, the description of correlation on the electron density-based Density Functional Theory (DFT) is discussed in section 2.2.

2.1.2.1 Configuration Interaction

Configuration Interaction (CI) considers Ψ_{HF} as its starting point. It improves the HF single determinantal wave function by representing the wave function by a linear combination of determinants, generated from the HF orbitals, as in equation 2.23. In CI, the determinants are constant functions and the coefficients $\{a_i\}$ of the functions are varied to determine the best CI wave function.

Since CI is a variational method, the best wave function Ψ_{CI} is described by $\{a_i\}$ for which the energy is a minimum. This leads to a CI matrix in the determinant basis, in which each matrix element results from the coupling of two determinants:

$$\begin{bmatrix} \langle\Psi_{\mathrm{HF}}|\hat{H}|\Psi_{\mathrm{HF}}\rangle & \langle\Psi_{\mathrm{HF}}|\hat{H}|\Psi_{\mathrm{S}}\rangle & \langle\Psi_{\mathrm{HF}}|\hat{H}|\Psi_{D}\rangle & \cdots \\ \langle\Psi_{\mathrm{S}}|\hat{H}|\Psi_{\mathrm{HF}}\rangle & \langle\Psi_{\mathrm{S}}|\hat{H}|\Psi_{\mathrm{S}}\rangle & \langle\Psi_{\mathrm{S}}|\hat{H}|\Psi_{\mathrm{D}}\rangle & \cdots \\ \langle\Psi_{\mathrm{D}}|\hat{H}|\Psi_{\mathrm{HF}}\rangle & \langle\Psi_{\mathrm{D}}|\hat{H}|\Psi_{\mathrm{S}}\rangle & \langle\Psi_{\mathrm{D}}|\hat{H}|\Psi_{\mathrm{D}}\rangle & \cdots \\ \vdots & & \ddots & \end{bmatrix}$$

Further, if all possible excitations using a given basis set are included in equation 2.23, all of the basis set correlation is included. CI returns the full basis set correlation energy (equation 2.24), both dynamical and non-dynamical, for a given set of basis functions, and this is known as full CI. In practice, this is prohibitively computationally intensive, and truncated CI methods are used, as is now discussed in the case of trying to solve the ground state of a system. Truncated CI methods focus on trying to correct for dynamical rather than non-dynamical correlation.

The CI matrix is simplified by considering the spin states of contributing determinants, and the determinants that have different spatial symmetry and

different spin states from the ground state are eliminated with the remaining determinants are replaced by configuration state functions (CSFs), i.e. linear combinations of determinants. This means that for the case of a singlet ground state, only combinations of determinants that correspond to singlet excited states are considered.[87] In addition, determinants that differ in occupation by more than two MOs result in zero overlap. The resulting CI matrix is still quite complicated and the extent of excitations that are considered is generally limited, so a cut-off point must be chosen.

First, there is no mixing of the ground state with single excitations, although mixing does occur indirectly through double excitations, etc. This means that if only single excitations are considered (CIS), the ground state is not improved. Much of the correlation energy, however, can be recovered by considering only double excitations (CID). Despite this, it is common to improve the description further by also including the indirect effects of the single excitations via CISD; the single excitations are relatively inexpensive to include because they only affect the ground state via mixing with the double excitation terms. Further improvements are often not computationally feasible, and including triple excitations perturbatively in CISD(T) provides a cheaper alternative to including them directly in CISDT.

The major disadvantage to CI methods is that truncated CI methods are not size extensive. A size extensive method returns the energy of two fragments at large separations that is equal to the sum of the energy of the separate fragments ($E_{A-B} = E_A + E_B$). This does not occur in truncated CI, since excitations of one type (e.g. single excitations) on a fragment can contribute to different excitation types when two fragments are considered together. Thus, the energy of two non-

interacting fragments is not necessarily equal to the sum of the energies of each fragment.

One way of overcoming this is by using the Quadratic CISD method (QCISD), which is derived from CISD, but has some higher order terms to make it size extensive. Alternatively, a different approach can be taken, e.g. Coupled Cluster theory.

2.1.2.2 Coupled Cluster Theory

As has been mentioned, truncated CI is not size extensive. Coupled Cluster (CC) theory is similar to CI in that it defines the wave function as an expansion of excited determinants, but it is size extensive even at the truncated level of theory. The CC wave function is defined by a Taylor expansion of the operator $e^{\hat{T}}$:

$$\begin{aligned} \Psi_{\mathrm{CC}} &= e^{\hat{T}}\Psi_{\mathrm{HF}} \\ \hat{T} &= \hat{T}_1 + \hat{T}_2 + \hat{T}_3 + \cdots + \hat{T}_N \end{aligned} \tag{2.25}$$

In other words, the CC wave function is generated from a Taylor expansion of the operator, $\hat{T}_i$, where the index i refers to the operation of generating an i^{th} excited determinant. For example, the double excitation operator $e^{\hat{T}_2}$ gives a power expansion of the operator $\hat{T}_2$.

When $e^{\hat{T}_2}$ operates on Ψ_{HF} it generates a wave function that is expressed as a function of all of the determinants that result from a double excitation. The solution to Ψ_{CC} corresponds to the set of variables $\{t_{\mathrm{D},i}\}$, known as amplitudes,

for which equation 2.25 is satisfied.

$$e^{\hat{T}_2}\Psi_{\mathrm{HF}} = \left(1 + \hat{T}_2 + \frac{\hat{T}_2^2}{2!} + \frac{\hat{T}_2^3}{3!} + \cdots\right)\Psi_{\mathrm{HF}} \tag{2.26}$$

$$\hat{T}_2\Psi_{\mathrm{HF}} = \sum_i t_{\mathrm{D},i}\Psi_{\mathrm{D}} \tag{2.27}$$

Since full CI and full CC wave functions consider all of the excited determinants, and differ only in how the excited determinants are generated, they are equivalent. However, the CC wave function does differ from the CI wave function for the truncated methods. To illustrate this, equation 2.26, which shows the operator that generates all of the doubly excited determinants, is discussed. This generates the wave function in the CC doubles (CCD) method. If the expansion included only two terms $(1+\hat{T}_2)$, this would represent the CI wave function, with $\{t_{\mathrm{D},i}\}$ corresponding to the linear coefficients $\{a_{\mathrm{D},m}\}$ of equation 2.23. It is the subsequent terms ($\hat{T}_2^2$, etc), that differentiate between CID and CCD. Whereas for the former case, only the doubly excited determinants relative to the ground state were included, in CCD all double excitations are included. This means that higher excitations (e.g. a quadruply excited state) are partially included from lower order excitations (a double excitation of a doubly excited state has amplitudes $\{t_{\mathrm{D},i}^2\}$).

In CC, as was the case for CI, spin and overlap considerations simplify the expressions but they remain complicated. Hence a cut-off point of excitations must be chosen, and it is dictated by the computational intensity of the calculations. Most commonly CCSD (CC involving single and double excitations) and CCSD(T) are used. The latter, in a similar manner to CISD(T) considers the triple excitations in a perturbative manner.

Although the issue of size extensivity is no longer a problem in CC methods,

the disadvantage of CC theory is that it is not variational. Thus, the energy obtained from a CC calculation can result in an energy value that is lower than the true energy.

2.1.2.3 Møller-Plesset Theory

The final post-HF method that is discussed here is Møller-Plesset (MP) theory. Similar to CI and CC, MP theory begins with the HF method as a starting point. It is based on 'many-body' perturbation theory, which defines the exact Hamiltonian operator as a sum of a known reference Hamiltonian $\hat{H}_0$, and a small perturbation, $\hat{H}'$. The extent of the perturbation is determined by a constant, λ, which can have any values between 0 and 1, the former representing the unperturbed case. In addition, the exact energy and wave function can be written in terms of λ.

$$\hat{H} = \hat{H}_0 + \lambda\hat{H}' \tag{2.28}$$

The SE of the reference system is

$$\hat{H}_0\Psi_0 = E_0\Psi_0 \tag{2.29}$$

The SE of the actual system is:

$$\hat{H}\Psi = E\Psi \tag{2.30}$$

$$E = E_0 + \lambda^1 E_1 + \lambda^2 E_2 + \cdots \tag{2.31}$$

$$\Psi = \Psi_0 + \lambda^1\Psi_1 + \lambda^2\Psi_2 + \cdots \tag{2.32}$$

By putting the expansions into equation 2.30, and collecting the terms which have the same λ^n, n equations are generated, the first, second,..., etc. of which correspond to the first, second,..., etc. order corrections to the unperturbed system. These equations can be manipulated to give expressions for the corrections to the energy, which depend on the unperturbed values and lower order corrections. This means that any correction can be written in terms of the perturbation operator, the unperturbed wave functions and the unperturbed energies.

Møller Plesset theory is a specific form of many-body perturbation theory, which begins with the HF system as its unperturbed system. The unperturbed Hamiltonian is taken as the sum of the Fock operators, and the difference between this and the exact Hamiltonian is the perturbation, which accounts for electron correlation. Thus the unperturbed energy is the sum of the orbital energies. In addition, one possible wave function for the unperturbed system is the Slater determinant, which is the lowest energy function, but so too are all of the possible determinants that are generated from the spin orbitals.

$$\hat{H}_0 = \sum_i \hat{f}_i \tag{2.33}$$

$$\hat{H}' = \hat{H} - \hat{H}_0 \tag{2.34}$$

$$E = \sum_i \varepsilon_i + \lambda^1 E_1 + \lambda^2 E_2 + \cdots \tag{2.35}$$

$$\Psi = \Psi_0 + \lambda^1 \Psi_1 + \lambda^2 \Psi_2 + \cdots \tag{2.36}$$

Recall that the HF energy is not the sum of the orbital energies because the electron-electron repulsion is counted twice. The first order correction to this system accounts for the double counting, and the energy which includes the first order correction (denoted MP1=E(MP0)+E(MP1)) is found to be the HF energy.

Thus, it is necessary to go to the second order correction to improve on the HF energy. This second order correction is found to be dependent on excited determinants as well as the Slater determinant. It is expressed as:

$$E(\mathrm{MP2}) = \sum_i \frac{\langle \Psi_{\mathrm{SD}} | \hat{H}' | \Psi_{\mathrm{D},i} \rangle \langle \Psi_{\mathrm{D},i} | \hat{H}' | \Psi_{\mathrm{SD}} \rangle}{E_0 - E_{\mathrm{D},i}} \tag{2.37}$$

where the subscript (D,i) indicates the i^{TH} double excitation. (Single excitations do not appear because there is no overlap between the ground state and singly excited states.) This term can be written in terms of two-electron integrals over the MOs, and in terms of the MO energies. It is also possible to include higher terms, denoted by MPn.

For the particular case of MP2, it provides an inexpensive method in which to include electron correlation. In addition to being computationally inexpensive relative to truncated CI and CC, MP2 is size extensive. Unfortunately, it is not variational. Also, the central assumption of perturbative methods, that the exact solution differs only slightly from the HF-based solution, should be valid in order to use MP theory, but this is not necessarily the case in practice.

To summarise, this section has begun with the SE, and through the description of a series of assumptions, the HF approach was considered. The HF method accounts for the interaction between electron-electron interactions only in an average way but provides a starting point for accounting for electron correlation via CI, CC and MP methods. Whereas truncated CI is variational but not size extensive, both truncated CC and MP methods are size extensive but not variational. The next section describes the alternative Density Functional Theory approach to the electronic structure, which depends on the electron density, and not the wave function.

2.2 Density Functional Theory

So far, the focus of this chapter has been on wave function-based methods. In each method, the aim was to solve the many-electron SE given an expression for the Hamiltonian operator and for the wave function. This section now discusses the evaluation of the energy of a system from an alternative to the wave function, the electron density. This quantity is the central tenet of Density Functional Theory (DFT).

The aim of this section is to give a brief introduction to DFT methods. First, the electron density as a possible alternative to the wave function is considered. In this context, it is necessary to mention two theorems proposed by Hohenberg and Kohn. These theorems encompass the foundations of DFT, by establishing the electron density as a valid function for the description of the properties of a quantum mechanical system e.g. total energy. Next, the Kohn-Sham method is discussed, which provides a practical approach to determining the properties of a system via the electron density. These concepts form the basis of DFT as currently used by chemists, and their importance was acknowledged in 1998, when Walter Kohn shared the Nobel Prize in Chemistry "for his development of the density-functional theory".

The Kohn-Sham method provides a conceptually simple, and, in principle, exact approach to the electronic structure of a system. In doing so, it provides an eloquent formulation of the solution to the electronic structure problem in terms of the electron density. However, it is not without its difficulties because it also introduces a new quantity, the exchange-correlation energy. Since the exact expression for the exchange-correlation energy is not known, it has been the focus of much of the development of DFT. Some of these developments are outlined in

the final part of this section.

2.2.1 Electron Density

For a many-electron system, the wave function is expressed as a function of four coordinates for each electron, three spatial coordinates and one spin coordinate. Practically, this means that as the number of electrons, n, in a system increases, the wave function rapidly becomes very complicated, depending on $4n$ variables. However, the energy of the system does not depend explicitly on all $4n$ variables, since it is an expectation value that can be represented by one- and two-electron integrals. Hence, it is not unreasonable to think that an alternative to the complicated wave function might be available.

The electron density, $\rho(\mathbf{r})$, is a probability density, defined as:

$$\begin{aligned} \rho(\mathbf{r}) &= \int |\Psi|^2 d\mathbf{r} \\ \rho(\mathbf{r}) &= \int_0^\infty |\Psi|^2 d\mathbf{r} = n \end{aligned} \tag{2.38}$$

that is, ρ defines the probability of finding an electron in the volume element $d\mathbf{r}$, which simply becomes the number of electrons when the total volume is considered. In this way, the electron density is capable of describing the total number of electrons in the system.

A second characteristic of the electron density is that it has a discontinuity as the nucleus is approached. This is a result of the Coulombic attraction between an electron and the nucleus, which is equal to $\frac{Z_A}{r_{iA}}$. So, as the distance between the electron and nucleus becomes small, and $r_{iA} \rightarrow 0$, $r_{iA}^{-1} \rightarrow \infty$, which results in a cusp at the nucleus. The importance of this property is that it shows that

the electron density is capable of describing the position of the nucleus and the nuclear charge of the system. Thus, by knowing the electron density of a system, it is also possible to find the number of electrons, and the position and charge of the nucleus, i.e. $\rho \Rightarrow \{n, R_A, Z_A\}$. The electronic Hamiltonian can also be written so that it depends only on these variables, indicating that the energy of a system might be obtainable from the electron density.

From an historical perspective, the electron density approach dates back to 1927, when the Thomas-Fermi model was proposed (see reference 90 for further details). However it was in 1964, nearly four decades later, that the legitimacy of the electron density as a variable was established by Hohenberg and Kohn through two conceptually simple theorems.

The first Hohenberg-Kohn (HK) theorem states that:

> "...the full many particle ground state is a unique functional of $\rho(\mathbf{r})$."[91]

Practically, this means that there is one electron density that determines the ground state properties of the system, and that if this electron density is known the ground state properties can be determined exactly.

The second Hohenberg-Kohn (HK) theorem can be summarised by:

> "...the functional that delivers the ground state energy of the system, delivers the lowest energy if and only if the input density is the true ground state density, $\rho(\mathbf{r})$."[91]

This theorem is the electron density equivalent of the wave function-based variational principle, that has already been discussed. Practically this means that, in a similar way to wave function-based methods, there is now a prescriptive ap-

proach to finding the best possible electron density of a system since it is the one that gives the lowest energy.

2.2.2 Kohn-Sham Method

The two HK theorems have formally proven two key concepts of the electron density: It is possible to calculate ground state properties from the electron density; and the best electron density is the one that yields the lowest energy. But, there are still practical considerations that have not been addressed. These theorems provide neither a method to calculate the energy from the density, nor a method to find the density without first finding the wave function. In 1965, these issues were addressed by Kohn and Sham when they suggested a formulation to find the energy within the DFT formalism. This has become known as the Kohn-Sham (KS) method.

The principle behind the KS method is to consider a reference system, in which the electrons do not interact. The electron density for this fictitious system can be chosen such that it is the same as the electron density for the real system of interest. This non-interacting system can easily be related to the HF method. Recall that the problem with the HF approach is that it cannot adequately describe the electron-electron interactions, so that if there are no such interactions, the HF approach is exact. With this in mind, beginning from the simple noninteracting electron approach makes sense.

The electronic energy of this noninteracting system is simply the kinetic energy:

$$E_{\text{nonint}}[\rho] = T_{\text{nonint}}[\rho] \tag{2.39}$$

Improving this model to include the particle interactions can now be achieved in a stepwise form, by first adding only the classical electrostatic interactions (via the Coulomb repulsion energy, $J[\rho]$, and the nucleus-electron attraction energy, $E_{\text{ne}}[\rho]$) and then by considering the non-classical terms, namely the difference between the real and non-interacting kinetic energy and the non-classical electrostatic contributions, in a collective term, $E_{\text{XC}}[\rho]$:

$$E_{\text{KS}}[\rho] = T_{\text{nonint}}[\rho] + E_{\text{ne}}[\rho] + J[\rho] + E_{\text{XC}}[\rho] \tag{2.40}$$

This equation now represents the energy of the true system and E_{XC} contains all of the difficult parts to calculate. Thus, E_{XC} can be defined as:

$$E_{\text{XC}}[\rho] = (T[\rho] - T_{\text{nonint}}[\rho]) + (E_{\text{ee}}[\rho] - J[\rho]) \tag{2.41}$$

A key point to this approach is the manner in which the electron density, ρ is constructed. As the interactions between the electrons are included, the expression for the total energy changes but ρ stays the same because the noninteracting energy was formulated to have the same density as the true system.

Returning to the noninteracting particle model, it is straightforward to include the nuclear-electron interaction term and the classical part of the electron-electron electrostatic term of the electron-electron interactions. If the wave function is reintroduced through a Slater determinant, the HF equations can account exactly for T_{nonint}, E_{ne} and J (equation 2.15).

$$\begin{aligned} \hat{f}_i\psi_i &= \varepsilon_i\psi_i \qquad i = 1, 2, \ldots, N \\ \hat{f}_i &= -\frac{1}{2}\nabla^2 - \sum_{A=1}^{M}\frac{Z_A}{r_{iA}} + \int \frac{|\chi_j(\mathbf{r}_2)|^2}{r} d\mathbf{r}_2 \end{aligned} \tag{2.42}$$

The HF equations provides an important step in the KS scheme since, if it were possible to take E_{XC} into account, the exact energy of the system would be known. The KS scheme does exactly this by using a one-electron potential, v_{xc} due to E_{XC} defined by:

$$v_{\mathrm{xc}}(\mathbf{r}) = \frac{\partial E_{\mathrm{XC}}[\rho]}{\partial \rho(\mathbf{r})} \tag{2.43}$$

A set of one electron KS equations can now be written as:

$$\begin{aligned} \hat{f}_i^{\mathrm{KS}}\chi_i &= \epsilon_i\chi_i \qquad i = 1, 2, \ldots, N \\ \hat{f}_i^{\mathrm{KS}} &= -\frac{1}{2}\nabla^2 - \sum_{A=1}^{M}\frac{Z_A}{r_{iA}} + \int \frac{|\chi_j(\mathbf{r}_2)|^2}{r} d\mathbf{r}_2 + v_{\mathrm{xc}}(\mathbf{r}) \\ \hat{f}_i^{\mathrm{KS}} &= -\frac{1}{2}\nabla^2 - \sum_{A=1}^{M}\frac{Z_A}{r_{iA}} + \int \frac{\rho_j(\mathbf{r}_2)}{r} d\mathbf{r}_2 + v_{\mathrm{xc}}(\mathbf{r}) \end{aligned} \tag{2.44}$$

In this case, the one electron orbitals are called the Kohn-Sham (KS) orbitals and are denoted χ_i to distinguish them from the HF orbitals, and the eigenvalues are denoted ϵ_i. The difference between the HF and KS equations is that the exchange integral in the Fock operator is replaced by v_{xc} in the KS operator. The electron density is simply the sum of the individual probability densities from χ_i, i.e. $\rho(\mathbf{r})=\sum_i^n |\chi_i|^2$.

It is possible to use the linear combination of atomic orbital (LCAO) approach to the KS equations, in a similar manner to the way that it is used in the HF equations (equation 2.17).

$$\chi_i(\mathbf{r}) = \sum_{a=1}^{P} c_{ia}\phi_a^{\mathrm{KS}}(\mathbf{r}) \tag{2.45}$$

Similar to the HF method, this leads to a matrix equation, which can be written in

terms of an overlap matrix (**S**), an orbital energy matrix (ϵ), a coefficient matrix (**C**) and instead of a Fock matrix, there is now an analogous Kohn-Sham matrix ($\mathbf{F}^{\mathrm{KS}}$).

$$\mathbf{F}^{\mathrm{KS}}\mathbf{C} = \mathbf{S}\mathbf{C}\epsilon \tag{2.46}$$

Equations 2.21 and 2.46 do contain similarities and the solution to the DFT problem, given a particular expression for v_{xc}, is to find the most suitable set of coefficients $\{c_i^{\mathrm{KS}}\}$ of the set of basis functions $\{\phi_i^{\mathrm{KS}}\}$, not unlike solving equation 2.21.

There are some quite significant differences between HF and KS methods that should be mentioned. First, while ε_i in the HF equations correspond to orbital energies, this is not necessarily the case for ϵ_i in the KS equations. It is the total electron density and the properties of the total system that are meaningful in the KS equations. However, it has been shown that in current DFT calculations, the KS orbitals do describe, at least qualitatively, the occupied MOs.[91]

Second, and most significantly, while the HF equations are approximate equations, the KS equations are, in principle, exact. This means that for an exact expression for E_{XC}, the system can be solved exactly. Because an exact expression has thus far not been found, approximate functionals must be used. This does complicate matters because while exact DFT is variational, introducing approximations means that this is no longer necessarily the case, and it is possible for the total energy from DFT calculations to be lower than the exact energy. Therefore, the best functional does not necessarily correspond to the one with the lowest energy, a similar situation to that in Møller-Plesset and Coupled Cluster theories in the post-HF methods. From a computational efficiency view, however,

approximate DFT methods are comparable with HF but often yield superior results. For this reason, they are often chosen, especially for large molecules, in which post-HF methods are prohibitively expensive.

2.2.3 Exchange-Correlation Functional

In equation 2.40, the only unknown quantity is the exchange-correlation (XC) energy. This part of the total energy encompasses the non-classical contributions to the energy. This means that it must account for the difference between the real and non-interacting kinetic energy, the non-classical part of the electron-electron interaction energy and it should also include the self-interaction energy. This latter term arises in DFT because, in contrast to the HF approach, there exists an unphysical interaction of an electron with itself arising from the Coulomb term of the energy (e.g. the Coulomb term for a one electron system is nonzero, in contrast to the HF scheme, in which the exchange term exactly cancels the Coulomb part).

It is often the case in DFT that, in an attempt to find an expression for the complicated XC functional, it is divided into two parts; the exchange functional and the correlation functional. However, it should be pointed out that the correlation energy via DFT is not the correlation energy via HF. This is a direct consequence of the HF method being an approximate method, and the Slater determinant being used to approximate the wave function. The basis set correlation energy using the wave function approach (equation 2.24) includes the errors due to having the incorrect wave function in the HF method as well as the error explicitly due to averaging the effects of the electrons. This aspect is not an issue in DFT since the exact electron density is used, at least in principle.

There is a large number of forms of the XC functional available. This is perhaps reflective of the major setback in DFT, that the approximate XC functionals are not variational, so there is no systematic way of improving the XC functional (although in developing a good functional it is necessary to satisfy some specific physical conditions). Therefore, many methods have been developed for reproducing different properties of molecules but there is currently no universally well-performing method.

The aim of the remaining part of this section is to give a brief overview of the types of DFT methods, especially those implemented in this research, and their advantages and disadvantages. The main types of DFT methods that are currently in use in chemistry, are local density approximation (LDA) methods, generalised gradient approximation (GGA) methods, and hybrid-DFT methods. More recently, a fourth type of method has emerged, called meta-GGA methods, but these methods will not be discussed since they were not used in this research.

2.2.3.1 Local Density Approximation

The local density approximation (LDA) to DFT assumes that the electrons form a uniform (or homogeneous) electron gas. Specifically, this means that the electrons move in a background uniform distribution of positive charge. This resembles a ideal metal, in which there is a sea of valence electrons moving in a positive charge that is smeared out to a uniform distribution. The expression for the LDA XC energy is given by:

$$\begin{aligned} E_{\mathrm{XC}}^{\mathrm{LDA}}[\rho] &= \int \rho(\mathbf{r})\epsilon_{\mathrm{xc}}(\rho(\mathbf{r}))d\mathbf{r} \\ &= \int \rho(\mathbf{r})\left(\epsilon_{\mathrm{x}}+\epsilon_{\mathrm{c}}\right)(\rho(\mathbf{r}))d\mathbf{r} \end{aligned} \tag{2.47}$$

In this case, E_{XC} is expressed in terms of the exchange-correlation energy per particle of the uniform electron gas, ϵ_{xc}, weighted by the probability of finding an electron at the point **r**.

ϵ_{xc} can be divided into ϵ_x and ϵ_c, the exchange and correlation terms respectively. The greater contributor to E_{XC}^{LDA} energy is the exchange, which can be written as:

$$\epsilon_x = -\frac{3}{4}\left(\frac{3\rho}{\pi}\right)^{\frac{1}{3}} \tag{2.48}$$

and when put into equation 2.47, it becomes proportional to $\rho^{4/3}$. This resembles an expression that had been previously proposed by Slater in 1951[92] before the HK theorems as a description for the HF exchange, and is often called the Slater exchange.

The correlation term ϵ_c is more complicated than ϵ_x, and the most commonly used expressions were developed by Vosko, Wilk, and Nusair.[93] One expression is based on a parameterisation scheme (VWN5) fitted to Monte Carlo simulations and an alternative expression was developed based on the random phase approximation. The usage of the Slater exchange expression combined with a VWN correlation expression is known as SVWN.

The LDA described by equation 2.47 is local because at all points, the XC energy depends only on the electron density at that point. This appears to be a severe oversimplification of a real system, since the electron density of most systems does not have a uniform electron density, but contains inhomogeneities. Nevertheless, LDA methods work surprisingly well for some molecular properties. However, they do have a tendency to produce energy values that are too negative, i.e. they overbind.

2.2.3.2 Generalised Gradient Approximation

The next major advancement in the search for an expression for E_{XC} was the generalised gradient approximation (GGA). Like LDA, GGA methods are local methods. They depend on the electron density only at a particular point. Unlike the LDA methods, however, they contain a dependence on the gradient of the density at a particular point, which attempts to account for the non-uniformity (inhomogeneity) of the electron density. This can be expressed as follows:[91]

$$E_{XC}^{GGA}[\rho(\mathbf{r})] = \int f\left(\rho(\mathbf{r}), \nabla\rho(\mathbf{r})\right) d\mathbf{r} \tag{2.49}$$

If the XC functional is considered in terms of a simple Taylor expansion of the density, such that the first term is the LDA term, and the second is in terms of $\nabla\rho(\mathbf{r})$, the gradient expansion approximation (GEA) functional is obtained. However, this does not lead to improvements over LDA and in fact gives worse results because it introduces some unphysical characteristics into the system.

However, in the closely related generalised gradient approximation (GGA) these unphysical parts are removed, and the results are much improved. As was the case for the LDA methods, E_{XC}^{GGA} is generally separated into the energy due to the exchange and the energy due to correlation. There are many different functionals that fall into the GGA category. Common E_X^{GGA} functionals include Becke's 1988 functional (generally denoted B or B88),[94] which has empirical parameters that were fitted to noble gas data. E_X^{GGA} functionals that have no empirical parameters fitted include the Perdew, Burke and Ernzerhof (PBE) functional[96,97] and Perdew and Wang's 1991 functional (PW91x).[95]

Common examples of E_C^{GGA} functionals include Perdew's 1986 functional (P86),[98]

which was developed by fitting to data from neon; Perdew and Wang's 1991 functional (PW91c),[95] which is parameter free, consistent with its exchange counterpart PW91x; and Lee, Yang and Parr's 1988 functional (LYP),[99] which does not come from the LDA model, but from wave function-based theory and uses one empirical parameter.

GGA methods generally give improved results over LDA methods, and are only slightly more computationally expensive. Given the large number of possible GGA methods that have been generated in a number of ways, it is necessary to consider the property of interest when choosing which GGA method to use, and it is also often desirable to carry out benchmark calculations to examine performance.

Further modifications to GGA methods can be obtained by incorporating a kinetic energy dependence in the XC functional. Including the total kinetic energy into E_{XC} means that the method is no longer local. These methods are known as meta-GGA methods, and form a relatively new type of functional in DFT.[91] As was mentioned earlier, this research does not use these methods so for the purposes here I note that these methods are available, and now move on to discuss hybrid-DFT methods.

2.2.3.3 Hybrid Density Functional Methods

So far, the exchange correlation energy functional has been written simply in terms of the individual exchange and correlation functionals of the density ($E_{\mathrm{XC}}^{\mathrm{DFT}} = E_{\mathrm{X}}^{\mathrm{DFT}} + E_{\mathrm{C}}^{\mathrm{DFT}}$). The individual terms generally contain contributions from the LDA and/or GGA methods. However, there is a slightly different approach to $E_{\mathrm{X}}^{\mathrm{DFT}}$, which is to consider the exchange functional as containing contributions

from the HF exchange in addition to E_X^{LDA} and E_X^{GGA}. The most well-known of these methods is B3LYP,[100] which can be summarised by the following equation:

$$E_{XC}^{B3LYP} = (1-a)E_X^{LDA} + aE_X^{HF} + bE_X^{B88} + cE_C^{LYP} + (1-c)E_C^{LDA}$$

There are three parameters in the case (hence the '3' in B3LYP). The first two parameters decide on how much HF exchange, LDA exchange and GGA exchange should be included, and the latter dictates the proportion of LDA and GGA correlation contributions.

B3LYP has become widely used since it was first published and it is often reputed to give comparable, or better, results than pure GGA methods. In addition, there are other hybrid methods, e.g. the more recently published PBE0[101] and it is also possible to consider correlation functionals other than LYP in conjunction with the B3 exchange functional, expanding the choice of functionals even more.

2.3 Which Method?

The main advantage of DFT methods over traditional post-HF methods is that they account for electron correlation, but with only slightly greater computational effort than HF. This is especially useful for polyatomic systems and systems with a large number of electrons, when the post-HF methods, even the truncated methods, would be prohibitively expensive.

It is possible to choose from a wide-range of DFT functionals, which means that it is generally possible to find different functionals that perform well for different system properties. However, there are properties that are not describable using current DFT methods, for example, most current DFT methods are

neither appropriate to look at multiconfigurational systems, nor are they capable of describing dispersive effects (see chapter 4) so there are still situations where post-HF methods become necessary. Hence, although DFT is a very useful and computationally efficient method, it can still be necessary to benchmark the methods against the property of interest.

Post-HF methods are highly accurate computational methods within a basis set limit, but one severe drawback is that they are often too computationally demanding to implement. Even if truncated methods are implemented, there are difficulties. Truncated CI methods are variational but not size extensive, and truncated CC and MP methods are size extensive but not variational. MP2 is the cheapest post-HF method, in which electron correlation is included, but it is not without its difficulties. Since MP theory assumes that correlation is a small perturbation to the Fock operators, if this is not a correct assumption, there is no guarantee that the results obtained using MP2 are accurate. Therefore, the method of choice depends strongly on the properties of interest.

Having chosen an appropriate electronic structure method, it is also necessary to decide on how the atoms should be described. In this case, a basis set must be chosen, and it is also possible that relativity should be incorporated. The rest of this chapter focuses on these issues.

2.4 Basis Functions

Equations 2.17 (page 40) and 2.45 (page 57) define the LCAO approach to the expansion of a molecular orbital (or spin orbital) in terms of a series of basis functions $\{\phi_i\}$ in the HF and KS schemes. In this section, the specific mathemat-

ical forms of ϕ are discussed. Specifically, the merits of two particular functions, Gaussian- and Slater-type orbitals, are first discussed. Since the necessary number of basis functions of atoms increases as the size of atoms and molecules increases proportionally, computational efficiency becomes increasingly important for heavy atoms. The second part of this section briefly discusses ways in which the core orbitals in large atoms can be described to aid computational efficiency.

One issue with using necessarily finite basis sets is the problem of basis set superposition error. This problem is briefly discussed focusing on the counterpoise correction method, which attempts to overcome this error. Finally, data that can be obtained from the LCAO approach, namely atomic populations and bond order indices are considered.

2.4.1 Gaussian- and Slater-Type Orbitals

The concept of atomic orbitals (AOs) combining to give molecular orbitals (MOs) provides the foundation of chemists' understanding of bond formation. In this way, the mathematical form of the LCAO

$$\psi_i(\mathbf{r}) = \sum_{a=1}^{P} c_{ia}\phi_a(\mathbf{r})$$

can be related to the bonding picture in chemistry. The molecular orbital (ψ in the HF method or χ in the KS method) consists of contributing functions ϕ, which represent the atomic orbitals.

The mathematical function that best represents an atomic orbital is known as a Slater type orbital (STO):

$$\eta^{\mathrm{STO}}(r,\theta,\varphi) = NY_{l,m}(\theta,\phi)r^{n-1}exp(-\zeta r) \tag{2.50}$$

(r, θ, φ) represent the polar coordinates (although η can also be written in cartesian coordinates), N is a normalisation constant, and $Y_{l,m}$ describes the angular part of the function. Most importantly here is the exponential term, which describes the radial part of the orbital. It consists of the Slater exponent, ζ and a $-r$ dependence. This $-r$ dependence of the exponent means that while STOs describe the AOs well, they cannot be integrated analytically. This makes them incompatible with many programs that evaluate the exchange and Coulomb terms of the Fock matrix using analytical methods. Instead numerical integration is required when using STOs.

As an alternative function, Gaussian type orbitals (GTOs) can be used:

$$\eta^{\mathrm{GTO}}(r, \theta, \varphi) = NY_{l,m}(\theta, \phi) r^{2n-2-1} exp(-\alpha r^2) \tag{2.51}$$

The main difference in the GTOs compared with STOs is the radial description of the function, i.e. the exponent, which now has an α exponent and depends on $-r^2$ instead of $-r$. GTOs are more suited to analytic integration so they are often preferred over STOs. However, they do not describe AOs as well as STOs because unlike STOs, they do not correctly describe the cusp behaviour of the orbitals close to the nucleus, and they tend to fall off too rapidly far from the nucleus. Because of these characteristics, more than one GTO is generally used to describe one AO (or one STO), and the GTOs are linearly combined using a set of fixed coefficients and α exponents. These are known as contracted Gaussian functions (CGFs), which are said to be comprised of primitive Gaussian functions (PGFs).

2.4.2 Beyond the Minimum Basis Set

For a given atom, an associated basis set is defined, which consists of a set of atomic orbital functions, ϕ, with each ϕ represented by η^{STO} or η^{CGF}. The smallest number of functions that is required to describe an atom corresponds to one STO or CGF per filled AO and is called a minimum basis set. One severe drawback to the minimum basis set arises when modelling the bonding between atoms. If only one STO or CGF is used to describe an atomic orbital (i.e. the equivalent of only one Slater exponent models the radial part of the orbital), this often does not provide enough flexibility to adequately describe the electron distribution of an atom in a molecule.

One way to improve this is to increase the number of orbitals associated with an atom, which adds flexibility to the radial part of the wave function. If the minimum basis set is increased by a factor of two, three, four,..., etc., the basis set is of double zeta (DZ) quality, triple zeta quality (TZ), quadruple zeta quality (QZ),..., etc. More commonly, only the quality of valence orbitals is improved and split valence zeta basis sets are used. For example, the valence double zeta (VDZ) basis set differs from the full DZ basis only in that in VDZ the core orbitals are single zeta. Like full DZ, VDZ is an improvement over the minimum basis set, but is more efficient than full DZ basis sets. This is particularly important for heavier atoms, in which there are many core orbitals that do not contribute to bonding.

In general, a chemical bond is not isotropic in the bonding region. There are two main aspects of this anisotropy, which arise due to dynamic correlation (section 2.1.2), namely radial and angular correlation. Radial correlation refers to the situation in which there is one electron close to the nucleus and one farther

away from the nucleus. The best way to incorporate this in the basis set formalism is to add extra functions which are of the same angular momentum as the filled orbitals but with different exponents. This is the case for the valence multiple zeta effects that have just been discussed.

The second aspect of the anisotropic bond is the angular correlation that must also be taken into account in the basis set. Angular correlation refers to the situation in which the two electrons are at different sides of the nucleus. In this case, it is necessary to add functions which have higher angular momenta to the filled valence orbitals, but have the same exponents. This introduces the concept of polarisation functions. They improve the description of the atom in a molecule because they allow greater variation in the shape of MOs, allowing charge density to move away from the atomic nucleus. Addition of a polarisation function is denoted by adding 'P' to the end of the existing acronym e.g. DZP.

Diffuse functions are used for cases where the electrons are far from the nucleus e.g. systems in their excited states, or the polarisability of the atom. These functions have the same angular momentum as the existing orbitals but their exponents are much lower so that they extend further in space. These type of functions are often used to describe anions.

2.4.3 Basis Set Contractions

It has been mentioned that a CGF consists of a combination of GTOs (PGFs) and represents an atomic orbital. As has just been seen, it is possible to improve basis sets by using a number of CGFs (DZ, polarisation functions and diffuse functions). However, it is also worth considering how the PGFs contract to give the individual CGFs that are used. The manner in which the PGFs are combined

to give CGFs can be divided into two groups, segmented and general contractions.

For the situation of nine PGFs combining via coefficients to give three CGFs, there are two main ways of combining these nine PGFs to give three CGFs. First, it is possible to divide the PGFs into three parts, for example five, three and one PGFs. This results in a segmented contraction scheme of three CGFs with five, three and one PGFs, and five, three and one corresponding coefficients respectively. In this case, each PGF appears in only one CGF. Alternatively, it is possible to take the nine PGFs, and generate three sets of nine fixed coefficients. This generates three CGFs, each with the same nine exponents of the PGFs, but differing only in their coefficients, and it is known as a generalised contraction scheme. The most flexible approach is to uncontract all of the functions, but it also the most computationally costly approach. For many programs including Gaussian, it is preferable to use the segmented scheme for computationally efficiency.

2.4.4 Core Orbitals

As the size of an atom increases, it contains many occupied atomic orbitals that do not change when the atom becomes involved in bonding. These orbitals are considered as core orbitals, and one approach that has been mentioned is to use fewer STOs or CGFs to describe them. However, this description of the core is still quite computationally demanding since each of these orbitals is involved in the two-electron integrals of the Coulomb operator. There are two ways of overcoming this problem that were used in this research, effective core potentials (ECPs) and frozen core orbitals (FCOs).

ECPs begin from an all electron HF-based calculation. From this description, the valence orbitals are replaced by a set of nodeless orbitals that replicate

the former orbitals in the valence region, but they have no radial nodes. Next, the core-valence interactions are replicated by generating a series of one-electron potentials, which replace the Coulomb and Exchange operators. Each angular momentum is represented by a series of Gaussian functions. Now the basis set description of the atom consists of ECPs to represent the core, and core-valence interactions, and the basis functions that represent the valence orbitals. ECPs can be implemented in both Gaussian and MOLPRO.

A second approach uses FCOs. This approach, like the ECP approach, begins with an all electron description. In this case, the core orbitals are considered first and are replaced by a linear combination of fixed functions that are solutions to the all electron calculations. Next, the valence orbitals are considered, and in order to attain core-valence orthogonality, a linear combination of valence orbitals with core functions is carried out. Now the two-electron integrals from the Coulomb term are replaced by fit functions instead of the density. FCOs are implemented in ADF.

In both cases, it is clear that the main objective is to reduce the number of multicentre integrals. This is done by replacing the basis functions of the chemically unimportant part of the basis set with an alternative mathematical description that allows greater efficiency in the electronic structure calculations. This approach can also provide a way of incorporating relativity in atoms in an computationally inexpensive manner, which is discussed in section 2.5.

2.4.5 Basis Set Superposition Error

So far, the merits of different approaches within the LCAO approach have been discussed. Unfortunately, there are also some difficulties with the basis set de-

scription, one of which is the problem of basis set superposition error (BSSE). This error is an important consideration in weakly bound systems (chapter 4), and warrants further discussion.

In general, in the first step of an electronic structure calculation a basis set for each atom is chosen. This introduces an approximation inherent in basis set calculations, because a finite basis set on each atom must be used. This becomes a significant approximation for weakly bound systems, which can be exemplified by considering its interaction energy. The interaction energy of two fragments, A and B, is simply the energy of the molecule AB minus the energy of each fragment, all at their equilibrium geometries:

$$E_{\text{int}} = E(AB) - E(A) - E(B) \tag{2.52}$$

This equation, however, generally results in an overestimation of E_{int}. The reason for this is because both sets of basis functions of the fragments A and B are available to both fragments in AB. This contrasts to the situation of one fragment, since only the basis functions of A are available in the fragment calculation of A. So, in addition to the stabilisation energy due to the interactions, there is an artificial lowering of the energy because the orbitals of A become available for the electrons that are centred at B and vice versa.

It is possible to account for BSSE by using the counterpoise (CP) correction method. Central to this method is the concept of a ghost fragment. A ghost atom is the collection of basis functions that remain after the electrons and neutrons of the atom have been removed. Now if B in the complex AB is replaced by its ghost fragment B, the resulting fragment is A^*_{ab} (* represents the fact that A is at the geometry of the complex, and the subscript ab indicates that both basis sets

associated with A and B are included). The difference between the energies of A^*_{ab} and A^*_a is a measure of the artificial lowering of energy of A^*_a due to the basis functions at B. Using this concept, the resultant expressions for the correction to the energy (E_{CP}) and the CP corrected interaction energy (E_{int}) are:

$$E_{\mathrm{CP}} = E(A^*_{ab}) - E(A^*_a) + E(B^*_{ab}) - E(B^*_b) \tag{2.53}$$

$$\begin{aligned} E_{\mathrm{int}} &= E_{\mathrm{int}}^{\mathrm{uncorr}} - E_{\mathrm{CP}} \\ &= E(AB^*_{ab}) - E(A_a) - E(B_b) \\ &\quad - (E(A^*_{ab}) - E(A^*_a) + E(B^*_{ab}) - E(B^*_b)) \end{aligned} \tag{2.54}$$

This is the commonly accepted method for correcting for BSSE for weakly bound systems, and it is the approach that was taken in chapter 4.

2.4.6 Population Analysis

The final aspect of this section on basis sets discusses information that can be obtained from calculations as a direct result of using basis sets to describe the atoms of a molecule. Recall that the Roothaan matrix equation is a consequence of using the LCAO (i.e. linear combination of STOs or CGFs) in both the HF method (equation 2.20) and the KS method (equation 2.46). This equation contains terms of an overlap matrix **S**, and indirectly through the Fock or KS matrix, the density matrix **P** is also present. The overlap matrix arises because the basis functions (AOs) are not orthogonal, so $\int \phi_i^* \phi_j d\mathbf{r}$ is not equal to zero, and it gives a measure of how much different basis functions overlap. The density matrix contains the variable coefficients in the LCAO, and it provides a measure of the extent to which each basis function ϕ_i accommodates electron density in the ground state.

These two matrices can be used to attribute the electron density of the molecule to the particular atoms or to the overlap region between atoms as follows. The i^{TH} MO (ψ_i^{HF} or χ_i^{KS}) can be occupied by 0, 1 or 2 electrons in the spin-restricted case, which can be defined by n_i, the occupation number. The occupation for this MO can be defined as:

$$n_i = n_i \int \rho_i(\mathbf{r}) d\mathbf{r} = \sum_{A,B}^{AO} n_i c_{iA} c_{iB} \int \phi_A^* \phi_B d\mathbf{r} \tag{2.55}$$

$$= \sum_{A,B}^{AO} n_i c_{iA} c_{iB} S_{AB} \tag{2.56}$$

$$= n_i c_{iA}^2 + n_i c_{iB}^2 + 2 \sum_{A \neq B}^{AO} n_i c_{iA} c_{iB} S_{AB} \tag{2.57}$$

In this way, the total occupation of the i^{TH} MO can be divided into the occupation on atom A (given by $n_i c_{iA}^2$), on atom B (given by $n_i c_{iB}^2$) and in the overlap region (given by $\sum_{A \neq B}^{AO} n_i c_{iA} c_{iB} S_{AB}$).

If the population of atom A is of interest, in addition to $n_i c_{iA}^2$, it is also possible to attribute to A half of the overlap contribution due to atom A with all other atoms B. This is the approach of the Mulliken population analysis,[102] which gives the gross population of atom A when all i MOs are considered. The gross population of atom A is defined as:

$$p_A = \sum_i n_i c_{iA}^2 + \frac{1}{2} \sum_{A \neq B} \sum_i n_i (2 c_{iA} c_{iB} S_{AB}) \tag{2.58}$$

This atomic population can give information about the population of the atoms in the molecule, but it is also strongly basis set dependent, especially as the quality of the basis set increases. This makes it impossible to compare populations from different basis set calculations, but it can provide useful qualitative information

about the differences between systems that use consistent basis sets. One other drawback is that it can also generate unphysical negative values.

One approach that attempts to overcome the problems with the Mulliken population analysis is natural population analysis.[103] This approach can be summarised in two steps. The first step of the natural population analysis is to orthogonalise the atomic basis. This is achieved by partitioning the density and overlap matrices of the Roothaan equations into subblocks, which correspond to a given angular momentum of the particular atom centre. These subblocks are transformed from a non-orthogonal basis to an orthogonal basis (i.e. the overlap matrix is transformed to unity). These AOs are then divided into the bonding orbitals with high occupancy (close to 2.0) and the virtual orbitals with low occupancy (close to 0.0).

The next step is the removal of interatomic overlap, by taking the orthogonalised AOs of each centre and orthogonalising them with respect to each other. The key aspect of this step is that the AOs that are occupied are weighted in order to preserve these orbitals as much as possible, and conversely, the greatest distortion is allowed for the virtual AOs. This has been found to substantially reduce the sensitivity of the populations towards the specific basis set, since the weighting of adding virtual polarisation and diffuse functions in the orthogonalisation process is low.

The result of this approach is a set of orthogonalised orbitals called Natural Atomic Orbitals (NAOs), and their occupation (0-2). The Natural Bond Orbital (NBO) population of an atom is the sum of the individual NAO occupations of that atom. The major advantage of this approach is that the resultant natural populations are non-negative and are relatively insensitive to the basis set used.

Recall that equation 2.57 contains terms associated with the atoms and also a term that describes the overlap. It is clear that instead of focusing on partitioning the overlap term to the atoms, the overlap might be used as a measure of the extent of interaction between two atoms. The total occupation of a system is found by summing the n_i occupation:

$$\sum_i n_i = \sum_i n_i c_{iA}^2 + n_i c_{iB}^2 + 2 \sum_i \sum_{A \neq B}^{AO} n_i c_{iA} c_{iB} S_{AB} \quad (2.59)$$

$$= \sum_A P_{AA} + \sum_A \sum_{A \neq B} P_{AB} S_{AB} \quad (2.60)$$

The last term is known as the Mulliken overlap populations,[102] which for the overlap between atoms A and B is simply the sum of the products of the off-diagonal elements of $\mathbf{P}$ and $\mathbf{S}$. This number gives a value for the extent of bonding, but like the Mulliken populations, these overlap populations are very basis set dependent.

One disadvantage to interpreting the Mulliken overlap population is that the number that is obtained is not a bond order, e.g. 1 for a single bond, 2 for a double bond, and so on. However, a mechanism called the Mayer Bond Order (MBO) analysis[104] has been proposed as an alternative to the Mulliken overlap population, which gives bond order indices for the bonds. It is calculated using the following equation:

$$B_{AB} = \sum_{A \neq B} (\mathbf{PS})_{AB} (\mathbf{PS})_{BA} \quad (2.61)$$

The resulting MBO index, corresponding to the interactions between atoms A and B, is an integer value for the minimum basis sets, although for larger basis sets when more interactions are possible, the index does become non-integer.

One important aspect of this analysis is that the total bond order index for a particular bond can be decomposed into the contributions due to the different symmetry types of the molecule. This can further be related to the notional σ, π, etc. bonding interactions between atoms, which is useful in understanding the type of bonding between atoms in a molecule, e.g. interactions between a central metal and its surrounding ligands (see chapter 3). One drawback, however, is that like the closely related Mulliken analysis, MBO analysis is basis set dependent, so consistent basis sets are required to be able to get a useful comparison between MBO indices.

2.5 Relativistic Effects in Chemistry

All of the methodology thus far involves the non-relativistic, time-independent situation. This is a valid approach for the early members of the periodic table but as the atomic number increases, relativistic effects become important. These effects

> "... in chemical and physical properties arise from the difference in the true velocity of light as opposed to infinite velocity."[105]

Elements from the lower part of the periodic table are particularly affected. They have a high nuclear charge, which exerts a strong electrostatic field on the core electrons, so they are pulled close to the nucleus. This decreases the volume of space that an electron in the core orbital can occupy and its radial velocity increases. In fact, the average radial velocity of an electron in a 1s orbital is proportional to the atomic number of the atom. In atomic units, this is $\langle v_r \rangle = \frac{Z}{137}$ where $c = 137$ a.u. Consequently, relativistic effects must be taken into account

for atoms with large Z.

One effect of the high radial velocity is a relativistic mass increase:

$$m = \frac{m_0}{\sqrt{1 - \frac{v^2}{c^2}}} \tag{2.62}$$

This increase in mass also means that the electron's kinetic energy increases.

Of the atomic orbitals, the core s and, to a lesser extent, the core p orbitals are contracted most significantly by the nuclear charge because they feel its effects most. This is the 'direct relativistic contraction'. Since the core s and p orbitals are contracted, the higher angular momentum d and f electrons are screened from the nucleus leading to an 'indirect relativistic expansion'.

The valence orbitals, which are of greater interest than the core orbitals in chemistry, are also affected by relativity. The outer s and p orbitals, like their core analogues, experience a direct relativistic contraction. There are two different reasons that have been proposed for this observation. The first is related to the orthogonality condition for the orbitals of the same angular momentum. This means that in addition to the core s and p orbitals experiencing a contraction, the valence counterparts are also contracted. Alternatively, it has been proposed that the relativistic effects on the valence orbitals is due to mixing of these orbitals with orbitals of higher energy. However, both explanations give the same outcome, that relativity contracts the valence s and p orbitals. Also, in a similar manner to the indirect relativistic expansion of the core d and f orbitals, the contraction of the valence s and p orbitals screens the valence d and f orbitals from the nucleus. Thus, relativity affects both the core and valence orbitals of relativistic atoms. The effect of relativity on the valence orbitals leads to many interesting

properties. Relativity in gold is discussed in chapter 4, and the effect of relativity on the lanthanide and actinide contractions is mentioned in chapter 5.

Although not considered explicitly in this research, another consequence of relativity that should be mentioned is spin-orbit coupling. The electron distribution that has so far been discussed has focused on the probability of finding the electron in a given volume. Thereafter, the electron can be thought of as being 'spin-up' or 'spin-down'. However, for many-electron atoms the situation can become more complicated. The electron generates a magnetic field due to its orbital motion, and since the electron has an intrinsic motion derived from its spin, this also generates a magnetic moment. The interaction between the magnetic field due to the orbital motion and that due to the electron's spin results in an interaction energy. This effect is known as 'spin-orbit coupling'.

For light atoms, spin-orbit coupling is small relative to the interelectronic repulsion, so it can be treated as a secondary effect compared with the relative orientation of the spins (S) and of the orbital angular momenta (L) of the electrons. In this case, Russell-Saunders coupling[6] is used to describe a system. However, as the velocity of the electrons increases, which necessitates using a relativistic description, the necessity to include spin-orbit coupling also increases. Russell-Saunders coupling is replaced by $j-j$ coupling.[6] Spin-orbit coupling is returned to briefly later, when it will be shown that, unlike the SE, the concept of spin arises quite neatly from the Dirac equation. Thus, for heavy atoms, relativity must be included for three reasons; the direct relativistic orbital contraction, the indirect relativistic orbital expansion and spin-orbit coupling.

In the relativistic limit, space coordinates and time coordinates should be treated on the same basis rather than separately, so a time-dependence must be

included in the SE.

$$\hat{H}\Psi(x.y,z,t) = i\hbar\frac{\partial}{\partial t}\Psi(x,y,z,t) \tag{2.63}$$

$$\hat{H} = -\nabla^2 + \hat{V} \tag{2.64}$$

In this time-dependent SE, however, the Hamiltonian contains second derivatives with respect to the position coordinates, and on the right-hand side there is a first order derivative of the time coordinates. This inconsistency between the space and time derivatives is not valid at the relativistic limit, so the time-dependent SE is inherently a non-relativistic equation.

One way of accounting for relativity is by replacing the SE with the relativistic Dirac equation, which for a free electron can be written as:

$$i\frac{\partial}{\partial t}\psi = \left(c\alpha\cdot\mathbf{p} + \beta mc^2 + \hat{V}\right)\psi \tag{2.65}$$

$$\alpha\cdot\mathbf{p} = -i\hbar\left(\alpha_x\frac{\partial}{\partial x} + \alpha_y\frac{\partial}{\partial y} + \alpha_z\frac{\partial}{\partial z}\right) \tag{2.66}$$

In this case $\alpha_{x,y,z}$ and β are 4×4 matrices, which can be written as:

$$\alpha_{x,y,z} = \begin{pmatrix} 0 & \sigma_{x,y,z} \\ \sigma_{x,y,z} & 0 \end{pmatrix} \quad , \quad \beta = \begin{pmatrix} \mathbf{I} & 0 \\ 0 & -\mathbf{I} \end{pmatrix} \tag{2.67}$$

$$\sigma_x = \begin{pmatrix} 0 & 1 \\ 1 & 0 \end{pmatrix}, \quad \sigma_y = \begin{pmatrix} 0 & -i \\ i & 0 \end{pmatrix} \quad , \quad \sigma_z = \begin{pmatrix} 1 & 0 \\ 0 & -1 \end{pmatrix}, \quad \mathbf{I} = \begin{pmatrix} 1 & 0 \\ 0 & 1 \end{pmatrix}$$

The Dirac equation depends on the first order derivatives of all four (x, y, z, t) coordinates, which is relativistically consistent. Having achieved this consistency, it is now practical to consider the time independent case as an approximation to

the Dirac equation.

$$E\psi = \left(c\alpha \cdot \mathbf{p} + \beta mc^2 + \hat{V}\right)\psi \tag{2.68}$$

As a consequence of the α and β 4×4 matrices in the Dirac equation, each wave function ψ that is a function of the equation contains four components. These components can be interpreted as two spin components of two types of particles, the electron and positron. The positron is the antiparticle of the electron, and both have exactly the same mass and spin, but opposite charges. Positrons introduce the concept of 'negative' states. Specifically a positron is what remains in these negative states if an electron is removed. These states occur much lower in energy than the electronic states, so they do not need to be considered in most chemistry applications, other to note that they might cause problems with the variational principle in certain circumstances (known as variational collapse[88]). Now, two components of the wave function correspond to electrons in the Dirac equation, and they correspond to the notion of 'spin-up' and 'spin-down'. Hence, unlike the SE, spin is a direct consequence of the Dirac approach, and, unlike the SE, the Dirac equation inherently describes spin-orbit coupling.

The Dirac equation is complicated and is simplified by using many different approaches. In this research two such approaches were used, the zero order regular approximation (ZORA) to the Dirac equation, and the use of relativistic effective core potentials (RECPs).

The ZORA method[106,107] is a DFT two-component approach to the Dirac equation. In this case, the ZORA Hamiltonian is written in terms of $\hat{V}$, a non-relativistic collective expression for the nuclear potential, the Coulomb potential

and the exchange-correlation potential. If the scalar, rather than spin-orbit coupling ZORA is considered, the expression for the kinetic energy is then written as a function of this non-relativistic potential.

$$\left(\hat{V} + \hat{T}[V]\right)\psi_i = \epsilon_i \psi_i \tag{2.69}$$

$$\hat{T}[V] = \mathbf{p} \cdot \frac{c^2}{2c^2 - V}\mathbf{p} \tag{2.70}$$

The key aspect to this approach is that the relativistic Hamiltonian varies from the non-relativistic case, only in its treatment of the kinetic energy, which it turns out is relatively straightforward to incorporate into the non-relativistic programs. In this research the ZORA method was used in the Amsterdam Density Functional (ADF) program, in conjunction with the frozen core approximation.

Alternatively, RECPs can be used to account for relativity. RECPs are very similar to ECPs; the core is represented by a pseudopotential, and the only difference in the relativistic case is that the potential describes the core of a relativistic atom, and the orbitals describe the valence orbitals of a relativistic atom. If this approach is used, standard non-relativistic molecular methods can be used, so RECPs can be implemented in most computational programs. In this research, RECPs were used in the Gaussian and MOLPRO programs.

2.6 Summary

The aim of this chapter was to give a brief introduction to the electronic structure methods that were used in this research. The uncorrelated Hartree-Fock method was first discussed, which uses the Slater determinant as a representation of the wave function. This was followed by a description of three different post-HF

methods which attempt to incorporate electron correlation, namely configuration interaction, coupled cluster and Møller-Plesset theories.

Having discussed these wave function-based methods, the concept of electron density was introduced, leading to Density Functional Theory. In this section, the Kohn-Sham method was discussed and the approaches to describing exchange-correlation functionals were briefly mentioned.

The third part of this chapter described basis functions, using Gaussian- and Slater-type orbitals as mathematical expressions. Approximations to increase computational efficiency via effective core potential and frozen cores were also mentioned. Also discussed in this section was the problem of basis set superposition error associated with finite basis sets, which can be overcome by using the counterpoise correction method. This section concluded with the concept of population analysis, which can provide information about charges on atoms and bond orders.

The final part of this chapter described relativistic effects, which are necessary when describing heavy atoms. Specifically, the zeroth order regular approximation to the Dirac equation and the incorporation of relativity in effective core potentials were described.

Chapter 3

Inverse *Trans* Influence in $[AnOX_5]^{n-}$ (An=Pa, n=2; An=U, n=1; An=Np, n=0; X=F, Cl, Br)[108]

3.1 Introduction

The purpose of this study is to establish, and to provide an explanation for, the inverse *trans* influence (ITI) in $[AnOX_5]^{n-}$ (An=Pa, n=2; An=U, n=1; An=Np, n=0; X=F, Cl, Br). The ITI provides an interesting contrast to the more widely studied *trans* influence (TI) that is generally associated with d-block transition metal complexes (e.g. $[OsNCl_5]^{2-}$). In this section, the ITI is introduced by first considering previous computational studies of the TI and then by introducing the less well-known ITI. Section 3.3 presents the results from this study of the ITI in $[AnOX_5]^{n-}$: The initial focus of the analysis is on the molecular orbitals of $[UOBr_5]^-$ with particular reference to previous studies of the TI in *pseudo*-octahedral $[OsNCl_5]^{2-}$ by Lyne and Mingos,[109] and in *pseudo*-octahedral *mer*-$[Ti(NR)Cl_2(NH_3)_3]$ (R=Bu^t, C_6H_5, $C_6H_4NO_2$-4), in which an NH_3 group is *trans* to the NR group, by Kaltsoyannis and Mountford.[110] Then, all nine $[AnOX_5]^{n-}$ complexes are considered. Thereafter, section 3.3.5 moves away from the specific MOs to a more general bonding picture by looking at Mayer Bond Order (MBO) population analyses of the complexes. Finally, this chapter concludes with a summary.

3.1.1 *Trans* Influence

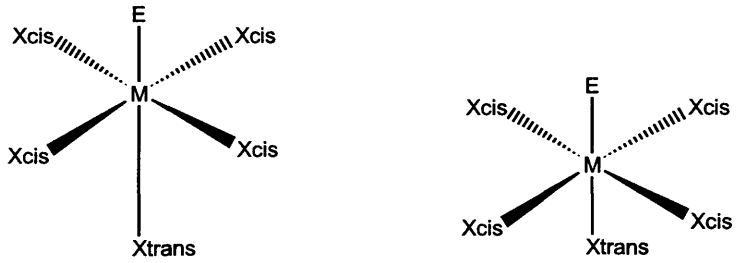

(a) *Trans* Influence

(b) Inverse *Trans* Influence

Figure 3.1: Representation of the *trans* and inverse *trans* influence in the hypothetical pseudo-octahedral [MEX_5] model.

The *trans* influence (TI) refers to the ground state structure, found mainly in transition metal pseudo-octahedral complexes, in which the bond *trans* to a tightly bound ligand (represented as E in figure 3.1) is longer than the corresponding *cis* bonds (figure 3.1(a)). This is related to the kinetic effect, known as the *trans* effect, the case in which the strongly binding ligand labilises the *trans* ligand towards substitution.

A number of arguments have been proposed to explain the *trans* influence and the related *trans* effect. Of these, a relatively simple argument was proposed by Grinberg in 1935 to explain the *trans* effect.[111] He suggested that the strongly binding ligand polarises the metal centre to give a dipole, with a slightly positive charge at the side of the metal towards the tightly bound ligand and a slightly negative charge on the opposite side. This means the *trans* ligand experiences a slight repulsion, resulting in a more labile *trans* than *cis* ligand, and an elongation of the *trans* bond relative to the *cis* bonds. From a molecular orbital viewpoint, the TI has been explained by noting that in the linear axial EMX_{trans} part of

the system, the two ligands, E and X, compete for the same metal orbital, which causes a weakening of the less strongly binding ligand (X in this case).[112,113]

More recently, Lyne and Mingos used Density Functional methods to investigate the TI in d^2 $[NOsCl_5]^{2-}$.[109] They found two structural features of interest in the optimised geometry, namely the $NOsCl_{cis}$ angle (α) of 96° and the directly related long *trans* bond. When they changed $\alpha(NOsCl_{cis})$ from 90.0° to its equilibrium value of 96°, they found that the HOMO-1 Os-N π interactions are enhanced. However, two other molecular orbitals (MOs) are destabilised because unfavourable nonbonding Cl_{cis}-Cl_{trans} interactions are increased. These interactions are alleviated by elongating the Os-Cl_{trans} bond. Thus, the TI of $[NOsCl_5]^{2-}$ is a result of minimising the orbitally-driven steric repulsions between the *trans* and *cis* chlorides.

In the case of the d^0 *mer*-$[Ti(NR)Cl_2(NH_3)_3]$ (R=Bu^t, C_6H_5, $C_6H_4NO_2$-4), steric repulsions between *cis* and *trans* ligands account for only about 25% of the TI present, that is, that even with $\alpha(N^{imido}TiCl)$ at 90.0°, about 75% of the TI persists.[110] This remaining contribution to the TI is attributed to the Ti-NH_3 bonding character of the *cis* and *trans* bonds. Whereas for the *trans* bond, both bonding and antibonding characteristics are evident in the MOs, only bonding characteristics are present for the *cis* bonds. Therefore, the TI is partly (25%) due to Ti-N^{imido} π-driven steric repulsion between the *cis* and *trans* ligands, but the majority (75%) of the TI is electronic - a result of Ti-$NH_{3,trans}$ antibonding character, absent for the analogous *cis* bonds.

3.1.2 Inverse *Trans* Influence

Much less information is available in the literature about the inverse *trans* influence (ITI) than the TI. In fact, the phrase inverse *trans* influence was only introduced in 1992 by Denning to describe the shortened U-Cl_{trans} bond relative to U-Cl_{cis} in $[UOCl_5]^-$ (see figure 3.1(b)).[41] He proposed a simple explanation for the difference between the TI and the ITI that is reminiscent of the earlier polarisation explanation of Grinberg. The polarisation effect depends on the parities of the highest core orbitals (p in both transition metal and actinide cases) and the formally empty f^0 or d^0 valence orbitals. For the case of the highest core and the empty valence orbitals having different parities (p and d), as for the transition metals, the polarisation is dipolar so the *trans* ligand is less tightly bound than the *cis* ligands. If, on the other hand, the highest core orbital and the empty valence orbital have the same parity, as is the case for the actinides, the dominant polarisation term is quadrupolar, and the *trans* bond is shorter than the *cis* bond. Thus, the interaction of the highest core and empty valence orbitals dictates whether the *trans* bond is longer or shorter than the *cis* bonds.

In this study, the ITI is initially approached from the core polarisation argument of Denning and then from the molecular orbital approach used in the TI studies of Lyne and Mingos, and of Kaltsoyannis and Mountford.

3.2 Computational Details

All of the calculations were carried out using the Amsterdam Density Functional version 2000 (ADF2000) program.[114–118] Both local density (LDA) and gradient-corrected density (GGA) methods were considered as potentially suitable Dens-

ity Functional approaches. The LDA method using Slater's description of the exchange with the correlation description of Vosko, Wilk and Nusair, denoted SVWN, was used.[93] Two GGA methods were considered: The non-local exchange and correlation approximations of Perdew and Wang combined with the local SVWN (denoted PW91),[95] and the non-local exchange of Becke with the local Slater exchange plus the non-local correlation description of Lee, Yang and Parr (denoted BLYP).[94,99] Relativistic effects were incorporated using ZORA.[106,107]

For the basis sets, a frozen core description and a valence description was used for each atom. The Dirac option was used to describe the frozen core. The core cut-off is indicated by a postscript to the atomic symbol denoting the highest core orbitals (e.g. Cl.2p; all of the orbitals up to and including the 2p orbitals in chlorine are considered core orbitals). For the ligands, O.1s, F.1s, Cl.2p and Br.3d were chosen, such that two s, two p and one d orbitals are in the valence region for each atom. For the actinides, An.5d was used unless specified otherwise (i.e. An.6p). For the actinides a triple zeta basis set (TZ) was chosen, and for the ligands, a double zeta basis set with a polarisation function (DZP) was chosen.

UX_6 (X=F, Cl) geometry optimisations were carried out under octahedral symmetry constraints and the $[AnOX_5]^{n-}$ (An=Pa, U, Np; X=F, Cl, Br) geometries were optimised under C_{4v} symmetry constraints.

Mayer Bond Order (MBO) population analysis was carried out using the program MAYER[119] on the ADF output file.

ADFrom99[120] was used to convert the ADF binary files to MOLDEN-readable format. The plots were generated using MOLDEN[121] with a consistent space contour value of 0.05.

3.3 Results and Discussion

Before considering the title complexes, the suitability of the three DFT methods, SVWN, PW91 and BLYP, were tested on the actinide structures $[UX_6]$ (X=F, Cl) and $[UOCl_5]^-$ by comparing the computational results with available experimental data. Having established the validity of the DFT methods, the most reliable method was used to calculate the ITI that is discussed in subsequent sections.

3.3.1 Performance of Density Functional Methods on Actinide Complexes

Table 3.1 gives a comparison of the DFT-optimised structural parameters with experimental values for $[UX_6]$ (X=F, Cl) and $[UOCl_5]^-$. From these parameters, it can be seen that the DFT results are in good agreement with experiment. The $[UF_6]$ results agree particularly well, especially when SVWN is used. The poorest agreement between experiment and theory occurs for $r(\text{U-Cl}_{trans})$ of $[UOCl_5]^-$, which still agrees to within 6 pm using SVWN. A comparison of the GGA (BLYP and PW91) methods with the LDA (SVWN) method shows that the computationally less expensive SVWN method better reproduces the experimental values. This is consistent with the conclusions of Deeth and co-workers,[122] in which it was found that for Werner-type complexes, LDA bond lengths, though slightly long, agree better than GGA bond lengths with experiment. Thus, SVWN was the chosen method for the proceeding analysis.

Table 3.1: Comparison of r(U-X)/pm for [UX_6] (X=F, Cl) and [$UOCl_5$]$^-$ optimised by DFT methods with the available experimental values. Relativistic U.5d TZ, O.1s, F.1s and Cl.2p DZP basis sets were used to describe the atoms.

	[UF_6]	[UCl_6]	[$UOCl_5$]$^-$		
	r(U-F)	r(U-Cl)	r(U-O)	r(U-Cl_{cis})	r(U-Cl_{trans})
BLYP	201.9	247.8	181.3	257.5	253.4
PW91	202.0	247.8	181.5	257.6	253.7
SVWN	199.5	244.0	179.9	253.1	249.0
Expt	199.6[1]	241[2]	177.4	253.6	243.3[3]

[1] [UF_6] data taken from ref. 123
[2] [UCl_6] data taken from ref. 124
[3] [$UOCl_5$]$^-$ data taken from ref. 125

3.3.2 Inverse *Trans* Influence in [$AnOX_5$]$^{n-}$

Table 3.2 shows the results of the geometry optimisations for the series of [$AnOX_5$]$^{n-}$. The extent of ITI was quantified by the following equation (which becomes a TI for values exceeding 100.0):

$$\%ITI = \frac{r(\mathrm{M} - \mathrm{X}_{trans})}{r(\mathrm{M} - \mathrm{X}_{cis})} * 100.0 \tag{3.1}$$

The results show that the computational ITI values (normal text refer to An.5d and values in italics refer to An.6p) are slightly larger than the available experimental ITI values (bold text). This means that computationally the ITI is underestimated. For [$PaOCl_5$]$^{2-}$, this is particularly obvious and is due to the large discrepancy (27 pm) in r(M-X_{trans}). The experimental values are taken from solid state [NEt_4]$_2$[$PaOCl_5$], which have a large estimated standard deviation for r(Pa-O) and large ranges of values for r(Pa-Cl_{cis}) (259-272 pm) and for the angles (α(OPaCl_{cis}): 83.4-98.8°). Given the large variation in these values and also, as noted in the original paper, the difficulties associated with finding

Table 3.2: SVWN-Optimised geometric parameters of $[AnOX_5]^{n-}$ (An=Pa, n=2; An=U, n=1; An=Np, n=0; X=F, Cl, Br). The values in normal text, in italics and in bold font are those with An.5d basis functions, with An.6p basis functions and experimental values respectively.

	$[PaOX_5]^{2-}$			$[UOX_5]^-$			$[NpOX_5]$		
	X=F	X=Cl	X=Br	X=F	X=Cl	X=Br	X=F	X=Cl	X=Br
r(An-O)	189.7	183.3	182.4	183.0	179.9	179.4	175.8	175.6	175.8
/pm	*193.3*	*186.2*	*185.1*	*185.0*	*181.0*	*181.0*	*181.3*	*178.9*	*179.0*
		174(9)			**176(1)**				
r(An-X_t)	215.4	261.3	276.9	204.0	249.2	265.9	194.0	234.4	251.6
/pm	*220.2*	*269.2*	*285.2*	*207.5*	*253.5*	*269.1*	*199.9*	*244.0*	*260.0*
		242(3)			**243.3(4)**				
r(An-X_c)	219.9	264.9	280.2	208.7	253.2	269.4	200.5	241.1	257.9
/pm	*222.0*	*270.5*	*285.8*	*210.5*	*255.9*	*271.0*	*203.3*	*246.9*	*262.1*
		264±0.05(5)			**253.6(2)**				
$OAnX_c$	93.0	90.7	90.4	91.7	90.3	89.9	89.4	88.5	88.4
/°	*94.4*	*92.5*	*92.1*	*91.9*	*90.5*	*90.1*	*90.5*	*89.6*	*89.8*
		91.6 av.			**89.7**				
$\%ITI$	97.9	98.6	98.8	97.7	98.4	98.7	96.7	97.2	97.5
	99.2	*99.7*	*99.8*	*98.6*	*99.1*	*99.3*	*98.3*	*98.8*	*99.2*
		91.7[1]			**95.9**[2]				

[1] $[PaOCl_5]^{2-}$ data taken from ref. 126
[2] $[UOCl_5]^-$ data taken from ref. 125

the position of light atoms in the actinide-containing structures, the comparison between experiment and theory is confined to the results of $[UOCl_5]^-$ from reference 125. Although an ITI is predicted by SVWN for $[UOCl_5]^-$, the extent of ITI is underestimated, mainly because of the slight overestimation of r(An-X_{trans}) (6 pm) mentioned earlier. However, SVWN reproduces the experimental $\%ITI$ sufficiently well to proceed with this analysis.

All of the complexes studied exhibit an ITI, that is they show a shorter r(An-X_{trans}) than r(An-X_{cis}). The extent of the ITI varies according to the ligand

and the actinide metal used. The largest ITI (smallest $\%ITI$ value) is seen for $[NpOF_5]$ and the smallest value corresponds to $[PaOBr_5]^{2-}$. In fact, there is a trend in the actinide metals toward increasing ITI for Pa $\rightarrow$ Np for a given halide, and a trend in the halides toward decreasing ITI for F $\rightarrow$ Br for a given metal.

As a first step towards rationalising these trends, the argument of Denning was considered. Recall that he proposed that the interaction of the valence 5f orbitals with the core 6p orbitals results in a quadrupolar polarisation of the metal centre. This causes a slight positive charge at the side opposite the tightly bound oxygen and slight negative charge in the equatorial plane of the metal, resulting in a short $r(\text{An-X}_{trans})$ relative to $r(\text{An-X}_{cis})$. If this explanation is correct, freezing the 6p orbitals during the SCF and geometry convergence will prevent them from being perturbed in any way, so the ITI should disappear. The data in italics in table 3.2, the geometries obtained when the An.6p frozen core is used, show that this is not the case. Although there is a slight decrease in the ITI (increase in $\%ITI$) for each complex, it does not disappear, and in all cases $\%ITI < 100.0$. Also, there is an increase in both $r(\text{An-X}_{trans})$ and $r(\text{An-X}_{cis})$, which would not be expected if the quadrupolar perturbation was removed. In that case, it would be predicted that $r(\text{An-X}_{trans})$ should increase but $r(\text{An-X}_{cis})$ should stay the same or even decrease slightly, as the slight negative charge in the equatorial positions are removed. The results here suggest that the 6p orbitals affect the actinide bonding in a more general way by enhancing bonding in all directions, but only slightly more in the equatorial position than in the axial position. It appears that although the 6p atomic orbitals (AOs) may play a role in the ITI, they do not provide a complete explanation.

The next step is to look at the role of the molecular orbitals in determining the

presence of the ITI. All subsequent discussion considers only the An.5d description in the calculations.

3.3.3 Molecular Orbital Analysis of $[UOBr_5]^-$

Rather than carrying out an exhaustive study of all nine complexes, the focus of this section is on the $[UOBr_5]^-$ molecular orbitals (MOs). There are two aims of the analysis of the molecular orbitals (MOs) of $[UOBr_5]^-$. The first aim is to gain some insight into why the driving force in $[OsNCl_5]^{2-}$ towards an obtuse $\alpha(NOsCl_{cis})$ (96.6°) that was found by Lyne and Mingos,[109] is not present for the actinide complex (89.9°). To do this, a series of constrained geometry optimisations was performed, in which $\alpha(OUBr_{cis})$ is varied from its equilibrium value (90°) to 102°. The second aim of this analysis is to find the source of the ITI in $[UOBr_5]^-$ at its equilibrium geometry. The MOs at the equilibrium geometry are analysed to establish their bonding character and the contributions from the different elements to each MO.

Before discussing either of these issues, however, there are a few points to note about the MOs of the molecule. Firstly, all of the calculations were carried out under C_{4v} symmetry. In this symmetry, the 18 molecular orbitals that can have metal-ligand bonding character (6 metal-ligand σ and 6x2 metal-ligand π MOs) are of a_1, a_2, b_1, b_2 or e symmetry. Table 3.3 considers the p_σ and p_π orbitals of the ligands, from which it is clear that there are four a_1, one a_2, one b_1, two b_2 and five sets of doubly degenerate e orbitals that are of potential interest in these complexes.

Although a more detailed analysis of the molecular orbitals is given in the proceeding section, table 3.4 gives a brief summary of the 18 MOs of $[UOBr_5]^-$

Table 3.3: Symmetries for the valence p_σ and p_π ligand atomic orbitals in C_{4v} $[AnOX_5]^{n-}$

	Oxygen	*trans* Halogen	*cis* Halogen
p_σ	a_1	a_1	a_1+b_2+e
p_π	e	e	$a_1+a_2+b_1+b_2+2e$

and their Mulliken % contributions from each of the elements. At first glance, it is clear from the amount of uranium character in the orbitals that there is significant covalent character in the complex. The relative electronegativities of oxygen and bromine are also a factor; the U-O MOs, containing the more electronegative oxygen, occur lower in energy than the U-Br MOs. (This distinction is less clear for the other halogen ligands that are more electronegative than bromine, because more mixing between the U-O and U-X MOs arises.)

The MOs with antibonding character are the $6a_1$ MO and the $9a_1$ MO. The lower energy $6a_1$ MO contains U-Br_{trans} σ^* character and the $9a_1$ MO contains U-Br_{cis} π^* character. The nonbonding MOs are the $7a_1$, the HOMO-1 (7e), HOMO ($1a_2$) and LUMO ($2b_2$). The $7a_1$ MO consists almost entirely of ligand character, as does the HOMO-1. The HOMO is a_2 which has no symmetry equivalent uranium AO in C_{4v} symmetry and finally, the LUMO is nonbonding because it is almost entirely U 5f character.

3.3.3.1 Dependence of Inverse *Trans* Influence of $[UOBr_5]^-$ on $OUBr_{cis}$ Angle

The variation of the energy of each MO with $\alpha(OUBr_{cis})$ is illustrated in figure 3.2. One interesting point to note about the geometry is that the $\%ITI$ varies from 98.7 at 89.9° to 100.8 at 102°, so there is a change from an inverse *trans* influence

Table 3.4: Energies of and Mulliken % contributions to the valence molecular orbitals for $[UOBr_5]^-$.

MO: E/(kJ/mol)		Bonding Character and Composition of MO	
3e	-594	U-O π	23% U, 66% O
$6a_1$	-590	U-O σ/U-Br_{trans} σ^*	22% U, 42% O, 22% Br_{trans}, 12% Br_{cis}
$7a_1$	-513	U-L nonbonding	17% Br_{trans}, 72% Br_{cis}
$2b_1$	-498	U-Br_{cis} σ	18% U, 81% Br_{cis}
$1b_2$	-457	U-Br_{cis} π	15% U, 85% Br_{trans}
4e	-440	U-Br_{trans} π	16% U, 60% Br_{trans}, 18% Br_{cis}
$8a_1$	-433	U-Br_{trans} σ/U-O σ	32% U, 7% O, 36% Br_{trans}, 23% Br_{cis}
5e	-388	U-Br_{cis} σ	8% U, 85% Br_{cis}
6e	-378	U-Br_{cis} π	15% U, 83% Br_{cis}
$3b_1$	-367	U-Br_{cis} π	14% U, 86% Br_{cis}
$9a_1$	-351	U-Br_{cis} π^*/U-O σ	7% U, 11% O, 75% Br_{cis}
7e	-321	U-L nonbonding	26% Br_{trans}, 69% Br_{cis}
$1a_2$ (HOMO)	-305	U-L nonbonding	100% Br_{cis} (by symmetry)
$2b_2$ (LUMO)	-151	U 5f	99% U

to a *trans* influence as the angle is increased. This supports the importance of the role of steric repulsion between *cis* and *trans* ligands in determining the TI, as has been suggested by Lyne and Mingos. It also poses the question: What determines the equilibrium angle of 89.9° for $[UOBr_5]^-$?

As the $OUBr_{cis}$ angle is increased, the most substantial changes in the MO energies occur for the 7e, $8a_1$ and 4e MOs (see figure 3.3 for MO representations). Both 7e and $8a_1$ are destabilised as $\alpha(OUBr_{cis})$ increases. The 7e is U-L nonbonding, because it has no metal character. It is made up of Br_{cis} and Br_{trans} p contributions that are out-of-phase with each other, and as the angle is increased, they are pushed towards each other. This increases the antibonding between the *cis* and *trans* components and hence the orbital becomes higher in energy. In a similar manner, the $8a_1$ is destabilised. In this case, however, the effect is less be-

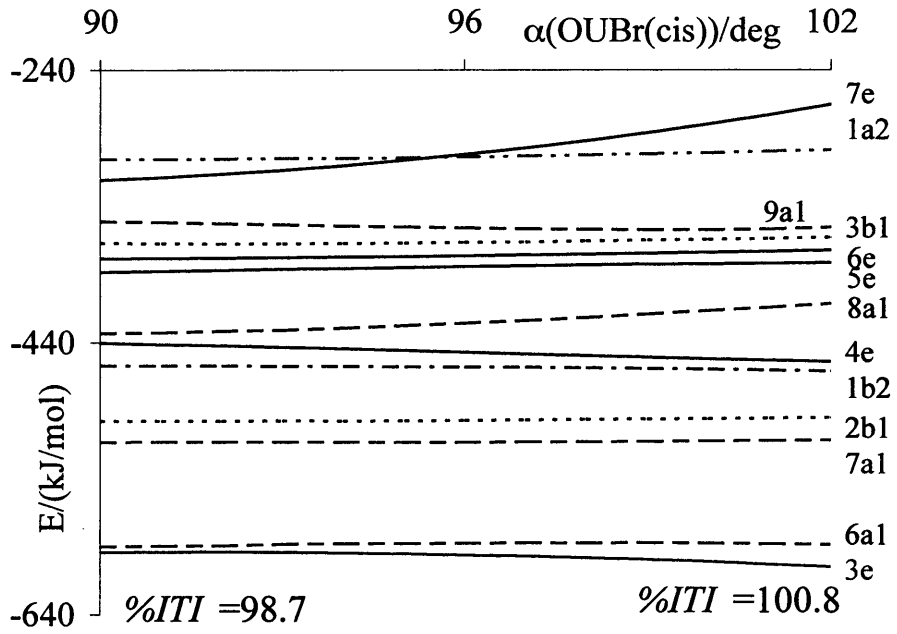

Figure 3.2: Walsh Diagram to show the Effect of Varying $\alpha(OUBr_{cis})$ on the $[UOBr_5]^-$ Molecular Orbital Energies.

cause the orbital also consists of U-O and U-Br_{trans} σ character which is unaffected as the angle is increased. Only the 4e set of doubly degenerate MOs is noticeably stabilised. The *cis* and *trans* bromide contributions are in-phase, so when $\alpha(OUBr_{cis})$ is increased, these favourable interactions are enhanced. The final geometry is a balance between these competing effects and clearly, the destabilising effects, especially from the 7e MOs, are the driving force to an equilibrium $\alpha(OUBr_{cis})$ value of 89.9°.

Thus, Walsh arguments can be used to establish why the equilibrium angle in $[UOBr_5]^-$ is 89.9°, but there is also the issue of how this differs from $[OsNCl_5]^{2-}$. In the latter case, the orbital that drives the $NOsCl_{cis}$ angle to 96.6° is Os-N π and Os-Cl_{cis} π^* bonding (labelled 4e in the original paper). As the angle is increased,

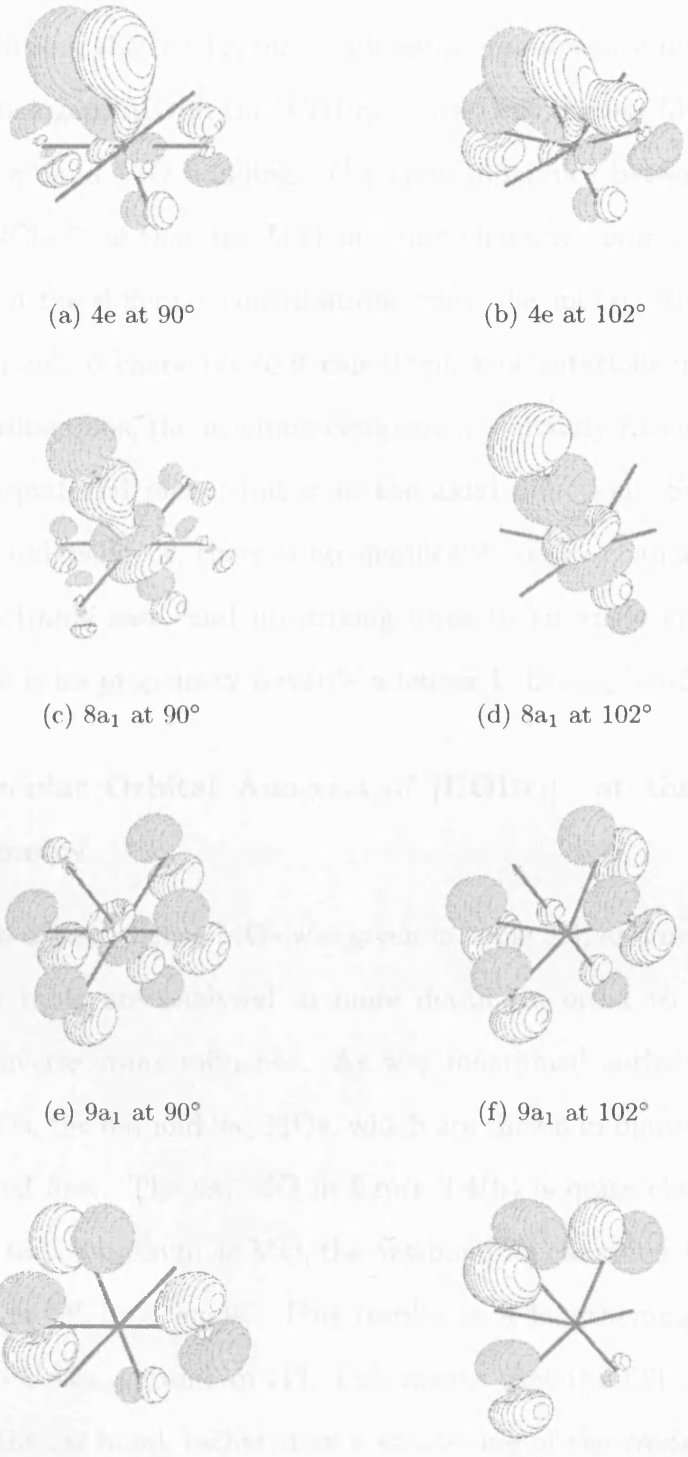

(a) 4e at 90° (b) 4e at 102°

(c) $8a_1$ at 90° (d) $8a_1$ at 102°

(e) $9a_1$ at 90° (f) $9a_1$ at 102°

(g) 7e at 90° (h) 7e at 102°

Figure 3.3: MOLDEN representations of the$[UOBr_5]^-$ Molecular Orbitals that are most affected by $\alpha(OUBr_{cis})$. The molecule is orientated with the O at the bottom right and Br_{trans} at the top left of each picture.

the Os-N π bonding character is enhanced, and the Os-Cl_{cis} π^* interactions are reduced. In addition, the N-Cl_{cis} out-of-phase interactions are minimised. There is no directly analogous MO in the $[UOBr_5]^-$ case, but the $9a_1$ MO comes closest as it is U-Br_{cis} π^* and U-O bonding. The main difference between this and the 4e MO of $[OsNCl_5]^{2-}$ is that the U-O bonding character is σ and not π. This is mainly due to the different contributions from the metal; while the osmium component is mainly d character so it can attain π orientations in both the axial and equatorial directions, the uranium component is mainly f_{z^3} character, so that it is π in the equatorial plane, but σ in the axial direction. Since the U-O σ is largely angle-independent, there is no significant energy change with changing angle for the actinide case, and no driving force to an angle greater than 90°. Therefore, there is no propensity towards a longer U-Br_{trans} bond.

3.3.3.2 Molecular Orbital Analysis of $[UOBr_5]^-$ at the Equilibrium Geometry

A brief overview of the valence MOs was given in table 3.4, and now some specific MOs from this table are analysed in more detail, in order to find a possible source of the inverse *trans* influence. As was mentioned earlier, there are two antibonding MOs, the $6a_1$ and $9a_1$ MOs, which are shown in figure 3.4. The latter MO is considered first. The $9a_1$ MO in figure 3.4(b) is quite clearly U-Br_{cis} π^*, and in contrast to the osmium 4e MO, the antibonding character is not alleviated by an increase in OUBr_{cis} angle. This results in a lengthening of the U-Br_{cis} bond relative to U-Br_{trans}, and an ITI. This means that the ITI is a result of the lengthening of the *cis* bond, rather than a shortening of the *trans* bond, which is supported by the relative bond lengths of r(U-Cl) in $[UCl_6]$, and r(U-Cl_{trans}) and

r(U-Cl_{cis}) in $[UOCl_5]^-$, which are 244.0 pm, 249.2 pm and 253.1 pm respectively. Further, BLYP calculations on the $[UO_2Cl_4]^{2-}$, in which the chlorides are in the equatorial plane around the dioxo UO_2^{2+} unit, find r(U-Cl), i.e. r(U-Cl_{cis}), to be further elongated to 273.0 pm.

(a) $6a_1$ MO (b) $9a_1$ MO

Figure 3.4: MOLDEN representations of the $6a_1$ and $9a_1$ MOs of $[UOBr_5]^-$. The molecule is orientated with the O at the bottom right, and Br_{trans} at the top left of each picture.

Although the $9a_1$ MO appears to provide an explanation for the ITI, before applying these arguments to the other eight $[AnOX_5]^{n-}$ complexes, it is worth considering the $6a_1$ MO, which is shown in figure 3.4(a). In the study of *mer*-$[Ti(NR)Cl_2(NH_3)_3]$ (R=Bu^t,C_6H_5,$C_6H_4NO_2$-4) by Kaltsoyannis and Mountford,[110] recall that the majority of the TI was found to result from the presence of bonding and antibonding Ti-$NH_{3,trans}$ MOs, but only bonding characteristics in the Ti-$NH_{3,cis}$ direction. In $[UOBr_5]^-$, the case is slightly less straightforward because there is evidence of bonding and antibonding U-Br in both the *cis* and *trans* bonds. However, from table 3.4 it appears that the $6a_1$ MO that has U-Br_{trans} σ^* in character, has greater contributions from O(42%) than Br_{trans} (22%) so it plays less of a role than the U-Br_{cis} π^*-based HOMO-2 $9a_1$ MO, which is dominated by 75% Br_{cis} compared with only 11% O character.

To summarise, the proposed source of the ITI of $[UOBr_5]^-$ at the equilibrium geometry is the $9a_1$ MO, which has significant U-Br_{cis} π^* character. This gives greater U-Br_{cis} than U-Br_{trans} antibonding character in the complex, which results in an elongated r(U-Br_{cis}) relative to r(U-Br_{trans}). In addition, the lack of driving force to a large equilibrium α(OUBr_{cis}), in contrast to the driving force in 4e of $[OsNCl_5]^-$, is also due to the $9a_1$ MO, which is U-O σ bonding as opposed to Os-N π bonding.

The next step is to extend this hypothesis to the other $[AnOX_5]^{n-}$ complexes to see if the argument remains consistent, and also to see if this argument can rationalise the trend in $\%ITI$.

3.3.4 Extent of Inverse *Trans* Influence in $[AnOX_5]^{n-}$ (An= Pa, n=2; An=U, n=1; An=Np, n=0; X=F, Cl, Br)

This section aims to address the following questions about $[AnOX_5]^{n-}$ (a) why does the extent of the ITI decrease down the halide series and (b) why does the extent of the ITI increase from protactinium to neptunium? Before that, there are a few points to note about the complexes. Since all of the OAnX_{cis} angles fall in the range of 90-93°, and the $[UOBr_5]^-$ constrained geometry optimisations show that in this angle range the $\%ITI$ is a constant 98.7, it is not unreasonable to assume that the $\%ITI$ is effectively independent of the angle over this small range of values. Also, although there are differences in the equivalent MOs for the different complexes, the principal bonding character of the MOs across the series is approximately consistent. Hence, it is possible to focus the analysis on the MOs of interest from the previous section.

For $[UOBr_5]^-$ it is clear that the $9a_1$ plays an important role in deciding the

extent of the ITI. However, although I have only briefly mentioned the other antibonding MO, the $6a_1$ MO, in the context of it having greater O than Br_{trans} character (in contrast to the $9a_1$ MO that has greater Br_{cis} character than O character), both contributions are almost certainly sensitive to the metal and the ligand in question. Hence, the compositions of both the $6a_1$ and $9a_1$ MOs are given for all nine target systems in table 3.5.

Table 3.5: Mulliken % contribution of $6a_1$ (normal text) and $9a_1$ (italics) MOs of the title systems. $\%ITI$ is given in brackets below the names of each complex.

	MO	An total	An p	An d	An f	O	X_{trans}	X_{cis}
$[PaOF_5]^{2-}$	$6a_1$	9	-	8	1	9	49	29
(97.9)	*$9a_1$*	*29*	*8*	*3*	*18*	*49*	*6*	*13*
$[PaOCl_5]^{2-}$	$6a_1$	14	1	13	-	25	38	20
(98.6)	*$9a_1$*	*22*	*6*	*1*	*15*	*31*	*12*	*33*
$[PaOBr_5]^{2-}$	$6a_1$	18	2	14	2	35	31	14
(98.8)	*$9a_1$*	*13*	*4*	-	*9*	*22*	*12*	*51*
$[UOF_5]^-$	$6a_1$	12	-	10	2	11	51	24
(97.7)	*$9a_1$*	*34*	*11*	*1*	*22*	*40*	*4*	*24*
$[UOCl_5]^-$	$6a_1$	16	-	14	2	33	30	17
(98.4)	*$9a_1$*	*13*	*4*	-	*9*	*18*	*8*	*60*
$[UOBr_5]^-$	$6a_1$	22	3	14	5	42	22	12
(98.7)	*$9a_1$*	*7*	*2*	-	*5*	*11*	*6*	*75*
$[NpOF_5]$	$6a_1$	12	-	10	2	16	50	20
(96.7)	*$9a_1$*	*30*	*7*	-	*23*	*18*	*3*	*46*
$[NpOCl_5]$	$6a_1$	18	-	13	5	39	24	15
(97.2)	*$9a_1$*	*15*	*5*	-	*10*	*10*	*6*	*67*
$[NpOBr_5]$	$6a_1$	22	1	12	9	44	20	11
(97.5)	*$9a_1$*	*10*	*4*	-	*6*	*8*	*5*	*76*

For a given actinide, the extent of ITI decreases ($\%ITI$ increases) from the fluorides to the bromides. This may be attributed to the relative contributions of the metal to the $6a_1$ and $9a_1$ MOs. For the fluorides, there is much greater metal contribution to the An-X_{cis} π^* $9a_1$ MO than for the An-X_{trans} σ^* $6a_1$ MO.

However, for the bromides the $9a_1$ MO has less metal contribution than the $6a_1$ MO. Hence, the metal contributes more to the antibonding An-X_{cis} π^* $9a_1$ MO in the fluorides than in the bromides, leading to a lower $\%ITI$ and a greater ITI in the fluorides.

An explanation in the trend in ITI from protactinium to neptunium cannot be explained in this manner, since there is a general increase in the metal character in the two MOs going across the series. However, what is interesting is that the f character in the $6a_1$ MO is very small for all nine complexes, and is more significant in the $9a_1$ MO. Moreover, it increases gradually from Pa $\rightarrow$ Np, and also from Br $\rightarrow$ F. Given the necessary part that the f contribution plays in order to achieve An-O σ and An-X_{cis} π^* character in the $9a_1$ MO, it is reasonable to suggest that it also plays an important role in determining the ITI, and that a greater f contribution to the $9a_1$ MO gives greater An-X_{cis} antibonding character, and a lower $\%ITI$. The $9a_1$ MOs for the two extreme $[NpOF_5]$, which exhibits the greatest ITI, and $[PaOBr_5]^{2-}$, which exhibits the least ITI, are shown in figure 3.5.

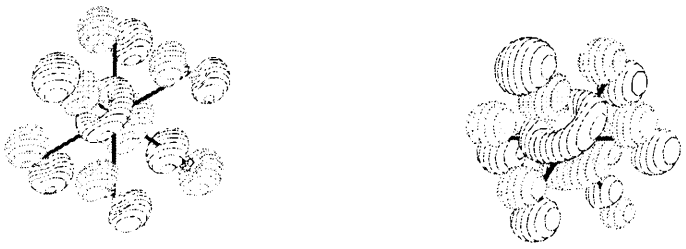

(a) $PaOBr_5^{2-}$ (b) $NpOF_5$

Figure 3.5: MOLDEN representations of the $9a_1$ MOs of $[PaOBr_5]^{2-}$ and $[NpOF_5]$. The molecule is orientated with the O at the bottom right and Br_{trans} at the top left of each picture.

To conclude the molecular orbital analysis in this section, the $9a_1$ MO has been found to be important in determining the ITI in $[AnOX_5]^{n-}$. Unlike for the 4e transition metal MO in $[OsNCl_5]^{2-}$, which is N-Os π bonding enhanced by an obtuse $\alpha(NOsCl_{cis})$, the $9a_1$ MO in $[AnOX_5]^-$ is An-O σ bonding, which shows no stabilisation in energy for large $OAnX_{cis}$ angles. Hence there is no driving force for the $OAnX_{cis}$ angle to exceed 90° and thus less steric repulsion between the *cis* and *trans* ligands, and no *trans* influence. In addition, the $9a_1$ MO is An-X_{cis} π^* bonding, the extent of which is determined by the amount of f character. This and, to a lesser extent, the actinide contribution to the An-X_{trans} σ^* $6a_1$ MO determines the resultant ITI.

3.3.5 Mayer Bond Order Analysis

In this section, an alternative to the molecular orbital (with Mulliken analysis composition) approach is used to gain insight into the bonding in $[AnOX_5]^{n-}$. Mayer Bond Order (MBO) calculations were carried out in order to quantify the extent of metal-ligand bonding, and the results are presented in table 3.6. In addition to calculating the total bond orders, a breakdown of the bond orders in terms of the point group irreducible representations (irreps) is also given. This is potentially useful in giving information about the notional σ and π bonds as well as the overall bond. (Table 3.3 has already equated the σ and π bonding ligand AOs with the irreps in C_{4v} symmetry.)

Before considering the significance of the numbers in table 3.6, it is worth considering two relevant cautionary notes, both mentioned by Bridgeman and co-workers in their initial survey of the MBO performance.[127] Firstly, the MBOs in fluorine-containing species should be considered with caution, due to the high

Table 3.6: Mayer Bond Orders in $[AnOX_5]^{n-}$ (An=Pa, n=2; An=U, n=1; An=Np, n=0; X=F, Cl, Br). There are no a_2 contributions given since there are no metal AOs of this symmetry, so all a_2 bond orders are necessarily 0.0.

	$[PaOF_5]^{2-}$		$[PaOCl_5]^{2-}$		$[PaOBr_5]^{2-}$	
	total	composition	total	composition	total	composition
Pa-O	1.85	$0.67a_1 + 1.18e$	1.94	$0.64a_1 + 1.30e$	1.93	$0.62a_1 + 1.31e$
Pa-X_t	0.78	$0.34a_1 + 0.44e$	1.02	$0.58a_1 + 0.44e$	1.09	$0.65a_1 + 0.44e$
Pa-X_c	0.74	$0.10a_1 + 0.16b_1$ $+0.11b_2 + 0.37e$	0.93	$0.14a_1 + 0.23b_1$ $+0.11b_2 + 0.45e$	0.99	$0.15a_1 + 0.25b_1$ $+0.11b_2 + 0.48e$
	$[UOF_5]^{-}$		$[UOCl_5]^{-}$		$[UOBr_5]^{-}$	
	total	composition	total	composition	total	composition
U-O	1.88	$0.66a_1 + 1.24e$	1.93	$0.61a_1 + 1.32e$	1.90	$0.60a_1 + 1.30e$
U-X_t	0.78	$0.32a_1 + 0.46e$	1.19	$0.59a_1 + 0.60e$	1.26	$0.60a_1 + 0.66e$
U-X_c	0.79	$0.08a_1 + 0.19b_1$ $+0.11b_2 + 0.41e$	1.13	$0.15a_1 + 0.28b_1$ $+0.12b_2 + 0.58e$	1.20	$0.17a_1 + 0.30b_1$ $+0.12b_2 + 0.61e$
	$[NpOF_5]$		$[NpOCl_5]$		$[NpOBr_5]$	
	total	composition	total	composition	total	composition
Np-O	1.91	$0.61a_1 + 1.30e$	1.93	$0.61a_1 + 1.32e$	1.91	$0.59a_1 + 1.32e$
Np-X_t	0.87	$0.37a_1 + 0.50e$	1.50	$0.80a_1 + 0.70e$	1.62	$0.90a_1 + 0.72e$
Np-X_c	0.93	$0.05a_1 + 0.23b_1$ $+0.10b_2 + 0.55e$	1.44	$0.13a_1 + 0.35b_1$ $+0.13b_2 + 0.83e$	1.55	$0.16a_1 + 0.37b_1$ $+0.13b_2 + 0.89e$

ionicity of the bonding. Secondly, the frozen core approximation in ADF can lead to underestimating the MBOs of multiple bonds in complexes relative to the analogous all electron Gaussian basis sets. That said, in these actinide complexes there is good correlation between the MBO and bond length, which is useful in the case of looking at the ITI.

Although the data in table 3.6 do not provide conclusive evidence for the source of ITI, there are some points to note about the bonding in the complexes, based on their MBO indices. They can be summarised as follows:

The An-O bond has consistent MBO values for all nine complexes. The values

for the total bond orders are 1.91±0.06. This might indicate that the bond order is 2.0, were it not for the point already mentioned that the MBOs are generally underestimated in frozen core calculations, and also that the breakdown indicates that the most appropriate bond representation is $1a_1 + 2e$. In other words, the An-O bond is most likely to be $1\sigma + 2\pi$, a triple bond, as has been previously reported.[41]

In all cases, except $[UOF_5]^-$ and $[NpOF_5]$, whose data are considered unreliable due to the ionicity of the bond, the bond orders for the *trans* bonds are greater than the *cis* bonds. This supports the ITI present in the geometries. Further insight into how the bonds are comprised is limited, however, especially given the complexity of the symmetry of the *cis* π bonds in C_{4v} symmetry. Despite this, some comments can be made. There is a trend for both the *cis* and *trans* bond orders to increase from the chloride to the bromide species and from the protactium to neptunium species, corresponding to greater covalency. A look at the decomposition of the An-X bonds into their irreps indicates that, based on the π-based irrep (e) for the *trans* bond and the only purely π-based irrep (b_2) for the *cis* bond, the An-X π character does not change much for the different halogens. This indicates that the greater covalency going from the chlorides to the bromides is probably localised in the σ bonds.

Changing the metal centre from protactinium to neptunium, for a given halogen, increases the total MBO. This also corresponds to a shorter bond. The change in the total MBO is due to an increase in the a_1 and e MBOs for the A-X_{trans} bond, and mainly in the b_1 and e MBOs for the An-X_{cis} bond, so it is not possible from these data to state whether the total increase is due to σ or π character, and is possibly a combination of both.

3.4 Concluding Remarks

This chapter has looked at the inverse *trans* influence (ITI) in the actinide-containing $[AnOX_5]^{n-}$ (An=Pa, n=2; An=U, n=1; An=Np, n=0; X=F, Cl, Br) series of complexes. In all cases, the An-X_{trans} bond was found to be shorter than the An-X_{cis} bonds, and the OAnX_{cis} angle was found to fall in the range of 90-93°. The data for $[UOCl_5]^-$ agree very well with experimental crystal structure data. There were discrepancies between the available experimental data for $[PaOCl_5]^{2-}$ and the computational data, but given the dubious quality of the experimental data, these discrepancies were not considered further.

In contrast to the transition metal $[OsNCl_5]^{2-}$ studied by Lyne and Mingos, there is no sterically induced TI in the actinide complexes. Using $[UOBr_5]^-$ as a model for the title complexes, the variation of the molecular orbital energies with varying $\alpha(OUBr_{cis})$ from 90° to 102° shows that the equilibrium $OUBr_{cis}$ angle of 90° is driven by out-of-phase interactions between the *cis* and *trans* ligands in the 7e and $8a_1$ MOs. This contrasts with the osmium case, with an equilibrium $NOsCl_{cis}$ angle of 96.6° which enhances the N-Os π interactions and reduces the Os-Cl_{cis} π^* interactions of the 4e MO of the complex. The closest resembling MO of $[UOBr_5]^-$ is the $9a_1$ MO, which is U-Br_{cis} π^* but U-O σ and the energy of the latter interaction is largely angle independent.

At the equilibrium geometry, the ITI is attributed to the An-X_{cis} π^* bonding character of the $9a_1$ MO, resulting in the *cis* bond being longer than the *trans* bond. For the complexes that have greater f_{z^3} character in the $9a_1$ MO, stronger antibonding character is seen, and a greater ITI results. This is consistent with the tendency towards greater ITI from protactinium to neptunium for a given halide. For a given metal, the tendency for a reduced ITI from the fluorides to

the bromides corresponds to less metal contribution to the $9a_1$ MO and greater contribution to the $6a_1$ MO. This means that there is greater *trans* and less *cis* antibonding character so the ITI is reduced.

Finally, Mayer Bond Order (MBO) analysis was carried out on all nine of the actinyl complexes, which gives the total bond order, as well as the individual bond orders from the irreducible representations of the given point group, C_{4v} in this case. The results for the fluoride species were neglected on the basis that this analysis does not adequately describe very ionic species. However, from this analysis, it was concluded that the An-O bond order does not noticeably change for the different complexes, and indicates a probable triple bond. The An-X bond orders for nearly all of the complexes support the ITI found in the geometry optimisations, with total bond orders for An-X_{trans} exceeding that of An-X_{cis}.

Chapter 4

Metallophilic Interactions in $[ClM(PH_3)]_2$ (M=Cu, Ag, Au, [111])[128]

4.1 Introduction

The effect of relativity on the properties of the heavier elements in the periodic table has been the focus of much interest in recent years.[1,2] In particular, the group 11 coinage metals provide a 'gold maximum' of relativistic effects, which refers to the greater difference between the relativistic and non-relativistic properties for this group compared with the other elements in the same period.[129] Gold, in particular, exhibits strong relativistic effects and the difference in colour between metallic silver and yellow gold can be attributed to the gold relativistic 6s orbital stabilisation. This results in the lower absorption energy appearing in the visible region for gold but in the ultraviolet region of the spectrum for silver.[130] The effect of relativity on the properties of gold compounds has been studied extensively. Notable contributions have been made by Schwerdtfeger in computational gold chemistry,[131] by Schmidbaur in experimental investigations of gold(I)-gold(I) interactions[132] and by Pyykkö in computational investigations of gold(I)-gold(I) interactions.[133]

Attractive interactions have been found to exist between d^{10} cationic coinage metals, especially between gold(I)-gold(I) cations. (Note that there are also examples of similar interactions for other metals such as $d^{10}s^2$ mercury-mercury interactions and tellurium-tellurium interactions, which are not discussed here.

For more details see reference 133.) For the specific case of gold, these 'aurophilic' interactions are often comparable with hydrogen bond strengths and can contribute to the formation of dimeric and oligomeric structures.[133]

The aim of the introduction is to give an overview of some of the main computational studies of relativity in gold(I) complexes. Thereafter, previous studies of gold(I)-gold(I) interactions are considered, in addition to studies of the more general d^{10}-d^{10} coinage metal interactions. Finally, the limited studies that have been carried out on element 111 are summarised. In the subsequent section, the computational approach used here, which has been used previously to study these complexes, is presented. Section 4.3 discusses the results of this study, looking at the effect of relativity on the geometries of the [ClM(PH_3)] (M=Cu, Ag, Au, [111]) compounds, and subsequently, the 'metallophilic' interactions between two of these monomers. To my knowledge, this is the first investigation of the metallophilicity of element 111, and the first comparison of the metallophilicity between all four members of the coinage metal group. In addition, this is the first study to use more comprehensive methods than second order perturbation (MP2) methods (e.g. coupled cluster methods), to study metallophilicity.

4.1.1 Gold(I) Complexes

The effect of relativity on a range of gold(I) diatomics and triatomics was considered by Schwerdtfeger et al.,[134,135] in which they found that relativity results in gold-ligand bond contractions, which they measured by $\Delta_R(r_{NR} - r_R)$, the difference between the non-relativistic and relativistic bond length of interest (r). The bond contraction in these complexes depends on the ligand, and it was found that for more electronegative ligands, there are smaller relativistic contractions,

than for the more electropositive ligands, which show greater relativistic bond contractions. This was explained by considering the two extreme ionic models Au^+X^- representing the cases involving the electronegative ligands, and Au^-X^+ representing the cases involving the electropositive ligands. In the former case, the gold configuration is formally $5d^{10}$ in contrast to $5d^{10}6s^2$ in the latter case. Since the 6s orbital experiences a strong relativistic contraction, it was suggested that there is a greater bond contraction for the cases in which the 6s orbital is occupied and participates to a greater extent in the bond.

4.1.2 Metallophilic Interactions

In 1991, Pyykkö and co-workers published the first of a series of computational studies of gold(I)-gold(I) interactions, modelled using the $[ClAu(PH_3)]_2$ dimer.[136–140] This study was prompted by the experimentally found $\{[2,4,6\text{-}(Bu^t)_3C_6H_2PH_2]AuCl\}_2$, in which the gold monomers are in an antiparallel orientation (figures 4.1(b) and 4.1(d)) so that in addition to Au—Au' interactions, there is the possibility of ligand-ligand interactions.[141] However, Pyykkö used the hypothetical orientation of the monomers at 90° to each other as shown in figure 4.1(c), to minimise the intermolecular ligand-ligand interactions and intermolecular dipolar effects, and hence to investigate the aurophilic interactions more explicitly. From these studies, it was found that at the HF level, there is a purely repulsive interaction energy curve, but at the MP2 level of computation there is a non-negligible interaction between the monomers (-27 kJ/mol), 27% of which is due to relativistic effects. This led to the conclusion that aurophilic interactions are due to correlation enhanced by relativity. It was also found that when Cl is replaced by other halides, the interaction energy decreases for the harder fluoride ligand and increases for

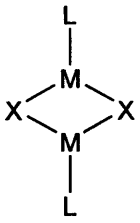

(a)
Rhombic

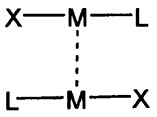

(b)
Anti-
parallel
(α(XMM'X')=180°)

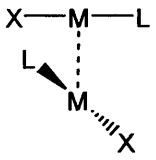

(c)
Staggered
(α(XMM'X')=90°)

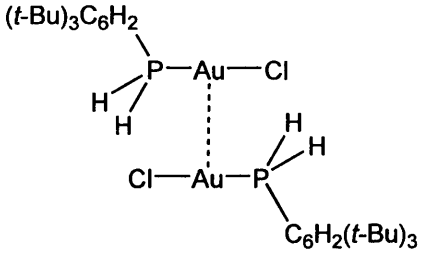

(d) Experimental complex

Figure 4.1: Three possible conformations for $M_2X_2L_2$ (M=coinage metal(I), X=monoanion and L is an electron-donating ligand) and the experimental $\{2,4,6\text{-}(Bu^t)_3C_6H_2PH_2]AuCl\}_2$ structure is also included (r(Au—Au')=344.0(1) pm and r(P—Cl')=352.5(3) pm).

the softer iodide ligand.

In reference 139, in addition to the MP2 calculations on $[ClAu(PH_3)]_2$, the cuprophilic and argentophilic interactions were examined (by replacing gold with copper and silver), and it was found that the interaction energies were 48% and 14% smaller than the aurophilic attractions respectively. The effect of using different ab initio correlated methods was briefly mentioned as an area requiring further work. This was discussed further in reference 142 for the A-shaped $S(AuPH_3)_2$, in which it was concluded that, of MP2, MP3, MP4, CCSD and CCSD(T), the lat-

ter level of theory was required to predict the experimental $S(AuPPh_3)_2$ Au—Au' distance.

Further calculations by Schütz, Werner and co-workers using local MP2 (LMP2) methods have also been carried out, initially on staggered $[XAu(PH_3)]_2$ (X=H, Cl)[143] and subsequently on staggered $[XM(PH_3)]_2$ (M=Cu, Ag, Au; X=H, Cl).[144] LMP2 has advantages over traditional MP2 because it reduces significantly the computational time and the extent of basis set superposition error (BSSE), and the correlation energy can be explicitly viewed as arising from double excitations from occupied to virtual orbitals. For the orbitals of two fragments A and B, these latter double excitation contributions can be decomposed into four factors; intramolecular excitations (i.e. the double excitations from occupied AOs on A to virtual orbitals on A, denoted A→A' or equivalently, B→B'), dispersion excitations (due to the simultaneous excitations from A→A' and B→B'), exchange-dispersion excitations (A→B' and B→A') and ionic excitations (A→A' and B→A'). In agreement with Pyykkö et al., the LMP2 studies find that close to the LMP2 equilibrium gold-gold separation, the HF interaction energies are repulsive and that relativity contributes to 28% of the interaction energy.[143] Looking at the correlation contributions to the interaction energy of $[ClAu(PH_3)]_2$, the authors found that the ionic contributions are almost as important as the dispersion contributions (with exchange-dispersion not contributing significantly, and the intramolecular contributions being repulsive). Furthermore, the Au(5d) orbitals are not solely responsible for the interaction energy but they do contribute significantly to it. Although about 40% of the interaction energy would be lost if excitations from the Au(5d)-Au(5d) orbitals were neglected, this would increase to 90% loss if contributions involving excitations from either Au(5d) were omitted.

The second LMP2 study, extending to the lighter coinage metals shows a reduction in the interaction energies for silver and for copper compared with gold, also consistent with Pyykkö et al.'s results. Double excitations involving at least one $(n-1)$d metal orbital (n is the period number; n=4 for Cu; n=5 for Ag; n=6 for Au) make up most of the intermolecular correlation energy with a decrease in the relative contribution from M($(n-1)$d)-M($(n-1)$d) excitations by a factor of about 4 in going from gold to copper. Relative contributions to the correlation energy that arise from neither set of M($(n-1)$d) orbitals increases from gold to copper by a factor of 1.4-1.8. A decomposition of the contributions to the uncorrelated SCF energies for all three complexes was found to contain attractive (electrostatic, polarisation and charge transfer), as well as repulsive (Pauli) terms, and conversely, the correlated interaction energy contains repulsive (intramolecular) as well as attractive (dispersion and ionic) terms.

Another MP2 study[145] on $[M(C_6F_5\{NH{=}CH_2\})]_2$ (M=Ag, Au) has shown that hydrogen bonds and aurophilic interactions can compete. In the case of the weaker argentophilic interactions, the hydrogen bonds provide the directionality for the structure, but the presence of aurophilic interactions reduces the hydrogen bonds' strength and directionality. More recently, Mendizabal et al. used LMP2 and showed that aurophilic and hydrogen bond interactions are comparable in energy.[146]

Although much of the literature on group 11 metal-metal interactions focuses mainly on aurophilic interactions, cuprophilicity has also been considered in more recent studies. MP2 studies on the existence of cuprophilic interactions, carried out by Alvarez and Novoa and co-workers,[147–149] have looked at three possible conformations of $[CuXL]_2$ (X=Cl, L=NH_3; rhombic, antiparallel and staggered

structures as in figures 4.1(a), 4.1(b) and 4.1(c)). They found evidence for cuprophilic interactions in the staggered conformation. However the greatest interaction energy was found for the antiparallel structure due to Cl—H' intermolecular hydrogen bonding, followed by the rhombic structure, and the lowest interaction energy is found for the staggered conformation. The existence of cuprophilic and argentophilic interactions in the rhombic structure of $[M_2X_2]L_n$ (n=0, M=Cu, Ag; X=Cl, Br, I; n=2, M=Cu, X=Cl, L=PH_3; n=3, M=Ag, X=Cl, L=PH_3) was studied elsewhere from a topological viewpoint, and it was found that there is evidence of M—M' interactions only when the L groups are absent.[150] Finally, for a series of Cu-containing monomers orientated in a perpendicular conformation, evidence of cuprophilic interactions was found but it is about three times smaller than aurophilic interactions.[151]

4.1.3 Element 111

The first successful discovery of the transactinide element 111 was reported in 1995 in Darmstadt, Germany.[152] However, the experimental investigations of element 111 and other similar superheavy elements are limited by 'atom-at-a-time' chemistry because of their short half-lives, so theoretical studies, which do not suffer from these limitations, can provide useful information that would otherwise be difficult to obtain. For the specific case of element 111 a theoretical study of the atom was published in 1994 by Schwerdtfeger et al.[75] This study established that its atomic ground state is $7s^26d^9$, in contrast to the $(n-1)d^{10}ns^1$ configuration of its lighter congeners, as was mentioned in section 1.6 earlier in this work. This has been attributed to relativity, which contracts the 7s shell and destabilises the 6d shell. Studies of compounds containing monovalent element 111 have so

far been confined mainly to diatomics[3,80,153–155] (although the stability of higher oxidation states of +3 and +5 in MF_4^- and MF_6^- (M=Cu, Ag, Au, [111]) were also considered in reference 86). From these studies, the bond length of [111]H was found to be slightly shorter than that of AuH due to relativistic effects,[3] whereas for MF_2^-, r(Cu-F) < r(Au-F) < r([111]-F) < r(Ag-F).[86] The study by Liu and Van Wüllen on element 111 and its diatomic compounds, [111]X (X=H, F, Cl, Br, O, Au), which included spin-orbit coupling, reported a $7s^26d^8$ ground state configuration in $[111]^+$, and bond lengths that are similar to but slightly longer than, equivalent gold compounds.[80]

4.2 Computational Details

In this study of coinage metal complexes, two types of geometry optimisations were carried out; unconstrained geometry optimisations on the [ClM(PH_3)] monomer and 'pseudo'-geometry optimisations on [ClM(PH_3)]$_2$ (M=Cu, Ag, Au, [111]). In this section, the monomer geometry optimisations are described first, followed by a description of the dimer geometry optimisations. The final part of this section describes the basis sets.

4.2.1 Monomer Geometry Optimisations

The [ClM(PH_3)] (M=Cu, Ag, Au, [111]) monomer geometries were optimised using the Gaussian98 program.[156] Although no symmetry constraints were imposed, the geometry optimised to a linear molecule with C_s symmetry in all cases, with α(ClMP) close to 180°. Two types of Density Functional Theory (DFT) geometry optimisations, using the GGA exchange and correlation functionals of Becke[94] and

Perdew[98] respectively (denoted BP86 in the text), and the hybrid-DFT method, B3LYP, which uses the gradient-corrected correlation functional of Lee, Yang and Parr[99] and Becke's exchange functional[100] that includes some Hartree Fock (HF) exchange, were carried out. In addition HF, MP2, QCISD, CCSD and CCSD(T) ab initio methods were used for the geometry optimisations. For the post-HF methods the lowest 16 molecular orbitals were not included in the correlation part of the calculation (but all other occupied and virtual orbitals were included).

4.2.2 Dimer Geometry Optimisations

For $Cl_2M_2(PH_3)_2$ three different structures were considered, the rhombic structure (as in figure 4.1(a)), the antiparallel structure (α(PMM'P')=150-180°, as in figure 4.1(b)) and the staggered structure (α(PMM'P')=90°, as in figure 4.1(c)). Both of the former were local minima, found from carrying out unconstrained geometry optimisations on guess input structures using Gaussian98 (except for the CCSD(T) case of element 111, due to computational limitations of the program). The latter staggered conformation is not a minimum energy structure, however, since if allowed to optimise, it changes to the antiparallel conformation. Because it is this latter structure that allows the more explicit study of metallophilic interactions, this structure was 'pseudo'-optimised. This refers to the technique whereby a series of single point calculations were carried out over a series of metal-metal distances. The PMM'P' angle was fixed to 90° and the monomer geometries were used since any change in their geometries due to dimerisation was considered negligible. At each metal-metal distance the Basis Set Superposition Error (BSSE) was accounted for using the counterpoise (CP) correction method. The minimum of this potential energy curve was taken as the

optimised metal-metal distance. In this way, the metal-metal distances and interaction energies were 'pseudo'-optimised on the CP corrected potential energy surface. Note that in CP correction calculations, the computational limitations of Gaussian98, which require that the maximum size of the scratch files does not exceed 16GB, were encountered, so MOLPRO[157] was used, since it did not suffer from the same limitations. Consistent with the monomer calculations, for the post-HF methods the lowest 32 molecular orbitals were uncorrelated.

4.2.3 Basis Sets

For both geometry optimisations, basis sets of DZP quality were used for Cl, P, and H, using the Pople 6-31G** basis set. For the description of Cu, Ag, Au and element 111, the basis functions and relativistic Effective Core Potentials (RECPs) published by the Stuttgart group were used to describe the core orbitals (10, 28, 60 and 92 electrons respectively) and the ns, np,nd and $(n+1)$s valence orbitals were described using the corresponding Stuttgart basis sets.[79,158,159] Two additional f polarisation functions (one diffuse and one compact) were added to each valence description of copper, silver and gold, but the description of element 111 was unaltered, with four f polarisation functions included in the original description. For the first f function (the diffuse function), the exponent was chosen such that the MP2 electric dipole polarisability of the monocation was maximised, and for the second function (the compact function), the exponent was chosen such that the CCSD(T) energy of the neutral metal atom was minimised. The coefficient of each function was set to 1.0 for each exponent. This method of determining the coefficients was that used by Pyykkö in an earlier study of gold-containing complexes.[139] The non-relativistic basis sets and ECPs of gold and element 111

Table 4.1: Exponents of copper, silver and gold that were added to the Stuttgart basis sets in Gaussian98 to represent the f polarisation functions. The coefficient for each α value was set to 1.0.

	First and Second Exponents	
	Diffuse f exponent (α_f^D)	Compact f exponent (α_f^C)
Copper	0.238	3.72
Silver	0.222	1.64
Gold	0.191	1.05
Gold (nonrelativistic)	0.217	1.22

were taken from reference 134 and 79, and for gold, consistent with the relativistic cases, two additional f polarisation functions were also added. As was the case for the relativistic element 111 basis set and ECP, there are already 4 f functions included, so it was unaltered.

In the final part of this study, the effect of the basis set was briefly considered. In this case, the basis set and RECPs for the metals were improved by replacing the 2 f functions of copper, silver and gold by the three f and two g functions, that were used by Magnko et al. in their study of metallophilicity.[144] The basis set and RECP of element 111 was unaltered. In addition, the non-hydrogenic ligand basis sets were improved to TZP quality (6-311G**) and for the case of the MP2 calculations, a diffuse function was also added (6-311+G**). These basis set combinations were denoted by 3f2g(4f)/6-311G*/6-31G** and 3f2g(4f)/6-311+G*/6-31G** respectively, and represent the largest basis sets that can could be implemented for the systems studied.

4.3 Results and Discussion

4.3.1 [ClM(PH_3)] (M=Cu, Ag, Au, [111]) Monomer

Table 4.2 shows the optimised geometries for [ClM(PH_3)] using both ab initio and density functional methods, and results from other computational studies where applicable. The current results using the variety of methods show general agreement, and also agree well with those of previous studies. There is little variation in the phosphine geometric parameters, r(P-H) and α(HPM), for the metals or the methods. The metal-ligand bond lengths, however, show dependence on both the coinage metal and also, in some cases, on the methods. A comparison of r(M-Cl) and r(M-P) between the correlated ab initio methods show that MP2 tends to predict shorter bond lengths than either QCISD or CCSD, and the general trend can be summarised as MP2 $<$ QCISD $\leq$ CCSD for the metal-ligand bond lengths.

The uncorrelated HF method overestimates the metal-ligand bond lengths for copper and silver compared with the correlated post-HF methods. This difference is smaller for the heavier gold and element 111 complexes. This is consistent with the study by Buijse and Baerends of a first row metal compound, MnO_4^-, in which they noted that the valence 3d orbitals are in close proximity with the 3s/3p core orbitals.[162] As a result, they found that HF underestimates the metal(3d) - ligand interaction because of Pauli repulsion between the ligand and the 3s3p shell. Going down group 11, the effect becomes less pronounced as the spatial gap between the $(n-1)$s/$(n-1)$p and $(n-1)$d increases. This is consistent with my results, which show that for the gold and element 111 monomers the difference between the uncorrelated and correlated ab initio methods becomes smaller.

Table 4.2: Optimised Geometric Parameters for [ClM(PH_3)] (M=Cu, Ag, Au, [111]). Values from previous studies are given in italics.

Method	r(M-Cl)/pm		r(M-P)/pm		r(P-H)/pm		α(HPM)/deg	
M=Cu								
HF	216.1		232.4		139.4		118	
MP2	205.2	*206.5*[1]	210.0	*211.9*[1]	139.7	*141.5*[1]	118	*119*[1]
		209.7[2]		*215.9*[2]		*140.2*[2]		*119*[2]
QCISD	208.4		218.3		140.4		118	
CCSD	209.1		218.5		139.6		118	
B3LYP	210.6	*212.3*[3]	217.5	*220.7*[3]	141.2	*141.8*[3]	119	*119*[3]
BLYP	211.3		216.8		142.4		119	
BP86	209.4		214.3		142.4		119	
M=Ag								
HF	238.0		254.2		139.4		118	
MP2	225.6	*227.4*[1]	230.2	*232.5*[1]	139.5	*141.5*[1]	118	*118*[1]
		230.6[2]		*237.2*[2]		*140.1*[2]		*119*[2]
QCISD	228.9		236.1		139.9		118	
CCSD	230.5		239.4		139.5		118	
B3LYP	231.0	*231.3*[3]	236.4	*237.3*[3]	141.1	*141.5*[3]	119	*118*[3]
BLYP	231.8		235.7		142.2		118	
BP86	229.4	*229.9*[4]	231.9	*233.3*[4]	142.3		119	
M=Au								
HF	233.4		232.4		139.1	117		
MP2	225.9	*226.3*[1]	222.1	*224.3*[1]	139.5	*141.3*[1]	117	*117*[1]
		230.0[2]		*224.9*[2]		*140.0*[2]		*118*[2]
QCISD	229.0		227.0		139.7		117	
CCSD	229.6		228.0		139.3		117	
B3LYP	230.2	*230.0*[3]	226.2	*227.3*[3]	141.0	*141.3*[3]	118	*117*[3]
BLYP	231.7		227.0		142.1		118	
BP86	228.9	*227.0*[4]	224.1	*222.2*[4]	142.2		118	
M=[111]								
HF	229.6		220.5		139.2		117	
MP2	226.0		218.0		139.8		117	
QCISD	228.7		221.1		139.3		117	
CCSD	228.7		221.1		139.3		117	
B3LYP	229.9		220.8		141.2		117	
BLYP	232.1		222.3		142.4		118	
BP86	229.3		220.4		142.5		118	

[1] MP2 data taken from ref. 139

[2] MP2 data taken from ref. 160

[3] B3LYP data taken from ref. 144

[4] BP86 data taken from ref. 161

A comparison of the DFT and hybrid-DFT optimised structures shows good agreement with the correlated ab initio methods. The general trend for r(M-Cl) and r(M-P) is BP86 < BLYP $\approx$ B3LYP, although the differences between the methods is small, less than 5 pm. It is notable that the monomer geometries do not change much with any of the correlated methods used.

An interesting aspect of the [ClM(PH_3)] geometries that has been noted in previous studies[160,161] is also reproduced in this study by all methods. There is a change in the metal-ligand bond length as the coinage metal becomes heavier, but whereas for the metal-chloride bond r(Cu-Cl) $\ll$ r(Ag-Cl) $\approx$ r(Au-Cl) $\approx$ r([111]-Cl), the metal-phosphorus bond follows the trend r(Cu-P) < r([111]-P) < r(Au-P) < r(Ag-P). The extent of this difference is illustrated in figures 4.2(a) and 4.2(b).

In an attempt to explain the differences between the metal-ligand bond lengths, the effect of relativity on the gold and element 111 bond lengths was considered by carrying out non-relativistic geometry optimisations on [ClM(PH_3)] (M=Au, [111]). The effect of relativity on copper and silver was assumed to be negligible for the purposes here. The resultant optimised geometries are given in table 4.3, which also includes the parameter $\Delta_R = P_{NR} - P_R$, the difference between the non-relativistic and relativistic property of interest. The data are also plotted in figure 4.3.

From table 4.3, it is clear that the effect of relativity on the phosphine geometric parameters, r(P-H) and α(HPM) is negligible. Also, all three methods predict that relativistic effects are more pronounced in the element 111 monomer than in the gold monomer, which might be expected based on their relative positions in the periodic table. Moreover, the effect of relativity on r(M-P) is greater than that

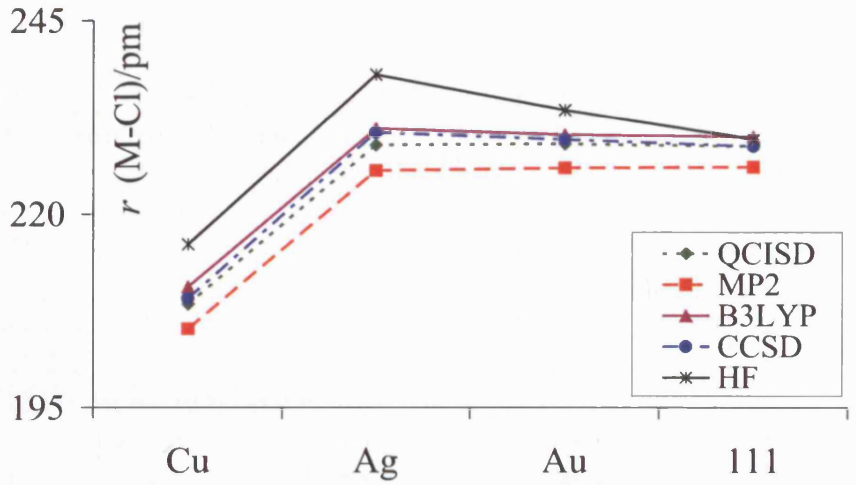

(a) r(M-Cl)

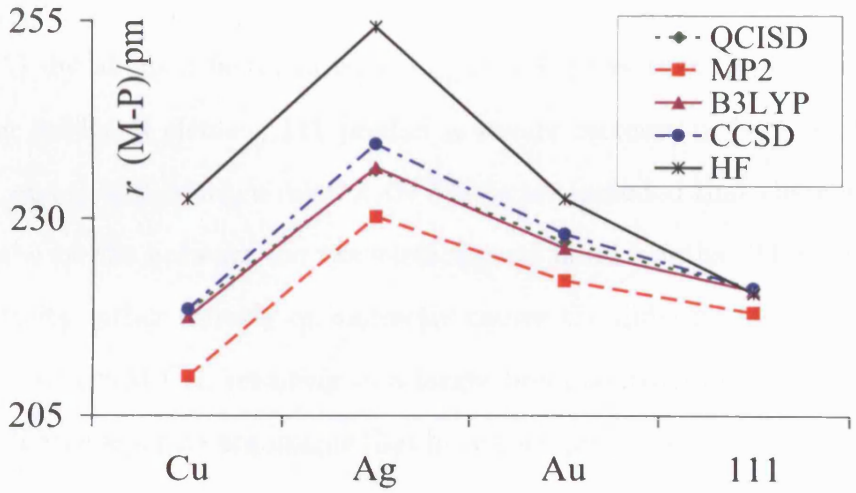

(b) r(M-P)

Figure 4.2: Variation of r(M-L)/pm with coinage metal (M=Cu, Ag, Au, [111]; L=Cl, P) in [ClM(PH_3)]. (The y-axes are set to a span of 50 pm in both graphs.)

Table 4.3: Effect of Relativity on Optimised Geometric Parameters for [ClM(PH_3)] (M=Au, [111]). Values from reference 139 are given in italics.

Method	r(M-Cl)/pm		r(M-P)/pm		r(P-H)/pm		α(HPM)/deg	
M=Au: non-relativistic								
MP2	238.3	*243.8*	246.3	*254.6*	139.6	*141.5*	118	*119*
QCISD	243.5		257.6		139.7		119	
B3LYP	245.6		256.8		141.1		119	
MP2 Δ_R	12.4	*17.5*	24.2	*30.3*	0.1	*0.2*	1	*2*
QCISD Δ_R	14.5		30.6		0.0		2	
B3LYP Δ_R	15.4		30.6		0.1		1	
M=[111]: non-relativistic								
MP2	256.3		270.3		139.8		119	
QCISD	261.8		283.6		140.0		120	
B3LYP	263.1		281.0		141.3		120	
MP2 Δ_R	30.3		52.3		0.0		2	
QCISD Δ_R	33.1		62.5		0.7		3	
B3LYP Δ_R	33.2		60.2		0.1		3	

of r(M-Cl), by about a factor of two. Figure 4.3 shows that the non-relativistic results for gold and element 111 predict a steady increase in both r(M-P) and r(M-Cl), and it is only when relativistic effects are included that there are differences in the trends between the two metal-ligand bond lengths. Thus, it appears that relativity, either directly or indirectly causes the differing trends in r(M-P) compared with r(M-Cl), resulting in a larger bond contraction for r(M-P) than r(M-Cl). Three separate arguments that have been proposed previously to explain this are now considered.

The first argument was proposed by Schwerdtfeger using relativistic orbital contraction arguments,[160] which was already mentioned on page 109. If the metal-ligand bond length is considered to be related to the metal's relativistic orbital contraction, for a more electronegative ligand (M^+-X^-) there is less metal s in-

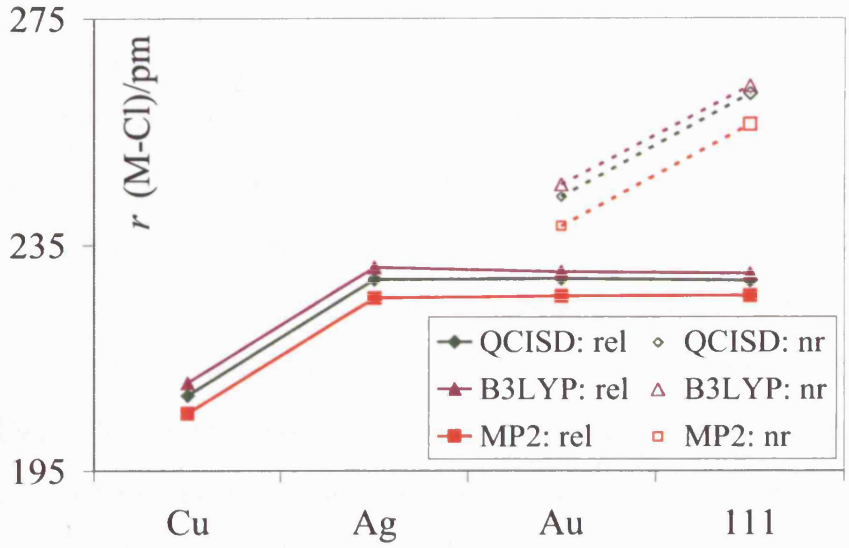

(a) r(M-Cl)

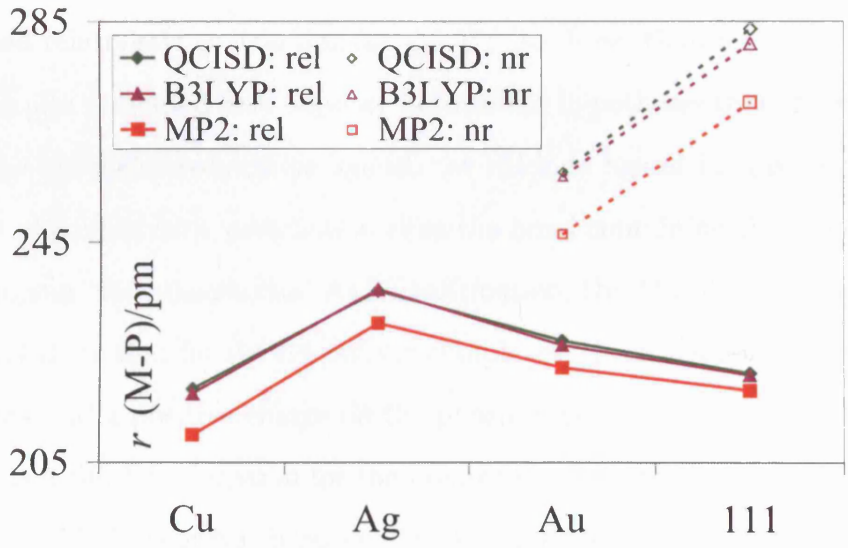

(b) r(M-P)

Figure 4.3: Effect of relativity on the variation of r(M-L)/pm with coinage metal (M=Cu, Ag, Au, [111]; L=Cl, P) in [ClM(PH_3)]. (The y-axes are set to a span of 80 pm in both graphs.)

volvement and so there is a smaller bond contraction than is the case for an electropositive ligand (M^-X^+), in which there is greater metal s population.

However, it has been shown by Snijders and Pyykkö,[163] and by Ziegler et al.[164] that the bond length contraction and orbital contraction, although both a direct result of relativity, should be considered as parallel but independent effects. In addition, Ziegler et al. attribute the relativistic bond length contraction to a shift of the minimum of the potential energy curve to smaller internuclear distances compared with the non-relativistic case, because there is a relativistic stabilisation of the kinetic energy as the atoms are pushed together. Thus, the extra bond contraction in diatomic gold(I) complexes with electropositive ligands (M^-X^+) should be considered as a result of a greater shift in the minimum of the potential energy curve to smaller internuclear distances because there is greater electron density on the more relativistic atom (M^-) than in M^+X^-. This results in a more pronounced relativistic contraction for the M^-X^+ bond than for M^+X^-.

The results presented here support both of the hypotheses that the bond containing the more electronegative ligand, the chloride ligand in this case, experiences less of a relativistic contraction than the bond containing the more electropositive ligand, the phosphorus. As a confirmation, the Mulliken atomic charges in table 4.4 show that for the relativistic complexes, there is a negative charge on the chloride and a positive charge on the phosphorus.

There is a third explanation for the greater bond contraction in r(M-P) compared with r(M-Cl) that was proposed by Bowmaker et al. for [ClMPR_3] (M=Ag, Au; R=H, Me).[161] In addition to a direct s orbital contraction, there is an indirect d orbital expansion due to relativity. This makes the filled d_π orbitals more available for M(d_π)-P(p_π) backbonding in the heavier gold compared with silver. The

Table 4.4: Mulliken atomic charges for [ClM(PH_3)] (M=Au, [111]).

	[ClAu(PH_3)]			[Cl[111]PH_3]		
	q(Au)	q(Cl)	q(P)	q([111])	q(Cl)	q(P)
MP2	-0.17	-0.27	0.48	-0.20	-0.32	0.60
QCISD	-0.17	-0.27	0.48	-0.20	-0.32	0.60
B3LYP	-0.20	-0.16	0.24	-0.19	-0.19	0.30

Table 4.5: Mulliken $(n-1)d_\pi$ orbital populations for [ClM(PH_3)] (M=Cu, Ag, Au, [111]).

	Cu(d_π)	Ag(d_π)	Au(d_π)	[111](d_π)
MP2	3.99	4.02	3.95	3.82
QCISD	4.00	4.02	3.96	3.79
B3LYP	3.95	4.01	3.93	3.80

validity of this explanation may be examined by looking at the Mulliken $(n-1)d_\pi$ populations of the four metals in [ClM(PH_3)], and are presented in table 4.5. In this case, there is a clear decrease in the d_π population for the later coinage metals, supporting the possibility of M-P backbonding in the case of the heavier metals. However, comparison of the d_π population of [111] in [Cl[111](PH_3)] with the Mulliken analysis of [111]H, in which no π effects would be expected, shows a d_π population of 3.85, which is very similar to the 3.8 quoted in table 4.5.[3] This questions whether the d_π data do in fact suggest that there is M(d_π)-P(p_π) bonding.

Perhaps Ziegler's explanation (i.e. that which uses the relativistic stabilisation of the kinetic energy to explain the bond length contraction) is most valid because it depends only on the number of electrons on the relativistic atom; since P is more electropositive than chlorine, there is more electron density on [111] in r([111]-P)

than in r([111]-Cl), so it has a greater relativistic bond contraction.

4.3.2 $[ClM(PH_3)]_2$ (M=Cu, Ag, Au, [111]) Dimer

Having discussed the effect of coinage metal on the intramolecular bond lengths of $[ClM(PH_3)]$ for the coinage metals, the next consideration is how the interactions between two monomers vary with coinage metal in the dimer $[ClM(PH_3)]_2$. Before explicitly looking at the metal-metal interactions, however, the relevance of the three possible structural arrangements of $M_2X_2L_2$ (M=Cu, Ag, Au, [111]; X=Cl; L=PH_3) shown in figures 4.1(a), 4.1(b) and 4.1(c) on page 111, in the context of metallophilicity is discussed. Thereafter, the metal-metal interactions will be analysed using the staggered model (figure 4.1(c)). At this point, the role of correlation, of the specific ab initio methods and of basis set are discussed. Finally, the metallophilicity of element 111 is addressed.

4.3.2.1 $M_2Cl_2(PH_3)_2$ Structures

There are three main factors that influence the geometry of $[ClM(PH_3)]_2$; metallophilic interactions, other intermolecular interactions and the preference of the metal for a given co-ordination number. Although in all three structures in figures 4.1(a), 4.1(b) and 4.1(c) there are metal-metal interactions present, in the staggered conformation of the two monomers they are most unencumbered. In the antiparallel conformation, the metal-metal interactions are present along with additional ligand-ligand interactions and if the monomers are allowed to rotate freely during a geometry optimisation, this latter structure is the more stable geometry. This can be seen from the higher interaction energies at the antiparallel geometry compared with at the staggered geometries in table 4.6.

Table 4.6: A comparison of the geometries of $[ClM(PH_3)]_2$ (M=Cu, Ag, Au, [111]) with the monomers orientated antiparallel (α(PMM'P') is allowed to vary) or staggered (α(PMM'P') is fixed to 90°). The data have been BSSE-corrected.

	Antiparallel (Unconstrained geom. opt.)			Staggered (α(PMM'P')=90°)	
	r(M-M)/pm	α(PMM'P')/°	E_{int}/(kJ/mol)	r(M-M)/pm	E_{int}/(kJ/mol)
M=Cu					
HF	363	178	-55.9	413	-1.5
MP2	288	150	-40.4	313	-13.5
B3LYP	330	180	-45.4	318	-4.0
QCISD	339	160[1]	-42.3	320	-11.2
M=Ag					
HF	380	180	-60.6	421	-1.2
MP2	292	180	-53.3	311	-21.2
B3LYP	341	177	-53.0	327	-6.2
QCISD	333	160[1]	-49.7	323	-14.4
M=Au					
HF	374	180	-48.3	455	-1.1
MP2	294	153	-53.8	317	-25.5
B3LYP	345	179	-38.6	358	-2.6
QCISD	339	160[1]	-49.7	345	-13.2
M=[111]					
HF	398	180	-30.5	512	-1.5
MP2	314	147	-53.0	324	-32.0
B3LYP	383	176	-24.7	no min. found	
QCISD	357	160[1]	-35.7	374	-9.4

[1] r(M-M) varied using monomer geometry, with α(PMM'P') fixed at 160°

The rhombic structure is a third possible structure of the form $M_2Cl_2(PH_3)_2$, which has a metal co-ordinated by three ligands in a trigonal planar arrangement compared with two ligands in a linear arrangement for the previous two structures. In the context of this study, it is interesting because it highlights a contrast between the copper and silver complexes, for which this is in fact the most stable structure, and the gold and element 111 structures, for which this structure was only found in the non-relativistic cases. This is consistent with the proposal

that whereas relativistic Au(I) prefers co-ordination to two ligands in a linear arrangement, Cu(I) and Ag(I) prefer higher co-ordination numbers and leads to oligomerisation in the early coinage metal complexes but dimerisation in the gold complexes.[160]

Since it is the metallophilicity that is of interest here, it is sufficient to note that although the antiparallel structures show greater interaction energies, presumably due to the ligand-ligand interactions, and the most stable structure for the various coinage metals is not necessarily a linear Cl-M-P arrangement, the staggered conformation allows a more suitable model for the study the metal-metal interactions, and hence it is this structure that is discussed more fully in the proceeding section.

4.3.2.2 Metallophilicity

In the staggered $[ClM(PH_3)]_2$, only the metal-metal distances were optimised since the monomer geometries are assumed to stay completely unaltered in the dimer. The computational details section (section 4.2) has outlined the methodology used to find the minimum energy metal-metal interactions on the counterpoise (CP) corrected surface. Before looking at the results of these pseudo-geometry optimisations, it is worth examining the differences between this approach and carrying out a non-corrected constrained geometry optimisation. Figure 4.4 shows both the uncorrected and CP corrected energy surfaces of $[ClAu(PH_3)]_2$ using MP2. There are three aspects to note about this figure. First, the depth of both potential energy curves is extremely shallow, for example there is a 5 kJ/mol difference between the energy at 290 pm and at 317 pm for the CP corrected surface. Second, there is quite a dramatic shift in the potential energy minimum when the BSSE

is taken into account. By carrying out a counterpoise correction, there is a shift from shorter to longer gold-gold distances that is almost 30 pm. Finally, at each point the CP corrected curve lies above the non-corrected curve, and the change in the curve is quite dramatic. In fact, the magnitude of the artificial stabilisation of the MP2 interaction of $[ClAu(PH_3)]_2$ due to BSSE (39 kJ/mol) is greater than the magnitude of the CP corrected interaction energy value of -25 kJ/mol. From these data, it can easily be seen that for the weak metallophilic interactions, the BSSE cannot be neglected, and that it should be accounted for in both the geometries and the energies. Thus, in the following analysis, only the CP corrected results are discussed.

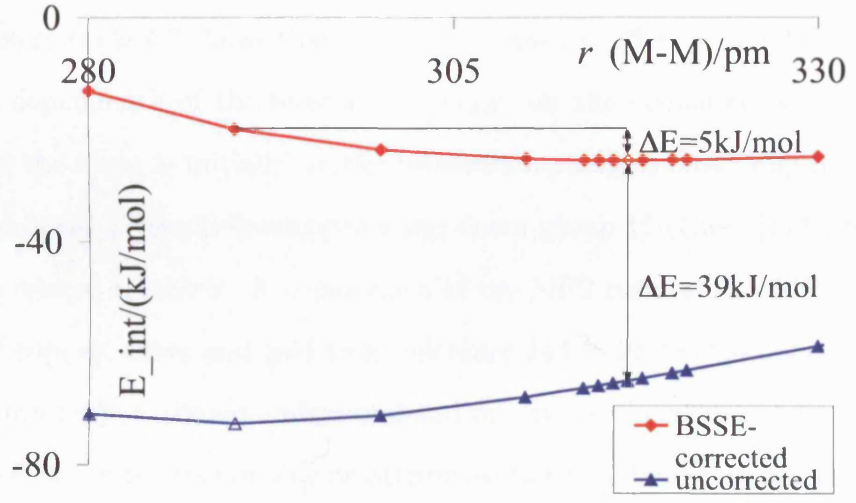

Figure 4.4: MP2 counterpoise corrected and non-counterpoise corrected interaction energies as a function of the gold-gold interatomic distances. The unfilled data points correspond to the minimum point of each curve.

The results for $[ClM(PH_3)]_2$ using ab initio and DFT methods are presented

in table 4.7. Firstly, it is reassuring to note that the HF interaction energies for all of the coinage metal complexes are approximately 0 kJ/mol, supporting earlier findings that metallophilicity is a correlation effect. Including correlation through DFT GGA methods does predict negative interaction energies but, especially for gold and element 111 metallophilic interactions, the values are very small. It is well-known that the R^{-6} dispersive-type forces cannot be described using DFT methods, so these results indicate that, particularly for the heavier elements, the metallophilicity at the relativistic level is due mainly to dispersion forces. Recall that Magnko et al.[144] found that ionic excitations also contribute to metal-metal interactions, which might account for the part of the interaction energies for copper and silver that is reproduced in the DFT methods. Notwithstanding, it is clear that correlated ab initio methods are necessary to describe metallophilicity.

Although table 4.7 shows that the r(M-M) values differ for the different methods, the dependence of the interaction energy on the geometry is neglected for now, and the focus is initially on the interaction energies only. Figure 4.5 shows the trend in the interaction energies going down group 11 (Cu→ [111]) for the ab initio correlated methods. A comparison of my MP2 results with MP2 literature values of copper, silver and gold from reference 144 indicates that the interaction energies from my study are underestimated relative to the values of Magnko et al. This difference in the values may be attributed to the different basis sets employed in the two studies, and there is also a difference in the equilibrium metal-metal distances, which will be mentioned later. Nonetheless, the trends between the different MP2 results with coinage metal do agree quite well that metallophilicity increases down the group.

Table 4.7: r(M-M)/pm and counterpoise-corrected interaction energies/(kJ/mol) for $[ClM(PH_3)]_2$ (M=Cu, Ag, Au, [111]) in a staggered conformation. The non-counterpoise corrected interaction energies/(kJ/mol) are given in parentheses.

	Cu			**Ag**			**Au**			**[111]**		
	r(Cu-Cu)	E_{int}		r(Ag-Ag)	E_{int}		r(Au-Au)	E_{int}		r([111]-[111])	E_{int}	
HF	413	-1.5	(-2.9)	421	-1.2	(-2.4)	455	-1.1	(-2.0)	512	-1.5	(+0.7)
MP2	313	-13.5	(-35.2)	311	-21.2	(-64.0)	317	-25.5	(-64.9)	324	-32.0	(-51.1)
MP2[1]	*314*	*-12.8*		*311*	*-21.3*		*321*	*-24.7*				
MP2[2]	*277*	*-24.4*		*290*	*-33.1*		*300*	*-37.0*				
LMP2[2]	*281*	*-22.1*		*292*	*-30.7*		*303*	*-34.8*				
QCISD	320	-11.2	(-25.3)	323	-14.4	(-36.1)	345	-13.2	(-30.6)	374	-9.4	(-18.0)
CCSD	No minimum located			325	-13.6	(-39.5)	343	-12.4	(-29.9)	374	-8.7	(-16.8)
CCSD(T)[3]	300	-15.3	(-33.1)	319	-16.7	(-38.3)	336	-15.4	(-33.6)	364	-11.2	(-21.9)
B3LYP	318	-4.0	(-9.3)	327	-6.2	(-9.5)	358	-2.6	(-5.5)	No minimum located		
BP86	270	-12.2	(-18.9)	304	-12.0	(-15.9)	326	-5.5	(-9.4)	382	-3.3	(+0.9)

[1]MP2 results taken from reference 139

[2]MP2 and LMP2 results taken from reference 144

[3]CCSD monomer geometry of $[Cl[111]PH_3]$ used

A comparison of my MP2 data with those from my QCISD, CCSD and CCSD(T) calculations shows some discrepancies despite using the same basis sets and effective core potentials. While the agreement between MP2 and the other methods is reasonable for the copper values, this agreement becomes progressively worse as the coinage metal becomes heavier. This results in rather poor agreement between the trend in the interaction energies using MP2 compared with the other ab initio methods. Whereas MP2 predicts a steady increase in the interaction energies from copper to element 111, QCISD, CCSD and CCSD(T) all show that the interaction energies are approximately constant for all of the coinage metals. A possible source of these differences that requires discussion is the geometry dependence of the interaction energies.

Looking at the metal-metal distances in table 4.7, also illustrated in figure 4.6, it is clear that the metal-metal distances do vary using the various methods. The MP2 values calculated here predict longer metal-metal distances than those reported previously but, as was the case for the interaction energies, the trends in r(Cu-Cu) $\rightarrow$ r(Au-Au) are in reasonable agreement. Addressing the role of the methods, however, shows that the trends between MP2 and other methods are once again slightly at odds; the numerical agreement between the copper results is quite good, but whereas MP2 r(M-M) results are reasonably consistent for all of the metals, there is a gradual increase in r(M-M) from M=Cu to M=[111] using QCISD, CCSD and CCSD(T). Given the discrepancy between the metal-metal distances calculated using MP2 and using the other ab initio methods, in order to see how much this discrepancy influences the differences between the interaction energy trends, the interaction energies were recalculated using only one set of geometries, the QCISD geometries. The results are presented in figure 4.7.

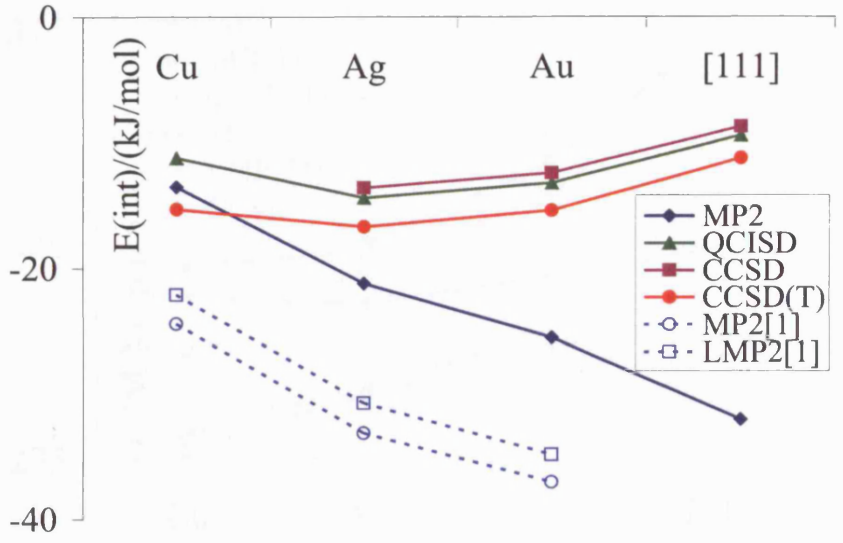

Figure 4.5: Counterpoise corrected interaction energies for $[ClM(PH_3)]_2$ (M=Cu, Ag, Au, [111]) using ab initio methods. [1] Values are taken from reference 144.

It is clear that the QCISD, CCSD, and CCSD(T) values agree quite well, although QCISD does slightly underestimate the copper-copper interaction energy relative to the other methods. However, as was the case in figure 4.5, the MP2 interaction energies form a different trend because whereas MP2 predicts greater interaction energies for gold and element 111 compared with copper and silver, the other methods predict comparable energies for all four coinage metals. Thus, the differences in geometries are not sufficient to explain the differences between the trends in the interaction energies for MP2 compared with the other methods.

As a final attempt to explain why MP2 differs from the other methods, the effect of basis set was examined. MP2 and CCSD(T) calculations were carried out

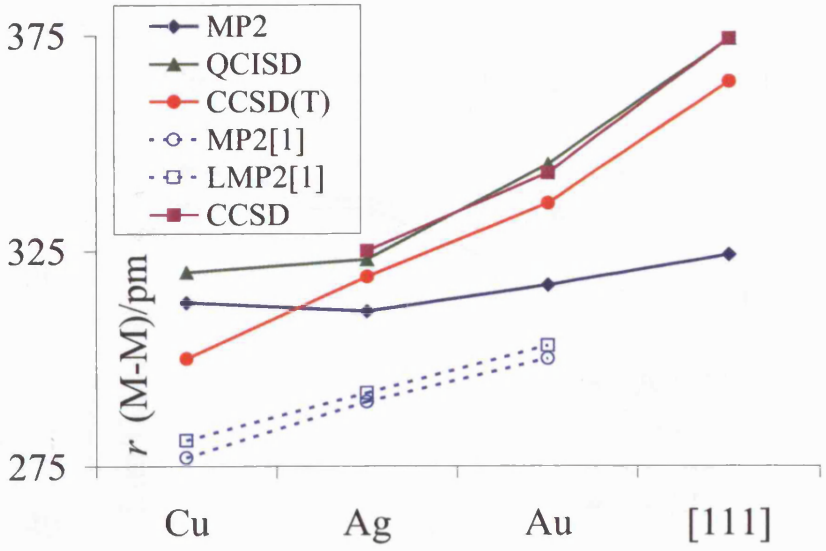

Figure 4.6: Counterpoise corrected metal-metal distances for $[ClM(PH_3)]_2$ (M=Cu, Ag, Au, [111]) using ab initio methods. [1] Values are taken from reference 144.

using improved basis sets on the metals and the non-hydrogenic ligands. Since the geometry was not found to dictate the interaction energy trends, counterpoise corrected single point energies were calculated at the geometries of the slightly lower quality basis sets were used. The results are presented in figure 4.8.

Generally, there is an increase in the interaction energy when the basis set is improved, with the exception of the MP2 results on $[Cl[111]PH_3]_2$, in which there is a slight decrease in the interaction energy. However, it should be noted that in contrast to the other metals, the basis set for element 111 is of the same quality in both calculations. The trend using CCSD(T) is changed only very slightly (and is due to a slight increase in the interaction energy values for the silver and gold

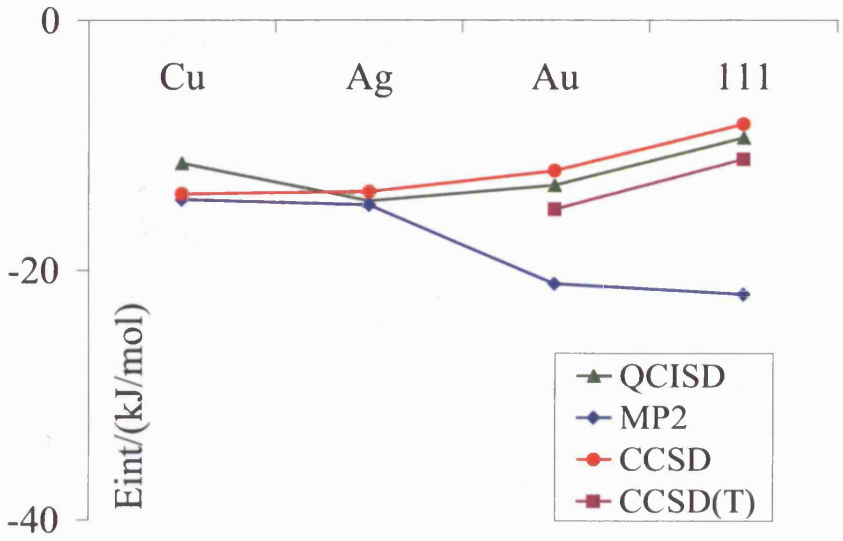

Figure 4.7: Counterpoise corrected interaction energies for $[ClM(PH_3)]_2$ (M=Cu, Ag, Au, [111]) using ab initio methods at the QCISD counterpoise corrected geometries.

complexes compared with no change in the interaction energy values for the copper and element 111 complexes). The net outcome is that the MP2 results using this slightly larger basis set agree better with the results of Magnko et al., and also agree slightly better with the other methods insofar as all methods predict that the gold and element 111 interaction energies are comparable.

4.3.2.3 Metallophilicity of Element 111

The present data for $[ClM(PH_3)]_2$ showed two conflicting trends as to how metallophilicity changes going down group 11. MP2 predicted that the metallophilicity increases down group 11, consistent with previous studies[144] and hence that element

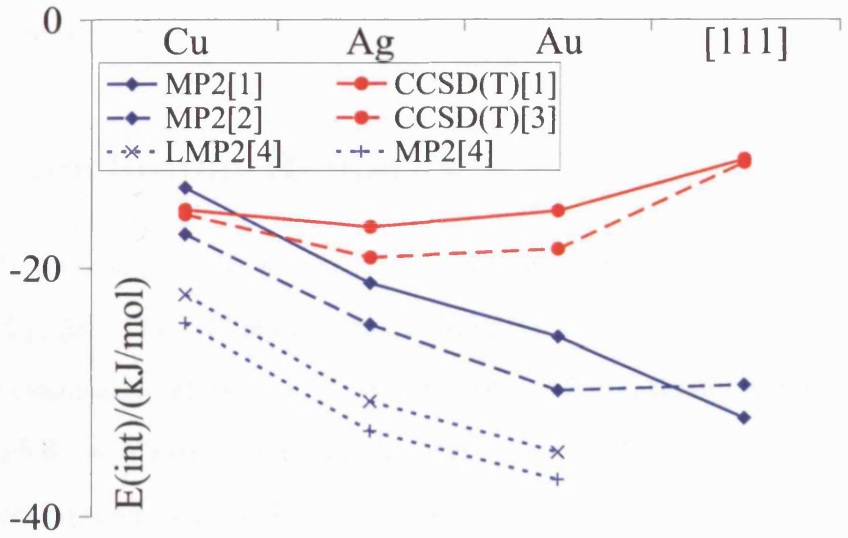

[1]Basis set [1]: 2f(4f)/6-31G*/6-31G**
[2]Basis set [2]: 3f2g(4f)/6-311+G*/6-31G**
[3]Basis set [3]: 3f2g(4f)/6-311G*/6-31G** (Further improvements of the basis set were prohibited by computational limitations.)
[4][4]: Data from reference 144

Figure 4.8: Effect of basis set on the $[ClM(PH_3)]_2$ (M=Cu, Ag, Au, [111]) interaction energies using MP2 and CCSD(T).

111 is more metallophilic than gold. However the QCISD, CCSD and CCSD(T) methods predicted that gold and element 111 exhibit very similar metallophilic interaction energies. Improvement of the basis sets suggested that both MP2 and CCSD(T) predict essentially no difference in the gold and element 111 metallophilic interactions using either MP2 or CCSD(T). Thus, it appears that there is no increase in metallophilic interactions going from gold to element 111, and

that there may even be a slight decrease in the metallophilicity. Furthermore, the metallophilic interactions between these elements are not significantly larger than for copper and silver.

4.4 Concluding Remarks

This study has looked at both the monomeric and dimeric forms of [ClM(PH_3)] (M=Cu, Ag, Au, [111]). The monomer studies indicate that in linear [ClM(PH_3)] there is a noticeable relativistic contraction of the metal-ligand bond lengths for gold, which is even more noticeable for element 111. The bond length contraction is more pronounced for the metal-phosphorus than the metal-chlorine bond. Three different explanations were looked at. The first explanation relates the bond length to the role of the *n*s orbital contraction and its occupation in the bond of interest. Since the role of the s orbital is greater in the M-P than in the M-Cl bond, this could explain why the former bond experiences a greater contraction. A second explanation that enhanced M(d_π)-P(p_π) bonding contracts the metal-phosphorus bond is difficult to assess, since the Mulliken analysis may be affected by the change in ground state of the metal atom from $d^{10}s^1$ to s^2d^9. The final possibility discussed, and perhaps the most valid for these complexes, was proposed by Ziegler et al., and uses the relativistic stabilisation of the kinetic energy of a system to account for a shift in the minimum of the potential energy to shorter internuclear distances. It was proposed that for an electropositive ligand attached to a relativistic atom, greater electron density resides on the more relativistic atom than in the case of an electronegative ligand attached to the relativistic atom. The relativistic stabilisation of the kinetic energy is increased

in the former case, and this leads to a greater shift in the minimum of the potential energy curve to shorter internuclear distances. This final argument has the advantage that it is not directly affected by the change in the ground state configuration from gold to element 111.

The $[ClM(PH_3)]_2$ dimer studies show that there is essentially no metallophilic interaction at the HF level, and that DFT does not reproduce the full metallophilic interactions relative to the correlated ab initio methods. From the ab initio post-HF methods, MP2 predicts a gradual increase in the metallophilic interactions down group 11, whereas QCISD, CCSD and CCSD(T) methods predict that the interaction energies are approximately constant. Given the previous study by Pyykkö and Tamm of $S(AuPH_3)_2$, in which they found that MP2 could not adequately describe the system and that it was necessary to go to CCSD(T) to reproduce experimental bond lengths,[142] this questions whether previous analyses, all of which have used MP2 and the closely related LMP2, have adequately described the metallophilic interactions. In addition, it is generally accepted the MP2 is the least reliable of the post-HF methods. Hence based on the results from the other post-HF methods, the metallophilic interactions are approximately the same in the gold and element 111 dimers. Clearly, it would be useful to carry out further studies to examine why MP2 and the other post-HF methods predict different results for these systems.

Chapter 5

Density Functional Studies of the Electronic and Geometric Structures of LnX_3 and AnX_3 (Ln=La-Lu; An=Ac-Lr; X=H, F, Cl, Br, I)

5.1 Introduction

The role of the 4f electrons in lanthanide chemistry has been studied extensively using computational methods and it is now recognised that although the f orbitals are higher in energy than the core 5s and 5p orbitals, they are radially compact and largely uninvolved in bonding (see chapter 1). For the reproduction of many properties of interest, it has been shown to be adequate to consider the f electrons only in the core description of the lanthanides and not explicitly in the valence region, which aids computational efficiency.[165]

The bonding in lanthanide compounds is predominately ionic, and the most common oxidation state is +3 (apart from Ce(IV), Yb(II) and Eu(II), for which the tendency to empty, filled and half-filled 4f shells dictates the oxidation state[0]). For the structure of LnX_3 compounds (Ln - lanthanide; X - monoanion e.g. halogen) simple electrostatic arguments might thus be used, predicting a trigonal planar structure. However, experimental and computational data show that many of the structures are pyramidal.[166] Various studies have looked at possible explan-

ations for the deviations from planarity in these and similar d^0 transition metal compounds, and in particular at the dependence of these deviations on the degree of ionicity or covalency.[167,168]

For mainly ionic MX_3 compounds, a core polarisation argument has been used. This is based on the assumption that the electronegative ligands that surround the metal centre distort the electron density of the metal, which results in the rearrangement of the core density depending on the orbitals in the core. This is often called 'inverse polarisation' to distinguish it from the situation when the positive metal centre polarises the surrounding ligands. This 'inverse polarisation' method was used to predict the shapes of the lanthanide trihalide compounds.[169] In this paper, the authors proposed that the partially filled f orbitals result in a non-spherical electron distribution at the metal, which influences the molecular structure.

An alternative, covalency-based argument uses the second-order Jahn-Teller (SOJT) effect to explain the shape of molecules that have covalent interactions between the ligand and the metal. The SOJT effect rationalises the change in structure by the mixing of filled or partially filled orbitals with unfilled orbitals that are close in energy to enhance bonding.[168]

Eisenstein et al.[170] used the SOJT effect to explain the extent of pyramidalisation for the LnX_3 (Ln - lanthanide; X = H, CH_3, F, Cl, Br, I, NH_2) set of compounds, using a relativistic effective core potential (RECP) to describe the lanthanide core: $[Kr]^{36}4d^{10}4f^n$ (n represents the occupancy of the 4f orbitals in the neutral lanthanide atom, and the 4f orbitals have $n-1$ occupancy when the Ln^{3+} situation is considered). They found that the geometric structure can be ration-

[0]In addition, Sm found as Sm(III) or as Sm(II). Only the former is considered here, however, because this allows a more direct comparison with the results reported by Eisenstein et al.[170]

alised by considering the role of the formally empty 5d orbitals. In the trigonal planar D_{3h} symmetry, the lanthanide $d_{x^2-y^2}$ and d_{xy} orbitals can σ bond with the ligands, but in the lower C_{3v} pyramidal symmetry, the previously nonbonding d_{xz} and d_{yz} also become available for σ bonding with the ligands. So, if σ bonding is enhanced by d_{xz} and d_{yz} interactions, then the pyramidal structure is favoured. Competing with this, M(d_π)-X(p_π) interactions for the double-faced π-donating halogens are enhanced by greater planarity, increasing for the later halogen compounds compared with the lighter halides. A study of $Sm[N(SiH_3)(SiH_2CH_3)]_3$ by Clarke et al.,[171] using the same lanthanide basis sets as Eisenstein et al., highlights the role of the d orbitals in bonding. They showed that removing the d basis functions from the valence Sm description such that the d orbitals cannot participate in bonding, changes the structure from a pyramidal structure with α(NSmN) of 112.5° to essentially trigonal planar with α(NSmN) of 119.4°. Hence, by preventing the lanthanide d orbitals from interacting with the ligands, the tendency for the structure to distort to a pyramidal structure is removed.

Both of these studies by Eisenstein et al. and by Clarke et al. consider the 4f orbitals of the lanthanides to be core-like and describe them using relativistic effective core potentials. However, in a study by Wang and Schwartz on the lanthanide contraction in lanthanide diatomics, and LaO in particular,[172] it was reported that inclusion of the 4f orbitals in the valence, compared with having them in the core, results in a transfer of electron density from ligand valence orbitals to the metal 4f orbitals, reducing the positive charge on the lanthanide. Moreover, there is a reduction in the lanthanide 5d orbital participation in the molecular orbitals in favour of 4f participation. Since the 4f orbitals are radially more compact than the 5d orbitals, the lanthanide and ligand can approach more

closely without experiencing the same Pauli repulsion. Hence, including the 4f orbitals in the valence reduces the lanthanide-ligand bond length. This is consistent with the findings of Laerdahl et al., that the 4f orbitals in the valence reduces the bond length.[9]

As was mentioned in section 1.3.3, the role of f orbitals in the bonding in triscyclopentadienyl lanthanides ($LnCp_3$; Cp=C_5H_5) and actinides ($AnCp_3$), was studied by Bursten and co-workers.[20,34–37] In C_{3v} (or D_{3h}) symmetry, Cp_3^{3-} has a π MO of a_2 (a_2') symmetry, which consists of π contributions from each of the Cp rings, and is destabilised relative to the energy of the π MO in a single Cp ring (see figure 1.6 on page 20). In the metal compound, this a_2 (a_2') MO can only interact with metal orbitals of the same symmetry. While there is no s, p or d metal orbital that fulfills this requirement, there is an a_2 (a_2') f orbital, which interacts with and stabilises this Cp_3^{3-} MO. This provides an explanation for the large number of examples of triscyclopentadienyl structures with f elements compared with the scarcity of equivalent transition metal structures. A comparison of UCl_3 with UCp_3, since Cl is isolobal with Cp in C_{3v} and D_{3h} symmetry,[36] finds Cl to be less effective than Cp as a π donor, because the π overlap between uranium and Cl is less than that between uranium and Cp.[36]

Comparison of D_{3h} $AnCp_3$ (An=U, Np, Pu, Am, Cm, Bk, Cf) with $LnCp_3$ (Ln=Ce, Pr, Nd, Sm, Gd, Dy) shows that the a_2' (a_2 in C_{3v}) Cp_3^{3-} MO in the lanthanide compounds is stabilised to a lesser extent than in the actinide compounds.[37] So, whereas the 5d and 6d were found to have similar bonding capabilities, the bonding capabilities of the 4f and 6s orbitals of the lanthanides were found to be less than that of the 5f and 7s orbitals of the actinides. Also, as the lanthanide (or actinide) becomes heavier, it was reported that there is a de-

crease in the d participation of the compounds and an increase in f participation, although not necessarily an increase in metal(f)-ligand interaction.

In this study, MX_3 (M=La-Lu, Ac-Lr; X=H, F, Cl, Br, I) are studied in order to determine the extent of pyramidality in each compound. For the lanthanide compounds, the metals' 4f orbitals are included in the valence region to examine their role in Ln-X bonding, allowing comparison with Eisenstein et al.'s results, in which the 4f are core orbitals. Furthermore, this study compares the lanthanide results with the actinide analogues, AnX_3. The early actinides show definite f contributions to bonding, so the need to consider the 5f orbitals as valence orbitals is less ambiguous but, for the later actinides (transamericium actinides), it is widely accepted that the chemistry becomes more like that of the lanthanides. It was hoped that this study would yield another test of this view.

5.2 Computational Details

All of the geometry optimisations of MX_3 were carried out using the hybrid-Density Functional B3PW91,[95,100] as used in reference 170, using the Gaussian03[173] suite of programs. The metals and halogens were described using the relativistic effective core potentials (RECPs) developed by the Stuttgart-Dresden group.[174–177] For the lanthanides and the actinides, the RECPs replace 28 and 60 electrons respectively, and the associated basis sets use a segmented contraction scheme[175,177,178] to describe the valence electrons. For the halogens, the RECPs and basis sets from the Stuttgart-Dresden group were augmented by the polarisation functions used in reference 170, that is, 2 α_d functions on F (α_1=3.3505 (0.357851) α_2=0.9924 (0.795561)), and 1 α_d on Cl (α=0.643 (1.0)), Br (α=0.389

(1.0)), and I (α=0.266 (1.0)). The Pople basis set 6-31G** was used for H.[179]

The geometry optimisations of MX_3 were initially carried out using the highest spin state for the compounds (i.e. the maximum number of unpaired 4f electrons) and without any symmetry constraints. For many of the compounds, an essentially C_{3v} or D_{3h} structure was obtained, but a few deviations from these symmetries were found. In these cases, the geometries were reoptimised using symmetry constraints and, since in all cases energy differences of <10 kJ/mol were obtained, the latter results are quoted. Finally, population analysis was carried out using the Natural Bond Orbital (NBO) method.[180]

All of the molecular orbital plots were generated using MOLDEN,[121] with a consistent contour value of 0.05.

5.3 Results and Discussion: Lanthanide Results

5.3.1 r(M-X)

Table 5.1 and figures 5.1 and 5.2 compare the bond lengths obtained from the current calculations (small core (SC)) with those from reference 170 (large core (LC)) and with the values recommended by Kovács and Konings.[166] In order to be consistent with the results from reference 170, LnX_3 are neutral except for CeX_3^+, EuX_3^- and YbX_3^-, corresponding to Ce(IV), Eu(II) and Yb(II) respectively, which are their most stable oxidation states. Both the LC and SC descriptions predict a lanthanide contraction, short bond lengths for CeX_3^+, and long bond lengths for EuX_3^- and YbX_3^-. The short r(Ce-X) relative to the compounds of the other lanthanides can be explained by the greater positive charge on cerium (formally +4), which has a smaller ionic radius than the formally +3 lanthanide ions. In a similar way, the longer r(Eu-X) and r(Yb-X) are explained by the lower, formal +2 charge and larger ionic radii than the +3 ions.

The well-established lanthanide contraction, attributed to the ineffective shielding of the increasing nuclear charge as the lanthanides are traversed, is predicted by both ECPs. Quantitatively, measured by r(La-X)-r(Lu-X), it is consistent using both ECPs, with only a slightly greater variation with ligands for the SC results compared with the LC results. Taking the average of the lanthanide contraction for the five ligands gives 17.8 pm for the SC and 17.6 pm for the LC, both of which agree well with the 17.1 pm calculated based on the 6-coordinated ionic radii of La^{3+} and Lu^{3+}.

Table 5.1: Comparison of r(M-X)/pm for LnX_3 (X=H, F, Cl, Br, I) optimised using the SC ECP (in normal text) with the LC ECP results reported in ref 170 (in italics). Values in bold text are taken from ref. 166, and are recommended by the authors on the basis of data obtained from experimental and theoretical studies. Δ=r(La-X)/pm-r(Lu-X)/pm, and the values are a measure of the lanthanide contraction in the specific compounds. *No converged geometry obtained.

	H		F			Cl			Br			I		
La	208.1	*212.5*	210.4	*214.5*	**207.7**	257.7	*261.0*	**253.4**	273.4	*277.1*	**268.9**	295.9	*300.8*	**286.7**
Ce	190.8	*194.2*	194.9	*202.2*		240.5	*244.2*		256.2	*259.4*		278.9	*282.0*	
Pr	203.4	*209.3*	207.0	*211.0*	**205.8**	252.7	*257.3*	**251.1**	268.5	*273.3*	**266.4**	291.9	*296.7*	**284.8**
Nd	202.4	*207.0*	205.6	*209.1*	**204.9**	251.5	*255.1*	**249.9**	268.0	*271.6*	**265.2**	289.9	*294.9*	**283.8**
Pm	202.2	*206.2*	204.9	*208.1*	**203.9**	250.6	*254.2*	**248.8**	266.0	*270.1*	**263.9**	288.3	*293.3*	**282.9**
Sm	204.2	*204.1*	204.1	*207.2*	**202.9**	249.3	*252.3*	**247.6**	265.5	*268.6*	**262.7**	289.5	*291.8*	**281.9**
Eu	226.5	*233.3*	222.1	*226.0*		269.6	*275.0*		285.3	*291.2*		308.1	*314.7*	
Gd	198.7	*202.1*	200.5	*205.1*	**201.0**	246.4	*250.0*	**245.3**	262.7	*265.7*	**260.3**	283.1	*289.2*	**280.0**
Tb	*	*201.4*	200.0	*204.5*	**200.1**	245.0	*250.1*	**244.2**	*	*265.9*	**259.0**	284.5	*287.7*	**279.0**
Dy	197.1	*200.2*	199.7	*202.1*	**199.1**	243.7	*247.4*	**243.0**	259.3	*263.3*	**257.8**	281.7	*286.4*	**278.1**
Ho	198.5	*199.1*	199.5	*201.0*	**198.1**	243.3	*246.1*	**241.9**	258.5	*261.9*	**256.6**	280.4	*285.3*	**277.1**
Er	195.6	*198.2*	198.4	*200.2*	**197.2**	242.2	*245.2*	**240.7**	257.3	*260.6*	**255.3**	279.2	*284.5*	**276.1**
Tm	195.6	*197.5*	198.0	*199.2*	**196.2**	241.2	*244.0*	**239.6**	256.4	*259.5*	**254.1**	278.6	*283.2*	**275.2**
Yb	215.9	*224.2*	212.7	*219.1*		259.1	*266.3*		274.9	*282.2*		297.6	*305.4*	
Lu	193.1	*196.0*	195.6	*198.0*	**194.3**	238.6	*242.5*	**237.3**	253.7	*258.7*	**251.6**	275.5	*282.8*	**273.3**
Δ	15.0	*16.5*	14.8	*16.5*	**13.4**	19.1	*18.5*	**16.1**	19.7	*18.4*	**17.3**	20.4	*18.0*	**13.4**
	17.1 using the ionic radii of 6-coordinate La^{3+} and Lu^{3+} from ref 181													

The recommended data from Kovács and Konings predict a slightly lower average value of 15.1 pm for the lanthanide contraction. This is mainly because, although there is good agreement with theory for the fluorides, chlorides and bromides, the value of 13.4 pm for the iodides is less than the 20.4 pm and 18.0 pm predicted by the SC and LC calculations respectively. This latter discrepancy may be attributed to the poor agreement between r(M-I) for the earlier lanthanide iodides.

The dependence of the lanthanide contraction on the ligand has been investigated by others (see, for example, references 172, 9 and 11), and will not be dealt with in detail here other than to mention that for the halides, the lanthanide contraction increases slightly from F $\rightarrow$ I, with the obvious exception of the aforementioned small value of 13.4 pm from reference 166. It has been shown that one factor that influences the lanthanide contraction is the s contribution to the Ln-X bond; larger s contributions tend to give larger contractions, because in addition to the contraction of the orbital due to the ineffective shielding of the increasing nuclear charge, there is a relativistic ns contraction as the lanthanides are traversed. Relativity has been shown to be responsible for 25% of lanthanide contraction in LnH_3 by Laerdahl et al.[9] Natural Bond Orbital (NBO) analysis of the SC results shows that there is indeed greater contribution from the s orbitals for the heavier halides than for the lighter halides (e.g. the LaF_3 and LuF_3 s populations are 0.01 and 0.06 respectively, compared with 0.14 and 0.39 of LaI_3 and LuI_3) consistent with the greater Δ(La-Lu) value of 20.4 pm for the lanthanide iodides compared with 14.8 for the fluorides. This suggests that the lanthanide contraction of 13.4 pm suggested by Kovács and Konings for LnI_3, calculated based on data fitting, may be an underestimate. Note, however, that the s con-

tribution is only one of many factors, and that others include bond rigidity, d contributions (e.g. the contraction of the 6s orbital across the lanthanides was calculated to be 43 pm compared with just under 10 pm for the 5d orbitals[9]) and the relativistic stabilisation of the kinetic energy (see chapter 4).

The main difference between the LC and SC results for r(M-X) is that the values predicted using the SC descriptions of the lanthanides are consistently shorter, by 4.1±1.7 pm, than those using the LC descriptions. One possible explanation for this, as noted by Wang and Schwartz, is that by allowing 4f orbitals to participate in the lanthanide bond, the bond is strengthened and shortened.[172] Another possible explanation for the differences was put forward by Laerdahl et al., based on their MP2 calculations.[9] They found that having the 4f orbitals in the core underestimates the correlation effect on the bond, and gives longer bond lengths compared with the case where the 4f orbitals are in the valence and are allowed to relax.

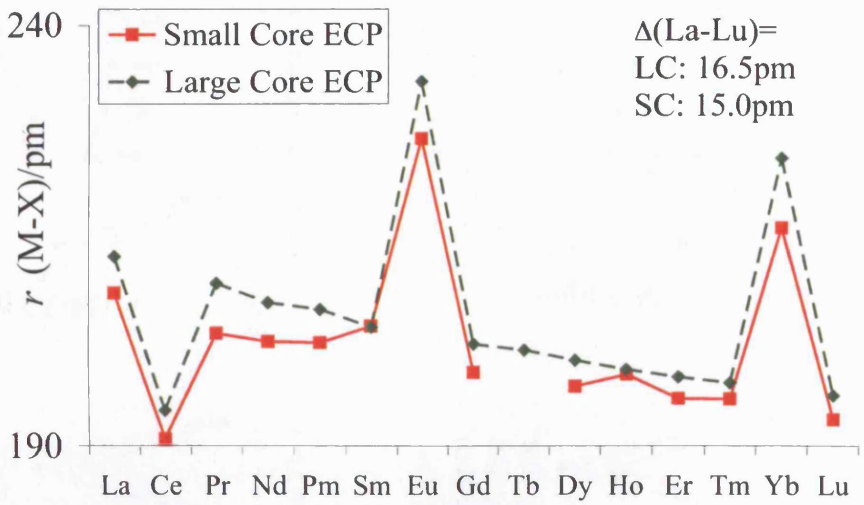

Figure 5.1: Variation of r(Ln-H) with lanthanide element in LnH_3, as predicted by the present calculations, employing SC ECPs, compared with those results from reference 170 (LC ECP).

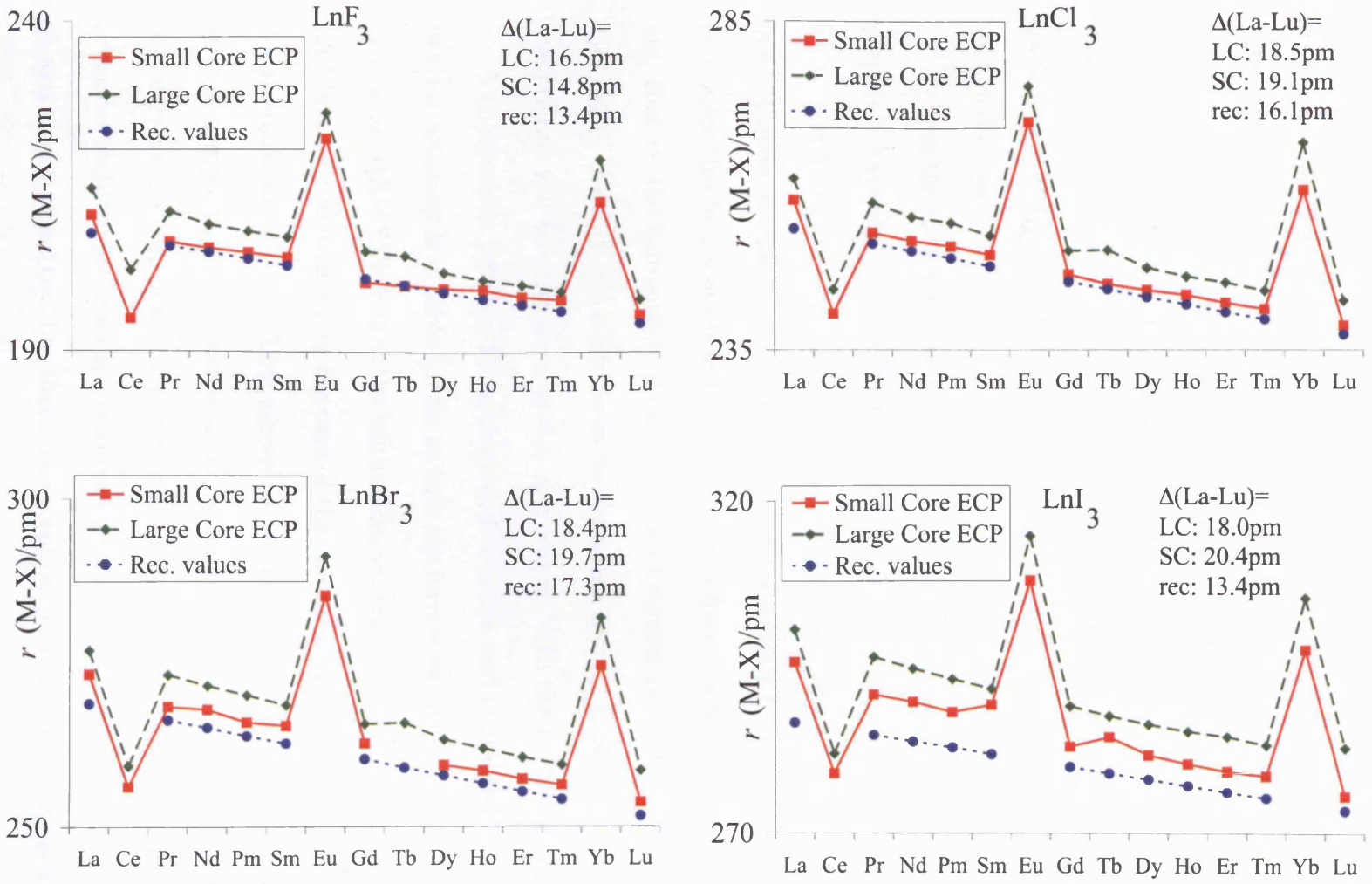

Figure 5.2: Variation of r(Ln-F), r(Ln-Cl), r(Ln-Br) and r(Ln-I) with lanthanide element in LnX_3 (X=F, Cl, Br, I) as predicted by the present calculations, employing SC ECPs, compared with those results from references 170 (LC ECP) and 166 (recommended values).

5.3.2 XMX angle

Table 5.2 and figures 5.3 and 5.4 present the α(XMX) values for LnX_3 calculated using the SC and LC ECPs. Also included in table 5.2 are the corresponding recommended values of Kovács and Konings.[166] Both basis sets predict that many of the calculated structures are pyramidal (α(XMX)<120°), the extent of which depends on the lanthanide, the ligands and the basis set used. There is quite good agreement between some of the SC and LC values of α(XMX), which will be discussed first.

As was the case for r(M-X), both basis sets predict that the charged compounds behave slightly differently to the neutral MX_3. For the negatively charged EuX_3^- and YbX_3^-, the structures are essentially planar. In contrast to the monoanionic compounds, the positively charged CeX_3^+ are strongly pyramidal. A possible reason for this behaviour is in the contributions from the 5d orbitals to the bonding, that is, the compounds show evidence of second order Jahn-Teller (SOJT) distortion. As this also contributes to the more general LnX_3 case, the charged compounds will be considered in the next section with the neutral compounds.

A comparison between the recommended values and computed values for the neutral compounds in table 5.2 shows that the former values form a linear trend of increasing α(XMX) values as the lanthanides are traversed, to a maximum value of 120° (e.g. at promethium in the case of the chlorides) and beyond this, all values are assumed to be 120°. This agrees to a certain extent with the trend in the neutral compounds of Eisenstein et al., although the latter results show greater planarity in the case of the fluorides, and greater pyramidality for the chlorides, bromides and iodides, than the recommended values. The results presented here show a similar trend too, but there are exceptions to this trend that are not found

in either of the other sets of results. Most notably, there is greater pyramidality in GdX_3 in the hydride and the halide cases using the SC lanthanide description, and SmH_3 tends to be more planar. In addition, for the halide cases the early lanthanides presented here show greater planarity than the LC results, such that for the heavier halides (Br, I), the neutral lanthanide compounds of neodymium, promethium and samarium, are planar, in contrast to the LC description, in which the early lanthanides are pyramidal.

Having remarked briefly on some of the aspects of table 5.2, the focus now changes to trying to rationalise these observations. The discussion will be presented in two parts, as the lanthanide trihydrides are considered separately to the lanthanide trihalides. In the discussion of the hydride compounds, the results obtained for the lanthanide series are rationalised using the second-order Jahn-Teller (SOJT) arguments. Then, the discussion of the π-donating halides will be introduced by comparing the lanthanide trihalides with the trihydrides. In addition, the trends for the lanthanide series and for the halide series (F $\rightarrow$ I) are analysed. In both the hydride and halide compounds, the role of the f orbitals is considered and, finally, having presented the arguments, there is a brief summary.

Table 5.2: Comparison of α(XMX)/° for LnX_3 optimised using the SC ECP (in normal text) with the LC ECP results reported in ref 170 (in italics). Values in bold text are taken from ref. 166 and are recommended by the authors on the basis of data obtained from experimental and theoretical studies. *No converged geometry obtained.

	H		F			Cl			Br			I		
La	110.9	*111.1*	115.3	*113.1*	**109.0**	119.4	*116.6*	**118.0**	120.0	*116.2*	**118.0**	120.0	*116.0*	**118.5**
Ce	110.4	*111.7*	110.4	*107.3*		108.4	*104.3*		106.9	*103.7*		104.9	*103.4*	
Pr	111.0	*111.0*	113.8	*113.8*	**110.0**	117.0	*116.9*	**119.0**	118.0	*116.9*	**119.0**	119.1	*116.8*	**119.5**
Nd	112.1	*111.0*	114.9	*114.0*	**110.5**	118.1	*117.0*	**119.5**	120.0	*117.2*	**119.5**	120.0	*117.1*	**120.0**
Pm	111.9	*111.4*	115.5	*114.7*	**111.0**	120.0	*117.3*	**120.0**	120.0	*118.5*	**120.0**	120.0	*117.9*	**120.0**
Sm	119.0	*111.5*	118.4	*115.0*	**111.5**	119.7	*117.5*	**120.0**	120.0	*118.5*	**120.0**	120.0	*118.5*	**120.0**
Eu	120.0	*120.0*	120.0	*120.0*		120.0	*120.0*		120.0	*120.0*		120.0	*120.0*	
Gd	104.4	*112.2*	109.5	*116.2*	**112.5**	112.1	*118.0*	**120.0**	113.5	*118.8*	**120.0**	116.7	*120.0*	**120.0**
Tb	*	*111.3*	116.6	*117.3*	**113.0**	118.3	*118.4*	**120.0**	*	*120.0*	**120.0**	120.0	*120.0*	**120.0**
Dy	112.3	*113.6*	119.1	*117.5*	**113.5**	117.2	*118.5*	**120.0**	119.6	*120.0*	**120.0**	120.0	*120.0*	**120.0**
Ho	115.8	*114.4*	118.6	*117.8*	**114.0**	120.0	*118.8*	**120.0**	120.0	*120.0*	**120.0**	120.0	*120.0*	**120.0**
Er	116.2	*115.2*	118.5	*118.2*	**114.5**	120.0	*120.0*	**120.0**	120.0	*120.0*	**120.0**	120.0	*120.0*	**120.0**
Tm	117.4	*116.3*	120.0	*118.5*	**115.0**	120.0	*119.3*	**120.0**	120.0	*120.0*	**120.0**	120.0	*120.0*	**120.0**
Yb	120.0	*120.0*	120.0	*120.0*		120.0	*120.0*		120.0	*120.0*		120.0	*120.0*	
Lu	117.3	*118.3*	119.2	*119.3*	**116.0**	120.0	*119.7*	**120.0**	120.0	*120.0*	**120.0**	120.0	*120.0*	**120.0**
					(±4°)			**(±2°)**			**(±2°)**			**(±2°)**

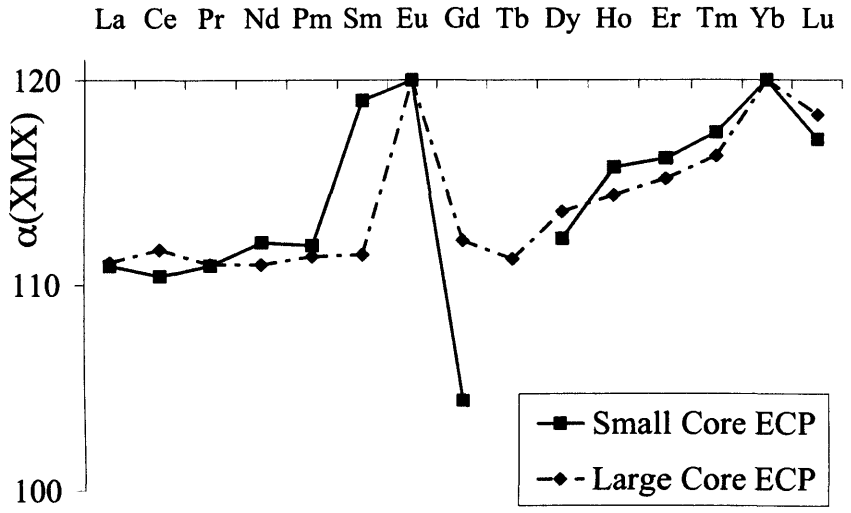

Figure 5.3: Variation of α(HLnH) with lanthanide element in LnH_3 as predicted by the present calculations, employing SC ECPs, compared with those results from reference 170 (LC ECP)

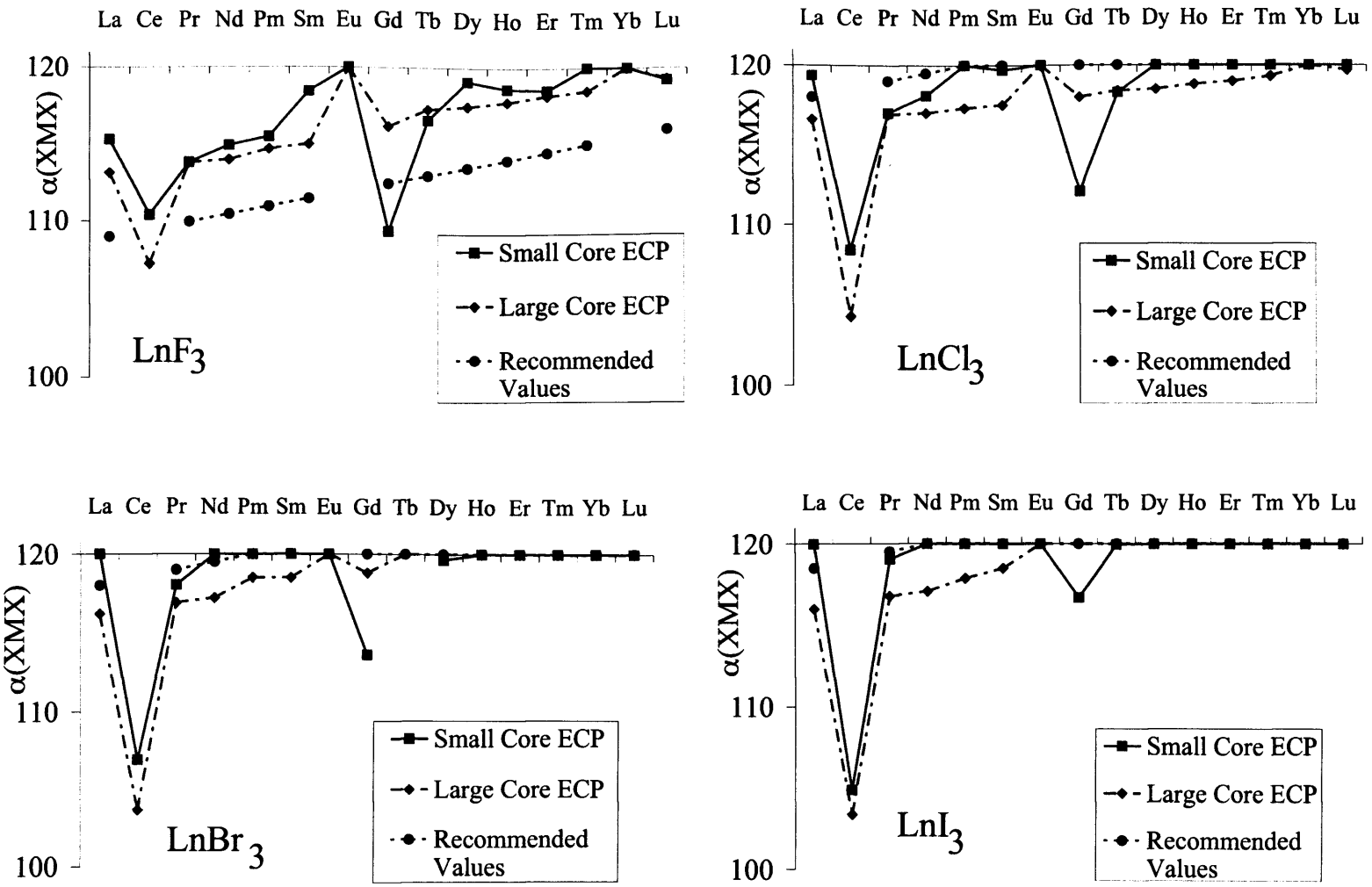

Figure 5.4: Variation of α(FLnF), α(ClLnCl), α(BrLnBr) and α(ILnI) with lanthanide element in LnX_3 (X=F, Cl, Br, I) as predicted by the present calculations, employing SC ECPs, compared with those results from references 170 (LC ECP) and 166 (recommended values).

5.3.2.1 σ-Donating Hydride: Second Order Jahn-Teller (SOJT) Effect in LnH_3

Figure 5.3 and table 5.2 show the variation of α(HLnH) with the lanthanide in LnH_3. Both the LC and SC results predict pyramidality and show a general tendency towards planarity across the lanthanide series. However, the SC results show deviations from this trend (at SmH_3 and GdH_3, in particular), which are absent in the LC results. The second-order Jahn-Teller (SOJT) effect, in conjunction with Natural Bond Orbital (NBO) populations, is now used to rationalise the structures from the SC results.

Table 5.3: Representation of the metal d and ligand σ orbitals in C_{3v} and D_{3h} symmetry.

	D_{3h}	C_{3v}
ligand σ	$a_1'+e'$	a_1+e
metal d_{z^2}	a_1'	a_1
metal d_{xy}, $d_{x^2-y^2}$	e'	e
metal d_{xz}, d_{yz}	e''	e

In d^0 LnX_3 compounds, the formally empty 5d orbitals are sufficiently low-lying in energy that they may become involved in covalent bonding with the surrounding ligands. Table 5.3 shows how the metal d orbitals and the ligand σ orbitals transform in D_{3h} and C_{3v} symmetry. In the D_{3h} trigonal planar structure, the metal d orbitals that can interact with the ligand σ orbitals are the d_{z^2} (a_1'), and the d_{xy} and $d_{x^2-y^2}$ (e') orbitals. By symmetry, the d_{xz} and d_{yz} orbitals are nonbonding, since there is no σ orbital of e'' symmetry. If the structure of LnX_3 is relaxed to a pyramidal structure, the molecular symmetry changes from D_{3h} to C_{3v}, and interactions between the ligand σ orbitals of e symmetry and the metal

$d_{x^2-y^2}$ and d_{xy} orbitals may be enhanced by the previously σ nonbonding d_{xz} and d_{yz} metal orbitals that are now also of e symmetry. Using these arguments, the SOJT distortion in MX_3 refers to the situation in which the D_{3h} structure is distorted to C_{3v} structure, in which greater interaction between the σ orbitals of the ligands and the d orbitals of the metal may occur (see figure 5.5).

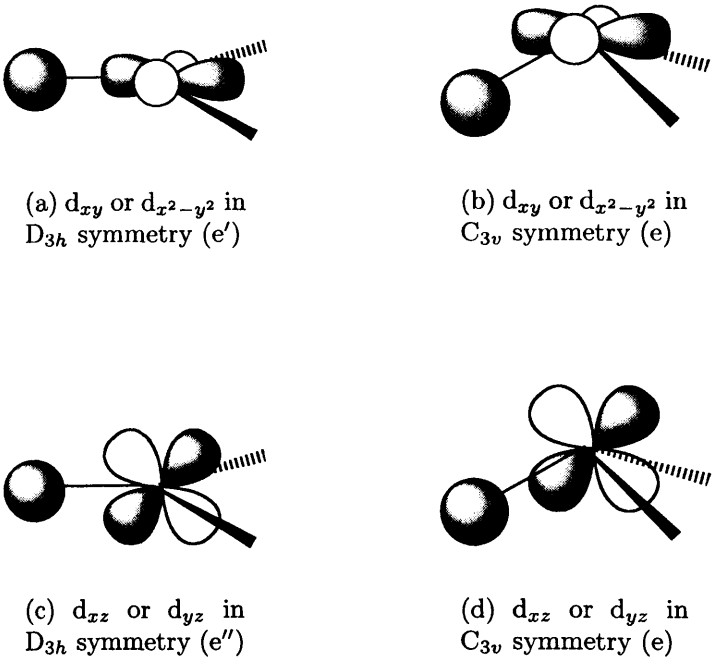

(a) d_{xy} or $d_{x^2-y^2}$ in D_{3h} symmetry (e′)

(b) d_{xy} or $d_{x^2-y^2}$ in C_{3v} symmetry (e)

(c) d_{xz} or d_{yz} in D_{3h} symmetry (e″)

(d) d_{xz} or d_{yz} in C_{3v} symmetry (e)

Figure 5.5: Extent of ligand σ/metal d overlap in D_{3h} and C_{3v} symmetry. For clarity, only the σ contributions from one ligand are shown.

I now turn to the specific case of LnH_3. The Natural Bond Orbital (NBO) metal charges indicate some covalency in the compounds (i.e. the charges differ significantly from their formal values) and the 5d populations from the SC ECP LnH_3 calculations (table 5.4) show that the 5d orbitals do participate in the bonding, and are populated by 0.1-0.8 electrons. The partitioning of the d orbitals into $d_{x^2-y^2}$ and d_{xy}, and d_{xz} and d_{yz} contributions shows that the $d_{x^2-y^2}$ and

d_{xy} orbitals are populated at both the planar and the pyramidal structures, in contrast to $d_{xz} + d_{yz}$ population, which is 0.00 for the planar structures (YbH_3^- and EuH_3^-) and increases as the structures become more pyramidal (0.25 for CeH_3^+ which has α(HCeH)=110.4°). These data are consistent with the symmetry arguments that, in contrast to the D_{3h} structure, at the C_{3v} structure the d_{xz} and d_{yz} orbitals can contribute to the M(d)-X(σ) interactions. Also, the increase in d_{xz}+d_{yz} populations reflects an increase in the total d population, which supports the argument that the D_{3h} to C_{3v} distortion enhances the σ donation from the ligand to the metal d orbitals.

In order to obtain further quantitative support of the SOJT argument, the ratio of d populations defined as:

$$\delta = \frac{d_{xz} + d_{yz}}{d_{x^2-y^2} + d_{xy}}$$

is plotted against HLnH angle in figure 5.6. There is excellent correlation between the HLnH angle and δ (R^2=0.99). For the trigonal planar structures, δ approaches 0.0 and for the pyramidal structures the δ values are much higher. This illustrates that for the case of high relative $d_{xz} + d_{yz}$ populations, there is a strong tendency toward pyramidality, and conversely, low relative $d_{x^2-y^2} + d_{xy}$ values leads to planarity.

Having ascertained how the d orbitals affect the α(XLnX), a question arises; what dictates the relative populations between the two types of d orbitals? One possible answer can be found by noting that apart from the charged compounds (CeX_3^+, EuX_3^- and YbX_3^-), the $d_{x^2-y^2} + d_{xy}$ values are approximately constant (about 0.3), and the $d_{xz} + d_{yz}$ values decrease for the more planar compounds. Alternatively, the greater the total d population, the greater the chance of d_{xz}+d_{yz}

d_{xy} orbitals are populated at both the planar and the pyramidal structures, in contrast to $d_{xz} + d_{yz}$ population, which is 0.00 for the planar structures (YbH_3^- and EuH_3^-) and increases as the structures become more pyramidal (0.25 for CeH_3^+ which has α(HCeH)=110.4°). These data are consistent with the symmetry arguments that, in contrast to the D_{3h} structure, at the C_{3v} structure the d_{xz} and d_{yz} orbitals can contribute to the M(d)-X(σ) interactions. Also, the increase in d_{xz}+d_{yz} populations reflects an increase in the total d population, which supports the argument that the D_{3h} to C_{3v} distortion enhances the σ donation from the ligand to the metal d orbitals.

In order to obtain further quantitative support of the SOJT argument, the ratio of d populations defined as:

$$\delta = \frac{d_{xz} + d_{yz}}{d_{x^2-y^2} + d_{xy}}$$

is plotted against HLnH angle in figure 5.6. There is excellent correlation between the HLnH angle and δ (R^2=0.99). For the trigonal planar structures, δ approaches 0.0 and for the pyramidal structures the δ values are much higher. This illustrates that for the case of high relative $d_{xz} + d_{yz}$ populations, there is a strong tendency toward pyramidality, and conversely, low relative $d_{x^2-y^2} + d_{xy}$ values leads to planarity.

Having ascertained how the d orbitals affect the α(XLnX), a question arises; what dictates the relative populations between the two types of d orbitals? One possible answer can be found by noting that apart from the charged compounds (CeX_3^+, EuX_3^- and YbX_3^-), the $d_{x^2-y^2} + d_{xy}$ values are approximately constant (about 0.3), and the $d_{xz} + d_{yz}$ values decrease for the more planar compounds. Alternatively, the greater the total d population, the greater the chance of d_{xz}+d_{yz}

Table 5.4: NBO lanthanide charges and d populations in LnH_3 using SC ECP to describe the metal centre. *No converged geometry obtained.

	q(Ln)	α(HLnH)/°	d_{total}	$d_{x^2-y^2} + d_{xy}$	$d_{xz} + d_{yz}$	$\frac{d_{xz}+d_{yz}}{d_{x^2-y^2}+d_{xy}}$ (δ)
La	2.05	110.9	0.57	0.33	0.17	0.50
Ce	2.33	110.4	0.78	0.44	0.24	0.54
Pr	1.97	111.0	0.55	0.34	0.16	0.46
Nd	1.97	112.1	0.52	0.34	0.14	0.41
Pm	1.93	111.9	0.48	0.31	0.13	0.40
Sm	1.95	119.0	0.39	0.32	0.02	0.05
Eu	1.26	120.0	0.13	0.11	0.00	0.00
Gd	1.74	104.4	0.42	0.23	0.18	0.80
Tb*						
Dy	1.95	112.3	0.43	0.29	0.10	0.34
Ho	1.92	115.8	0.36	0.27	0.05	0.19
Er	2.01	116.2	0.39	0.30	0.05	0.17
Tm	2.00	117.4	0.35	0.29	0.03	0.10
Yb	1.24	120.0	0.08	0.07	0.00	0.00
Lu	1.79	117.3	0.56	0.46	0.05	0.11

orbitals being populated, and of there being a SOJT effect. Thus, extending this argument to the negatively charged compounds, there is a small d population, so the EuX_3^- and YbX_3^- have planar geometries, and conversely, for the positively charged CeH_3^+ the total d population is 0.8, which leads to significant population of the $d_{xz} + d_{yz}$ orbitals and hence significant pyramidalisation.

Before considering the π donors, there is one aspect of the lanthanide trihydrides still to be considered, and that is whether the f orbitals play a role in determining the structures of the compounds. The NBO populations of the 4f orbitals for LnH_3 are presented in table 5.5. As expected, the 4f population increases across the lanthanide series, from 0 to 14, as the orbitals are gradually filled. However, in almost every case, the actual values differ from that expected from a purely Ln^{3+} ionic viewpoint, an indication that the f orbitals may be

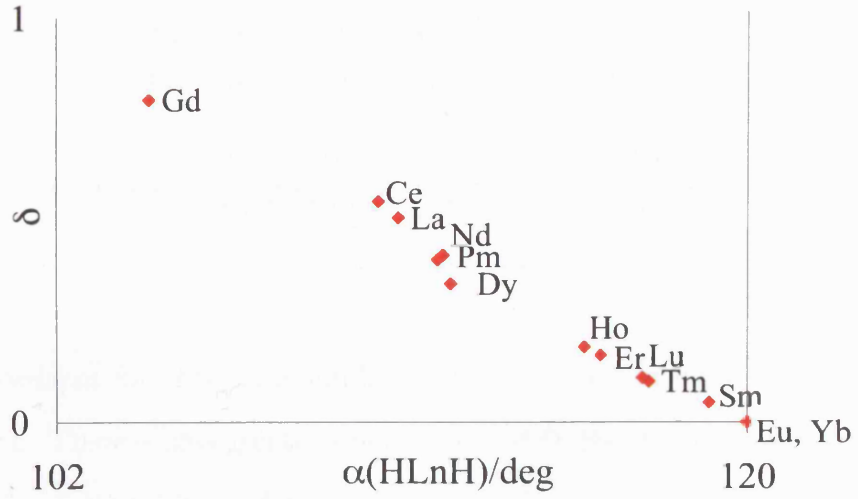

Figure 5.6: Graphical representation of the dependence of α(HLnH) on Natural Bond Orbital d population in LnH_3.

involved in the bonding. Recall that it has been found in the lanthanide diatomics that by including the 4f orbitals in the valence, the 5d participation of the lanthanide is reduced in favour of 4f participation. In the lanthanide trihydrides, the 4f NBO population is greater than the 'core' populations (i.e. $4f^m$ where m is the occupation of the 4f orbitals in the ionic limit). Moreover, this difference is greatest for SmH_3, which has 0.28 electrons over and above the 'core' population of 5.00. This also corresponds to the lowest d participation for the early lanthanides, and, consistent with the SOJT effect, also the most planar neutral early lanthanide compound (α(HSmH)=119.0°).

In contrast to the other lanthanides, in DyH_3 the f population is less than its 'core' population (by 0.4 electrons). This implies that there is a different type

Table 5.5: NBO 4f populations of the lanthanides in LnH_3 using the SC ECP description of the lanthanide.

La	Ce	Pr	Nd	Pm	Sm	Eu
0.06	0.78	2.12	3.13	4.20	5.28	6.99

Gd	Tb	Dy	Ho	Er	Tm	Yb	Lu
7.01		8.62	10.19	11.07	12.11	13.97	14.00

of f involvement for this compound, and is accompanied by a relatively large d population. There is also greater s population of DyH_3, 0.8 compared with 0.4-0.5 for the other lanthanides so, for DyH_3, a better description of the Dy configuration might be $4f^{n-2}s^1$ rather than $4f^{n-1}s^0$. This appears to have only a small effect on the bond angle in the compound, with the angle from the SC calculations slightly smaller than the angle from the LC results.

In fact, GdH_3 also has a relatively high s population of 0.80, but in this case the f orbital has its formal 7.0 electrons, and the high s and f populations are reflected in a less positive charge on the gadolinum centre than for dysprosium. It is not clear from the populations why the gadolinium compound is so pyramidal, but it could be that, although the f orbitals may not be explicitly involved in the bonding, the correlation of the f orbitals, as was discussed in reference 9 and mentioned in section 5.3.1, may be important. By allowing the 4f orbitals in the valence space, there is a greater number of electrons that are correlated. It makes sense that inclusion of more electrons in the valence space could result in the system experiencing greater correlation. Indeed, I have conducted an uncorrelated UHF geometry optimisation and found an almost planar geometry (α(HGdH)=117.9°) for GdH_3.

As a final comparison of how the f electrons affect bonding, the geometries of PmH_3 and HoH_3, an early and a late lanthanide compound that have similar excess f populations, were reoptimised using the large core ECP and basis set used by Eisenstein et al. The optimised PmH_3 and HoH_3 bond angles were found to be 111.4° and 114.6° respectively, consistent with their results. Table 5.6 shows the similarities and differences between the NBO populations using each description. In both the LC and SC calculations, the s and d orbitals are populated. There is less d population in holmium than in promethium using both ECPs, which, in agreement with the SOJT effect, corresponds with a more planar HoH_3 than PmH_3 in both cases.

When the 4f orbitals are considered in the valence, the charge on the metal is reduced, consistent with the reduction of positive charge found by Wang and Schwartz when they included the 4f orbitals in the valence.[172] This may be attributed in part to the increase in the 4f population in the SC compound, relative to the LC compound, although for HoH_3, in which there is a difference in metal charge of 0.5 electrons between SC and LC cases compared with only 0.1 for PmH_3, there is also greater s population in the SC calculation. For the SC results of both PmH_3 and HoH_3, the 4f population exceeds its 'core' population, by about 0.2 electrons. Concurrently, the d orbital populations are slightly lower (by about 0.06 electrons). Thus, consistent with the SOJT effect, there is a slightly more planar geometry when the 4f orbitals are considered in the valence in both PmH_3 and HoH_3 compared with when they are considered in the core description.

The above analysis of the data for LnH_3 suggests that the f electrons do affect the geometry adopted. It is not always obvious how this participation affects the pyramidality, but in many cases, the structures do become slightly more pyram-

Table 5.6: NBO populations of PmH_3 and HoH_3 using both LC and SC ECPs and basis sets.

	Large Core Lanthanide				Small Core Lanthanide				
	α(HLnH)/°	q(M)	p(s)	p(d)	α(HLnH)/°	q(M)	p(s)	p(d)	p(f)
PmH_3	111.4	2.06	0.48	0.53	111.9	1.93	0.40	0.48	4.20
HoH_3	114.4	2.46	0.12	0.43	115.8	1.92	0.53	0.36	10.19

idal when the 4f orbitals are placed in the core; the slight increase in f population relative to the 'core' 4f population appears to lower the d populations of the lanthanide resulting in slightly more planar structures. For SmH_3, there is a noticeably high 4f population, which also corresponds to an almost planar structure (α(HSmH)=119.0°). There is a notable effect of the valence 4f orbitals in GdH_3, despite the 4f population being approximately equal to the 'core' population; the structure is significantly more pyramidal using the SC ECP description, possibly because the f electrons are correlated, since UHF predicts a much more planar structure. Thus, it is not completely satisfactory to assume that the f orbitals are completely inactive in determining the geometry of LnH_3.

5.3.2.2 π-Donating Halides: π-Effects in LnX_3 (X=F, Cl, Br, I)

Having considered the σ interactions in the lanthanide trihydrides, the next step is to consider the effect of having possible π donations from the halide ligands. Figures 5.3 and 5.4 show that, in general, the halides are more planar than the hydrides, particularly in the case of the heavier halides. This is consistent with Eisenstein et al.'s study, where they attributed the greater planarity to the π interactions, and stated that increased covalency for the heavier halogens gives greater π interactions and a greater tendency to planarity.

From table 5.7, it can be seen that, similar to the hydrides, all of the lanthanides in the halides have a charge of less than three. This indicates that there is some covalency in the compounds. There is also a clear decrease in the charge from the fluoride to the iodide compounds, suggesting an increase in covalency going down the halogen series.

Table 5.7: NBO charges of the lanthanides in LnX_3 (X=F, Cl, Br, I) using the SC ECP description of the lanthanide. *No converged geometry obtained.

	X=F	X=Cl	X=Br	X=I
La	2.47	2.27	2.23	2.11
Ce	2.85	2.31	2.18	2.01
Pr	2.42	2.22	2.17	2.04
Nd	2.46	2.25	2.12	2.02
Pm	2.49	2.26	2.18	2.03
Sm	2.51	2.26	2.15	1.96
Eu	1.81	1.72	1.68	1.61
Gd	2.45	2.12	2.01	1.96
Tb	2.53	2.29	*	1.98
Dy	2.54	2.28	2.18	2.03
Ho	2.59	2.32	2.22	2.06
Er	2.56	2.33	2.22	2.06
Tm	2.61	2.33	2.22	2.04
Yb	1.83	1.72	1.67	1.59
Lu	2.30	1.76	1.54	1.23

Recall the SOJT effect that was invoked to rationalise the HLnH angle in the lanthanide trihydrides. In D_{3h} symmetry, of the low-lying d orbitals of the lanthanides, $d_{x^2-y^2}$ and d_{xy} can form σ bonds with the ligands. However, in C_{3v} symmetry, d_{xz} and d_{yz} can also interact in a σ manner with the ligands, so greater d_{xz} and d_{yz} participation from the lanthanide can lead to greater pyramidalisation. In the case of the halides, there are potentially additional π interactions. Table 5.8 shows the representations of the ligand σ, π and metal d orbitals. It is clear that

Table 5.8: Representations of the metal d and ligand σ and π orbitals in C_{3v} and D_{3h} symmetry.

	D_{3h}	C_{3v}
ligand σ	$a_1'+e'$	a_1+e
ligand $\pi_{in-plane}$	$a_2'+e'$	a_2+e
ligand $\pi_{out-of-plane}$	$a_2''+e''$	a_1+e
metal d_{z^2}	a_1'	a_1
metal d_{xy}, $d_{x^2-y^2}$	e'	e
metal d_{xz}, d_{yz}	e''	e

in D_{3h} symmetry, the σ nonbonding d_{xz} and d_{yz} orbitals can participate in a metal-ligand π bond (with the π MOs that are out of the plane of the molecule), so population of these orbitals does not necessarily result in pyramidalisation of the compound, but might be a result of π interactions at the planar geometry. Thus, unlike for the hydrides, the lanthanide $d_{xz}+d_{yz}$ populations for the halides should never be exactly 0.0, even at α(XLnX)=120° (table 5.9).

The potential for π effects therefore introduces a complication when applying NBO-based analyses, as there is no easy way of decoupling the σ and π effects in terms of the d populations. Indeed, a plot of the δ $(\frac{d_{xz}+d_{yz}}{d_{x^2-y^2}+d_{xy}})$ against α(XLnX) shows as planarity is approached (figure 5.7), there is little correlation between the δ and the bond angle (in contrast to the high angle region of figure 5.6). Conversely, for the more pyramidal structures, there does seem to be some correlation in these variables (figure 5.8), indicating that the σ factors present in the hydrides may also influence the bond angle in the more pyramidal halides, and that the π interactions might only dominate at the near-planar structures.

Table 5.9: NBO populations of the lanthanides in LnX_3 (X=F, Cl, Br, I) using the SC ECP description of the lanthanide. *No converged geometry obtained.

	X=F			X=Cl			X=Br			X=I		
	d_t	$d_{x^2-y^2}+d_{xy}$	$d_{xz}+d_{yz}$	d_t	$d_{x^2-y^2}+d_{xy}$	$d_{xz}+d_{yz}$	d_t	$d_{x^2-y^2}+d_{xy}$	$d_{xz}+d_{yz}$	d_t	$d_{x^2-y^2}+d_{xy}$	$d_{xz}+d_{yz}$
La	0.33	0.17	0.11	0.49	0.29	0.14	0.52	0.31	0.15	0.60	0.35	0.18
Ce	0.45	0.21	0.18	0.76	0.36	0.29	0.82	0.39	0.32	0.89	0.42	0.35
Pr	0.34	0.18	0.12	0.51	0.29	0.15	0.54	0.32	0.16	0.60	0.36	0.18
Nd	0.35	0.18	0.12	0.50	0.29	0.15	0.48	0.31	0.13	0.56	0.35	0.16
Pm	0.34	0.18	0.12	0.49	0.29	0.14	0.51	0.31	0.15	0.57	0.34	0.17
Sm	0.33	0.19	0.10	0.47	0.28	0.13	0.48	0.29	0.13	0.48	0.30	0.14
Eu	0.15	0.09	0.04	0.18	0.11	0.04	0.18	0.11	0.04	0.19	0.12	0.05
Gd	0.34	0.17	0.14	0.46	0.25	0.16	0.47	0.27	0.16	0.58	0.34	0.19
Tb	0.36	0.19	0.12	0.51	0.29	0.16		*		0.51	0.31	0.16
Dy	0.34	0.19	0.10	0.48	0.29	0.14	0.50	0.31	0.15	0.56	0.34	0.17
Ho	0.33	0.18	0.10	0.47	0.29	0.14	0.50	0.30	0.15	0.56	0.34	0.17
Er	0.32	0.16	0.11	0.46	0.28	0.14	0.49	0.30	0.15	0.55	0.33	0.17
Tm	0.32	0.18	0.10	0.45	0.26	0.14	0.47	0.28	0.15	0.51	0.30	0.16
Yb	0.13	0.08	0.04	0.14	0.09	0.03	0.14	0.09	0.03	0.15	0.09	0.04
Lu	0.62	0.36	0.20	0.97	0.56	0.34	1.09	0.64	0.38	1.28	0.76	0.44

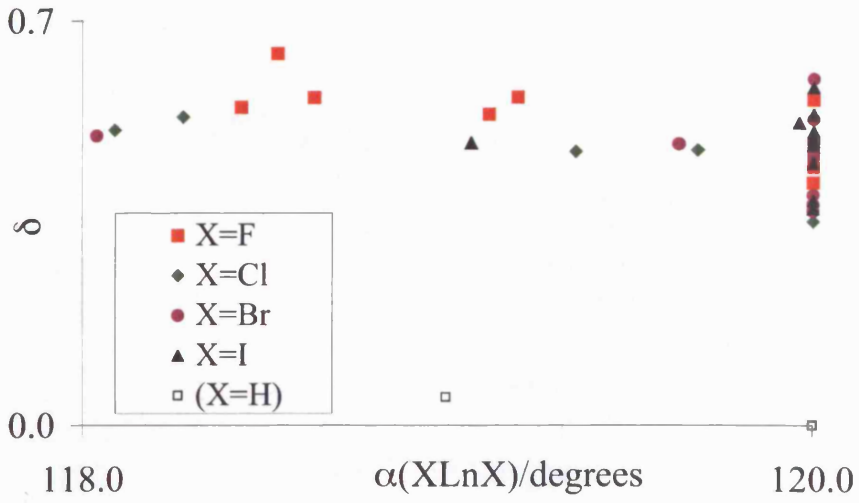

Figure 5.7: Graphical representation of the dependence of α(XLnX) on Natural Bond Orbital d population in LnX_3 (X=F, Cl, Br, I) and selected LnH_3 values are included for comparison. $118° < \alpha(XLnX) \leq 120°$.

It is expected that the fluorides will exhibit the smallest π effects, and hence that the SOJT σ arguments will be more applicable than for the heavier halogens. Figure 5.9 suggests that this is indeed the case, with a reasonable correlation between δ and bond angle.

For almost all of the lanthanide chlorides, bromides and iodides, the compounds are planar, and only CeX_3^+ and GdX_3 differ significantly from this. For the former, the strong pyramidality corresponds to a very high d population, which indicates that, in this compound, the SOJT distortion may be present, and that it overshadows the π interactions. This is supported by the fact that both the SC and LC ECPs predict the same pyramidality. The reason for the pyramidality

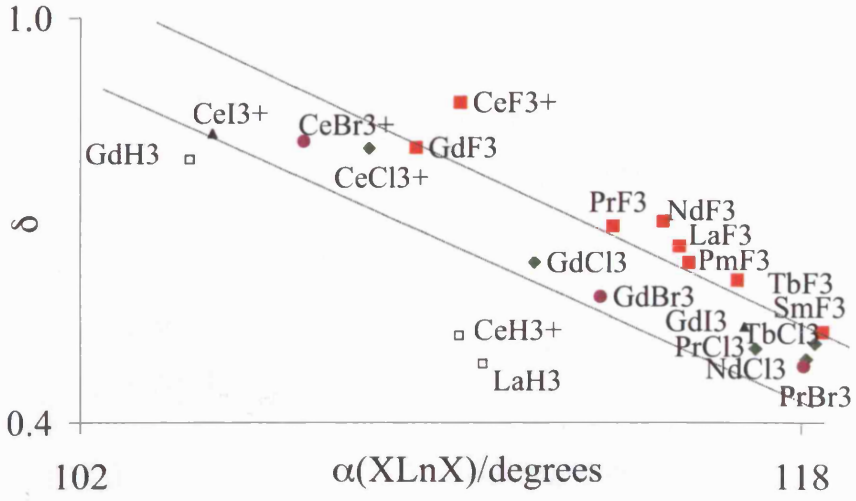

Figure 5.8: Graphical representation of the dependence of α(XLnX) on Natural Bond Orbital d population in LnX_3 (X=F, Cl, Br, I) and selected LnH_3 values are included for comparison. $\alpha(XLnX) \leq 118°$ (The lines indicate the separation between the points that correspond to the LnH_3 data, the similar $LnCl_3$, $LnBr_3$ and LnI_3 data, and the LnF_3 data.).

for the gadolinium compounds using the SC ECP and basis set is less clear, but, as was discussed for the case of the hydrides, the fact that this strong pyramidalisation is not seen in the LC results suggests that the f orbitals play a role; UHF calculations using the SC ECPs and basis sets optimise the geometries of all of the gadolinum halides to planar structures, which supports the explanation that the correlation of the f electrons is important.

Apart from the strong pyramidality of GdX_3, present for all of the halides, there is one other interesting aspect in the comparison of the SC and LC ECP results; the early lanthanide results from Eisenstein et al. show greater pyram-

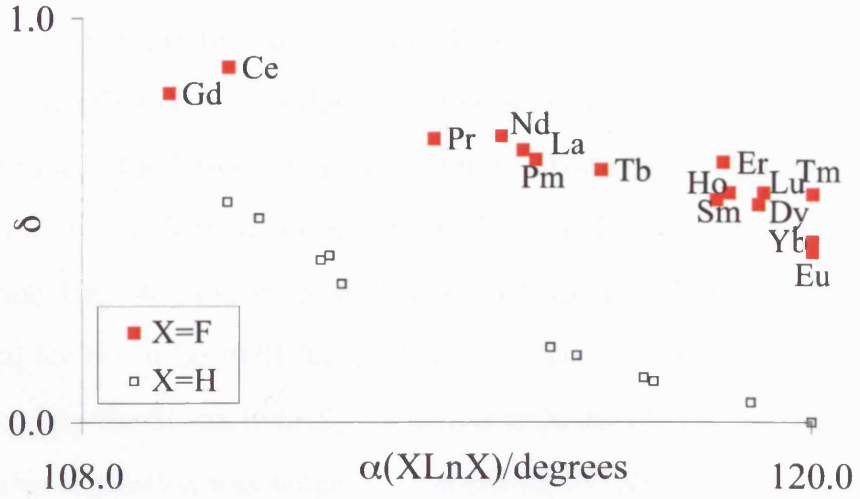

Figure 5.9: Graphical representation of the dependence of α(FLnF) on Natural Bond Orbital d population in LnF_3.

idality than the SC results, but both sets of data show strong planarity for the later lanthanides. So while the SC ECP results suggest planarity for almost all of the compounds of the chlorides, bromides and iodides, there is a more gradual tendency to planarity as the lanthanides are traversed using the LC ECPs.

Table 5.10 shows the NBO f populations for the lanthanide trihalides using the SC ECP and basis sets. Again, as was the case for the hydrides, the 4f population increases across the lanthanide series as the orbitals are gradually filled. Also in agreement with the hydrides, the f populations, in general, do not match exactly the formal f occupations, suggesting some involvement of the f orbitals in the halide compounds. For DyX_3 and TbX_3, the f populations are less than the 'core' 4f populations by 0.4-0.6. As was the case of DyH_3, this is accompanied

by a relatively larger s population compared with the other neutral compounds (0.6-0.8 compared with 0.0-0.3), so again a lanthanide configuration of $4f^{n-2}s^1$ may be more appropriate, especially for TbF_3, which has NBO values of $4f^{7.4}s^{0.7}$. However, any effect of this on the structures is negligible.

One trend in the NBO 4f populations in the lanthanide trihalides that is not clear in the lanthanide trihydrides, is that while for the early lanthanides, there is a reasonably large 4f population relative to the 'core' populations (0.14-0.31), this is reduced for Ho to Lu (0.01-0.07). This may account for the greater planarity experienced by the SC early LnX_3 compared with the LC results. Further evaluation of this suggestion was sought by comparing the NBO populations of PmX_3 and HoX_3 using both ECPs, which are given in table 5.11.

Table 5.10: NBO 4f populations of the lanthanides in LnX_3 (X=H, F, Cl, Br, I) using the SC ECP description of the lanthanide. *No converged geometry obtained.

	H	F	Cl	Br	I
La	0.06	0.19	0.18	0.15	0.13
Ce	0.78	0.69	0.86	0.87	0.89
Pr	2.12	2.20	2.17	2.16	2.15
Nd	3.13	3.18	3.15	3.27	3.21
Pm	4.20	4.14	4.14	4.15	4.16
Sm	5.28	5.14	5.16	5.21	5.31
Eu	6.99	6.98	7.00	7.00	7.00
Gd	7.01	6.90	6.97	6.99	7.03
Tb	*	7.41	7.47	*	7.65
Dy	8.62	8.51	8.55	8.57	8.57
Ho	10.19	10.04	10.04	10.05	10.04
Er	11.07	11.07	11.04	11.04	11.03
Tm	12.11	12.02	12.03	12.04	12.07
Yb	13.97	13.92	13.98	13.99	13.99
Lu	14.00	14.01	14.01	14.01	14.01

For the trihalides, as was also noted for the hydrides, in both the LC and SC calculations the s and d orbitals are populated. In addition, the SC description predicts a lower charge on the metal than the LC description. This effect is more pronounced in HoX_3 for the heavier halogens, and is consistent with the additional differences in the s populations between SC and LC holmium, as was found for HoH_3, also. Turning to the d populations, it is notable that for the LC results, there are lower d populations in holmium than in promethium, particularly for the heavier halides, in agreement with the greater planarity in HoX_3. However, the SC d populations for HoX_3 and PmX_3 agree to within 0.02 electrons, and the bond angles are all equal to 120° (except for the fluorides). The different Ho/Pm d populations found from the SC and LC calculations accounts for the fact that while for the LC ECP, HoX_3 is more planar than PmX_3, using the SC ECP, the angles are equal. Also note that for the heavier halides, the SC d populations match the LC d populations of HoX_3 more closely than PmX_3, suggesting that the higher d population calculated for PmX_3 using the LC accounts for the smaller bond angle found using this approach.

Although I have attributed the greater planarity of the lanthanide trihalides compared with the lanthanide trihydrides to π interactions, increasing from the fluorides to the iodides, so far I have made no attempt to distinguish between competing σ interactions that lead to pyramidalisation and π interactions that lead to planarity. In the context of including the 4f orbitals in the valence region, this also means that $M(f_\pi)$-$X(p_\pi)$ interactions have not explicitly been considered. The total halide p_σ and p_π NBO populations of PmX_3 and HoX_3, presented in table 5.12, are now discussed in this context.

Both the LC and SC results show a slight decrease in both the halide p_σ and

Table 5.11: NBO lanthanide populations in PmX_3 and HoX_3 (X=F, Cl, Br, I) using both LC and SC ECPs and basis sets.

	Large Core Lanthanide				Small Core Lanthanide				
	α(XLnX)/°	q(M)	p(s)	p(d)	α(XLnX)/°	q(M)	p(s)	p(d)	p(f)
PmF_3	114.8	2.61	0.03	0.38	115.5	2.49	0.02	0.34	4.14
HoF_3	118.0	2.65	0.01	0.35	118.6	2.59	0.03	0.33	10.04
$PmCl_3$	117.9	2.35	0.09	0.55	120.0	2.26	0.08	0.49	4.14
$HoCl_3$	120.0	2.47	0.03	0.49	120.0	2.32	0.12	0.47	10.04
$PmBr_3$	118.6	2.26	0.14	0.59	120.0	2.18	0.12	0.51	4.15
$HoBr_3$	120.0	2.42	0.04	0.52	120.0	2.22	0.19	0.50	10.05
PmI_3	119.8	2.11	0.21	0.66	120.0	2.03	0.20	0.57	4.16
HoI_3	120.0	2.33	0.06	0.58	120.0	2.06	0.28	0.56	10.04

the p_π populations from the fluoride to the iodide compounds, suggesting that there is an increase in covalency for the heavier halides. The LC results show that as the angle increases from PmX_3 to HoX_3, there is very little change in the X p_π populations but the X p_σ populations increase for the heavier halogens, suggesting comparable π but less σ donation from the ligand to the metal in HoX_3. On the other hand, except for a slightly lower X p_π in PmX_3 than in HoX_3 for the lighter halogens, the SC results show little variation in either populations, which is consistent with the similar bond angles for PmX_3 and HoX_3.

Comparing the SC results with the LC results shows that in the former there are slightly smaller X p populations, consistent with increased covalency and the slightly lower lanthanide charges in the SC results in table 5.11. This is especially apparent for the holmium X p_σ results, which are smaller in the SC case, and this difference is most apparent for the heavier halides. This indicates that the σ donation from the ligand to the lanthanide is stronger in the SC case. So, despite similar HoX_3 bond angles between the LC and SC results, the X p data suggest

Table 5.12: NBO X(p) populations in PmX_3 and HoX_3 (X=F, Cl, Br, I) using both LC and SC ECPs and basis sets.

	Large Core Lanthanide		Small Core Lanthanide	
	X $p(p_\sigma)$	X $p(p_\pi)$	X $p(p_\sigma)$	X $p(p_\pi)$
PmF_3	5.82	11.79	5.78	11.73
HoF_3	5.84	11.80	5.82	11.78
$PmCl_3$	5.69	11.67	5.66	11.63
$HoCl_3$	5.75	11.69	5.68	11.68
$PmBr_3$	5.64	11.63	5.61	11.59
$HoBr_3$	5.73	11.66	5.63	11.62
PmI_3	5.56	11.57	5.54	11.52
HoI_3	5.69	11.60	5.54	11.56

that in the LC case, the planarity of HoX_3 may simply be due to the reduction in the σ SOJT effect in HoX_3 relative to PmX_3 rather than an increase in π interactions. In contrast, in the SC case the X p_σ populations are similar in both PmX_3 and HoX_3.

Since PmX_3 are more planar when the 4f orbitals are in the valence region, it is interesting to compare the ligand p populations between the LC and SC results. Based on the significance of the a_2' MO in $LnCp_3$ and $AnCp_3$ in previous studies,[20,34–37] the greater planarity in the SC PmX_3 might be expected to result from M(f_π)-X(p_π) interactions. A comparison of the X(p) data for the SC and LC PmX_3 shows there are slightly lower X(p_σ) and X(p_π) populations in the former, indicating that there may be greater σ and π interactions due to the 4f orbitals, although the differences in the populations are relatively small. Therefore, it is difficult to ascertain from these X(p) populations whether the greater planarity in the SC PmX_3 compared with the LC analogues is due to an electronic rearrangement within the lanthanide 5d and 4f orbitals leading to reduced d population and hence greater planarity, or due to direct Ln(f_π)-X(p_π) interactions, which would

also lead to greater planarity.

5.3.2.3 Summary

The extent of pyramidality in LnH_3 shows strong correlation with the 5d population of the lanthanides. More specifically, greater $d_{xz} + d_{yz}$ population relative to $d_{x^2-y^2} + d_{xy}$ correlates with greater pyramidality, suggesting that a second order Jahn-Teller effect mechanism is operating. For the π-donating lanthanide trihalides, $M(d_\pi)$-$X(p_\pi)$ interactions lead to greater planarity, except for the positively charged CeX_3^+, in which the σ interactions dominate, and strongly pyramidal structures are seen.

The 4f orbitals have been shown to affect the XLnX bond angle in LnX_3, in general resulting in slightly greater planarity. When the 4f orbitals are included in the valence, the population of the 5d orbitals is slightly lowered in favour of an increase of the 4f orbital population, which leads to a slightly greater tendency to planarity than is the case when the 4f orbitals are frozen in the core. This is especially evident for SmX_3, and provides an explanation as to why the early lanthanide trichlorides, tribromides and triiodides are more planar when the f orbitals are in the valence region. GdX_3 (X=H, F, Cl, Br, I), however, is exceptional since it is more pyramidal using the SC ECPs than the LC ECPs. UHF geometry optimisations give much larger α(XGdX), which suggests that correlation of the 4f electrons is important.

Halogen p populations from LnX_3 indicate that the increased planarity of HoX_3 compared with PmX_3 using the LC description is due to a reduction in σ interactions for the heavier halogens. This contrasts to the SC description, in which PmX_3 and HoX_3 are both planar, and have comparable $X(p_\sigma)$ populations.

Comparison of the LC and SC halogen p populations for PmX_3 do not conclusively show whether the increased planarity using the SC description of the lanthanide is a result of $Ln(f_\pi)$-$X(p_\pi)$ interactions or due to electronic rearrangement within the lanthanide d and f orbitals.

Further discussion of the presence of $Ln(f_\pi)$-$X(p_\pi)$ interactions is postponed until section 5.5, in which π MOs of NdX_3 featuring f orbitals are presented. Comparison of NdX_3 with the actinide analogues, UX_3 are also made.

5.4 Results and Discussion: Actinide Results

Having examined the pyramidality in the trivalent lanthanides, this study was extended to the trivalent actinides. The AnX_3 (X=H, F, Cl, Br, I) optimised geometries are presented and discussed, and comparison is made with the analogous lanthanide structures.

5.4.1 r(M-X)

The metal-ligand bond lengths from the AnX_3 geometry optimisations are presented in table 5.13 and in figures 5.10 and 5.11. As was the case for the lanthanides, the positively charged ThX_3^+ has shorter bond lengths than its neutral counterparts, consistent with the smaller ionic radius of the +4 ion compared with the +3 ion, and conversely the negatively charged AmX_3^- and NoX_3^- have longer bond lengths.

The general variation of bond length across the 5f series clearly demonstrates the actinide contraction, which is calculated to be larger than the lanthanide contraction by 3-8 pm depending on the ligand. This has been noted previously and attributed to relativistic effects, which contract the ns shell more than if only ineffective shielding of the nucleus by the $(n-2)$f shell were considered.[10,182] Laerdahl et al. found that, for the lanthanide and actinide trihydrides at the nonrelativistic level, the lanthanide and actinide contractions are equal. Inclusion of relativity, however, leads to a bigger actinide than lanthanide contraction, with relativity contributing to 25% of the lanthanide contraction of the trihydrides, compared with 50% of the equivalent actinide contraction.[9]

Table 5.13: r(M-X)/pm for AnX_3 and LnX_3 (X=H, F, Cl, Br, I). The actinide values are given in normal font and the corresponding lanthanides are given in italics. Δ=r(La-X)/pm-r(Lu-X)/pm and Δ=r(Ac-X)/pm-r(Lr-X)/pm for the lanthanides and actinides respectively. These values are a measure of the lanthanide or actinide contraction in the specific compounds. *No converged geometry obtained.

	H		F		Cl		Br		I	
Ac/La	218.4	*208.1*	218.8	*210.4*	267.9	*257.7*	283.6	*273.4*		*295.9*
	221.5[1]	*211.1*[1]								
Th/Ce	198.0	*190.8*	201.7	*194.9*	246.7	*240.5*	262.2	*256.2*	284.6	*278.9*
Pa/Pr	202.5	*203.4*	205.3	*207.0*	252.8	*252.7*	269.3	*268.5*	292.6	*291.9*
U/Nd	204.8	*202.4*	206.6	*205.6*	253.2	*251.5*	269.7	*268.0*	292.7	*289.9*
Np/Pm	202.9	*202.2*	207.8	*204.9*	252.0	*250.6*	268.1	*266.0*	290.7	*288.3*
Pu/Sm	201.7	*204.2*	206.8	*204.1*	251.5	*249.3*	266.7	*265.5*	289.5	*289.5*
Am/Eu	222.7	*226.5*	216.2	*222.1*	268.8	*269.6*	284.5	*285.3*	307.3	*308.1*
Cm/Gd	199.9	*198.7*	206.2	*200.5*	249.8	*246.4*	265.1	*262.7*	287.3	*283.1*
Bk/Tb	198.2	*	204.5	*200.0*	248.3	*245.0*	264.0	*	286.2	*284.5*
Cf/Dy	197.2	*197.1*	203.9	*199.7*	247.1	*243.7*	262.4	*259.3*	284.5	*281.7*
Es/Ho	195.5	*198.5*	202.1	*199.5*	246.1	*243.3*	260.8	*258.5*	283.3	*280.4*
Fm/Er	197.3	*195.6*	201.1	*198.4*	244.4	*242.2*	259.9	*257.3*	282.7	*279.2*
Md/Tm	202.9	*195.6*	202.1	*198.0*	246.4	*241.2*	262.2	*256.4*	290.6	*278.6*
No/Yb	217.4	*215.9*	218.0	*212.7*	261.9	*259.1*	277.0	*274.9*	299.3	*297.6*
Lr/Lu	195.2	*193.1*	200.9	*195.6*	243.2	*238.6*	258.4	*253.7*	280.6	*275.5*
	193.4[1]	*192.2*[1]								
Δ	23.2	*15.0*	17.8	*14.8*	24.7	*19.1*	25.2	*19.7*		*20.4*
	28.1[1]	*18.9*[1]								

[1] data computed using relativistic MP2, taken from reference 9

As was the case for the lanthanide contraction, the present results reveal a dependence of the contraction on the ligand. For the case of the halides, there is an increase in the actinide contraction for the heavier halogens, and, in a similar manner to the lanthanides, this corresponds to an increase in the s population of

the actinide centre (e.g. the s populations for AcF_3 and LrF_3 are 0.03 and 0.12 respectively compared with 0.13 and 0.38 for $AcBr_3$ and $LrBr_3$).

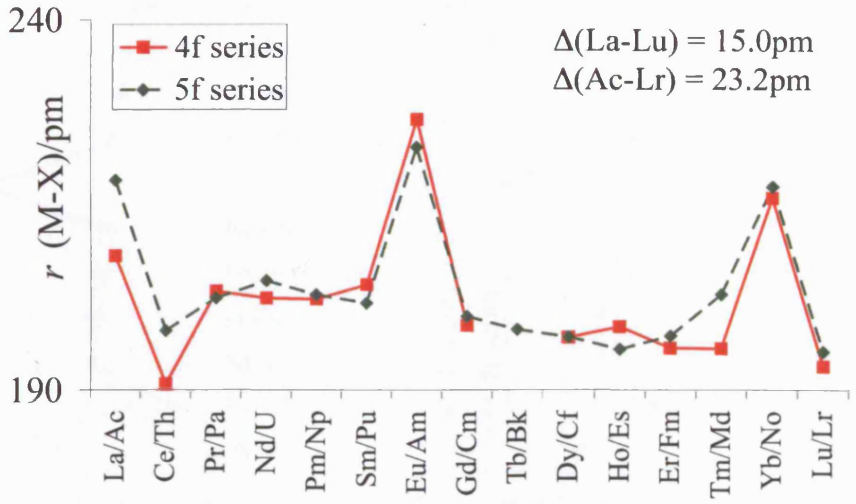

Figure 5.10: Variation of r(An-H) with actinide element in AnH_3 as predicted by the present calculations, compared with r(Ln-H) in LnH_3.

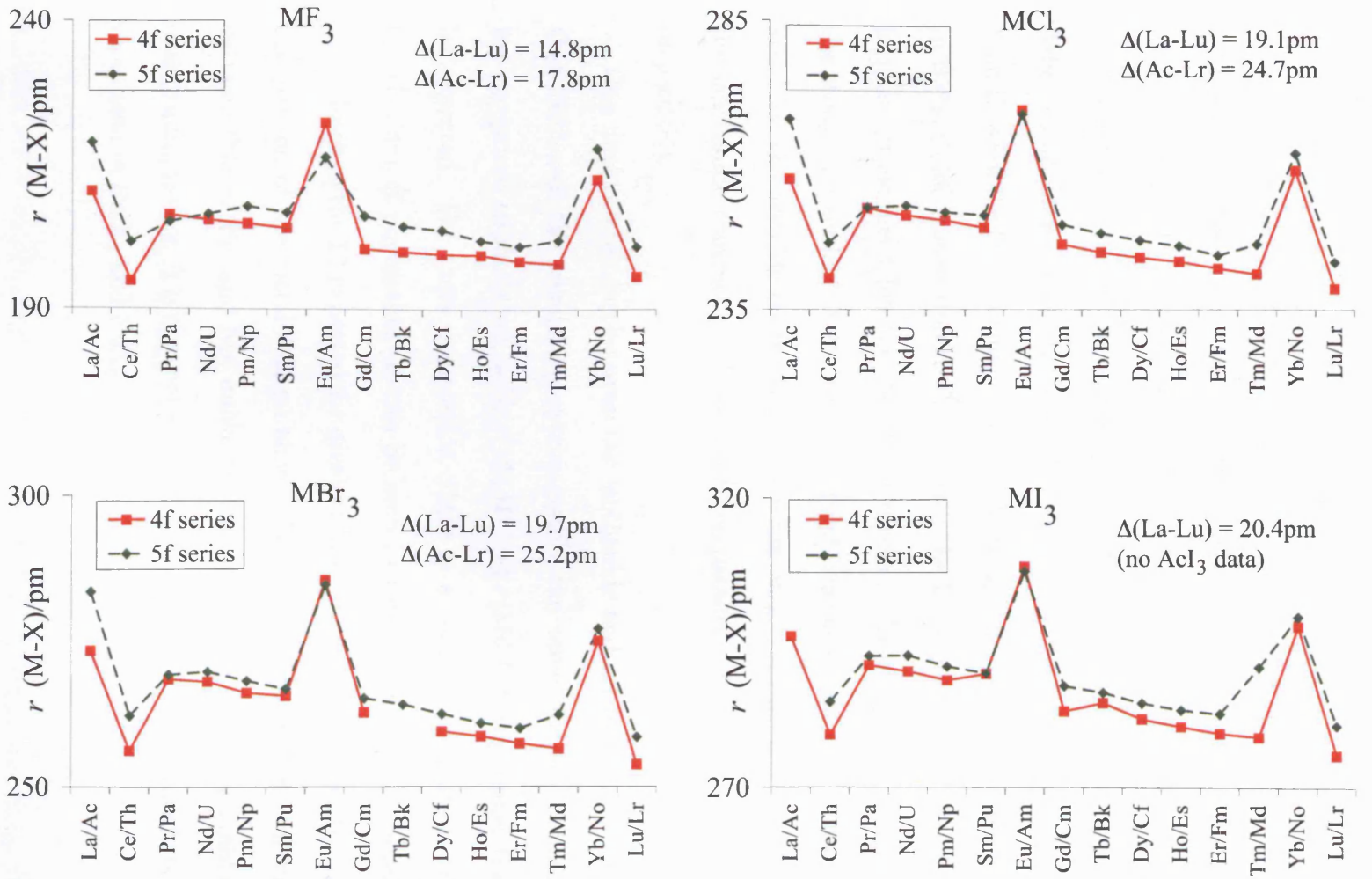

Figure 5.11: Variation of r(An-X) (X=F, Cl, Br, I) with actinide element in AnH_3 as predicted by the present calculations, compared with r(Ln-X) in LnX_3. No value of the actinide contraction for the AnI_3 compounds could be obtained since the geometry of AcI_3 failed to converge.

Interestingly, for the trihydrides, r(An-H) is comparable with r(Ln-H), for most of the compounds, with the exception of actinium and thorium, which have slightly longer bond lengths than lanthanum and cerium. The values for MH_3 from reference 9 similarly show that r(La-H) is 10 pm shorter than r(Ac-H), compared with a difference of only 1 pm for r(Lu-H) and r(Lr-H), and are consistent with the greater actinide contraction compared with the lanthanide contraction. For the halide compounds, however, the actinide bond lengths are almost always longer than those of the lanthanides, such that, although the halides do show an increase in the actinide contraction compared with the lanthanide contraction, the effect is more pronounced for the metal trihydrides. Again, this is consistent with the study by Laerdahl et al., whose calculations show that for the diatomic MF and MH, the actinide contraction is 14.6 pm and 20.4 pm respectively, whereas the lanthanide contractions have more comparable values of 12.2 and 12.3 pm respectively.

One final comparison between the lanthanide and actinide compounds shows that, although the trends are approximately the same, for the actinides there are exceptions to the trend, with r(Md-H) and r(Md-I) being longer than would be expected. For these compounds, there is a high 5f population relative to the thulium 4f population, as can be seen in table 5.14. The 5f population is 12.7, closer to the 13 expected for divalent Md^{2+} than the 12 expected for Md^{3+}. Comparison of the metal charges shows that the charge on Md is intermediate between that of Fm and No, unlike the charge on Tm, which resembles the Er charge quite closely. It is thus not surprising that r(Md-X) is intermediate between those seen in FmX_3 and NoX_3^-.

Table 5.14: 5f (4f) NBO populations in FmX_3 (ErX_3), MdX_3 (TmX_3), and NoX_3^- (YbX_3^-).

	ErX_3	TmX_3	YbX_3^-	FmX_3	MdX_3	NoX_3^-
X=H:						
f pop.	11.07	12.11	13.97	11.32	12.68	13.98
q(M)	2.01	2.00	1.24	1.79	1.56	1.17
X=I:						
f pop.	11.03	12.07	13.99	11.26	12.73	13.99
q(M)	2.06	2.04	1.59	1.92	1.67	1.53

5.4.2 XMX Angle

The XAnX angles from the AnX_3 geometry optimisations are presented in table 5.15 and in figures 5.12 and 5.13. As was the case for the lanthanides, the positively charged ThX_3^+ exhibits quite a pyramidal structure, especially for the heavier halides, and the negatively charged AmX_3^- and NoX_3^- exhibit planar structures, although AmF_3^- is an exception. Also notable is the pronounced pyramidality of CmX_3, as was found for GdX_3.

One striking difference between the actinide and lanthanide compounds is the greater tendency to pyramidal structures in the actinides compared with the lanthanides. I will now attempt to rationalise this difference, first by considering the applicability of the second order Jahn-Teller (SOJT) effect to the actinide compounds, and then by considering the role of π interactions in the actinide and lanthanide trihalides. In addition, a comparison between the valence molecular orbitals of one lanthanide and one actinide compound is presented in an attempt to gain further insight into the bonding.

Table 5.15: α(XMX)/° for AnX_3 and LnX_3 (X=H, F, Cl, Br, I). The actinide values are given in normal font and the corresponding lanthanides are given in italics. *No converged geometry obtained.

	H		F		Cl		Br		I	
Ac/La	106.2	*110.9*	111.2	*115.3*	117.0	*119.4*	117.8	*120.0*		*120.0*
Th/Ce	104.3	*110.4*	106.3	*110.4*	104.2	*108.4*	104.2	*106.9*	104.5	*104.9*
Pa/Pm	111.0	*111.0*	108.9	*113.8*	113.6	*117.0*	116.2	*118.0*	117.4	*119.1*
U/Nd	103.0	*112.1*	104.2	*114.9*	109.9	*118.1*	112.1	*120.0*	114.7	*120.0*
Np/Pm	100.3	*111.9*	104.4	*115.5*	110.1	*120.0*	113.4	*120.0*	114.0	*120.0*
Pu/Sm	105.6	*119.0*	104.6	*118.4*	113.4	*119.7*	112.2	*120.0*	112.7	*120.0*
Am/Eu	118.6	*120.0*	109.2	*120.0*	120.0	*120.0*	120.0	*120.0*	120.0	*120.0*
Cm/Gd	104.1	*104.4*	108.2	*109.5*	112.0	*112.1*	113.5	*113.5*	115.3	*116.7*
Bk/Tb	104.3	*	107.0	*116.6*	112.4	*118.3*	116.1	*	118.0	*120.0*
Cf/Dy	106.6	*112.3*	112.9	*119.1*	115.9	*120.0*	118.3	*119.6*	120.0	*120.0*
Es/Ho	105.8	*115.8*	106.9	*118.6*	116.4	*120.0*	117.1	*120.0*	120.0	*120.0*
Fm/Er	116.7	*116.2*	107.9	*118.5*	115.7	*120.0*	118.3	*120.0*	120.0	*120.0*
Md/Tm	120.0	*117.4*	115.1	*120.0*	120.0	*120.0*	120.0	*120.0*	120.0	*120.0*
No/Tb	120.0	*120.0*	120.0	*120.0*	120.0	*120.0*	120.0	*120.0*	120.0	*120.0*
Lr/Lu	108.7	*117.3*	110.7	*119.2*	115.2	*120.0*	117.3	*120.0*	120.0	*120.0*

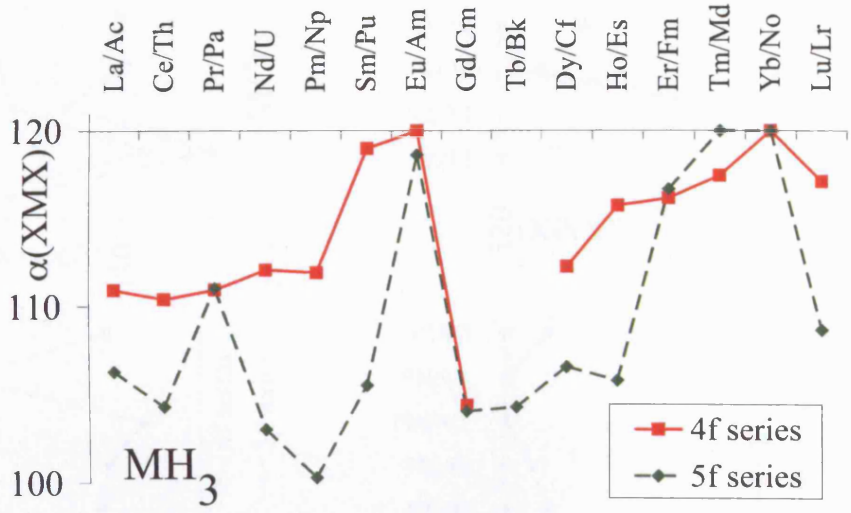

Figure 5.12: Variation of α(HAnH) with actinide element in AnH_3 as predicted by the present calculations compared with the lanthanide results.

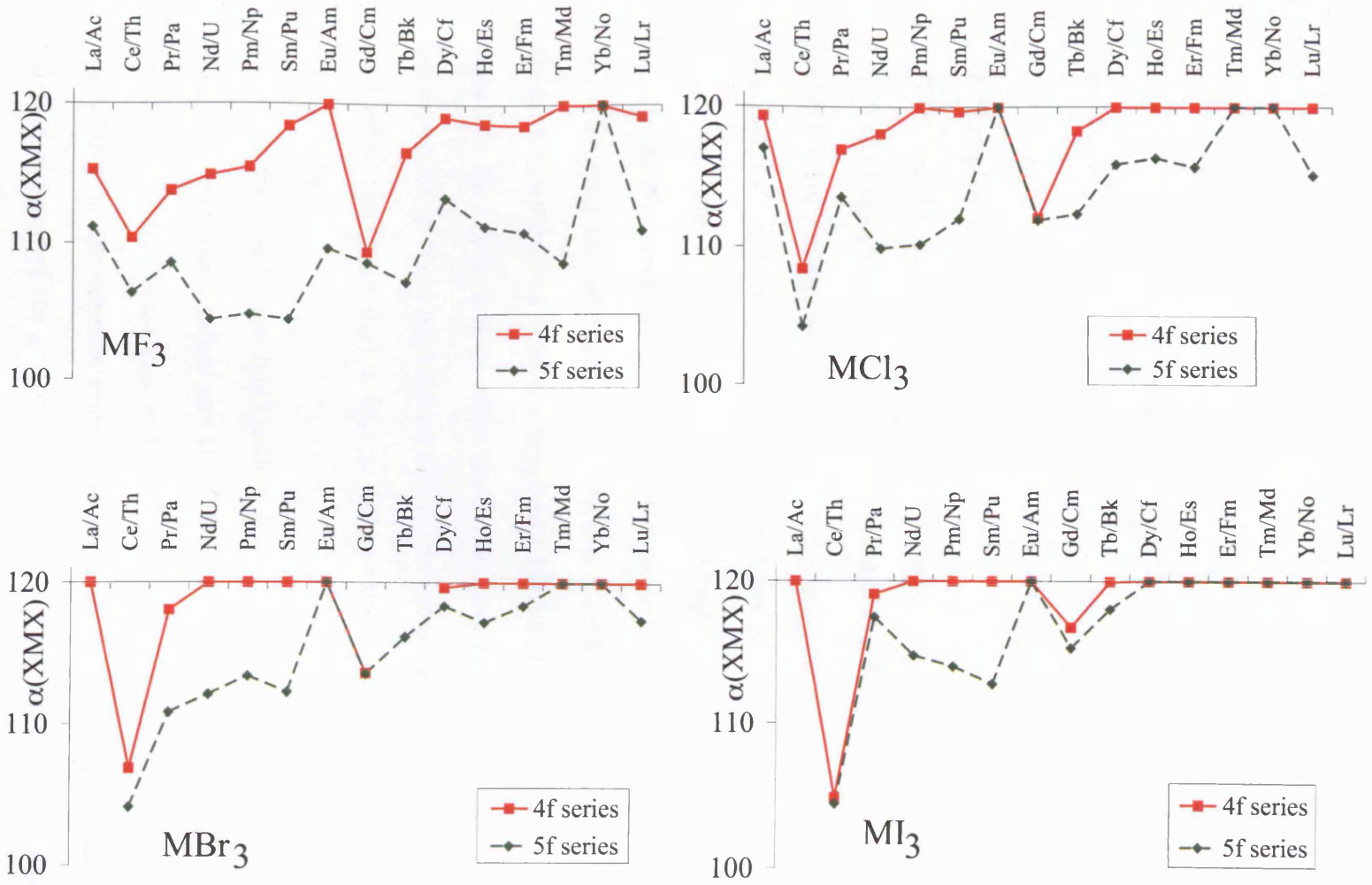

Figure 5.13: Variation of α(FAnF), α(ClAnCl), α(BrAnBr) and α(IAnI) with actinide element in AnX_3 (X=F, Cl, Br, I) as predicted by the present calculations compared with the lanthanide results.

5.4.2.1 Second Order Jahn-Teller (SOJT) Effect in AnH_3

The second order Jahn-Teller (SOJT) distortion was used to rationalise the pyramidality of LnH_3, and it was found that the more pyramidal lanthanide trihydrides have greater $d_{xz} + d_{yz}$ populations relative to $d_{x^2-y^2} + d_{xy}$. As the lanthanide series is traversed, it was found that greater planarity is due to a small decrease in the total d population, which leads to smaller relative $d_{xz}+d_{yz}$ populations, and more planar structures.

The actinide charge in AnH_3 is, in all cases, less than 3.0, as can be seen in table 5.16. In general, the charge on the actinide is less than on the corresponding lanthanide, indicating that the actinide compounds are less ionic. The 6d orbitals are populated, and there is a generally tendency towards decreasing 6d population as the series is traversed, which is more apparent than was the case for the lanthanides. So, while for the early members of the series, the d populations of the lanthanides and actinides in the hydrides are similar, the later members have smaller 6d populations than the equivalent lanthanide 5d populations. In order to see how the d populations affect the SOJT distortion and the bond angles, the decomposition of the d populations into its components is given in table 5.16, and the δ value, the $(d_{xz} + d_{yz})$ to $(d_{x^2-y^2} + d_{xy})$ ratio, versus HAnH angle is plotted in figure 5.14.

As was the case for the lanthanide trihydrides in figure 5.6, there is good correlation between the δ values and the extent of pyramidality for the actinide trihydrides (R^2=0.96), consistent with a SOJT distortion. Furthermore, the greater pyramidality of the actinide trihydrides compared with the lanthanides can be explained in terms of the greater the $d_{xz} + d_{yz}$ values relative to the $d_{x^2-y^2} + d_{xy}$ values, resulting from lower $d_{x^2-y^2} + d_{xy}$ populations. This indicates that the

Table 5.16: NBO actinide charges and d populations in AnH_3. Lanthanide charges and total d populations of LnH_3 are also included for comparison. *No converged geometry obtained.

	q(An)	d_{total}	$d_{x^2-y^2}+d_{xy}$	$d_{xz}+d_{yz}$	$\frac{d_{xz}+d_{yz}}{d_{x^2-y^2}+d_{xy}}$ (δ)	q(Ln)	Ln d_{total}
Ac/La	2.07	0.41	0.22	0.17	0.80	2.05	0.57
Th/Ce	2.64	0.74	0.35	0.35	0.99	2.33	0.78
Pa/Pr	1.89	0.84	0.35	0.15	0.43	1.97	0.55
U/Nd	1.87	0.48	0.23	0.23	1.03	1.97	0.52
Np/Pm	1.82	0.48	0.23	0.23	1.00	1.93	0.48
Pu/Sm	1.85	0.44	0.25	0.18	0.73	1.95	0.39
Am/Eu	1.17	0.16	0.13	0.01	0.06	1.26	0.13
Cm/Gd	1.82	0.45	0.24	0.20	0.84	1.74	0.42
Bk/Tb	1.79	0.42	0.23	0.18	0.78		*
Cf/Dy	1.84	0.39	0.23	0.14	0.63	1.95	0.43
Es/Ho	1.79	0.35	0.20	0.14	0.71	1.92	0.36
Fm/Er	1.79	0.28	0.22	0.03	0.14	2.01	0.39
Md/Tm	1.56	0.17	0.15	0.00	0.00	2.00	0.35
No/Yb	1.17	0.09	0.09	0.00	0.00	1.24	0.08
Lr/Lu	1.62	0.56	0.36	0.19	0.52	1.79	0.56

population of the d orbitals of the actinides compared with the lanthanides shows less preference for the $d_{x^2-y^2}+d_{xy}$ orbitals, and it is this difference that appears to lead to greater pyramidalisation in the actinide trihydrides.

The focus now changes slightly to the role of the 5f orbitals in the An-H bond compared with that of the 4f orbitals to the Ln-H bond. Recall that for the lanthanides, it was suggested that the role of the 4f orbitals in the valence slightly reduces the 5d contribution relative to the situation with the 4f orbitals as core orbitals. This was especially apparent for SmH_3. It was also suggested that for GdH_3, correlation of the 4f orbitals is important in determining a pyramidal structure. Table 5.17 shows the 5f NBO populations for the actinide trihydrides and the corresponding lanthanides. For the actinides, as for the lanthanides, the

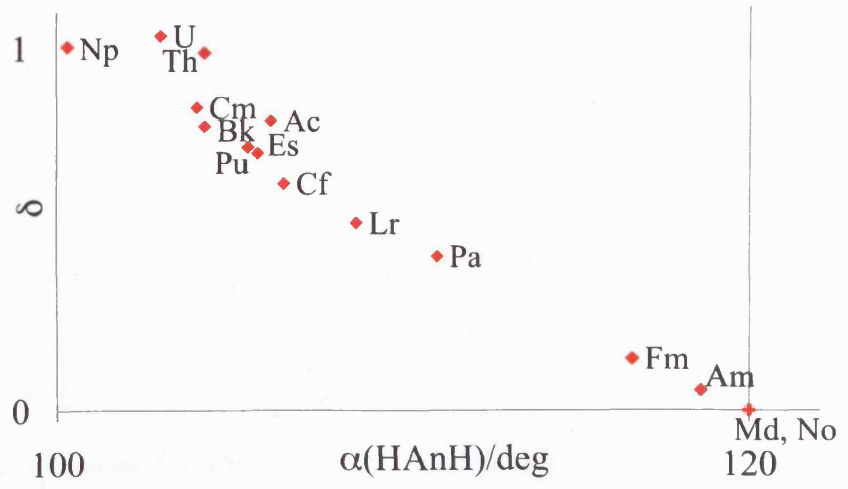

Figure 5.14: Graphical representation of the dependence of α(HAnH) on Natural Bond Orbital d population in AnH_3.

5f orbital populations do not equal to their formal ionic populations (i.e. f^{n-1} when n is the number of f electrons in the neutral atom). In general, the early actinides have a lower f population than the early lanthanides, which is reversed for the later part of the series. There are two cases in which there are strong deviations from the formal valence, PaH_3, 1.4 compared with 2.0 for the formal case, and MdH_3, 12.7 compared with 12.0 for the formal case.

The relatively low 5f population of protactinium in PaH_3 is accompanied by relatively high s and d populations. The f population of 1.4 indicates that the configuration of PaH_3 may not be best represented by $5f^2 7s^0$. There is a high s population of 0.8 and a high d population of 0.8. The latter is interesting because the value reflects the large d_{z^2} population of 0.3, compared with an average value

Table 5.17: NBO 5f populations of the actinides in AnH_3. The corresponding values for LnH_3 are included in italics. *No converged geometry obtained.

Ac *(La)*	Th *(Ce)*	Pa *(Pr)*	U *(Nd)*	Np *(Pm)*	Pu *(Sm)*	Am *(Eu)*
0.01	0.24	1.42	3.05	4.06	5.18	6.89
0.06	*0.78*	*2.12*	*3.13*	*4.20*	*5.28*	*6.99*

Cm *(Gd)*	Bk *(Tb)*	Cf *(Dy)*	Es *(Ho)*	Fm *(Er)*	Md *(Tm)*	No *(Yb)*	Lr *(Lu)*
7.08	8.12	9.14	10.20	11.32	12.68	13.98	14.00
7.01	*	*8.62*	*10.19*	*11.07*	*12.11*	*13.97*	*14.00*

of 0.02 is obtained for the other actinides of the hydrides. This is consistent with previous studies on Cp_3An (An=Th, Pa, U, Np, Pu) that found for Th and Pa, the nonbonding d_{z^2}-like metal orbital is of similar energy to the 5f orbitals, resulting in a $6d^15f^1$ configuration for Cp_3Pa and more ambiguously $5f^36d^0$ or $6d^15f^2$ configuration for Cp_3U.[35]

It was also found that the d_{z^2}-based MO in UCp_3 lies below the 5f-based MOs and consists of 66% U d_{z^2} and 14% U s, whereas in UCl_3 it consists of 69% U d_{z^2} and 21% U s but lies above the 5f-based MOs and is therefore unoccupied.[36] In my case, it is not possible to establish the contributions of atomic orbitals to specific MOs, but the HOMO of PaH_3 does appear to have d_{z^2} character (see figure 5.15), and the total s and d_{z^2} populations do indicate that there is s contribution to the bonding MOs. On the other hand, the 5f population of UH_3 indicates that its ground configuration is $5f^36d^0$, so the d_{z^2}-based MO is unoccupied.

The high 5f population of 12.7 in MdH_3 is accompanied by a low d population relative to the other neutral actinide hydrides, in a similar manner to SmH_3 of the lanthanides. In fact, the d population of 0.17 resembles the d populations of

Figure 5.15: HOMO of PaH_3

the negatively charged AmH_3^- and NoH_3^-, 0.16 and 0.09 respectively, more closely than its neutral counterparts, and is reflected in the planar structure of MdH_3.

It is interesting to compare the f population of CmH_3 with that of GdH_3. In both cases, the values are approximately 7.0, there is a relatively high d population, and both are strongly pyramidal. Since in GdH_3 this was attributed to the correlation of the 4f electrons, a UHF geometry optimisation was carried out on CmH_3. The resultant bond angle of 112.4°, compared with 104.1° for CmH_3 using B3PW91, shows that correlation may well play a role in determining the extent of pyramidality in this compound. This role is more obvious in GdH_3 ($\Delta\{\alpha(HGdH_{UHF}) - \alpha(HGdH_{B3PW91})\} = 13.5°$) than in CmH_3 ($\Delta\{\alpha(HCmH_{UHF}) - \alpha(HCmH_{B3PW91})\} = 8.3°$), and it can be argued that correlation effects should be larger in the more radially contracted 4f orbitals compared with the more diffuse 5f orbitals, which would lead to greater correlation effects in GdH_3 than CmH_3, as is the case here.

5.4.2.2 Second Order Jahn-Teller (SOJT) Effect and π-donation in AnX_3 (X=F, Cl, Br, I)

The optimised structures of the actinide trihalides have been found to be more pyramidal than those of the lanthanides. Since in section 5.3.2.2, the planarity of the lanthanide compounds was attributed to π interactions, maximised at 120°, which exceed the σ interactions associated with the SOJT effect, the pyramidality in AnX_3 is likely to be due to enhanced σ interactions or diminished π interactions (or a combination of both). This ambiguity is addressed by again looking at the Natural Bond Orbital (NBO) populations of the compounds (table 5.18).

As expected, the charges on the actinide centres are less than three, and decrease from the fluorides to the iodides as in the lanthanide compounds, but in general the charge is lower for the actinides. This indicates that like for the lanthanide trihalides, there is a reduction in the ionicity of the actinide trihalides as the halogen becomes heavier, and also the actinide trihalides are less ionic than the lanthanide trihalides. Also, the 6d orbitals are populated for all of the actinide trihalides.

Fluorine is the weakest π donor of the halogens, and it was suggested in section 5.3.2.2 that the bond angle in lanthanide fluorides can be rationalised in terms of the σ SOJT effect, especially for the early lanthanides. This appears to be the case in the 5f series also. Figure 5.16 shows the strong correlation between the relative d populations and α(FAnF), suggesting that π effects do not dominate the bond angle for the actinide trifluoride compounds. Note, however, that even for the planar structure of NoF_3^-, there is some d_{xz}+d_{yz} population, indicating that there are π effects present, since, by symmetry, these orbitals cannot contribute to σ bonding.

Table 5.18: NBO populations of the actinides in AnX_3 (X=F, Cl, Br, I).

	X=F			X=Cl			X=Br			X=I		
	d_t	$d_{x^2-y^2}+d_{xy}$	$d_{xz}+d_{yz}$	d_t	$d_{x^2-y^2}+d_{xy}$	$d_{xz}+d_{yz}$	d_t	$d_{x^2-y^2}+d_{xy}$	$d_{xz}+d_{yz}$	d_t	$d_{x^2-y^2}+d_{xy}$	$d_{xz}+d_{yz}$
Ac	0.27	0.13	0.11	0.39	0.22	0.12	0.41	0.24	0.13			
Th	0.40	0.17	0.18	0.73	0.32	0.31	0.80	0.35	0.33	0.93	0.43	0.38
Pa	0.42	0.19	0.14	0.59	0.27	0.17	0.62	0.30	0.17	0.69	0.34	0.19
U	0.37	0.19	0.14	0.49	0.26	0.18	0.51	0.27	0.19	0.56	0.31	0.19
Np	0.36	0.16	0.15	0.48	0.25	0.17	0.50	0.27	0.17	0.55	0.30	0.19
Pu	0.34	0.15	0.15	0.46	0.25	0.16	0.49	0.27	0.17	0.55	0.31	0.19
Am	0.25	0.12	0.09	0.20	0.13	0.05	0.19	0.13	0.05	0.20	0.13	0.05
Cm	0.33	0.16	0.13	0.47	0.25	0.17	0.49	0.27	0.17	0.54	0.31	0.18
Bk	0.33	0.15	0.13	0.46	0.25	0.16	0.46	0.27	0.15	0.50	0.31	0.16
Cf	0.31	0.16	0.11	0.43	0.25	0.14	0.44	0.27	0.13	0.47	0.29	0.14
Es	0.32	0.15	0.13	0.41	0.24	0.13	0.43	0.25	0.14	0.45	0.28	0.13
Fm	0.31	0.15	0.12	0.41	0.24	0.13	0.41	0.25	0.13	0.41	0.26	0.12
Md	0.28	0.16	0.10	0.34	0.22	0.09	0.32	0.20	0.09	0.24	0.16	0.06
No	0.13	0.08	0.03	0.14	0.10	0.03	0.14	0.09	0.04	0.15	0.10	0.04
Lr	0.56	0.29	0.21	0.92	0.51	0.32	1.02	0.59	0.35	1.15	0.70	0.39

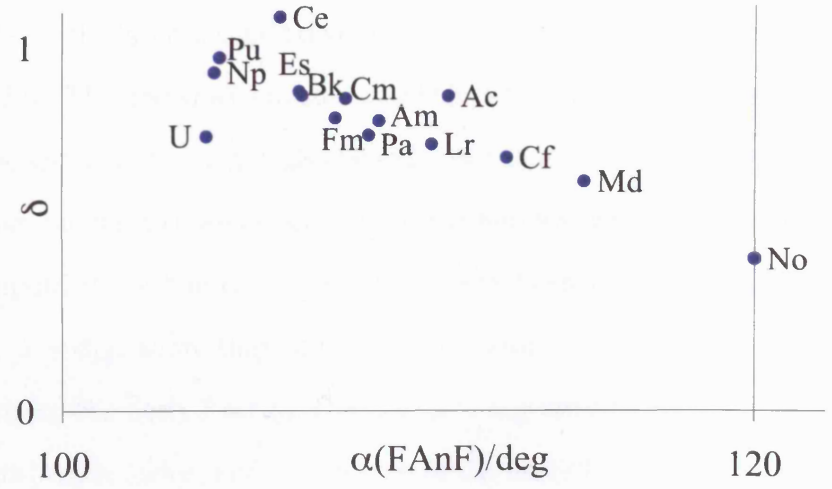

Figure 5.16: Graphical representation of the dependence of α(FAnF) on Natural Bond Orbital d population in AnF_3.

For the lanthanide compounds of the heavier halogens, the π effects seem greater, and the compounds become more planar. Figure 5.13 (page 185) shows that the actinide trihalides behave in a similar manner, although the tendency towards planarity relative to the lanthanide compounds is reduced. The compounds of the heavier halogens do exhibit greater planarity than those of the lighter halogens, and for the iodide compounds, the later members of the actinide series are planar. As has been consistently done throughout this study, the d populations are considered to examine how they affect the structures. The d populations for the actinide trihalides are presented in table 5.18.

A comparison of the lanthanide and actinide d populations shows that for the early part of the f series, the d populations are similar (compare tables 5.7

and 5.18). By the end of the series, however, the actinide d population has generally decreased, in contrast to the values in the lanthanide series that change very little, so the later actinide d values are generally lower than the corresponding lanthanides. This trend within the actinides is consistent with increasing planarity across the series, but it might also be expected that the actinide bond angles would be comparable with those of the lanthanide halides, which is clearly not the case. The components of the d orbitals that have been of interest so far, $d_{xz} + d_{yz}$ and $d_{x^2-y^2} + d_{xy}$, show that, although the total d populations are comparable, especially for the early f series, the $d_{x^2-y^2} + d_{xy}$ orbitals have higher populations in the lanthanide series, and in the case of the early f series, $d_{xz} + d_{yz}$ populations are greater for the actinide compounds. The population of the latter component has been associated with greater pyramidality in the σ compounds, and provides a plausible explanation for the greater pyramidality in the case of the actinide halides.

Having examined the d populations, the f orbital populations are now considered. Table 5.19 shows the 5f populations for AnX_3, and the corresponding 4f LnX_3 values. The hydride values are included for comparison only, since they have been discussed briefly earlier. In general, the 5f population exceeds the formal 'core' valence. The exception to this is PaF_3, in which there is a value of 1.6, compared with the formal value of 2.0. There is also a slightly low f population for the other protactinium halides, but to a lesser extent than for the fluoride. In addition to the low f population, there is a high s value (0.5-0.6) and a high d_{z^2} value (0.1-0.2) for the protactinium halides, and is consistent with what was found for PaH_3. However, as the halogen becomes heavier, the d_{z^2} population is lowered and for $PaCl_3$, $PaBr_3$ and PaI_3, the LUMO looks more similar to the d_{z^2} atomic

Table 5.19: NBO 5f populations of the actinides in AnX_3 (X=H, F, Cl, Br, I) and the lanthanide values are included for comparison. *No converged geometry obtained.

	H	F	Cl	Br	I
Ac	0.01	0.10	0.15	0.13	
La	*0.06*	*0.19*	*0.18*	*0.15*	*0.13*
Th	0.24	0.41	0.52	0.53	0.56
Ce	*0.78*	*0.69*	*0.86*	*0.87*	*0.89*
Pa	1.42	1.62	1.85	1.92	1.92
Pr	2.12	*2.20*	*2.17*	*2.16*	*2.15*
U	3.05	3.07	3.24	3.21	3.17
Nd	*3.13*	*3.18*	*3.15*	*3.27*	*3.21*
Np	4.06	4.16	4.24	4.19	4.17
Pm	*4.20*	*4.14*	*4.14*	*4.15*	*4.16*
Pu	5.18	5.19	5.22	5.20	5.16
Sm	*5.28*	*5.14*	*5.16*	*5.21*	*5.31*
Am	6.89	6.56	6.95	6.97	6.99
Eu	*6.99*	*6.98*	*7.00*	*7.00*	*7.00*
Cm	7.08	7.12	7.12	7.11	7.11
Gd	*7.01*	*6.90*	*6.97*	*6.99*	*7.03*
Bk	8.12	8.15	8.14	8.14	8.14
Tb	*	*7.41*	*7.47*	*	*7.65*
Cf	9.14	9.13	9.13	9.14	9.17
Dy	*8.62*	*8.51*	*8.55*	*8.57*	*8.57*
Es	10.20	10.10	10.15	10.14	10.18
Ho	*10.19*	*10.04*	*10.04*	*10.05*	*10.04*
Fm	11.32	11.12	11.15	11.18	11.26
Er	*11.07*	*11.07*	*11.04*	*11.04*	*11.03*
Md	12.68	12.13	12.29	12.42	12.73
Tm	*12.11*	*12.02*	*12.03*	*12.04*	*12.07*
No	13.98	13.96	13.98	13.99	13.99
Yb	*13.97*	*13.92*	*13.98*	*13.99*	*13.99*
Lr	14.00	14.00	14.00	14.00	14.00
Lu	*14.00*	*14.01*	*14.01*	*14.01*	*14.01*

orbital than does the HOMO, which now shows f atomic orbital characteristics. The HOMO and LUMO of PaI_3 are shown in figure 5.17.

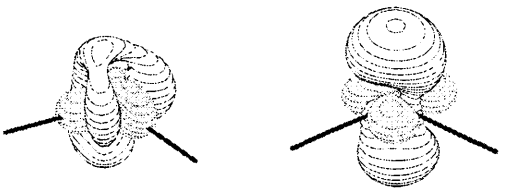

(a) HOMO (b) LUMO

Figure 5.17: HOMO and LUMO of PaI_3

It was noted for the lanthanide halides that the values of the 4f populations above the 'core' values was greater for the early members compared the later members of the lanthanide series. This is no longer obvious for the actinides, but in general, as the f series are traversed, there is a tendency for the actinide 5f populations to gradually exceed those of the lanthanides. This may be the reason for the gradual decrease in relative d populations and hence the gradual tendency towards planarity in the case of the actinide trihalides.

Also, a comparison of the f populations in CmX_3 and GdX_3 shows that there is slightly greater f population in the actinide case. Since the strong pyramidality in GdX_3 was found to be significantly reduced for the uncorrelated UHF, geometry optimisations of CmX_3 using UHF were carried out. The optimised values were found to be 115.4° for the CmF_3 and 120.0° for the other halides, which suggests that correlation may play a role in the 5f CmX_3, as was the case for GdX_3. As was the case for the metal trihydrides, the effect of correlation is slightly greater in GdX_3 than in CmX_3: $(\Delta\{\alpha(XGdX_{UHF}) - \alpha(XGdX_{B3PW91})\} =$

10.5°, 7.9°, 6.5° and 3.3° for GdF_3, $GdCl_3$, $GdBr_3$ and GdI_3 compared with $(\Delta\{\alpha(XCmX_{UHF}) - \alpha(XCmX_{B3PW91})\} = 7.2°, 8.0°, 6.5°, 4.7°$ for CmF_3, $CmCl_3$, $CmBr_3$ and CmI_3 respectively. These data are again consistent with the argument that the 4f orbitals, being more contracted, experience greater correlation effects than the 5f orbitals.

Finally, in a similar manner to the approach to the lanthanide trihalides, the π interactions in the actinide compounds are considered by looking at the halogen and p_σ and p_π NBO populations of NpX_3 and EsX_3, the actinide analogues of PmX_3 and HoX_3 respectively. These values are given in table 5.20. The p_σ and p_π NBO populations of PmX_3 and HoX_3 are included for comparison.

Table 5.20: NBO X(p) populations in NpX_3, EsX_3, and the lanthanide analogues, PmX_3 and HoX_3.

	Small Core Lanthanide			Actinide		
	α(XMX)/°	X(p_σ)	X(p_π)	α(XLnX)/°	X(p_σ)	X(p_π)
PmF_3/NpF_3	115.5	5.78	11.73	104.4	5.75	11.69
HoF_3/EsF_3	118.6	5.82	11.78	106.9	5.77	11.76
$PmCl_3$/$NpCl_3$	120.0	5.66	11.63	110.1	5.62	11.50
$HoCl_3$/$EsCl_3$	120.0	5.68	11.68	116.4	5.65	11.60
$PmBr_3$/$NpBr_3$	120.0	5.61	11.59	113.4	5.56	11.54
$HoBr_3$/$EsBr_3$	120.0	5.63	11.62	117.1	5.55	11.61
PmI_3/NpI_3	120.0	5.54	11.52	114.0	5.50	11.49
HoI_3/EsI_3	120.0	5.54	11.56	120.0	5.49	11.52

There is an increase in the XAnX bond angle in EsX_3 compared with NpX_3 for all of the halides. Looking at the X p populations shows approximately constant p_σ populations and a slight increase in p_π for EsX_3, which is more obvious for the lighter halides. This indicates that the metal-ligand interactions are approximately constant with a slight reduction in the π interactions in EsX_3 compared with NpX_3. Thus, although there is a reduction in the actinide d populations across

the 5f series, the ligand p data suggest that this does not lead to substantial loss in σ interactions. This may be because there is a concurrent increase in the actinide 7s orbital population, since the 7s orbital can also participate in actinide-ligand σ bonding.

Comparison of the X p_σ and p_π AnX_3 data with the corresponding lanthanide data shows slightly lower values in the actinide compounds. This is consistent with the metal charges, which indicate slightly greater covalency in the actinide compounds compared with the lanthanide analogues. Apart from the increased covalency in the actinide compounds, there is no evidence to suggest that the bonding in AnX_3 is different in character from the LnX_3 analogues.

5.5 Results and Discussion: Molecular Orbitals in MX_3 (M=Nd, U; X=H, F, I)

Thus far, the analysis of MX_3 has focused on the atomic orbital populations. I now turn to a discussion of the valence molecular orbitals (MOs), to which these atomic orbitals contribute. Neodymium and uranium have been chosen as representative 4f and 5f elements respectively, as an MO analysis of all of the lanthanide and actinide compounds is not feasible. The hydride compounds are presented first.

Both the NdH_3 and UH_3 geometries were reoptimised constraining the HMH angles to be 120°, 112.1° (NdH_3 equilibrium angle), and 103.0° (UH_3 equilibrium angle). The difference in bond lengths at 103.0° and 112.1° is less than 3 pm for each metal, indicating that the angle is reasonably independent of bond length, and the energy difference between the two optimised geometries, 103.0° and 112.1°,

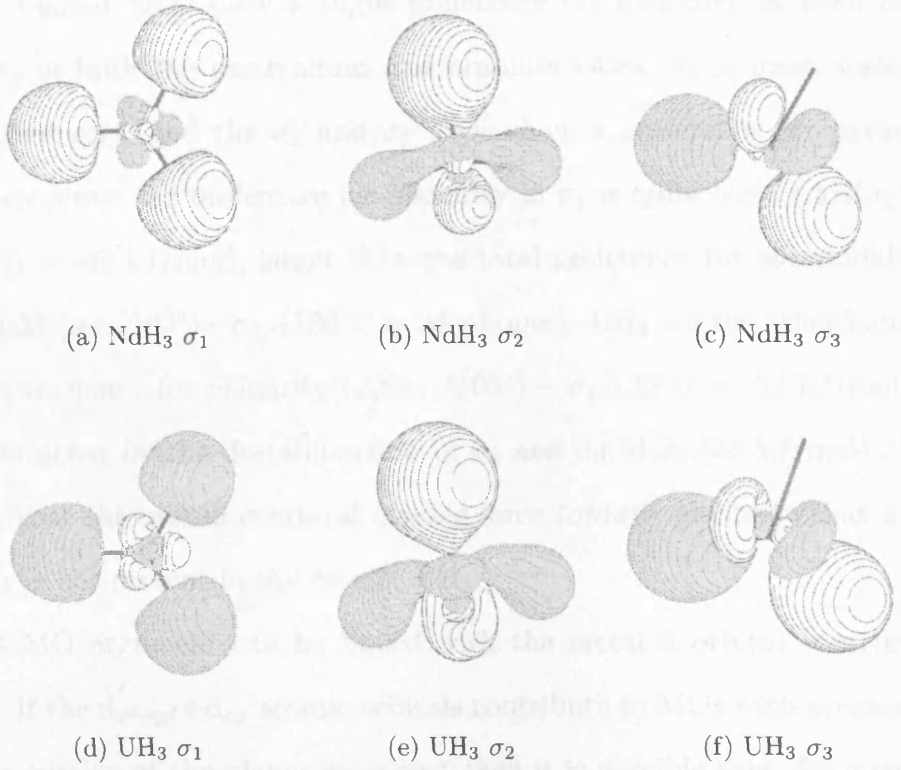

(a) NdH_3 σ_1 (b) NdH_3 σ_2 (c) NdH_3 σ_3

(d) UH_3 σ_1 (e) UH_3 σ_2 (f) UH_3 σ_3

Figure 5.18: NdH_3 and UH_3 σ molecular orbitals at their equilibrium geometries.

was only 3 kJ/mol for both uranium and neodymium, indicating a very shallow potential energy surface.

The three σ molecular orbitals (MOs) can be identified for both UH_3 and NdH_3, three dimensional representations of which are shown in figure 5.18. It may be seen that the Nd-H σ and U-H σ MOs are similar to one another. The main differences between the compounds are, firstly that for NdH_3, the f-based MOs (not shown) lie below the σ bonding MOs, in contrast to the UH_3 case, in which the f orbitals are higher in energy than the σ bonding MOs, and secondly, there are differences in the sensitivities of the energies of the specific MOs with

respect to the pyramidality of the structures.

The f-based MOs show a slight preference for planarity in both cases. In addition, in both the neodymium and uranium cases, σ_1 is most stable at the planar geometry, and the σ_2 and σ_3 MOs show a preference for pyramidality. For neodymium, the preference for planarity in σ_1 is quite large ($\Delta E(\sigma_1(103°) - \sigma_1(120°))$ = -45 kJ/mol), larger than the total preference for pyramidality in σ_2 and σ_3 ($\Delta E(\sigma_{2,3}(103°) - \sigma_{2,3}(120°))$ = 38 kJ/mol). UH_3, on the other hand, shows less of a tendency for planarity ($\Delta E(\sigma_1(103°) - \sigma_1(120°))$ = -32 kJ/mol), which is counteracted by the destabilisation of σ_2 and σ_3 MOs (33 kJ/mol). Thus, it appears that the overall σ orbital driving force towards planarity that is present in NdH_3 is not present in the case of UH_3.

This MO argument can be linked with the metal d orbital contribution as follows. If the $d_{x^2-y^2}+d_{xy}$ atomic orbitals contribute to MOs with greatest metal-ligand σ overlap at the planar geometry, then it is possible that, for a compound with less $d_{x^2-y^2}+d_{xy}$ orbital contributions, there is less tendency towards a planar geometry. The $d_{x^2-y^2}+d_{xy}$ populations of UH_3 and NdH_3 at their equilibrium geometries are 0.23 and 0.34 respectively.

The constrained geometry optimisations that were carried out to compare the bonding in NdH_3 and UH_3, were also carried out for the fluoride compounds, NdF_3 and UF_3, and the iodide compounds, NdI_3 and UI_3. The fluoride and iodide compounds were chosen as they contain the weakest and strongest π donors respectively. It is worth emphasising that it is not expected that all of the lanthanide compounds resemble the neodymium compounds, or that all of the actinide compounds resemble the uranium compounds, but the aim of this part of the study is to use NdX_3 versus UX_3 as an example of how the analogous lanthanides

and actinides differ.

The metal trifluorides are considered first. NdF_3 is more planar than UF_3. This was attributed to the greater relative $d_{xz}+d_{yz}$ to $d_{x^2-y^2}+d_{xy}$ populations in the actinide case, compared with the lanthanides, and hence greater SOJT distortion towards pyramidality. Recall that for the MOs of NdH_3 and UH_3, σ_1 in figure 5.18 was found to be more stable at the planar geometry, and that σ_2 and σ_3 were found to be less stable at the planar geometry, and that the balance of both effects may well influence the equilibrium geometry. For the halides, the situation is expected to be more complicated as there are now π effects, and hence π-type MOs that now need to be considered. Formally, it is expected that there are three p_σ and six p_π MOs in the fluorides.

Three different NdF_3 and UF_3 geometries corresponding to three values for α(FMF) were considered, specifically 104.2°, 114.9° and 120°. These three values were chosen since they correspond to the UF_3 equilibrium bond angle, the NdF_3 equilibrium bond angle and planarity respectively. As was found for the hydride cases, the values of the bond lengths changed by only a small amount (<3 pm) between 104.2° and 120°, and the potential energy curves are extremely shallow (the maximum energy difference over the bond angle range of 104.2° and 120° is <10 kJ/mol).

Figure 5.19 shows the nominally σ MOs for NdF_3 and UF_3, although it can be seen that there is π character mixed with the σ character. These three MOs are essentially degenerate at the equilibrium angles, although this does not necessarily stay the case when the angle is changed. There are two filled MOs that show antibonding characteristics (figure 5.20), which again are essentially degenerate. Although this indicates that there are 5 σ type MOs, they are not exclusively

σ bonding, and some mixing from the π MOs occurs. There is non-negligible metal character in the MOs, confirming the presence of covalency despite the high electronegativity of fluorine. This is the case for both the lanthanide and actinide compounds.

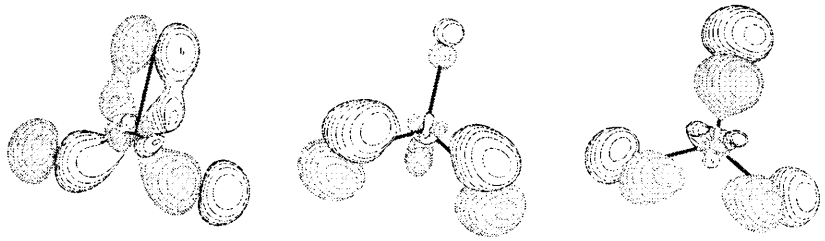

(a) NdF_3 σ_1 (b) NdF_3 σ_2 (c) NdF_3 σ_3

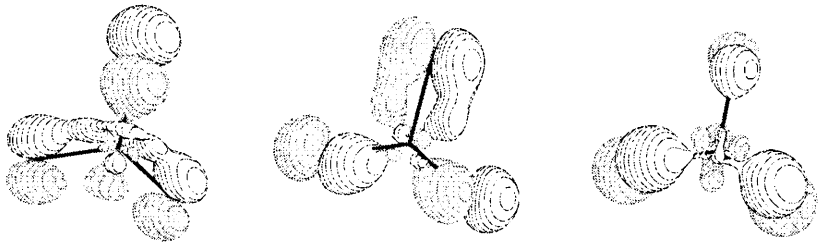

(d) UF_3 σ_1 (e) UF_3 σ_2 (f) UF_3 σ_3

Figure 5.19: NdF_3 and UF_3 σ molecular orbitals at their equilibrium geometries.

Comparison of figure 5.19 with figure 5.18 shows similarities between NdH_3 (UH_3) σ_1 and NdF_3 (UF_3) σ_3 MOs, and as for MH_3, this MO is most stable at the planar geometry ($\Delta E(\sigma_3(104) - \sigma_3(120))$ = -26 kJ/mol for both NdF_3 and UF_3). In contrast to the other σ MOs of the hydride, however, there is no driving force in the MF_3 σ_1 or σ_2 MOs towards a pyramidal structure. This is presumably due to the π interactions in the molecular plane that are absent in the hydride case, which is consistent with the explanation that the compounds with π ligands are

more likely to be planar. In fact, there is a negligible energy difference for these fluoride MOs as the bond angle becomes more pyramidal, except for the NdF_3 σ_1 MO, which experiences a destabilisation of 16 kJ/mol at 104.2° relative to the equilibrium angle of 114.9°. Increasing the angle beyond 114.9° to 120.0° does not stabilise this MO any further. Hence, while in the case of the trihydrides, the σ_2 and σ_3 MOs were stabilised by a pyramidal structure, in the case of the trifluorides this stabilisation energy is reduced, so based on these MOs, a planar structure might be expected. In order to ascertain why the trifluorides are not planar, I now turn to other occupied MOs in the trifluoride compounds.

The effect of the extent of pyramidality on the MOs labelled as antibonding in figure 5.20 is quite small (<5kJ/mol) for NdF_3, but for UF_3, the σ_1^* and σ_2^* MOs are stabilised by 24 and 23 kJ/mol at 104.2° relative to 120° respectively. Although it is not obvious from looking at the MOs why this would be the case for one set of MOs and not the other, it indicates some differences in the nominally similar MOs. It also provides an explanation as to why the actinide fluoride, UF_3, is more pyramidal than the lanthanide fluoride; the antibonding σ-like MOs in UF_3 provide a driving force to a more pyramidal structure than the analogous NdF_3 MOs, in which this driving force is largely absent.

One final aspect of the fluoride MOs was also considered, that of the role of the π orientated MOs, two of which (π_3 and π_4) are shown in figure 5.21. Two other π-type MOs that lie lower in energy than π_3 and π_4 are not shown here, as their energies are not affected by changing the bond angles for either compound. The reason for including these MOs is two-fold; firstly, they are stabilised in a more planar structure, with $\Delta E(\pi(104) - \pi(120))$ = -32 kJ/mol and -34 kJ/mol respectively for π_3 and π_4 in NdF_3 and -19 and -9 kJ/mol for UF_3, showing clearly

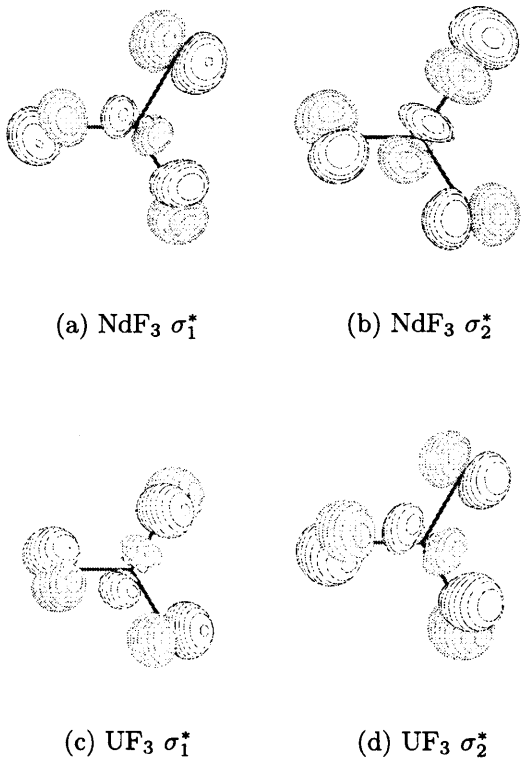

(a) NdF_3 σ_1^* (b) NdF_3 σ_2^*

(c) UF_3 σ_1^* (d) UF_3 σ_2^*

Figure 5.20: NdF_3 and UF_3 σ^* molecular orbitals at their equilibrium geometries.

a stronger preference for planarity in the neodymium case. Secondly, π_3 illustrates that the f orbitals might play a role in π interactions in these species, even in the case of the 4f series.

Thus, analysis of the dependence of MO energy on bond angle rationalises (a) why there is a greater tendency towards planarity for the π-donor compounds compared with the σ-only species, and (b) the greater tendency towards planarity in the case of the lanthanide fluoride compared with the actinide fluoride. Furthermore, it suggests that the f orbitals play a role in the MO structure of both the neodymium and the uranium compounds.

Although fluorine is a π donor, it is a relatively weak one compared with the heavier halogens, so as a final examination of how π donation affects the MOs of

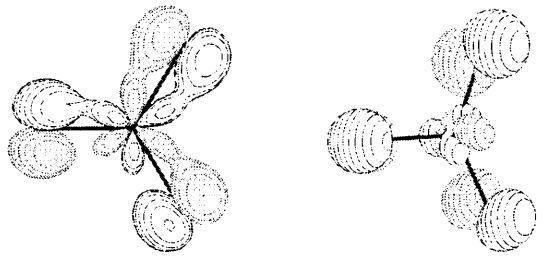

(a) NdF_3 π_3 (b) NdF_3 π_4

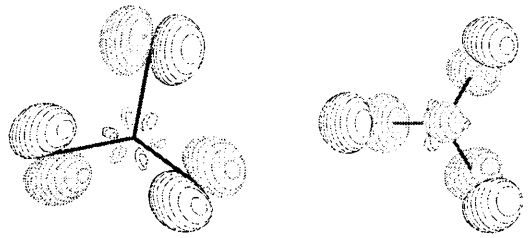

(c) UF_3 π_3 (d) UF_3 π_4

Figure 5.21: NdF_3 and UF_3 π molecular orbitals at their equilibrium geometries.

MX_3, the MOs of NdI_3 and UI_3 were considered. Figure 5.22 shows the σ MOs analogous to figures 5.18 and 5.19, the hydride and fluoride σ MOs respectively. In this case, the energy difference between the optimised UI_3 structure, which has a bond angle of 114.7°, and planar UI_3 is less than 2 kJ/mol, so the driving force towards pyramidality is almost negligible. Similarly, the difference in energy between the optimised NdI_3 angle of 120.0° and 114.7° is also less than 2 kJ/mol. This is probably the reason why any driving force towards planarity/pyramidality was difficult to see in the individual MOs. For this reason, although the MOs are shown, their discussion is confined mainly to a comparison with the fluoride MOs.

Figure 5.23 shows the MI_3 π MOs. The MOs that resemble the π_3 and π_4 of MF_3 in figure 5.21 are labelled I p_{π_5} and I p_{π_6} for NdI_3 and I p_{π_3} and I p_{π_6}

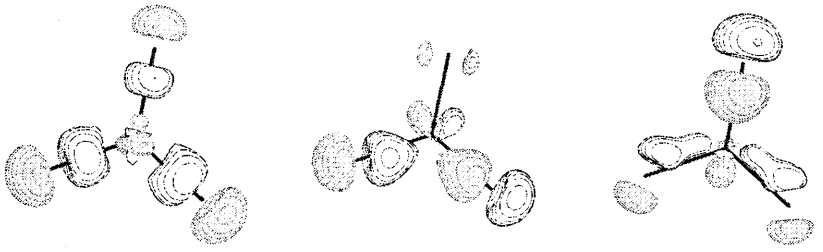

(a) NdI_3 σ_1 (b) NdI_3 σ_2 (c) NdI_3 σ_3

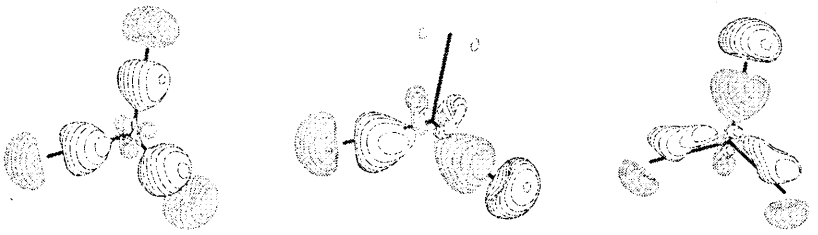

(d) UI_3 σ_1 (e) UI_3 σ_2 (f) UI_3 σ_3

Figure 5.22: NdI_3 and UI_3 σ molecular orbitals at their equilibrium geometries.

for UI_3. Also included in figure 5.23 are the MOs that are similar to the MOs labelled σ^* in the case of MF_3 (I p_{π_3} and I p_{π_4} for NdI_3 and I p_{π_5} and I p_{π_4} for UI_3) since there is no longer σ^* character in these MOs and they are now better classified as I p_π MOs in both NdI_3 and UI_3. One of the most notable differences between the fluoride and iodide MOs is that for the latter case, there is less metal character visible in the π MOs. It is only really in the σ type orbitals that much metal contribution is seen. Also there is no evidence of σ antibonding character in the iodide MOs. Hence, the driving force toward pyramidality, seen in the antibonding MOs of NdF_3 and especially UF_3, is not present in the iodides. Thus, the greater pyramidality in MF_3 compared with MI_3 appears to the due to greater driving force towards pyramidality due to σ^* interactions in MF_3, and not

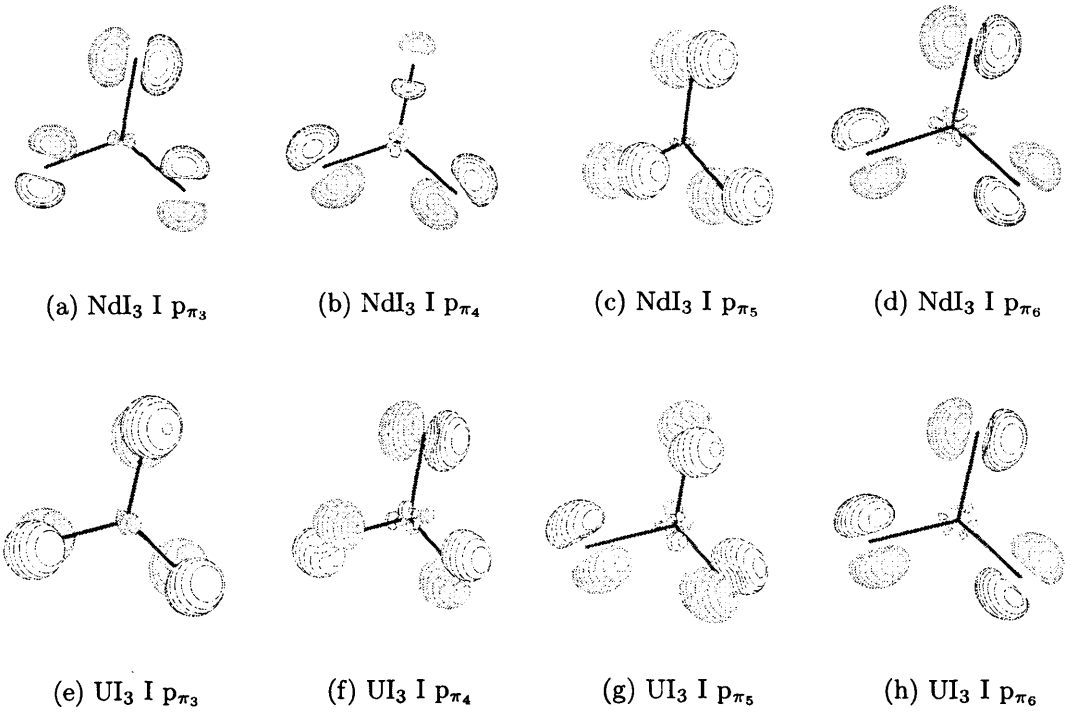

(a) NdI_3 I p_{π_3} (b) NdI_3 I p_{π_4} (c) NdI_3 I p_{π_5} (d) NdI_3 I p_{π_6}

(e) UI_3 I p_{π_3} (f) UI_3 I p_{π_4} (g) UI_3 I p_{π_5} (h) UI_3 I p_{π_6}

Figure 5.23: NdI_3 and UI_3 π molecular orbitals at their equilibrium geometries.

to any geometric preference in MI_3.

At this point, it is worth mentioning that although MF_3 showed greater $M(f_\pi)$ contributions to the π MOs than in the case of MI_3, this observation does not provide conclusive evidence that there are greater $M(f_\pi)$-$F(p_\pi)$ interactions than $M(f_\pi)$-$I(p_\pi)$ interactions. The authors in reference 37 attribute an apparently large M(f)-Cp interaction energy of $CfCp_3$ to the 'coincidental energy match' of the 5f orbitals of Cf with the Cp π_2 orbitals, rather than greater metal-ligand overlap. It was also mentioned that the radial extension of the metal f orbitals is also a contributing factor, so the more contracted 5f orbitals of the later actinides compared with the earlier actinides in their study results in poorer overlap with the ligand orbitals.

Therefore, although the MOs in figure 5.21 show M(f_π)-F(p_π) interactions, the extent of these interactions should not be overemphasised. Indeed, it may be the case that the influence of the valence f orbitals on the geometries of LnX_3 and AnX_3 is a combination of two factors: They may facilitate electron rearrangement between the d and f orbitals within the metal and they may participate in M(f_π)-X(p_π) interactions.

5.6 Concluding Remarks

The aim of this study was two-fold; the initial aim was to examine the role of 4f orbitals in LnX_3 by considering the optimised structures when the 4f orbitals are in the valence region compared with the previous study by Eisenstein et al.,[170] in which the 4f orbitals are considered as core orbitals. The second aim was to compare these results with the optimised structures of AnX_3.

The results presented here suggest that the pyramidality in the lanthanide trihydrides can be explained by the second order Jahn-Teller (SOJT) distortion, as was proposed by Eisenstein et al. More specifically, there is a strong correlation between the participation of the $d_{x^2-y^2}$ and d_{xy}, and d_{xz} and d_{yz} orbitals with the resultant equilibrium bond angle. For the lanthanide trihalides, greater planarity is seen than in the case of the lanthanide trihydrides due to M-X π bonding.

For all of the LnX_3 series of compounds, the NBO 4f populations tend to be slightly greater than the 'core' 4f populations, especially for the early lanthanides, which suggests that the 4f orbitals do play a role in the bonding. The slightly increased 4f populations seem to reduce the extent of SOJT distortion slightly via a removal of d electron density, and result, for many cases, in slightly more

planar structures. There is also a bond length contraction when the 4f orbitals are in the valence, consistent with the proposal that the 4f participation in the bond strengthens, and hence shortens the bond.

Analysis of the halide p populations from LC PmX_3 and HoX_3 for the heavier halogens suggests that the increased planarity of HoX_3 in the LC results might be due to reduced σ interactions for the later lanthanides. Comparison of the SC and LC $X(p_\pi)$ NBO populations of PmX_3 does not provide conclusive evidence of $Ln(4f_\pi)$-$X(p_\pi)$ bonding, although it suggests that including the 4f orbitals in the valence results in slightly greater σ and π interactions between the lanthanide centre and the ligands. This aspect was considered again in section 5.5 for both neodymium and uranium, in which there was some evidence to suggest that there might be $M(f_\pi)$-$X(p_\pi)$ bonding present. However, the extent of these interactions should also be balanced with the possibility of the coincidental energy match that was mentioned in reference 37. Further, including the 4f orbitals in the valence region of the lanthanides leads to greater planarity in LnH_3, in which no π interactions are possible, suggesting that the f contributions to the σ interactions are important. Therefore, I propose that having the 4f orbitals in the valence region in LnX_3 (X=H, F, Cl, Br, I) results in greater planarity partly because the metal electrons rearrange themselves between the d and f orbitals, which reduces the extent of SOJT distortion. There is also evidence of greater covalency using the SC description of the lanthanide. For the case of the trihalides, the greater covalency may result from contributions from both σ interactions and the presence of a small amount of $M(f_\pi)$-$X(p_\pi)$ bonding.

The extension of this study to compare the lanthanide and actinide compounds shows that, in general, the compounds of the 5f series are more pyramidal than

those of the 4f series, with a gradual tendency towards planarity for the heavier actinides. This increase in pyramidality is consistent with an increase in the SOJT distortion for the actinides, and the tendency towards planarity towards the latter part of the series, is consistent with a decrease in the 6d populations. There is also a tendency for r(An-X) to be slightly longer than r(Ln-X) for the halides, in contrast to more comparable bond lengths in the hydrides.

The pyramidality of GdX_3 and CmX_3 relative to the other neutral MX_3 compounds has been attributed to the correlation of the 4f and 5f electrons. This effect is more pronounced in the gadolinium compound, which may be a consequence of the 4f orbitals being more contracted than the 5f orbitals, leading to the greater correlation effects experienced by the 4f electrons in the gadolinium compounds compared with the curium compounds.

Further comparison between 4f and 5f MX_3 was carried out by looking at selected MOs for NdX_3 and UX_3. This shows that for the metal trihydrides, there is a σ MO that is more stable in a planar structure and two σ MOs that are more stable in more pyramidal structures. The latter is a greater driving force in UH_3 than in NdH_3, consistent with greater pyramidality. For the halides, the characteristics of the MOs change from purely σ MOs, to σ and π MOs. This lowers the tendency for the structures to pyramidality. For the fluorides, pyramidality has been shown to stabilise MOs that exhibit some σ antibonding characteristics, particularly in UF_3. This leads to greater pyramidality in MF_3 compared with MI_3, in which this driving force is absent, which is consistent with more planar metal iodides compared with the metal fluorides. As was the case for the lanthanide trihalides, there is evidence that the role of the f orbitals in the actinide trihalides may both reduce the actinide d population and participate in

$An(f_\pi)$-$X(p_\pi)$ interactions.

Finally, a comparison is made between lanthanide-like behaviour and the later members of the actinide series. In these MX_3 structures that are sensitive to small changes at the metal centres, the structural data do suggest that there are differences between the actinides and lanthanides even for the actinides towards the end of the f-block. From the Natural Bond Orbital population analysis of MX_3, the late actinides show greater s populations and smaller d populations than the lanthanides, a trend which is consistent with increasing relativistic effects, i.e. relativistic s contraction and d expansion in going from the 4f to the 5f series. Therefore, for these compounds it is not fully correct to assume that the late actinides will behave in a lanthanide-like manner.

Chapter 6

Summary

Experimental and computational research on elements of the late part of the periodic table is an active area in chemistry. Computational studies can provide useful information to both theoreticians and experimentalist, information that would be extremely difficult or impossible to obtain experimentally. In this research, Density Functional Theory (DFT) and ab initio methods were used to examine the electronic properties of selected heavy element complexes in their ground state. Having first introduced computational studies of the lanthanides, actinides and 6d transactinides in chapter 1 through examples from the literature, and then electronic structure methods in chapter 2, the results from the current studies were presented in chapters 3, 4 and 5.

Chapter 3 presented DFT results on the inverse *trans* influence (ITI) of $[AnOX_5]^{n-}$ (An=Pa (n=2), U (n=1), Np (n=0); X=F, Cl, Br). Having established the presence of an ITI, that is, that the *trans* bond is shorter than the *cis* bonds, a comparison was made between these actinide complexes and the transition metal complex, $[OsNCl_5]^{2-}$, which exhibits a *trans* influence (TI). In contrast to the osmium complex, which has an equilibrium structure with $\alpha(NOsCl_{cis})$ of 96.6°, the equilibrium structures for the actinide complexes all have $\alpha(OAnX_{cis})$ values of about 90°. Hence, while the TI of the osmium complex is attributed to steric repulsion between the *cis* and *trans* ligands, which is alleviated by elongating the *trans* bond, no such steric repulsion exists for the actinide complexes. Further, the 4e MO of the osmium complex shows Os-N π and Os-Cl_{cis} π^* character, the latter of which is reduced by the equilibrium bond angle of 96.6°. The $9a_1$ MO

of $[AnOX_5]^{n-}$, on the other hand, is An-O σ and An-X_{cis} π^* in character, and since the bond angle is 90°, the latter results in a longer *cis* bond and hence, the actinide complexes exhibit an ITI.

The second results chapter (chapter 4) looked at the metallophilicity in the dimer $[ClM(PH_3)]_2$ (M=Cu, Ag, Au, [111]). Initially, the greater effect of relativity on r(M-P) compared with r(M-Cl) in the monomer was considered; whereas non-relativistic geometry optimisations of $[ClM(PH_3)]$ (M=Au, [111]) showed a steady increase in the metal-ligand bond lengths for both ligands from gold to element 111, the analogous relativistic geometry optimisations showed that r(M-Cl) is approximately equal for gold and element 111, but that r(M-P) exhibits a slight bond contraction from gold to element 111. This was attributed to the greater relativistic contraction of the bond in which there is greater electron density on the relativistic atom (or alternatively, the bond between the relativistic atom and the less electronegative ligand) i.e. r(M-P) compared with r(M-Cl).

Metallophilic interaction energies of $[ClM(PH_3)]_2$ (M=Cu, Ag, Au, [111]) were calculated using HF, MP2, QCISD, CCSD and CCSD(T). The uncorrelated HF method fails to find any metallophilic interaction. Whereas MP2 predicted a steady increase in the interaction (that is, the interaction energies become more negative) from Cu $\rightarrow$ [111], all other post-HF methods predict approximately constant values for all four metals. Given that MP2 is generally considered to be the least reliable of the correlated ab initio methods, this indicates that metallophilicity is approximately constant for all of the coinage metals in $[ClM(PH_3)]_2$. Further studies, in which the differences between the MP2 and other post-HF results are examined, could provide a more definite conclusion as to how the metallophilic interaction energies change for the four coinage metals.

The final results chapter (chapter 5) considers the extent of pyramidality in MX_3 (M=La-Lu, Ac-Lr; X=H, F, Cl, Br, I) using B3PW91, a hybrid-DFT method. Initially the lanthanide compounds were considered, and it was found that the LnH_3 compounds are pyramidal, and that although many of the lanthanide trihalide compounds are pyramidal, the extent of pyramidality decreases from F→I. In agreement with a study by Eisenstein et al.,[170] this was attributed to a second-order Jahn-Teller (SOJT) distortion from trigonal planarity, due to the role of the formally empty 5d orbitals of the lanthanides. This distortion is reduced for the heavier halides because of increased π interactions that favour a trigonal planar structure.

In contrast to Eisenstein et al.'s results,[170] in which the 4f orbitals were considered as core orbitals, the results presented here, in which the 4f orbitals were treated as valence orbitals, show less pyramidality. This study reported greater 4f orbital Natural Bond Orbital (NBO) populations than would be expected from a '4f core' picture, and a concurrent reduction in the NBO 5d orbital populations than was the case for the 4f core orbital picture. Thus, the reduction in pyramidality was attributed to the reduction in the SOJT distortion due to the participation in the 4f orbitals, which remove electron density from the 5d orbitals. In addition, there is evidence, albeit inconclusive, that suggests that the 4f orbitals may participate in some $Ln(4f_\pi)$-$X(p_\pi)$ bonding.

Extension of this study to the actinides, that is, AnX_3, shows that there is greater pyramidality in the actinides than in the corresponding lanthanide compounds. This is consistent with an increase in SOJT distortion for the actinide compounds. These data suggest that there may be differences in the behaviour of the late actinides compared with the lanthanides, although it is not yet appar-

ent whether these differences will be present in compounds other than the MX_3 compounds considered here. Further systematic studies of the late actinides and the analogous lanthanides could provide useful information on this issue.

The research presented in this thesis suggests that computational electronic structure methods can now provide reliable information to theoreticians and experimentalists. In particular, issues concerning members of the lower part of the periodic table, namely heavier d-block elements and f-block elements, can be tackled reliably by theoretical means. Hence, there is greater scope than ever to gain further insight into heavy element complexes through a combined computational and experimental approach.

References

[1] N. Kaltsoyannis. *J. Chem. Soc., Dalton Trans.*, page 1, 1997.

[2] P. Pyykkö. *Chem. Rev.*, 88:563, 1988.

[3] M. Seth, P. Schwerdtfeger, M. Dolg, K. Faegri, B. A. Hess, and U. Kaldor. *Chem. Phys. Lett.*, 250:461, 1996.

[4] M. Dolg and H. Stoll. *Handbook on the Physics and Chemistry of Rare Earths*, Chapter 5, 1996.

[5] N. Kaltsoyannis and P. Scott. *The f Elements.* Oxford University Press, Oxford OX2 6DP, UK, 1999.

[6] D. F. Shriver and P. W. Atkins. *Inorganic Chemistry.* Oxford University Press, Oxford OX2 6DP, UK, third edition, 1999.

[7] M. R. Russo, N. Kaltsoyannis, and A. Sella. *J. Chem. Soc., Chem. Commun.*, page 2458, 2002.

[8] W. J. Evans and B. L. Davis. *Chem. Rev.*, 102:2119, 2002.

[9] J. K. Laerdahl and K. Faegri, Jr. *J. Chem. Phys.*, 109(24):10806, 1998.

[10] M. Seth, M. Dolg, P. Fulde, and P. Schwerdtfeger. *J. Am. Chem. Soc.*, 117:6597, 1995.

[11] W. Küchle, M. Dolg, and H. Stoll. *J. Phys. Chem. A*, 101:7128, 1997.

[12] M. Dolg, H. Stoll, and H. Preuss. *J. Mol. Struct. (Theochem)*, 231:243, 1991.

[13] W. Liu, M. Dolg, and P. Fulde. *J. Chem. Phys.*, 107(9):3584, 1997.

[14] P. J. Hay, W. R. Wadt, L. R. Kahn, R. C. Raffenetti, and D. H. Phillips. *J. Chem. Phys.*, 71(4):1767, 1979.

[15] R. D. Fischer. *Theor. Chim. Acta (Berlin)*, 1:418, 1963.

[16] A. Streitweiser Jr. and U. Müller-Westerhoff. *J. Am. Chem. Soc.*, 90:7364, 1968.

[17] A. Greco, S. Cesca, and G. Bertolini. *J. Organomet. Chem.*, 113:321, 1976.

[18] P. M. Boerrigter, E. J. Baerends, and J. G. Snijders. *Chem. Phys.*, 122:357, 1988.

[19] A. H. H. Chang and R. M. Pitzer. *J. Am. Chem. Soc.*, 111:2500, 1989.

[20] N. Kaltsoyannis and B. E. Bursten. *J. Organomet. Chem.*, 528:19, 1997.

[21] J. Li and B. E. Bursten. *J. Am. Chem. Soc.*, 120:11456, 1998.

[22] M. Pepper and B. E. Bursten. *Chem. Rev.*, 91:719, 1991.

[23] K. O. Hodgson, F. Mares, D. F. Starks, and A. Streitweiser Jr. *J. Am. Chem. Soc.*, 95:8650, 1973.

[24] C. S. Neumann and P. Fulde. *Z. Phys. B*, 74:277, 1989.

[25] M. Dolg, P. Fulde, W. Küchle, C. S. Neumann, and H. Stoll. *J. Chem. Phys.*, 94(4):3011, 1991.

[26] N. M. Edelstein, P. G. Allen, J. J. Bucher, D. K. Shuh, C. D. Sofield, N. Kaltsoyannis, G. H. Maunder, M. R. Russo, and A. Sella. *J. Am. Chem. Soc.*, 118:13115, 1996.

[27] M. Dolg, P. Fulde, H. Stoll, H. Preuss, A. Chang, and R. M. Pitzer. *Chem. Phys.*, 195:71, 1995.

[28] W. Liu, M. Dolg, and P. Fulde. *Inorg. Chem.*, 37:1067, 1998.

[29] G. Hong, F. Schautz, and M. Dolg. *J. Am. Chem. Soc.*, 121:1502, 1999.

[30] J. G. Brennan, F. G. N. Cloke, A. A. Sameh, and A. Zalkin. *J. Chem. Soc., Chem. Commun.*, page 1668, 1987.

[31] D. M. Anderson, F. G. N. Cloke, P. A. Cox, N. Edelstein, J. C. Green, T. Pang, A. A. Sameh, and F. Shalimoff. *J. Chem. Soc., Chem. Commun.*, page 53, 1989.

[32] J. Li and B. E. Bursten. *J. Am. Chem. Soc.*, 121:10243, 1999.

[33] G. Hong, M. Dolg, and L. Li. *Int, J. Quant. Chem.*, 80:201, 2000.

[34] B. E. Bursten and R. J. Strittmatter. *J. Am. Chem. Soc.*, 109:6606, 1987.

[35] B. E. Bursten, L. F. Rhodes, and R. J. Strittmatter. *J. Am. Chem. Soc.*, 111:2756, 1989.

[36] B. E. Bursten, L. F. Rhodes, and R. J. Strittmatter. *J. Am. Chem. Soc.*, 111:2758, 1989.

[37] R. J. Strittmatter and B. E. Bursten. *J. Am. Chem. Soc.*, 113:552, 1991.

[38] B. E. Bursten and R. J. Strittmatter. *Angew. Chem. Int. Ed. Engl.*, 30:1069, 1991.

[39] B. E. Bursten, M. Casarin, S. DiBella, A. Fang, and I. L. Fragala. *Inorg. Chem.*, 24:2169, 1985.

[40] K. Tatsumi and A. Nakamura. *J. Organomet. Chem.*, 272:141, 1984.

[41] R. Denning. *Struct. Bonding*, 79:215, 1992.

[42] H. H. Cornehl, C. Heinemann, J. Marcalo, A. P. de Matos, and H. Schwarz. *Angew. Chem. Int. Ed. Engl.*, 35(8):891, 1996.

[43] K. G. Dyall. *Mol. Phys.*, 96(4):511, 1999.

[44] Z. Zhang and R. M. Pitzer. *J. Phys. Chem. A*, 103:6880, 1999.

[45] W. A. de Jong, L. Visscher, and W. C. Nieuwpoort. *J. Mol. Struct. (Theochem)*, 458(1-2):41, 1999.

[46] N. Kaltsoyannis. *Inorg. Chem.*, 39(26):6009, 2000.

[47] C. K. Jørgensen and R. Reisfeld. *Struct. Bonding*, 50:121, 1982.

[48] K. Tatsumi and R. Hoffmann. *Inorg. Chem.*, 19:2656, 1980.

[49] W. R. Wadt. *J. Am. Chem. Soc.*, 103:6053, 1981.

[50] P. Pyykkö, L. J. Laakkonen, and K. Tatsumi. *Inorg. Chem.*, 28:1801, 1989.

[51] G. Schreckenbach, P. J. Hay, and R. L. Martin. *Inorg. Chem.*, 37:4442, 1998.

[52] G. Schreckenbach, P. J. Hay, and R. L. Martin. *J. Comp. Chem.*, 20:70, 1999.

[53] P. Pyykkö, Jian Li, and N. Runeberg. *J. Chem. Phys.*, 98:4809, 1994.

[54] R. D. Hunt, J. T. Yustein, and L. Andrews. *J. Chem. Phys.*, 98:6070, 1993.

[55] D. W. Green and G. T. Reedy. *J. Chem. Phys.*, page 2921, 1976.

[56] T. J. Tague Jr., L. Andrews, and R. D. Hunt. *J. Phys. Chem.*, 97:10920, 1993.

[57] C. Heinemann. *Chem. Eur.J.*, 1:7, 1995.

[58] L. Andrews, B. Y. Liang, J. Li, and B. E. Bursten. *Angew. Chem. Int. Ed. Engl.*, 39(24):4565, 2000.

[59] B. E. Bursten, M. L. Drummond, and J. Li. *Faraday Discussions*, 124(1-24):2003, 2003.

[60] L. Andrews, B. Y. Liang, J. Li, and B. E. Bursten. *New. J. Chem.*, 28(2):289, 2004.

[61] P. J. Hay, R. L. Martin, and G. Schreckenbach. *J. Phys. Chem. A*, 104:6259, 2000.

[62] J. Onoe, K. Takeuchi, J. Nakamatsu, T. Mukoyama, R. Sekine, and H. Adachi. *Chem. Phys. Lett.*, 196(6):636, 1992.

[63] J. Onoe, K. Takeuchi, H. Nakamatsu, T. Mokoyama, R. Sekine, B. Kim, and H. Adachi. *J. Chem. Phys.*, 99(9):6810, 1993.

[64] N. Kaltsoyannis and B. E. Bursten. *Inorg. Chem.*, 34:2735, 1995.

[65] G. Malli and J. Styszynksi. *J. Chem. Phys.*, 104(3):1012, 1996.

[66] P. J. Hay and R. L. Martin. *J. Chem. Phys.*, 109(10):3875, 1998.

[67] Y. K. Han and K. Hirao. *J. Chem. Phys.*, 113(7):7345, 2000.

[68] E. R. Batista, R. L. Martin, P. J. Hay, J. E. Peralta, and G. E. Scuseria. *J. Chem. Phys.*, 121(4):2114, 2004.

[69] W. R. Wadt and P. J. Hay. *J. Am. Chem. Soc.*, 101(18):5198, 1979.

[70] J. Onoe, H. Nakamatsu, T. Mukoyama, R. Sekine, H. Adachi, and K. Takeuchi. *Inorg. Chem.*, 36:1934, 1997.

[71] M. Schädel. *Acta Phys. Pol. B*, 34(3):1701, 2003.

[72] V. Pershina. *Chem. Rev.*, 96:1977, 1996.

[73] V. A. Glebov, L. Kasztura, V. S. Nefedov, and B. L. Zhuikov. *Radiochim. Acta*, 46:117, 1989.

[74] E. Eliav, U. Kaldor, and Y. Ishikawa. *Phys. Rev. Lett.*, 74:1079, 1995.

[75] E. Eliav, U. Kaldor, P. Schwerdtfeger, B.A. Hess, and Y. Ishikawa. *Phys. Rev. Lett.*, 73(24):3203, 1994.

[76] G. L. Malli and J. Styszynski. *J. Chem. Phys.*, 109(11):4448, 1998.

[77] G. L. Malli. *J. Chem. Phys.*, 116(3):5476, 2002.

[78] G. L. Malli. *J. Chem. Phys.*, 117(23):10441, 2002.

[79] M. Seth, P. Schwerdtfeger, and M. Dolg. *J. Chem. Phys.*, 106(9):3623, 1997.

[80] W. Liu and C. van Wüllen. *J. Chem. Phys.*, 110(8):3730, 1999.

[81] Y. K. Han, S. K. Son, Y. J. Choi, and Y. S. Lee. *J. Phys. Chem. A*, 103:9109, 1999.

[82] C. S. Nash and B. E. Bursten. *J. Am. Chem. Soc.*, 121:10830, 1999.

[83] V. Pershina and J. V. Kratz. *Inorg. Chem.*, 40:776, 2001.

[84] V. Pershina and T. Bastug. *J. Chem. Phys.*, 113(4):1441, 2000.

[85] V. Pershina, T. Bastug, B. Friske, and S. Varga. *J. Chem. Phys.*, 115(2):792, 2001.

[86] M. Seth, F. Cooke, P. Schwerdtfeger, J.-L. Heully, and M. Pelissier. *J. Chem. Phys.*, 109(10):3935, 1998.

[87] A. Szabo and N. S. Ostlund. *Modern Quantum Chemistry : Introduction to Advanced Electronic Structure Theory.* McGraw-Hill, Inc., New York, first (revised) edition, 1989.

[88] F. Jensen. *Introduction to Computational Chemistry.* John Wiley & Sons Ltd., West Sussex, PO19 1UD, England, 1999.

[89] C. J. Cramer. *Essentials of Computational Chemistry: Theories and Models.* John Wiley & Sons, Ltd., West Sussex, PO19 1UD, England, 2002.

[90] R.C. Parr and W. Yang. *Density-Functional Theory of Atoms and Molecules.* Oxford University Press, Inc., New York, 1989.

[91] W. Koch and M. C. Holthausen. *A Chemist's Guide to Density Functional Theory.* WILEY-VCH, Weinheim, Germany, second edition, 2001.

[92] J. C. Slater. *Phys. Rev.*, 81:385, 1951.

[93] S. H. Vosko, L. Wilk, and M. Nusair. *Can. J. Phys.*, 58:1200, 1980.

[94] A. D. Becke. *Phys. Rev. A*, 38:3098, 1988.

[95] J. P. Perdew and Y. Wang. *Phys. Rev. B*, 45:13244, 1991.

[96] J. P. Perdew, K. Burke, and M. Ernzerhof. *Phys. Rev. Lett.*, 77:3865, 1996.

[97] J. P. Perdew, K. Burke, and M. Ernzerhof. *Phys. Rev. Lett.*, 78:1396, 1997.

[98] J. P. Perdew. *Phys. Rev. B*, 33:8822, 1986.

[99] C. Lee, W. Yang, and R. G. Parr. *Phys. Rev. B*, 37:785, 1988.

[100] A. D. Becke. *J. Chem. Phys.*, 98:5648, 1993.

[101] J. P. Perdew, K. Burke, and M. Ernzerhof. *J. Chem. Phys.*, 105:9982, 1996.

[102] R. S. Mulliken. *J. Chem. Phys.*, 36:3428, 1962.

[103] A. E. Reed, R. B. Weinstock, and F. Weinhold. *J. Chem. Phys.*, 83(2):735, 1985.

[104] I. Mayer. *Chem. Phys. Lett.*, 97:20, 1983.

[105] K. Balasubramanian. *J. Phys. Chem.*, 93:6585, 1989.

[106] E. van Lenthe, R. van Leeuwen, E. J. Baerends, and J. G. Snijders. *Int. J. Quant. Chem.*, 57:281, 1996.

[107] E. van Lenthe, E. J. Baerends, and J. G. Snijders. *J. Chem. Phys.*, 105:6505, 1996.

[108] This work is published by E. O'Grady and N. Kaltsoyannis in. *J. Chem. Soc., Dalton Trans.*, page 1233, 2002.

[109] P. D. Lyne and M. P Mingos. *J. Chem. Soc., Dalton Trans.*, page 1635, 1995.

[110] N. Kaltsoyannis and P. Mountford. *J. Chem. Soc., Dalton Trans.*, page 781, 1999.

[111] A. A. Grinberg. *Acta Physicochim. URSS*, 3:573, 1935.

[112] E. M. Shustorovich, M. A. Proai-Koshits, and Y. A. Busalev. *Coord. Chem. Rev.*, 17:1, 1975.

[113] J. K. Burdett and T. A. Albright. *Inorg. Chem.*, 18:2112, 1979.

[114] Department of Theoretical Chemistry. *ADF2000.* Vrije Universiteit, 2000.

[115] E. J. Baerends, D. E. Ellis, and P. Ros. *Chem. Phys.*, 2:41, 1973.

[116] L. Verslius and T. Ziegler. *J. Chem. Phys.*, 88:322, 1988.

[117] G. te Velde and E. J. Baerends. *J. Comput. Phys.*, 99:84, 1992.

[118] C. Fonseca Guerra, J. G. Snijders, G. te Velde, and E. J. Baerends. *Theor. Chem. Acc.*, 99:391, 1998.

[119] A. J. Bridgeman. *MAYER.* University of Hull, 2001.

[120] F. Mariotti. http://sgich1.unifr.ch/ac/phd/fmariotti/ADFrom.html.

[121] http://www.cmbi.kun.nl/ schaft/molden/molden.html.

[122] R. J. Deeth, M. R. Bray, V. J. Paget, and P. D. Sheen. *Int. J. Quant. Chem.*, 61:85, 1997.

[123] B. Weinstock and G. L. Goodman. *Adv. Chem. Phys.*, 9:169, 1965.

[124] J. C. Taylor and P. W. Wilson. *Acta Crystallog.*, B30:1481, 1974.

[125] K. W. Bagnall, J. G. H. du Preez, and B. J. Gellatly. *J. Chem. Soc., Dalton Trans.*, page 1963, 1975.

[126] D. Brown, C. T. Reynolds, and P. T. Moseley. *J. Chem. Soc., Dalton Trans.*, page 857, 1972.

[127] A. J. Bridgeman, G. Cavigliasso, L. R. Ireland, and J. Rothery. *J. Chem. Soc., Dalton Trans.*, page 2095, 2001.

[128] This work is published by E. O'Grady and N. Kaltsoyannis in. *Phys. Chem. Chem. Phys.*, page 680, 2004.

[129] P. Pyykkö. *Angew. Chem. Int. Ed. Engl.*, 41(19):3573, 2002.

[130] P. Pyykkö and J. P. Desclaux. *Acc. Chem. Res.*, 12:276, 1979.

[131] P. Schwerdtfeger. *Hetero. Chem.*, 13(6):578, 2002.

[132] H. Schmidbaur. *Gold Bull.*, 33:3, 2000.

[133] P. Pyykkö. *Chem. Rev.*, 97:597, 1997.

[134] P. Schwerdtfeger, M. Dolg, W. H. E. Schwarz, G. A. Bowmaker, and P. D. W. Boyd. *J. Chem. Phys.*, 91(3):1762, AUG 1 1989.

[135] P. Schwerdtfeger, P. D. W. Boyd, A. K. Burrell, W. T. Robinson, and M. J. Taylor. *Inorg. Chem.*, 29(18):3593, SEP 5 1990.

[136] P. Pyykkö and Y. Zhao. *Angew. Chem. Int. Ed. Engl.*, 30(5):604, 1991.

[137] J. Li and P. Pyykkö. *Chem. Phys. Lett.*, 197(6):586, 1992.

[138] P. Pyykkö, J. Li, and N. Runeberg. *Chem. Phys. Lett.*, 218(1,2):133, 1994.

[139] P. Pyykkö, N. Runeberg, and F. Mendizabal. *Chem. Eur.J.*, 3(9):1451, 1997.

[140] P. Pyykkö and F. Mendizabal. *Chem. Eur.J.*, 3(9):1458, 1997.

[141] H. Schmidbaur, G. Weidenhiller, O. Steigelmann, and G. Müller. *Chem. Ber.*, 123:285, 1990.

[142] P. Pyykkö and T. Tamm. *Organometallics*, 17(22):4842, 1998.

[143] N. Runeberg, M. Schütz, and H. J. Werner. *J. Chem. Phys.*, 110(15):7210, 1999.

[144] L. Magnko, M. Schweizer, G. Rauhut, M. Schütz, H. Stoll, and H. J. Werner. *Phys. Chem. Chem. Phys.*, 4:1006, 2002.

[145] A. Codina, E. H. Fernández, P. G. Jones, A. Laguna, J. M. López de Luzuriaga, M. Monge, M. E. Olmos, H. Pérez, and M. A. Rodriguez. *J. Am. Chem. Soc.*, 124:6781, 2002.

[146] F. Mendizabal, P. Pyykkö, and N. Runeberg. *Chem. Phys. Lett.*, 370:733, 2003.

[147] X. Y. Liu, F. Mota, P. Alemany, J. J. Novoa, and S. Alvarez. *J. Chem. Soc., Chem. Commun.*, page 1149, 1998.

[148] A. Carvajal, X. Y Liu, P. Alemany, J. J. Novoa, and S. Alvarez. *Int, J. Quant. Chem.*, 86:100, 2002.

[149] M. A. Carvajal, S. Alvarez, and J. J. Novoa. *Chem. Eur.J.*, 10:2117, 2004.

[150] J. El-Bahraoui, J. A. Dobado, and J. M. Molina. *J. Mol. Struct. (Theo)*, 493:249, 1999.

[151] H. L . Hermann, G. Boche, and P. Schwerdtfeger. *Chem. Eur.J.*, 7(24):5333, 2001.

[152] S. Hofmann, V. Ninov, F. P. Heßberger, P. Armbruster, H. Folger, G. Münzenberger, H. J. Schött, A. G. Popeko, A. V. Yeremin, A. N. Andreyev, S. Saro, R. Janik, and M. Leino. *Z. Phys. A*, 350:281, 1995.

[153] M. Seth and P. Schwerdtfeger. *Chem. Phys. Lett.*, 318:314, 2000.

[154] Y.-K. Han and K. Hirao. *Chem. Phys. Lett.*, 328:453, 2000.

[155] M. Dolg, H. Stoll, M. Seth, and P. Schwerdtfeger. *Chem. Phys. Lett.*, 345:490, 2001.

[156] *Gaussian 98, Revisions A.9, A.10 and A.11.3.* M. J. Frisch, G. W. Trucks, H. B. Schlegel, G. E. Scuseria, M. A. Robb, J. R. Cheeseman, V. G. Zakrzewski, J. A. Montgomery, Jr., R. E. Stratmann, J. C. Burant, S. Dapprich, J. M. Millam, A. D. Daniels, K. N. Kudin, M. C. Strain, O. Farkas, J. Tomasi, V. Barone, M. Cossi, R. Cammi, B. Mennucci, C. Pomelli, C. Adamo, S. Clifford, J. Ochterski, G. A. Petersson, P. Y. Ayala, Q. Cui, K. Morokuma, D. K. Malick, A. D. Rabuck, K. Raghavachari, J. B. Foresman, J. Cioslowski, J. V. Ortiz, A. G. Baboul, B. B. Stefanov, G. Liu, A. Liashenko, P. Piskorz, I. Komaromi, R. Gomperts, R. L. Martin, D. J. Fox, T. Keith, M. A. Al-Laham, C. Y. Peng, A. Nanayakkara, M. Challacombe, P. M. W. Gill, B. Johnson, W. Chen, M. W. Wong, J. L. Andres, C. Gonzalez, M. Head-Gordon, E. S. Replogle, and J. A. Pople, Gaussian, Inc., Pittsburgh PA, 1998.

[157] MOLPRO is a package of *ab initio* programs written by H.-J. Werner and P. J. Knowles, with contributions from R. D. Amos, A. Bernhardsson, A. Berning, P. Celani, D. L. Cooper, M. J. O. Deegan, A. J. Dobbyn, F. Eckert, C. Hampel, G. Hetzer, T. Korona, R. Lindh, A. W. Lloyd, S. J. McNicholas, F. R. Manby, W. Meyer, M. E. Mura, A. Nicklass, P. Palmieri, R. Pitzer, G. Rauhut, M. Schutz, H. Stoll, A. J. Stone, R. Tarroni and T. Thorsteinsson.

[158] M. Dolg, U. Wedig, H. Stoll, and H. Preuss. *J. Chem. Phys.*, 86:866, 1987.

[159] D. Andrae, U. Häussermann, M. Dolg, H. Stoll, and H. Preuss. *Theor. Chim. Acta*, 77:123, 1990.

[160] P. Schwerdtfeger, H. L. Hermann, and H. Schmidbaur. *Inorg. Chem.*, 42:1334, 2003.

[161] G. Bowmaker, H. Schmidbaur, S. Krüger, and N. Rösch. *Inorg. Chem.*, 36:1754, 1997.

[162] M.A. Buijse and E. J. Baerends. *J. Chem. Phys.*, 93(6):4129, 1990.

[163] J. G. Snijders and P. Pyykkö. *Chem. Phys. Lett.*, 75(1):5, 1980.

[164] T. Ziegler, J. G. Snijders, and E. J. Baerends. *Chem. Phys. Lett.*, 75(1):1, 1980.

[165] O. Eisenstein and L. Maron. *J. Organomet. Chem.*, 647:190, 2002.

[166] A. Kovacs and R. J. M. Konings. *J. Phys. Chem. Ref. Data*, 33(1):377, 2004.

[167] M. Hargittai. *Chem. Rev.*, 100(6):2233, 2000.

[168] M. Kaupp. *Angew. Chem. Int. Ed. Engl.*, 40:3534, 2001.

[169] J. Molnar and M. Hargittai. *J. Phys. Chem.*, 99(27):10780, 1995.

[170] L. Perrin, L. Maron, and O. Eisenstein. *Faraday Discussions*, 124:25, 2003.

[171] E. D. Brady, D. L. Clark, J. C. Gordon, P. J. Hay, D. W. Keogh, R. Poli, B. L. Scott, and J. G. Watkin. *Inorg. Chem.*, 42(21):6682, 2003.

[172] S. G. Wang and W. H. E. Schwartz. *J. Phys. Chem.*, 99:11687, 1995.

[173] *Gaussian 03, Revision B.04.* M. J. Frisch, G. W. Trucks, H. B. Schlegel, G. E. Scuseria, M. A. Robb, J. R. Cheeseman, J. A. Montgomery, Jr., T. Vreven, K. N. Kudin, J. C. Burant, J. M. Millam, S. S. Iyengar, J. Tomasi, V. Barone, B. Mennucci, M. Cossi, G. Scalmani, N. Rega, G. A. Petersson, H. Nakatsuji, M. Hada, M. Ehara, K. Toyota, R. Fukuda, J. Hasegawa, M. Ishida, T. Nakajima, Y. Honda, O. Kitao, H. Nakai, M. Klene, X. Li, J. E. Knox, H. P. Hratchian, J. B. Cross, C. Adamo, J. Jaramillo, R. Gomperts, R. E. Stratmann, O. Yazyev, A. J. Austin, R. Cammi, C. Pomelli, J. W. Ochterski, P. Y. Ayala, K. Morokuma, G. A. Voth, P. Salvador, J. J. Dannenberg, V. G. Zakrzewski, S. Dapprich, A. D. Daniels, M. C. Strain, O. Farkas, D. K. Malick, A. D. Rabuck, K. Raghavachari, J. B. Foresman, J. V. Ortiz, Q. Cui, A. G. Baboul, S. Clifford, J. Cioslowski, B. B. Stefanov, G. Liu, A. Liashenko, P. Piskorz, I. Komaromi, R. L. Martin, D. J. Fox, T. Keith, M. A. Al-Laham, C. Y. Peng, A. Nanayakkara, M. Challacombe, P. M. W. Gill, B. Johnson, W. Chen, M. W. Wong, C. Gonzalez, and J. A. Pople, Gaussian, Inc., Pittsburgh PA, 2003.

[174] A. Bergner, M. Dolg, W. Küchle, H. Stoll, and H. Preuss. *Molecular Physics*, 80:1431, 1993.

[175] X. Cao and M. Dolg. *J. Molec. Struct. (Theochem)*, 581:139, 2002.

[176] X. Cao and M. Dolg. *J. Chem. Phys.*, 118:487, 2003.

[177] X. Cao and M. Dolg. *J. Molec. Struct. (Theochem)*, 673:203, 2004.

[178] X. Cao. Segmented Contracted Basis Sets for Ln and An. Correspondence.

[179] W. J. Hehre, R. Ditchfield, and Pople J. A. *J. Chem. Phys.*, 56:2257, 1972.

[180] E.D. Glendening, A. E. Reed, J. E. Carpenter, and F. Weinhold. NBO version 3.1.

[181] R. D. Shannon. *Acta. Cryst.*, A 32:751, 1976.

[182] S. Bagus, Y. S. Lee, and K. S. Pitzer. *Chem. Phys. Lett.*, 33:408, 1975.